

**REPORT DOCUMENTATION PAGE**

Form Approved  
OMB No. 0704-0188

The public reporting burden for this collection of information is estimated to average 1 hour per response, including the time for reviewing instructions, searching existing data sources, gathering and maintaining the data needed, and completing and reviewing the collection of information. Send comments regarding this burden estimate or any other aspect of this collection of information, including suggestions for reducing the burden, to Department of Defense, Washington Headquarters Services, Directorate for Information Operations and Reports (0704-0188), 1215 Jefferson Davis Highway, Suite 1204, Arlington, VA 22202-4302. Respondents should be aware that notwithstanding any other provision of law, no person shall be subject to any penalty for failing to comply with a collection of information if it does not display a currently valid OMB control number.  
**PLEASE DO NOT RETURN YOUR FORM TO THE ABOVE ADDRESS.**

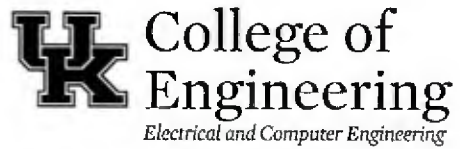
<b>1. REPORT DATE (DD-MM-YYYY)</b> 07/08/2019		<b>2. REPORT TYPE</b> Final Technical Report		<b>3. DATES COVERED (From - To)</b> 05/05/2015-05/04/2019	
<b>4. TITLE AND SUBTITLE</b> Market-Based Control of Shipboard Engineering Plants				<b>5a. CONTRACT NUMBER</b>	
				<b>5b. GRANT NUMBER</b> N00014-15-1-2475	
				<b>5c. PROGRAM ELEMENT NUMBER</b>	
<b>6. AUTHOR(S)</b> Cramer, Aaron, M.				<b>5d. PROJECT NUMBER</b>	
				<b>5e. TASK NUMBER</b>	
				<b>5f. WORK UNIT NUMBER</b>	
<b>7. PERFORMING ORGANIZATION NAME(S) AND ADDRESS(ES)</b> University of Kentucky Research Foundation 500 South Limestone 201 Kinkead Hall Lexington, KY 40526-0001				<b>8. PERFORMING ORGANIZATION REPORT NUMBER</b>	
<b>9. SPONSORING/MONITORING AGENCY NAME(S) AND ADDRESS(ES)</b> Office of Naval Research 875 N. Randolph St. Arlington, VA 22203				<b>10. SPONSOR/MONITOR'S ACRONYM(S)</b> ONR	
				<b>11. SPONSOR/MONITOR'S REPORT NUMBER(S)</b>	
<b>12. DISTRIBUTION/AVAILABILITY STATEMENT</b> Approved for Public Release; Distribution is Unlimited					
<b>13. SUPPLEMENTARY NOTES</b>					
<b>14. ABSTRACT</b> In the project, market principles were formally applied to the development of a shipboard power system control method, explicitly linking the economic behavior of the actors in the system (the commanding officer and the equipment in the engineering plant) with the physical behavior of the equipment in the system. Contributions have been made in terms of modeling and simulation, the principles of market-based control for systems, including decision functions, equivalence with optimal control, and clearing algorithms, and evaluation of system value based on an optimal control problem.					
<b>15. SUBJECT TERMS</b> Shipboard power system, optimal control, market-based control, modeling and simulation					
<b>16. SECURITY CLASSIFICATION OF:</b>			<b>17. LIMITATION OF ABSTRACT</b>	<b>18. NUMBER OF PAGES</b>	<b>19a. NAME OF RESPONSIBLE PERSON</b>
<b>a. REPORT</b>	<b>b. ABSTRACT</b>	<b>c. THIS PAGE</b>			<b>19b. TELEPHONE NUMBER (Include area code)</b>
U	U	U	UU	178	

# **Market-Based Control of Shipboard Integrated Engineering Plants**

Award No: N00014-15-1-2475

Final Technical Report

Aaron M. Cramer



## Contents

Introduction.....	1
Background .....	2
Microeconomic Theory .....	2
Market-Based Control .....	3
Technical Objectives and Approach .....	4
Research Objectives .....	4
Objective 1: Formulate market-based control method .....	4
Objective 2: Evaluate market-based control method performance .....	4
Objective 3: Identify the impact of market-based control method on system design .....	4
Research Plan .....	4
Overview .....	4
Task 1: Develop control method for consumer .....	5
Task 2: Develop control method for firms .....	7
Task 3: Integrate market-based control method .....	7
Task 4: Identify appropriate notional system, metrics, and scenarios .....	8
Task 5: Assess market-based control method with notional system .....	9
Task 6: Study impact of market-based control on early-stage system design.....	10
Technical Progress .....	10
Objective 1: Formulate market-based control method.....	10
Objective 2: Evaluate market-based control method performance .....	11
Objective 3: Identify the impact of market-based control method on system design .....	11
Accomplishments .....	11
Summary of Supported Work .....	12
Shipboard Power Systems.....	12
Control System Modeling in Early-Stage Simulation for Cyber Vulnerability Assessment	12
Market-Based Control of Electric Ship Power Systems.....	13
Early Stage Evaluation of Shipboard Power Systems Using Multi-Period Power Flow .....	13
Early-Stage Shipboard Power System Simulation of Operational Vignettes for Dependability Assessment.....	14
Light-Weight, Early Stage Power System Model for Time-Domain Simulation.....	15
Operational Vignettes-Based Electric Warship Load Demand .....	16
The Role of Future Information in Control System Design for Shipboard Power Systems .	16
Market-Based Control as a Paradigm for Power System Control .....	17

Power Electronics.....	18
Reactive Power Control Methods for Photovoltaic Inverters to Mitigate Short-Term Voltage Magnitude Fluctuations .....	18
Generalized Average Method for Time-Invariant Modeling of Inverters .....	19
Three-Phase Inverter Modeling using Multi-Frequency Averaging with Third Harmonic Injection .....	20
Electric Machinery .....	20
Hybrid Position Observer for Brushless DC Motor Drives with Improved Noise Immunity	20
Unified Model Formulations for Synchronous Machine Model with Saturation and Arbitrary Rotor Network Representation .....	21
Numerical Average-Value Modeling of Rotating Rectifiers in Brushless Excitation Systems .....	22
Formulation of Rectifier Numerical Average-Value Model for Direct Interface with Inductive Circuitry.....	22
Optimization Methods.....	23
Genetic Algorithm with Integrated Computing Budget Allocation for Stochastic Problems	23
Computing Budget Allocation in Multi-Objective Evolutionary Algorithms for Stochastic Problems .....	24
Appendices.....	25

## Introduction

Naval ships are evolving from efficient transport platforms to mobile power stations, supporting diverse missions ranging from littoral strike to ballistic missile defense. Advances in sensors and weaponry are increasing the demand for electric power throughout the warship, and such nonpropulsion loads are reaching historically high proportions of the total ship load. These advanced loads and the power system infrastructure that serves them also have escalating cooling requirements. Simultaneously, technology and affordability are driving the Navy toward more automated ships with reduced crew sizes. These conflicting requirements and constraints provide a compelling need for a new engineering and damage control system paradigm. In response to these changes, the Navy has established long-term technology priorities that will enable a transition to an electric fleet.

The integrated engineering plant (IEP) of an electric warship provides the escalating resources required by the ship such as electric power and thermal management to the ship. Recent developments in IEP design, such as the next generation integrated power system (NGIPS) architectures and novel thermal management techniques, are having two effects: they are making systems more capable, but they are also increasing system complexity. Existing conventional and rule-based control methods are brittle and not sufficiently resilient for such complex systems. Technologies such as distributed agents are promising, but much of their application has been ad hoc based on heuristic rules. If not addressed, the limitations of existing control methods threaten to jeopardize the gains achieved by insertion of new IEP technologies. The development of advanced control methodologies will ensure that advances in IEP design can continue to be realized in fielded systems.

The principal investigator (PI), Dr. Aaron Cramer, proposed to develop a market-based control method for agile, resilient, effective, and efficient control of progressively more complex electric warship IEPs. This goal was accomplished through three objectives. First, the PI formulated a market-based control method. Next, he evaluated the market-based control method performance. Finally, the impact of the market-based control method on system design was identified. Market-based control is an approach in which resources are artificially priced according to laws of supply and demand and the operation of equipment is governed by profit-seeking behavior. For example, given the price of power at its input and output terminals, a power converter will be programmed to convert an amount of power that corresponds to its profit-maximizing output. The prices of goods in the system reach equilibrium values when the demand for resources is equal to the supply of those resources. When insufficient resources are available, prices rise, and resources are diverted toward their most productive uses.

The PI formally applied market principles to the development of the control method, explicitly linking the economic behavior of the actors in the system (the commanding officer (CO) and the equipment in the IEP) with the physical behavior of the equipment in the system. The proposed method can handle general systems with multiple resources, allowing the complex dynamic interdependence between electrical and thermal management systems to be considered when making resource allocation decisions. The proposed method also treats energy storage and other dynamic elements that transform the static resource allocation optimization problem into a dynamic optimal control problem in which the performance of the system over time is of interest. As mission priorities change, prices in the system will adjust automatically to reach the optimal allocation of resources, resulting in an agile system. The proposed control method is also

applicable to multiple classes of ship, a marked departure from existing power control design approaches that only apply to one class of ship.

The U.S. Navy has developed an NGIPS roadmap that leads to medium voltage dc (MVDC) systems. This proposed market-based control method allows for the benefits of an MVDC system to be realized. The increased quantity of power converters in an MVDC system allows the control system to take a more active role in the distribution of electric power. Increasingly sophisticated thermal management systems will allow similar control over the allocation of cooling capacity. The integration of electric, and even thermal, energy storage devices will provide opportunities for dynamic market behavior analogous to that of a broker, buying when prices are low and selling when prices are high. These developments create an opportunity for the successful application of a market-based control method to the IEPs of electric warships.

Market-based control algorithms can maximize resource management under highly dynamic and uncertain conditions. These attributes are critical to the success of complex, dynamically interdependent distributed combat systems. The proposed market-based control method provides a mathematical foundation for distributed control systems which are:

- Agile: can quickly redirect power when and where it is needed,
- Resilient: can reconfigure and adapt,
- Dependable: can provide power continuity to maintain the operational status of mission-critical systems,
- Effective: obtain maximum utility from the installed power, and
- Efficient: reduce fuel consumption and thus extend ship range and capabilities.

## ***Background***

### **Microeconomic Theory**

The proposed market-based control method involves the construction of an artificial market in which resources are bought and sold. Economics can be defined as the study of the allocation of scarce goods that have alternative uses. As electric power and thermal management resources are scarce and have alternative uses, the control of shipboard IEPs is inherently an economics problem. The proposed development of a market-based control method based on microeconomic principles is both novel and likely to provide agile, resilient, effective, and efficient control of electric ship IEPs because of the underlying economic nature of this control problem.

The PI proposed to develop a market-based control method for shipboard IEPs, while advancing the theory of market-based control for complex systems. In economic systems, firms produce output goods using input goods. These input goods can be either goods purchased from other firms or goods purchased from individuals (e.g., labor or capital). The profit a firm receives is the difference of the revenue from the sale of the output goods and the cost of the necessary input goods. Firms produce goods at an output level that maximizes their profit. In a perfectly competitive market, firms are price takers; they cannot individually affect the prices of either their input or output goods. Instead, these prices are set by the larger operation of the economy, Adam Smith's invisible hand. By the law of supply, firms will produce a higher quantity of a good when the price of that good increases. This action represents movement along the supply curve, a graphical representation of the function that maps each price to the quantity of the good that the firm will produce at that price.

Consumers make decisions designed to maximize their utility, a measure of benefit associated with a state of being, typically a certain level of consumption of a good. Utility typically

increases as consumption increases, but it will usually increase at slower rates, resulting in diminishing marginal utility. By maximizing utility subject to their budget constraints, consumers will purchase certain quantities of goods at each price. By the law of demand, consumers will purchase less of a good as the price of the good rises. This behavior stems from the fact that as the price of the good rises, alternative goods can be substituted less expensively. The demand function maps each price to the quantity of goods a consumer will purchase at that price.

Equilibrium occurs when the price is such that the quantity supplied is equal to the quantity demanded. This is illustrated in Fig. 1. When total equilibrium in an economy is reached, the prices of all goods in the economy are such that the quantities supplied and demanded for each good in the economy are equal. Under certain conditions, it can be shown that a perfectly competitive market economy in total equilibrium is Pareto-efficient. This means that goods are being allocated in such a way that no consumer can receive more utility without another consumer receiving less. In other words, the market economy efficiently allocates resources such that the preferences of all the consumers are met. This operation happens organically, in a decentralized manner, where no central controller has to tell each firm how much to produce. These decisions are made by the firms pursuing profit, and the competition of the market results in an optimal allocation to the consumers. The central idea of this project was to develop an artificial perfectly competitive market in which various shipboard resources are distributed according to market forces that guide each resource toward its most productive use.

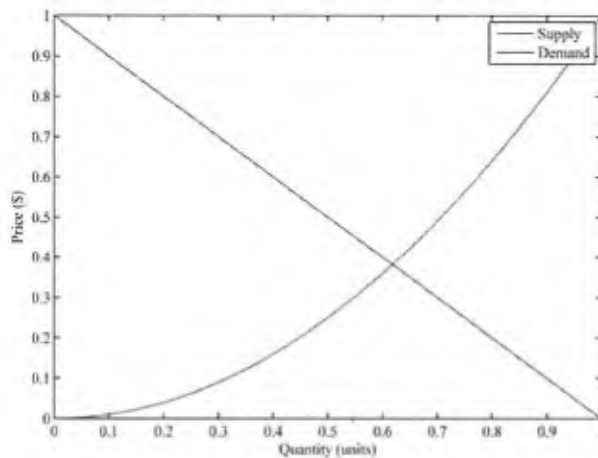


Fig. 1. Example Supply and Demand Curves

### Market-Based Control

Market-based control has been applied in a variety of settings. It is commonly used for resource allocation within communication networks, but it has also been applied to building climate control systems, the control of structures, and other areas. The ordinary operation of power system markets and the economic dispatch problem are themselves related to market-based control; however, market-based control often implies an artificial market structure.

The use of auctions in agent-based control techniques represents a heuristic market-based approach. This approach is seen in several agent-based approaches. The principal distinction between the proposed approach and these agent-based approaches is the level of formalism with which the economic phenomena are treated. The agent-based techniques tend to approach the price of goods as a useful heuristic instead of an intrinsic property that stems from the scarcity present in the system. They construct somewhat arbitrary supply and demand functions that have

appropriate characteristics but do not explicitly correspond to the physical behavior of the system. The proposed market-based control method involves the use of supply and demand functions that are formally derived from the physical characteristics of the shipboard equipment and the mission requirements of the CO.

## **Technical Objectives and Approach**

### ***Research Objectives***

The overall goal of the proposed research was to develop a market-based control method for shipboard IEPs. This goal was realized through the following objectives.

#### **Objective 1: Formulate market-based control method**

The proposed market-based control method needed to be mathematically formulated. This required the development of control methods for the consumer (the CO) and for firms (the equipment within the IEP) and the integration of these control methods to form the overall market-based control system for shipboard IEPs.

#### **Objective 2: Evaluate market-based control method performance**

The performance of the proposed market-based control method needed to be evaluated. First, an appropriate notional IEP was identified; performance metrics and operational scenarios were selected. Then, the market-based control method was assessed in steady state under various conditions and during dynamic events caused by changes in mission or plant lineup or equipment failures. Finally, the small- and large-signal stability of the market-based control method was analyzed.

#### **Objective 3: Identify the impact of market-based control method on system design**

How and to what extent the use of the proposed market-based control method will affect the design of shipboard IEPs must be identified. Highly successful early-stage design techniques for shipboard engineering systems often assume quasi-optimal behavior from the control system. This is a limiting assumption necessitated by the difficulty of modeling existing control approaches during the early design stage. It is desirable to understand how the application of the market-based control method will affect the arrangement, sizing, and configuration of IEP components. As the market-based control method is generalizable to various shipboard IEPs, it is possible to represent it effectively during the early design stage. This is not possible with existing control methods because they are generally based on specific IEP designs and cannot be well understood until more detailed design is performed. An understanding of the impact of the market-based control method on system design can lead to standards development that will facilitate an open-architecture approach and wide-scale application of the control method.

### ***Research Plan***

#### **Overview**

The proposed control method will consist of an artificial market in which various actors (a consumer and firms) behave according to microeconomic principles. Examples of such actors include generation, distribution, conversion, energy storage, pumps, air conditioning plants,

throttle valves, and the CO. Each piece of equipment within the engineering plant will behave as a firm, attempting to maximize its profit. The CO will behave as a consumer, attempting to maximize his or her utility. Herein, the CO designates the actual CO and/or any other individual(s) acting on behalf of him or her. As the CO has full responsibility for and authority over the ship, optimal performance of the shipboard IEP entails meeting the objectives of the CO. If the market is designed properly, it will allocate the resources within the system efficiently to meet the objectives of the CO.

This control strategy does not inherently depend on the mode of operation. If the CO's objectives change (e.g., cruising vs. battle), the market reacts, prices shift, and resources are allocated to new purposes. If the structure of the system changes (e.g., due to a change in plant lineup or due to battle damage), the prices will change to reflect the new conditions, and the market will attempt to meet the CO's objectives in the most efficient manner under the new configuration. In this way, a unified control strategy can be applied to achieve various objectives, such as fuel efficiency, continuity of service, and survivability.

In order to formulate the market-based control method, the control methods for the consumer (the CO) and the firms (IEP equipment) were developed. These control methods were then integrated to constitute the proposed market-based control method. After an appropriate notional IEP, performance metrics, and operational scenarios were identified, the performance of the proposed market-based control method was assessed. Finally, the impact of the market-based control method on system design was evaluated using Dr. Cramer's previous work in early-stage modeling, simulation, and analysis. The objectives described above were satisfied by the successful completion of the tasks described below.

### **Task 1: Develop control method for consumer**

Because engineering systems exist to provide value to stakeholders, the satisfaction of stakeholder objectives is the objective criteria by which system performance should be measured. In the case of electric warships, the stakeholder is the CO, who enjoys full authority over the ship. In an electric warship IEP, the IEP itself provides no direct war-fighting ability; its value stems from its ability to provide services to mission loads. For this reason, the measure of system performance should be primarily load oriented: The IEP is performing well if it is serving the most important loads, i.e., those that the CO requires in order to accomplish his or her mission.

Translation of CO objectives into a utility function drives the entire operation of the market-based control strategy. A utility function measures the benefit derived by an individual from a specific state of affairs. Economically, this state is often a certain level of consumption of various goods. The utility function and the budget of the consumer determine the consumer's demand for goods and the combination of goods that the consumer will ultimately purchase. This is shown in Fig. 2. Utility functions define indifference curves that represent combinations of goods between which the consumer is indifferent. The consumer will select the combination of goods that maximizes utility subject to the consumer's budget constraint.

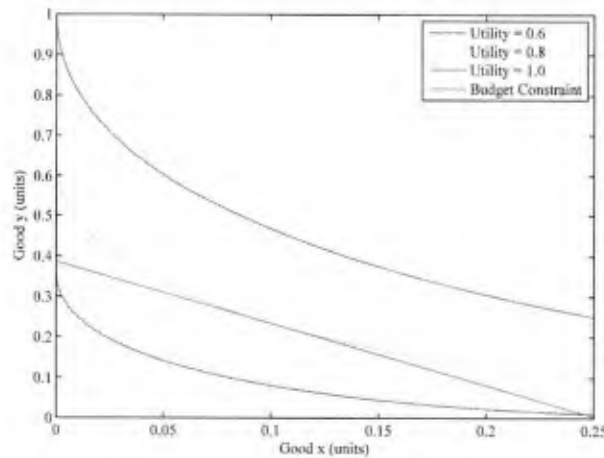


Fig. 2. Consumer Indifference Curves and Budget

An important aspect of utility theory is that utility functions encode an individual's risk preferences. This means that the individual will attempt to maximize the expected value of utility. Risk-averse individuals will have a concave utility function and diminishing marginal utility. Even if two alternatives have the same expected value, they may have different expected utilities due to differences in perceived risk. Proper characterization of the CO's objectives includes the CO's risk preferences in order to allow risk-conscious decision making by the control system.

Another aspect of CO objectives is the time dependence of these objectives. Rational decision makers are commonly held to discount future utility, that is, they are likely to prefer a reward today than the same reward tomorrow. A common method of discounting utility involves exponential discounting wherein the decision maker seeks to maximize a weighted temporal average of an instantaneous measure of utility. The interplay between discounting and risk aversion explains the choices that individuals make between present consumption and saving (future consumption). It drives the behavior of time-dependent elements such as energy storage. For example, this interplay is the reason for charging uninterruptible power supplies in the present (saving) to allow for use of that energy in the future (consumption).

Having defined the CO's utility function, the behavior of the CO is modeled using the economic theory of the consumer. A consumer acts to maximize his or her expected utility, and this behavior consists of two key attributes. The first attribute is consumption. Consumption of resources by mission loads helps to fulfill the CO's objectives, thereby providing utility. The CO chooses how to consume resources by maximizing utility subject to budget constraints as shown above in Fig. 2. However, the budget of the CO is constrained by the prices of the resources that mission-critical loads require.

The other attribute of consumer behavior is the investment decisions of the consumer. As the CO is the sole consumer in the shipboard resource market economy, he or she is responsible for all investment within the economy. Investment in this context represents a firm purchasing a good now so that it may sell a good later and realize a return. Equipment that requires such investment must offer a rate of return sufficiently high to incentivize the CO to invest. For example, an energy storage device requires the CO to expend some power charging it. The CO will only pay the price to charge it because he or she expects that there is a high enough probability that prices will increase. If prices rise (e.g., due to a generator tripping offline), then there is an increase in utility (e.g., operation of loads that would otherwise have to shut down).

The control method for the consumer balances consumption and investment decisions in order to maximize the expected utility of the consumer. Such a model requires the solution of an optimal control problem in order to determine the optimal consumption path of the CO. The model is used to specify the demand curves of the CO for resources needed by mission loads and the supply curves of the CO for investment needed to operate devices like energy storage devices.

### **Task 2: Develop control method for firms**

The behavior of firms, i.e., the equipment within the IEP, is modeled using the economic theory of the firm, where the firm acts to maximize profit. As a component within the IEP, the firm must purchase certain inputs (e.g., input power, thermal management resources) in order to produce a given level of output (e.g., output power). By incorporating a profit motive in the action of the firms, the overall system behavior is coordinated.

An interesting aspect of the behavior of firms that must be considered in this effort is their management of consumer investment. If a firm instantaneously converts inputs to outputs, there is no need to consider the stewardship of consumer investment. The firm can instantaneously pay for its inputs from the proceeds of the sale of its outputs. However, in the case of an electric warship with multiple resources, investment must be considered because of the varying time scales involved with the resources. For example, consider a power converter that converts an amount of input power to an amount of output power with a given efficiency. The power conversion process happens approximately instantaneously. However, the power converter also generates a certain amount of heat that must ultimately be removed. Because thermal time constants are slower than electrical time constants and the constraint on the converter is that its temperature must not exceed some threshold, it is possible for the converter to buy less cooling in the short run, thereby warming up. This scenario is particularly beneficial if the price of cooling resources is expected to fall in the near future, at which time the converter can purchase additional cooling in order to return to equilibrium temperature. The difference between the converter's maximum and ordinary operating temperatures represents operating capital held by the converter. The firm will seek capital from the consumer based on the prevailing interest rate.

### **Task 3: Integrate market-based control method**

In this task, the control methods for the consumer and for the firms developed in Tasks 1 and 2 were combined to complete the market-based control method. By the first theorem of welfare economics, a perfectly competitive market economy in total equilibrium is Pareto-efficient under certain conditions. This means that goods are being allocated in such a way that no consumer can receive more utility without another receiving less. Because the only consumer in the proposed artificial market is the CO, the system will reach an equilibrium point that maximizes the CO's utility, i.e., the optimal operating condition. The key limitations of practical markets are avoidable because the proposed market is artificial. For example, the exercise of market power, i.e., the ability of a single actor to influence prices, results in suboptimal market performance. Market power is possible when there are few actors in a market, as there are in the proposed market. However, these actors are not self-interested market participants; they can be designed to operate as price takers instead of price setters, restoring efficient operation of the market economy. A novel aspect of this approach is that each actor is pursuing its own local objectives and the resulting equilibrium is globally optimal.

Another aspect of integrating the market-based control method is clearing the market. The market is said to be cleared when prices are such that the quantities of each good supplied and

demand are equal. This corresponds to market equilibrium, which is reached by arriving at a set of prices that corresponds to this condition. By the laws of supply and demand, prices will move in order to reach this equilibrium.

Several approaches to solving the market clearing problem have been demonstrated in Dr. Cramer's previous efforts. In particular, he has applied a distributed approach in which the pricing information is encoded into the droop controls that are used to facilitate load sharing. This type of approach requires no communication among the actors, but can have slower convergence than other methods. To improve convergence, a combination structure in which distributed techniques are supplemented with hierarchical data was pursued. Using this technique, the hierarchical approach may be used when it is available, speeding the convergence of the algorithm. Stable methods for reaching global equilibrium using Lyapunov's method have also been demonstrated. However, the combined method should not rely on the existence of the hierarchical structure. Thus, the survivability benefits associated with a distributed approach are preserved. The three approaches are illustrated in Fig. 3. As demonstrated in this figure, three levels of communication between market actors are available. In the first level, every actor can communicate with every other actor, and the general equilibrium for the system can be calculated directly. In the second level, actors can only communicate with actors that participate in the same market (i.e., that buy or sell the same good as the actor). In the third level, no direct communication between actors is available.

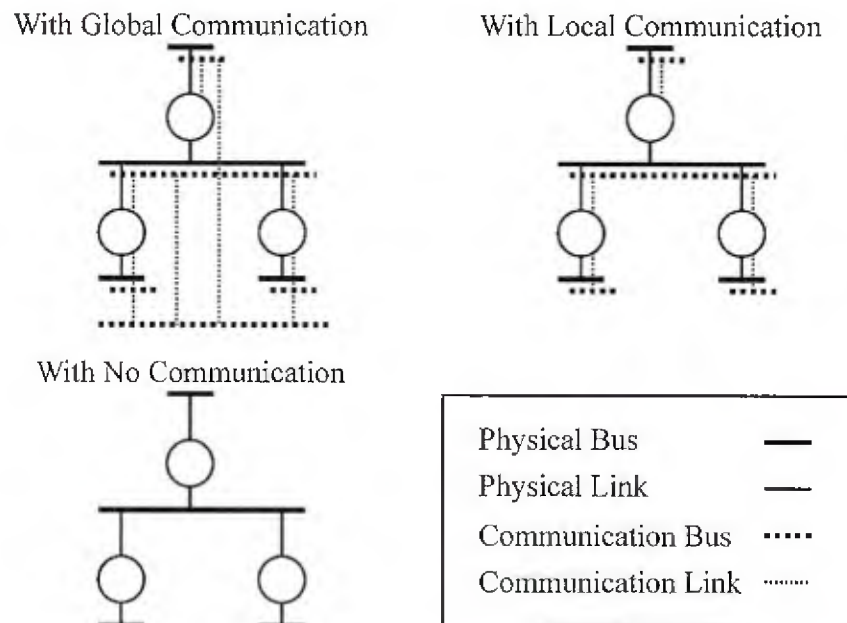


Fig. 3. Hierarchical/Distributed Control Approach

#### Task 4: Identify appropriate notional system, metrics, and scenarios

The PI worked with the electric ship research community to identify an acceptable notional system to perform preliminary testing of the proposed control system. There are widely available models of notional electric warship IEPs. The model shown in Fig. 4 and Fig. 5 was developed by the PI and is based on the Electric Ship Research and Development Consortium (ESRDC) notional MVDC system and was used as a baseline for this task. An appropriate system model is sufficiently complex to test the control method rigorously, include different types of energy storage (e.g.,

power vs. energy dense), and have different operational modes (e.g., cruise vs. battle). The physics-based models of the equipment in the system were analyzed to establish the behavior of the firms in the system in accordance with the results of Task 1.

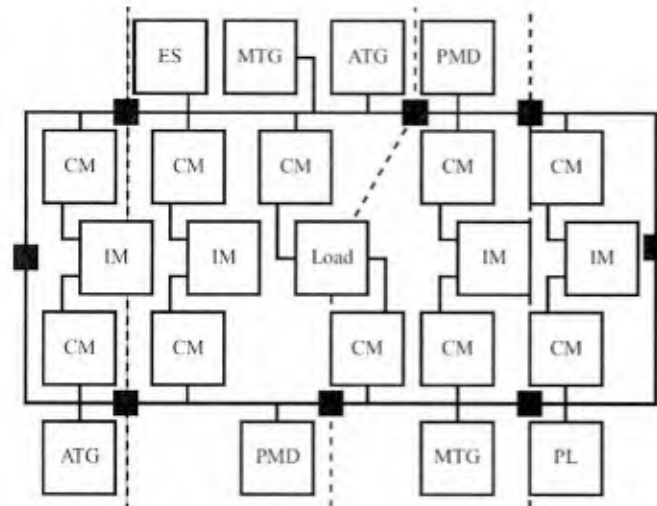


Fig. 4. Notional MVDC System

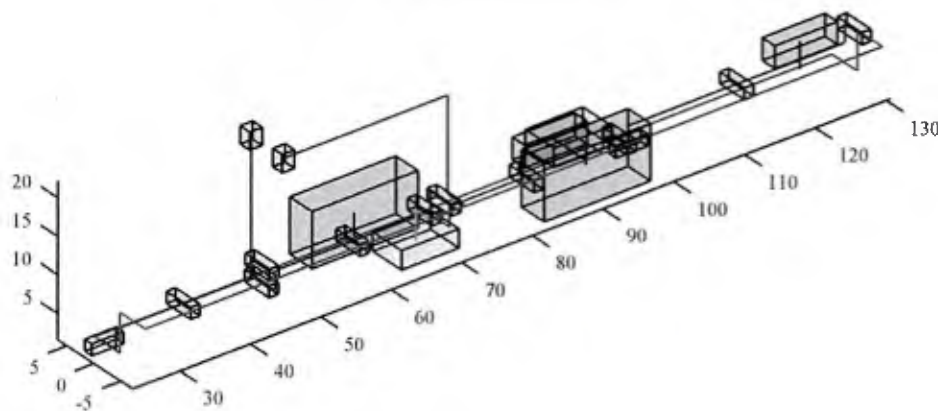


Fig. 5. Arrangement of Notional System

Additionally, representative control metrics were identified. The control metrics represent the objectives of the CO and include efficiency, quality of service, and mission-based prioritization of loads. These metrics were used to establish the behavior of the consumer in the system. These metrics also guided the selection of operational scenarios in which the control system performance was evaluated.

**Task 5: Assess market-based control method with notional system**

For this task, the market-based control method developed in Task 3 was assessed using the notional system, metrics, and operational scenarios identified in Task 4. Simulation studies of the system in steady-state conditions were conducted corresponding to various operational modes (e.g., cruise vs. battle) wherein different loads may be operational and different performance objectives may be of importance.

The system was also simulated during dynamic events caused by changes in mission or plant lineup or equipment failures. This step included the study of equipment that fails randomly due to reliability limitations, the effects of battle damage, and the effects of compromised equipment incorrectly participating in the control system (e.g., due to cyber vulnerability). These dynamic studies assessed the agility and resilience of the IEP control system.

### **Task 6: Study impact of market-based control on early-stage system design**

The sixth task was to examine the effect of the market-based approach on IEP design. This task used the market-based control method developed in Task 3 and previous work by the PI on early-stage design to examine the effect of the market-based control method on early-stage system design. It is necessary to understand how application of a market-based control method may alter the assumptions that are made during the design process. For example, highly successful early-stage design techniques for shipboard IEPs developed by the PI assume quasi-optimal behavior from the control system. Such assumptions can be improved upon by consideration of the market-based control.

One of the impediments to considering the control system formally in early-stage design is that control systems are generally poorly defined at that point in the design process. However, the market-based control method is generalizable to various shipboard IEPs. Furthermore, it behaves similarly for alternative IEPs. Therefore, it is possible to represent the behavior of the control system in the early design stage. By developing an appropriate early-stage model of the market-based control method, it will be possible to assess how the market-based control system affects the arrangement, sizing, and configuration of IEP components.

An understanding of the impact of the market-based control method on system design can then lead to standards development, which will facilitate an open-architecture approach and lead to wide-scale application of the control method. Also in this task, transition opportunities for the market-based control method will be explored, which will allow the research sponsored by the Office of Naval Research (ONR) to transition to the fleet.

## **Technical Progress**

The overall goal of the proposed research was to develop a market-based control method for shipboard IEPs. This goal was realized through the following objectives.

### ***Objective 1: Formulate market-based control method***

Objective 1 was addressed by integrating the market-based control method. The control methods for the consumer and for the firms were combined to complete the market-based control method. By the first theorem of welfare economics, a perfectly competitive market economy in total equilibrium is Pareto-efficient under certain conditions. This means that goods are being allocated in such a way that no consumer can receive more utility without another receiving less. Because the only consumer in the proposed artificial market is the CO, the system will reach an equilibrium point that maximizes the CO's utility, i.e., the optimal operating condition.

Another aspect of integrating the market-based control method is clearing the market. The market is said to be cleared when prices are such that the quantities of each good supplied and demanded are equal. This corresponds to market equilibrium. By the laws of supply and demand, prices will move in order to reach this equilibrium.

Several approaches to solving the market clearing problem have been demonstrated, and their convergence properties have been studied. Completion of this objective completes the

proposed market-based control method, resulting in a control system that can automatically respond to changes in mission, changes in plant lineup, or equipment malfunction. The system will be extensible to alternative IEP designs and will handle multiple resources, allowing optimal control of the IEP.

### ***Objective 2: Evaluate market-based control method performance***

Objective 2 was addressed by identifying an appropriate notional system, metrics, and scenarios. The PI has worked with the electric ship research community to identify an acceptable notional system to perform preliminary testing of the proposed control system. There are widely available models of notional electric warships. The model considered was developed by the PI and is based on the Electric Ship Research and Development Consortium notional MVDC system and was to be used as a baseline for this effort. An appropriate system model will be sufficiently complex to test the control method rigorously, include different types of energy storage (e.g., power vs. energy dense), and have different operational modes (e.g., cruise vs. battle). The physics-based models of the equipment in the system will be analyzed to establish the behavior of the firms in the system in accordance with the resulting control method for the consumer.

### ***Objective 3: Identify the impact of market-based control method on system design***

Objective 3 was addressed by examining the effect of the market-based approach on IEP design. The market-based control method developed from Objective 1 was to be simulated to examine the effect of the market-based control method on early-stage system design.

One of the impediments to considering the control system formally in early-stage design is that control systems are generally poorly defined at that point in the design process. However, the market-based control method is generalizable to various shipboard IEPs. Furthermore, it behaves similarly for alternative IEPs. Therefore, it is possible to represent the behavior of the control system in the early design stage. By developing an appropriate early-stage model of the market-based control method, it will be possible to assess how the market-based control system affects the arrangement, sizing, and configuration of IEP components.

An understanding of the impact of the market-based control method on system design can then lead to standards development, which will facilitate an open-architecture approach and lead to wide-scale application of the control method. Transition opportunities for the market-based control method will be explored, which will allow the research sponsored by the Office of Naval Research (ONR) to transition to the fleet.

This represents a step towards further development and maturation of the market-based control method. It will facilitate future development efforts involving market-based control methods and other advanced control methods for electric warship IEPs. The primary work in this area has been the incorporation of the market-based control principles into the use of optimal-control-theory-based evaluation of shipboard systems.

### ***Accomplishments***

Progress has been made toward the research objectives as presented below.

A number of contributions have been made in terms of modeling and simulation. These include splitting representations of physical and control systems, examination of cyber disruptions, multi-period analysis for approximation of optimal behavior, and representation of market-based control in simulation studies.

The principles of market-based control for systems involving various resources in different locations have been formalized for shipboard systems, including specific decision functions for various equipment types. The equivalence of these methods with optimal shipboard power system control have been demonstrated, and the application of these methods in dynamic loading and fault situations has been studied. New methods with better convergence properties for clearing market systems based on both the alternating direction method of multipliers and the Broyden-Fletcher-Goldfarb-Shanno algorithm have been developed. These have shown a capability to arrive at the market-clearing set of prices robustly and quickly.

The work evolved into a direction in which it became necessary to have a closer understanding of how a CO should value certain system states, which led to consideration of the underlying optimal control problem. A power allocation strategy that uses state-space models to represent the evolution of both the mission and the engineering system that is supporting the mission was developed. An optimal control problem is solved to maximize a functional over the mission state and actions. By doing so, it indicates the capability of the engineering system to support such missions. The uniqueness of this approach is that solutions become far more mission specific. This approach has been demonstrated on a simple two-function platform—each competing for the same limited power resources—, and it is shown that this approach can be used to assess the probability of success given a certain initial allocation of power.

In addition to work that directly supported the main research objectives of the project, the graduate students involved in the project have made other significant progress in related areas of power electronics, electric machinery, and optimization with the support of the project.

## **Summary of Supported Work**

The published works that have been supported by this project are summarized below, and these works are included within the appendices of this document. First, the work directly related to the main project objectives is described, and this is followed by the related work in power electronics, electric machines, and optimization methods.

### ***Shipboard Power Systems***

#### **Control System Modeling in Early-Stage Simulation for Cyber Vulnerability Assessment**

Time-domain simulation techniques often used in quantifying the performance of power systems, e.g. shipboard power system, are expected to be computationally efficient and exhibit adequate level of details for the particular simulation.

Thus, in this research effort, the shipboard power system's reduced-order model is combined with an independent depiction of the control system. This enables faster simulation and a retained reduced modeling effort, which enhances better understanding of the control system's effect on shipboard power system performance.

To illustrate this approach, false set points representing a cyberattack are injected into a compromised control system. By calculating the system dependability, the performance of a compromised control system is compared with that of an uncompromised control system, using a conceptual MVDC system and a representative operational vignette. Using a linear programming problem, the behavior of the power system is estimated. The compromised controller is depicted as behaving as an idealized controller until an attack.

The operability metric is observed during the vignette. It determines the extent to which the power system performance will contribute to effectiveness of mission during a particular scenario. The calculated operability of the power system for the representative vignette is 98.97% for the uncompromised control system and 95.51% for the compromised control system.

The expected value of dependability over a distribution of events that the system could face is known as average dependability. Using the Monte Carlo approach, the average system dependability is 98.43% after the disruptions. The worst case system operability using the Monte Carlo approach is 69.46%.

An approach in which a controller model is represented within a mathematical programming-based simulation approaches for shipboard power system is presented in this research effort. Based on the calculation results of the average and minimum system dependability, it is shown that the system is susceptible to some disruptions despite the fact that the average dependability remains high.

In general, this paper tends to serve the following purposes: to demonstrate a methodology for integrating non-ideal controller into the simulation model, illustrate the approach on a compromised control system prone to cyber disruption, and to determine the dependability of a notional system prone to cyber disruption during an operational vignette.

### **Market-Based Control of Electric Ship Power Systems**

The gradual evolution of naval ships from efficient transport system to mobile power system will require consideration of a new paradigm of control, in order to meet up with the conflicting requirements of providing power to support diverse missions, automation of ships and reduced crew sizes. Integration of ship power system with energy storage (for managing the energy 'bank account') also provides more support for the argument for a new control paradigm.

A market-based approach for the control of power flow in a shipboard power system is presented in this work. It consists of an artificial market in which micro-economic principles dictate the behavior of the consumer (commanding officer) and firms (each piece of equipment), who are the actors in the representative market economy. Market prices automatically adjusts itself due to change of mission priorities or objectives (e.g. cruising vs battle), to attain optimal allocation of resources.

The proposed control method is demonstrated on both simple illustrative example system and a notional Medium Voltage DC (MVDC) system. The illustrative example system consists of a generator, an interconnect, a non-linear load and a consumer. The four-bus zone MVDC has a variety of components such as generators (two main generators and two auxiliary generators), interconnects, converters, energy storage and loads. Market-based control clearly links the economic behavior of the actors in the system (consumer and firms) with the physical behavior of the equipment in the system.

Simulations studies of a notional electric power system in both normal and faulty conditions are performed. The proposed-market based control system results in performance equal to that of an idealized controller.

### **Early Stage Evaluation of Shipboard Power Systems Using Multi-Period Power Flow**

Rising demand for power from various mission loads coupled with emerging generation and storage technologies have made the design and analysis of shipboard power system more challenging. In this work, a technique for early stage evaluation of the relative performance of

various shipboard power system design is described. A known future is assumed and the performance of the various controller designs, subject to some six-mission scenarios on a representative multi-bus power system configuration is calculated.

The proposed early stage design evaluation of power system of the shipboard include energy storage and dynamic loads. Using an optimization-based algorithm, a set of probable mission scenarios with known future load is considered and a best-case upper bound for any controller performance is produced. Any controller cannot exceed this upper-bound limit. Thus, analysis of the power system is possible without any special controller design for each candidate power system. This allows for fast, automated evaluation of the system prior to the design of the controllers. Since comparison of the performance of various power system architecture does not depend on any particular controller design, but on the architecture itself, the proposed method provides a fair comparison. The feasibility of providing power to various mission loads, rather than fuel consumption or other metric optimization is of primary interest in this research endeavor.

For each mission scenario, the algorithm determines the feasibility of serving the loads and if not, how much energy and power shortfall there is. This can provide early awareness of the generator and energy storage ratings. The missions that can be achieved using a given power system architecture and the underserved load that are left for infeasible scenarios are identified. This feasibility study can be reformulated as an optimization problem, such that one or more infinite generators capable of supplying unconstrained power are added to the initial system, for simulation purposes. If the infinite generator is accessed, it signifies limited power availability for the particular mission. The amount of virtual power required from the high cost infinite generator is indicative of failure and success of missions.

By assuming perfect knowledge of the past and present, the Multi-Period Optimal Power Flow (MP-OPF) optimizes power and energy management for the entire mission concurrently. This is unlike the single period power flow that solves for power flow at each time step. The MP-OPF is conceptually constructed by considering candidate power system at some time step.

In addition, the available energy in the energy storage system evolves with time, making this optimization a multi-period power flow. The energy storage model used is independent of the technology of storage and thus allows for bidirectional power flow. The architecture of the power system consist of a 21-bus evaluated for six mission scenarios, with separate bus and branches. A total of 82MW of power is generated on-board. This comprise of two main generators rated 35MW each, and two auxiliary generators rated 6MW each.

The simulation is limited to DC power flow without line-limits and ramp rates, for simplicity purposes. From the results obtained, this method provides an upper-bound on the best case performance of any type of controller design and also points out the limitation of each power system architecture itself.

### **Early-Stage Shipboard Power System Simulation of Operational Vignettes for Dependability Assessment**

The performance of a candidate system for given operational vignettes is simulated, using an early stage simulation technique. By using this early stage simulation approach, quick simulations and many vignettes consideration are possible. Thus, overall system dependability can be assessed. Time-domain performance metrics have been proposed for dependability assessment. One of such is operability- which indicates the measure of the degree to which the power system performance contributes to the overall mission effectiveness in a particular scenario or operational

vignette. Dependability assessment have been proposed to aggregate operability values over a set of operational vignettes, as the system must perform over a wide range of operational vignette.

The need to reduce the computational burden of simulation techniques arising from multiple time-domain simulations for the calculation of dependability metrics, establishes the motivation for the development of modeling and simulation technique at the early design stage. In this research endeavor, a complex distribution of operational vignette representing a given mission profile is considered. The ship is involved in a mission while it responds to probable threats and disruptions. Early stage simulation technique application is an improved capability for trade space exploration. The vignettes considered herein are more complicated than the ones considered in previous similar work. A high power load is used to engage in the mission. The technique used in the simulation involves the use of a linear program to represent the power system. In the linear program, power control is modeled such that weights are assigned to each load, indicating their relative importance. These weights are also useful for calculating system operability during events.

The set of operational vignettes considered corresponds to a given mission profile. The notional system performance is considered using two specific architectures. The operability of each architecture is calculated for each of the 1000 sample operational vignettes. The mean operability values i.e. average dependability, for the first and second architectures are 98.5% and 98.6% respectively.

The results suggest that improving control of energy storage or management of shipboard power system ‘energy account’ may not improve performance significantly during unchallenging or very challenging scenarios but can improve performance for situations in between these extremes.

### **Light-Weight, Early Stage Power System Model for Time-Domain Simulation**

It is desirable to investigate the impact of various power systems technology alternatives on ships, at the early stage. It is thus necessary that a time-domain simulation of the power system be performed. Many of such simulations in most cases are required. In addition, limited information at this stage is available for robust simulation to be possible. In order to combat these dual challenges, a light-weight power system model is developed. By lightweight, it implies that low computational burden required for many simulations within a short time period and limited information required to parametrize the power system model is possible.

Static analysis of power system in the past was sufficient to ensure proper system sizing and performance metric assessment. However, the introduction of high, pulsed mission loads has brought about the need to perform dynamic analysis that requires time-domain simulation. A lightweight power system model that recognizes that, neglecting certain system dynamics will not affect performance at the early stage is proposed. With this model, the simulation speed is increased, computational burden is reduced, and limited information is used for system parametrization.

The fundamental principle of the proposed model is to “locate a level of fidelity and computational efficiency between that of static models and dynamic models”. In order to use this approach, information about the system components and their ratings are imported from a suitable database. The information is used to formulate a light-weight model. Subsequently, it can be combined with operational vignette description to allow for time-domain simulation.

An improved linear programming model of the power system is used for the light-weight simulation studies. In particular, two structural improvements to the linear programming approach is made in this work. These improvements include the representation of limits associated with the

generator loading and unloading dynamics, and the representation of load sharing. By using linear programming approach for formulating the system model, it is assumed that the controller will maximize the weighted functions given in the model equations.

The light-weight approach is demonstrated on a notional medium voltage dc system, and results are presented in the research paper. The simulation requires about 3.2s run time, which is 100 times faster than real time speed.

### **Operational Vignettes-Based Electric Warship Load Demand**

In this paper, a methodical approach for the generation of load demand profiles, based on the anticipated ship's usage is developed. Based on different types of specific mission scenarios; mission load features, human-in-the loop decision-making, and a group of test cases that offer load demand dynamics are described.

Here, a representative power system configuration with locations for the different generators and load is recommended. As such, the load profile represent a spatial constituent to the simulation. This tool enables the possibility of a realistic study of the design of power system topology, dynamic load flow, control, and protection for the early design trade space.

All loads are characterized and modeled, resulting in a comprehensive set of independent load demand profiles for each time interval. In formulating the load demand, several important features were put into cognizance: scalable, tunable, stochastic, and expandable.

To demonstrate that the load generation model is scalable, a comparison between two ships is presented with identical set of mission loads, but with different power scaling requirements. Ship A has a total installed power of 82 MW while ship B has a total installed power of 48 MW, with representative mission loads of higher power. The service and radar load models exhibit two states; cruise (during peacetime load demand) and battle (increase in load demand because of the need for additional redundancy) states. The mission loads are described by peak power pulse duration and slew rates. The load model can be modelled stochastically. The propulsion loads characteristics of both ships A and B are assumed to be identically scaled, and thus maintains the same per unit values.

Six alternatives of a notional operational 10-minute vignette were considered in the simulation of the ship's multi-mission capability and in the severe stressing of the integrated power system. The service and radar loads start with cruising and then change to battle situation in order to support an impending operational threat occurrence. The ship begins a succession of pulse power mission loads through a sequence of simulated detect-to-engage series and human-in-the loop responses. Ship A and B thus undergo, the same set of operational scenario with constant, moderate, and aggressive propulsion load dynamics for a total of six variants based on the same operational vignette, and detailed results are shown and included in the research paper.

The premise that constant steady state should not be assumed in the early stage design trade space studies, is established in this work. Rather, realistic assessments based on highly disruptive conditions and dynamic loading conditions is of higher appropriateness.

### **The Role of Future Information in Control System Design for Shipboard Power Systems**

A technique by which quantification of the potential value of information of the future is presented in this paper. This is important because acquiring future forecast information and controller design could be a difficult task. The quantitative value enables system designers to decide if forecasting is necessary or not and to determine which controller to use the forecasted

information. Analysis of power system can be done in steady state, to determine if the load requirements is met by the generator capacity, but as the elements of the system gradually depends on time, the complexity of the system increases, making analysis more cumbersome.

Rapid load decreases or increases can become a problem in the system. Several system control configuration have been proposed which put into consideration the system dynamics. The Model Predictive Control (MPC)-which could be linear or nonlinear- is useful in predicting the effects of potential control action over a fixed time range. For MPC, the best input is selected by the controller and applied to each time step of the simulation. The analysis and control difficulty of incorporating power system components that are time dependent, plus the comparative advantages of future predictions to mission success is described.

Two methods of optimization are used to produce the behavior of controllers. The first optimization algorithm/method defined as instantaneous, possesses knowledge of the present moment i.e. only current information, while the second optimization method/algorithm described as multi-period, possesses precise future knowledge of load requirements. Comparison of the two optimization algorithms and quantification of the forecast value is a goal in this work.

The two optimization algorithms are illustrated, using a hypothetical naval ship (with electric propulsion and demanding mission loads) and drill service vessel (with both slow and fast –ramping generator line-ups). Parameters of both platforms (naval ship and drill service vessel) are provided in the research paper. Each of the control algorithms serves as an upper-bound performance based on the existing information. Thus, finding a difference between the two represent the information value.

As anticipated, future information is of value with time-dependent systems. Future forecasting could be of no value for some power systems. However, it is useful for systems with energy storage or ramp rates of load generator capacity.

Simulation results are explicitly explained in the paper.

### **Market-Based Control as a Paradigm for Power System Control**

Prior to this work, market-based control has been proposed as one method of controlling power flow in shipboard power system. It encompasses a “fake” power market where the market forces or actors- consumers and firms- behaves in accordance to the principles of economics.

In this work, control method improvements with respect to time-dependent components such as energy storage are presented. Method of equipment operation, such that future operation depends on present decisions are discussed. This method enables optimal system control “over uncertain and dynamic future.”

When faced with the problem of optimal-decision making, such as optimum energy allocation from energy storage during change of system states and objectives, consideration of the energy storage is required to be done. Formulating this problem as a market-based control problem, is posing or describing how the energy storage will respond to both known and probable market situations, of which optimal decision is dependent on. Consideration of load and generator is more direct because their behavior is independent of time and they deplete or produce energy respectively as required to attain optimal performance. Nevertheless, the optimal performance of the entire power system is highly dependent on the energy storage’s charging and discharging characteristics.

In addition, approaches to attaining the equilibrium of market, and hence the optimal power system condition is discussed in this work. Specifically, the Alternating Direction Method of Multipliers (ADMM) and prevailing issues with distributed control methodologies are highlighted.

More details of the current methodologies of naval shipboard modeling and simulation are provided. It is further argued that the projected market-based control method can offer a mathematical basis for the approach of distributed control, which are “agile, resilient, dependable, efficient and effective.” The approach for modeling involves the incorporation of a mathematical programming problem at each time step solution of the simulation. The system dynamic state is updated at each time step. Mathematical programming is a kind of optimization where from a group of elements, the best element is selected. In the same vein, linear programming is a type of mathematical programming where requirements are expressed using linear relationships.

Results from optimization approach and market based approach under similar simulation circumstances, indicates that they both find solution to same problem. The ADMM is a mathematical algorithm that solves complex optimization problems by breaking it into two simpler sub-problems. ADMM has slow convergence and requires high volume of information but has moderately high accuracy.

It is suggested that a more effective market-based control method will involve putting future information into consideration, yielding a more robust system. This is made possible by expressing the system configuration similar to a multi-period model configuration. The feasibility of shipboard power system control in several domains is advanced, with emphasis on the similar nature of the electrical energy storage system and heat-energy storage system expressed by all large power system elements.

## ***Power Electronics***

### **Reactive Power Control Methods for Photovoltaic Inverters to Mitigate Short-Term Voltage Magnitude Fluctuations**

Incorporating renewable energy sources into the distribution system comes with some technical difficulties. Substantial oscillations of voltage of distribution systems can arise because of variations in output power of intermittent sources of renewable energy. Several control methods that exploit the reactive power capability of a three-phase inverter is advanced in this work. The methods include the replacement of reactive power generation with real power generation.

The reactive power output is expressed as a linear function of the instantaneous solar power, in these methods. A scope, an objective and a domain describe each control method. These three aforementioned features serve as the necessary criteria for the selection of control parameters, used by the reactive power controller.

For quantification and comparison of each control method performance, voltage magnitude violation and variation performance yardsticks are set. With the aid of IEEE 123-bus feeder distribution system, each control method performance is verified using three different case studies.

In response to solar power fluctuations, the several proposed reactive power control methods allow the three-phase PV inverter to regulate its three phase reactive power injections. The controller objective is to alleviate variations of the voltage magnitude of the system due to the fluctuation of the real power injection of PV. The choice of controller parameters can have some influence on system response in terms of voltage magnitude during solar power oscillations. The scope of a method specifies the bus under consideration for voltage magnitude fluctuation. A local scope control method uses voltage magnitude vector of the local bus (i.e. bus associated with the PV inverter) and local sensitivity factors while the control method of global scope uses the voltage magnitude vector of the global bus (i.e. all voltage buses across the system) and the global sensitivity factors.

Furthermore, the proposed control methods are characterized by local or global scope, sensitivity minimization (reduce response of voltage magnitude of the bus under consideration, due to perturbations of solar power) or violation optimization (maximize solar power perturbations such that bus voltage magnitudes are still within acceptable limits), and balanced domain (injection of same amount of reactive power into each phase of the PV inverter)- or unbalanced domain i.e. unbalanced reactive power injection. In general, the proposed reactive power control methods are found to have the ability to mitigate voltage magnitude fluctuations of the distribution system.

In conclusion, this work contributes three ideas. These include various control methods proposal, performance metrics identification to assess the performance of each of the control methods, and the illustration of the reactive power control methods on test system (IEEE 123-bus system) using three different cases (detail of the cases are found in the paper).

### **Generalized Average Method for Time-Invariant Modeling of Inverters**

In order to evaluate inverter behavior, development of inverter models for simulation is of importance. Every switching action of inverter is accurately represented using detailed models, yielding precise simulation results. As accurate as the detailed inverter model might be, it can be challenging when long simulation times, larger power converter numbers and repeated simulation are required for proper simulation studies.

The use of State Space Averaging (SSA) method for inverter modeling can be helpful in reducing simulation run times. This is made possible by the substitution of inverter switching function with its fast average. However, this method has the demerit of reduced model accuracy.

Generalized modeling is used for modeling converter average and switching behavior with a retention of faster simulation times. In this work, a Generalized Average Method (GAM) for modeling single-phase and three-phase pulse width modulation (PWM) inverters is presented. The quasi-Fourier series depiction of the switching function, which incorporates the fundamental, and switching frequencies constituents, including sideband components of the switching frequency provide the basis for the GAM. Models founded on GAM allows for the possibility of studies of the steady state and dynamic features of the switching ripple without the consequence/demerit of long simulation runtime associated with detailed model.

The broad approach for the design of GAM model begins with a set of ordinary differential equations for depicting the detailed model, from which a new set of ordinary differential equations is created where the instantaneous state variables are depicted with a QFS representation. In general, the GAM model is a set of ordinary differential equations created with respect to some average vectors and their time derivatives, as detailed in the research paper. The connection between the QFS depiction of a signal's time derivative and the time derivative of the QFS depiction of the signal is an important feature in the creation GAM model. The modulation signal of the PWM inverter is presumed to be sinusoidal. It becomes feasible to construct GAM model for several PWM inverter if the characteristics of the QFS-represented signals and the QFS depiction of the switching functions of the inverter is combined.

The proposed model is subjected to both simulation and experimental demonstration. Comparison of the detailed model, SSA model and GAM model of the inverter is made, in each simulation. Plots comparing simulation waveforms of approximately the fundamental period and of approximately the switching period are shown. It is discovered that using the side band components enables the correct depiction of switching ripple magnitude that happens at steady state. Faster simulation runtimes are also associated with GAM model as compared to detailed

models but slightly slower than SSA model. Experimental results also closely match the simulation results.

In conclusion, results obtained from both demonstration precisely portray both the fundamental and switching characteristics of the inverter.

### **Three-Phase Inverter Modeling using Multi-Frequency Averaging with Third Harmonic Injection**

In this paper, a Multi-frequency Averaging (MFA) model of a three-phase Pulse Width Modulation (PWM) inverter, with third harmonic injection is proposed. A Quasi-Fourier Series (QFS) representation of the switching functions of the inverter is presented, and used in the formulation of the MFA model of the three-phase PWM inverter with third harmonics. The fundamental frequency and third harmonic component of the modulating signal, multiples of the switching frequency's components, and the side band component of the multiples of the switching frequency are used in representing the state variables of the MFA model.

The switching functions' component magnitudes are found by using discrete Fourier transform. By making a comparison between a 10-kHZ carrier signal with two different a-phase 60-kHZ modulation signal that are sampled at 30MHZ, two switching functions are generated.

The equations representing the mathematical model (MFA model) of the inverter is presented in the paper. It is seen that "the magnitudes of high frequency components of three-phase switching functions on the same frequency are equal in the balanced system". This implies that three phase switching functions have almost same harmonic components.

The three-phase inverter simulation is done in MATLAB, and the Bessel function of the first kind is implemented using MATLAB interpreter. The simulation results reveal that the MFA model exhibits a higher level of accuracy and faster simulation run times than other models with many details.

In conclusion, the three major contributions that forms the main thrust of this work include: the representation of the switching function of a three-phase PWM inverters using QFS, the proposal of MFA model for three phase PWM inverter with third harmonic injection and the model implementation via simulation in MATLAB.

## ***Electric Machinery***

### **Hybrid Position Observer for Brushless DC Motor Drives with Improved Noise Immunity**

An improvement to the noise immunity of the hybrid position observers of brushless dc motor drive is proposed in this research endeavor. This is to help in addressing the Hall-effect sensor noise obtained experimentally. In order to ascertain if Hall-effect sensor transitions are true or just a result of temporary glitches, a finite machine is used for detecting the transitions. This filter can cause a delay in the detection ability of Hall-effect sensors, which is compensated in the proposed observer. Using simulation methods, comparison is made between the proposed observer and the original hybrid position observer in noisy and non-noisy conditions, and for both steady and variable speed operation.

The finite state machine is used for noise filtration of a given sensor. It maintains a Hall-effect state and a counter. It is argued that the finite state machine's application will lead to a lowering of the consequences of false Hall-effect transitions, but could also lead to a delay in the

detection of true Hall-effect transitions. The equations for the instantaneous sine and cosine of the electrical position, and rotor speed equations are provided in the research paper.

The responses of the original position observer and the proposed position observer are simulated. Two groups of studies are performed, namely steady-state performance and transient performance. In the steady state studies, the electrical rotor speed is kept constant at  $120\pi$  rad/s, and the observers are simulated for two electrical periods. For the transient performance studies, the electrical rotor speed is increased linearly from  $40\pi$  rad/s to  $160\pi$  rad/s over 0.1-s simulation time.

Generally, the simulation results obtained in this work; show that the proposed model performs well under high noise level in both transient and steady state conditions.

### **Unified Model Formulations for Synchronous Machine Model with Saturation and Arbitrary Rotor Network Representation**

Several models and formulations have been used to represent and study synchronous machines, looking from diverse perspectives. Park's transformation provides the basis for several of these model formulations. The consequences of rotor reference frame transformation are as follows: equivalent equations become independent of time, constancy of state variables during steady state, and the analysis of machine becomes simple.

Depending on the kind of simulation required, models of a machine can be formulated in different ways. For instance, modeling a machine-rectifier could require a conventional voltage-in, current-out formulation, which is more appropriate in circuit depiction but lead to mismatch of the interface of the machine and rectifier. However, incorporating a 'fake' resistor of large resistance value could help assuage this mismatch effect, but could result in longer simulation run times.

As a major focus of this paper, "a unified derivation of the various model formulations, which support direct interface to external circuitry in a variety of scenarios, is presented. A synchronous machine model with magnetizing path saturation including cross saturation and an arbitrary rotor network representation is considered". The marked difference between the presented derivation in this research piece, and prior derivations is that the presented derivation circumvents various symbolizations, realizations and transformations, inherent in prior derivations. A field-only voltage behind reactance (FVBR) formulations is obtained, to complement the group of formulations. Comparison of each formulations and their relative merits in diverse simulation applications are illustrated.

In this research work, four machine model formulations (qd, SVBR, FVBR, and SFVBR formulations) are compared in four different cases. The machine model is a 59-kW, 560-V, 4-pole machine, which has been sufficiently validated with experiments. It consists of a discretionary linear network, which is used to characterize the rotor circuits and magnetizing path saturation with cross saturation inclusive. Results reveal that if the formulation has appropriate interface for the required simulation application, then likely, correct results with lesser time steps and lower simulation run times will be obtained.

In summary, three basic contributions are the hallmark of this paper. They include an incorporated model derivation of synchronous machine model, a creation of FVBR formulations and the exposure of the relative merits of each formulation.

This work was also presented at the IEEE Power and Energy System meeting, based on invitation. It received the best paper award for the year 2016-2017 from IEEE Transactions on Energy Conversion.

## **Numerical Average-Value Modeling of Rotating Rectifiers in Brushless Excitation Systems**

Brushless excitations are widely used in synchronous machines because of its advantages, which include high reliability and low maintenance cost, compared with static excitation. These advantages stem from the exclusion of brushes, slip rings, circuit breakers and carbon dust.

Rotating rectifiers are engaged in brushless excitation. The main machine field circuit is fed from the output of the rotating rectifier that rectifies the output voltages of the exciters. For qualitative simulation of power electronics and analysis of power system, efficient modeling of brushless excitation system is of the essence, especially as machine field voltage and power system dynamic behavior has some correlation with brushless exciters.

Average-Value Modeling (AVM) of machine-converter system alleviates the disadvantage- expensive computation, because of diode switching repetition- inherent in detailed modeling of the system by discarding the details of diode fast switching.

Some of the previous works related to the subject of this research piece, as highlighted in this research paper, pose computational expense because many of the AVM methods explored for the machine-converter modeling, requires solutions to nonlinear equation and numerical integration at each simulation step.

Therefore, in this paper, a numerical AVM of the rotating rectifier in brushless excitation system is advanced. A dynamic machine model is integrated with the numerical functions obtained from the averaged rectifier switching behavior, such that the nonlinear and dynamic brushless excitation system characteristics are merged with simulation models of a conventional voltage-in, current-out main machine formulation. This yields a correct and efficient simulation, which is less computationally expensive.

The proposed alternative AVM approach used for rotating rectifier uses open-circuit voltages in determining the dynamic impedance. Current-in, voltage-out formulation are used in representing the windings of the armature of the exciter machine.

In order to describe the rectifier performance across a widespread loading range, transient simulations are necessary. In order to do this, a 3-phase resistive load that draws rated power at rated voltage is connected to the main machine. The system model consist of a 4-pole, 59kVA, 560V synchronous generator and an exciter system. The simulation was ran on MATLAB/Simulink 2016a platform. The elements of the circuit are represented using a software package called Automated State Model Generator (ASMG), which creates a state-space model using circuit configuration and switch states.

The proposed brushless excitation system AVM is validated with the detailed model and compared with analytical AVM, in three (3) different cases. In each of the three cases, the main machine field winding is fed through a rotating rectifier.

The waveform predicted by the proposed AVM model follows the same pattern as that predicted by the detailed model. The results of the proposed model represents the low-frequency system attribute and it exhibits high computational efficiency.

## **Formulation of Rectifier Numerical Average-Value Model for Direct Interface with Inductive Circuitry**

The simulation of machine-rectifier systems using their detailed models causes computational expense and burden. This is because of iterative switching of diodes. In order to limit this effect, the use of Average-value Models (AVMs) was adopted in the simulation of such systems. AVMs tends to neglect diode-switching details.

Many other methods for the modeling and simulation of machine-rectifier system has been proposed in the past. This includes the use of detailed models, static AVMs, dynamic AVMs, etc. Long simulation run times are generally typical of detailed models of machine-rectifier systems during simulation. Hence, the adoption of AVMs, which maintains the system average behavior while disregarding diode switching specifics.

There exists the analytical and parametric (or numerical) approaches for the construction of rectifier AVMs. The analytical approach seeks to establish a relationship between the variables of the ac and dc sides of the rectifier. The computational efficiency associated with this approach is expensive as the approach demands solution to nonlinear equation. On the other hand, the parametric or numerical approach makes simple, the Average-value Model (AVM) development of machine-rectifier systems. It obtains the parameters of the model from an initial detailed simulation during early developmental stage of the model, using numerical methods.

Earlier approaches using numerical approach for rectifier AVM development, involved the introduction of low-frequency approximation to boycott inappropriate transfer function on the ac or dc side of the rectifier.

The main idea of this paper is the presentation of another numerical approach for the formulation of the AVM of machine-rectifier system, which exploits the natural dynamic impedance of the rectifier, while avoiding the low-frequency approximations and algebraic loop. The proposed numerical AVM approach of the system includes in the brushless excitation system, stationary and rotating rectifiers. Comparison of the proposed approach to existing numerical AVMs and experimentally validated detailed model simulation, in six cases is done. The mathematical relationships used in the proposed approach is similar to existing AVMs.

A block diagram summarizing the structure of the proposed model is presented in the research paper. The Automated State Model Generated (ASMG) is used to depict the elements of the circuit, while stator-only voltage-behind reactance (SVBR) formulation is used for machine modeling in stationary rectifier characterization. The field-only voltage-behind reactance (FVBR) formulation is used for machine modeling, for rotating rectifier characterization.

For each of the six cases considered, the waveforms of the simulation results, simulation runtimes, number of required time steps for simulation, and how they compare with their prior AVM counterparts and detailed models are presented in this work. The proposed model proves to be correct during simulation of both steady state and transient state, even in cases where prior AVMs fail in providing accurate waveforms. Yet, the proposed model maintains the computational advantage of prior AVMs over detailed models.

## ***Optimization Methods***

### **Genetic Algorithm with Integrated Computing Budget Allocation for Stochastic Problems**

In many applications, stochastic problems are of great interest and the use of Genetic Algorithms (GAs) to solve these problems have become popular. Stochastic problems are generally found in engineering and science. In this work, a GA is presented such that the computing budget allocation techniques are incorporated into the selection operator instead of being used during fitness evaluation.

Stochastic modeling can be applied to problems that are subject to uncertainty. Comparatively high computational expense involved in performing required simulation is a common characteristic of these problems. A direct method of large sample collection can be

computationally expensive, thus enhancement of this approach is possible by utilizing efficient sampling in the search algorithm. Hence, the search algorithm's runtime and accuracy can be possibly improved.

Methods of solving optimization problems, e.g. Genetic Algorithms (GAs), particle swarm optimization, simulated annealing and ant colony optimization have recorded some success when objective function's derivative is not known or is extinct. Optimal Computing Budget Allocation (OCBA) methods are useful for sample allotment performed on a group of individuals to disclose the comparative advantage of the individual. Merging CBA methods with GAs can help in sampling efficiency improvements in robust optimization methods. Evaluation-Integrated GA (EIGA) is an algorithm in which the OCBA method of choosing certain number of individuals out of a group of individuals is incorporated with GA evaluation to improve search efficiency.

For a stochastic problem, by computing the mean of the small number of random samples, the fitness function can be approximated. Understanding the relative fitness of a small group of individuals rather than the exact fitness of each individual is the requirement of GA. The information is proposed to be obtained by the GA from the Selection-Integrated GA (SIGA). The equal allocation method, OCBA methods and the proportional to variance (PTV) methods are the CBA methods applied in this study. Largely, this work focuses on making comparison between EIGA and SIGA. Of less importance to the way in which the CBA method is performed, is the consideration of the specific genetic operators employed by each of these algorithms or their parameters.

Three test functions used in this work-Griewank, HappyCat and HGBat- are shifted and rotated. These test functions have additive Gaussian noise. It is discovered that the SIGA performs better than the EIGA, with respect to the mean error for a particular CBA method. This is ascribed to the way in which the SIGA allots fitness evaluation to particular individuals of which the GA wants considerable information. It is also found that the EIGA achieves peak performance generally with EQU method of CBA. The SIGA performance is less sensitive to the CBA method chosen. With significantly fewer test problems samples, the SIGA's solution mean error can be compared with EIGA's when EQU method is used.

## **Computing Budget Allocation in Multi-Objective Evolutionary Algorithms for Stochastic Problems**

Real-life problems are essential practical problems whose solution are found using Multi-Objective Evolutionary Algorithms (MOEAs). Operators such as mating selection combined by MOEAs selects features such as child genes, crossover, and mutation to create new generation of individuals. Among MOEAs, popular elitist approaches archive non-dominated solutions from the previous generation and combine them with non-dominated solutions from the current generation to produce the subsequent generation, a process, referred to as environmental selection.

Different method for handling noise, in the course of proffering solution to stochastic problems have been developed by researchers, with the purpose of bringing accuracy and efficiency improvement to the algorithms. In order for each individual's fitness to be determined, MOEAs undergo iterative computationally expensive simulation of samples, hence the need for noise handling techniques e.g. Optimal Computing Budget Allocation (OCBA)-, to obtain more precise results from smaller samples.

In this research work, the question of application of Computing Budget Allocation (CBA) methods to MOEAs is considered. The method of CBA concerns how few number of total samples are allocated to a group of individuals in the stochastic problem's solution space. Investigation into

the effects of incorporating CBA methods into either the evaluation or environmental selection on MOEAs is done. This work is principally motivated by a prior work, which proposed CBA integration into the selection rather than evaluation process of genetic algorithms (GA) for single-objective stochastic problems. Owing to the inspiration gotten from this prior work, a description of an amalgamation of studies that compare alternative methodologies to incorporating CBA methods into GAs, such as Evaluation-Integrated GA (EIGA) and Selection-Integrated GA (SIGA) is considered herein. Within an NSGA-II implementation, comparison between several CBA techniques e.g. equal allocation (EQU) method, OCBA method, and proportional-to-variance (PTV) method is done on both 2D and 3D stochastic problems. The EQU represents the basic method serving as a standard for comparison, with computing budget equally allocated to individuals. The OCBA method helps to maximize the chance of choosing the Pareto optimal set in stochastic problems. The PTV method allots computing budget in proportion to the sum of variance over all the objectives. In essence, the PTV exploits the variance data from the current samples.

Results from this work show that the SIGA performs better than the EIGA with respect to the Generation Distance (GD) and Inverse Generation Distance (IGD) performance metrics. In other words, the SIGA yields more correct results in providing solution to multi-objective stochastic problems. This is because of the way in which fitness evaluations is assigned by the SIGA towards certain individuals of which much information is desired in developing the Pareto front. It is intended that this idea would be extended to studies of photovoltaic inverters optimization subject to solar changes in irradiation of the sun and shipboard power system design subject to disruptions, in which the advantages of CBA integration techniques will be determined on more real-world optimization problems.

## **Appendices**

# Control System Modeling in Early-Stage Simulation for Cyber Vulnerability Assessment

Allen W. Flath, III, Aaron M. Cramer, Xiao Liu

Department of Electrical and Computer Engineering

University of Kentucky

Lexington, Kentucky 40506

Email: allen.flath@uky.edu, aaron.cramer@uky.edu, xiao.liu@uky.edu

*Abstract*—Previous approaches for early-stage shipboard-power-system simulation were driven by a need to perform time-domain simulation during the early design stage and included an internal idealized representation of the control system. Herein, the reduced-order physical model of the power system is combined with an independent representation of the control system. This allows the benefits of faster simulation and reduced modeling effort to be retained while improving understanding of the effects of the control system on system performance. This approach is demonstrated by studying a compromised control system subjected to false set point attacks that drive the system operation away from ideal behavior. Using a notional MVDC system and a representative operational vignette, the performance of the uncompromised system is compared with the performance of the compromised system over a set of potential cyber disruptions by calculating the system dependability.

## I. INTRODUCTION

Shipboard power systems are service providers [1], [2], [3] and should be assessed based on their ability to deliver power during the operational vignettes through which they must operate [2], [4], [5], [6]. Time-domain performance metrics are often used to quantify the performance of such systems, and the consideration of such metrics requires numerous simulations. It is important for simulation methods used to evaluate these metrics to be computationally efficient and to exhibit appropriate levels of detail for the simulations being performed. A great deal of development of techniques for early-stage simulation of shipboard-power-system models has occurred [7], [8], [9], [10]. This work has focused on the two key aspects mentioned above: reduced modeling effort and fast simulation run time. Throughout the development of these methods, there has been a constant understanding that there were two key limitations. The first limitation is that the modeling approach substitutes an idealized surrogate control system model that acts with perfect knowledge and seeks an instantaneously optimal solution. The second limitation is that the representation of the power system and the surrogate control system model are fundamentally intertwined. Herein, an approach for representing the control system (without surrogate model) while retaining the modeling and computational advantages of the early-stage simulation model is presented, alleviating the limitations of previously presented methods for early-stage modeling.

The proposed approach receives set points from the control system model and uses these to formulate a quadratic programming problem in which the nearest physically feasible state of the power system is located. This approach mimics the process by which local controllers would respond to deviations from programmed set points (e.g., droop control). In this way, the computational efficiency of the modeling technique is preserved while allowing the control system to be represented.

This approach is demonstrated by examination of a compromised control system in which false set points are injected to model the response of the system to cyber attacks. The performance of both the uncompromised and compromised control systems are compared for a representative operational vignette. This sets the stage for work involving other control system models and more sophisticated cyber attack models (e.g., [11]). Specifically, this work serves to:

- 1) Present an approach for including nonideal controller models within the simulation model.
- 2) Demonstrate the approach using a compromised control system subject to cyber attack.
- 3) Evaluate the dependability characteristics of a notional system during a representative vignette when subject to cyber disruption.

The remainder of this paper is organized as follows. The simulation models for both idealized and alternative controller representations are presented in Section II, along with the model of a compromised control system. The notional system, representative vignette, and applicable performance metrics are described in Section III. In Section IV the simulations are discussed, and conclusions are drawn in Section V.

## II. SIMULATION MODEL

The simulation approach used herein, shown in Fig. 1, involves the embedding of a mathematical programming problem within the solution for each time step of the simulation. Specifically, the system has dynamic state that is updated from time step to time step. Within the calculations of a given time step, this dynamic state is used to establish a mathematical programming problem that represents the characteristics of the system at that time. By solving the optimization problem, the state of the power system at that time is calculated. This is used to update the dynamic state of the system and to advance time.

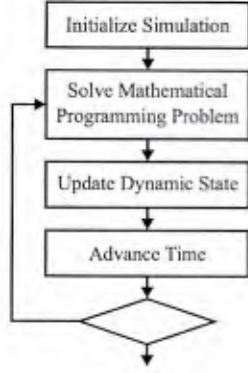


Fig. 1. Simulation approach.

The structure of the mathematical programming problems are described in the subsections below.

### A. Idealized Controller Representation

The behavior of the power system (with an idealized controller representation) in a given time step is approximated using a linear programming problem with the following structure:

$$\begin{aligned}
 & \underset{\mathbf{x}}{\text{maximize}} && \mathbf{c}^T \mathbf{x} \\
 & \text{subject to} && \mathbf{A} \mathbf{x} \leq \mathbf{b}, \\
 & && \mathbf{A}_{eq} \mathbf{x} = \mathbf{b}_{eq}, \\
 & && \mathbf{x} \geq \mathbf{0}.
 \end{aligned} \tag{1}$$

The vector  $\mathbf{x}$  contains the decision variables of the optimization problem, which represent the various power flows in the system in a given time step. The vector  $\mathbf{c}$  represents the weights of different power flows in the objective function of the controller. The matrix  $\mathbf{A}$  and the vector  $\mathbf{b}$  represent inequality constraints associated with each component (e.g., maximum power ratings). The matrix  $\mathbf{A}_{eq}$  and the vector  $\mathbf{b}_{eq}$  represent the conservation of power at each bus. Each component in the system contributes decision variables (i.e., elements of  $\mathbf{x}$ ), terms in the objective function (i.e., linear terms appearing in  $\mathbf{c}^T \mathbf{x}$ ), and inequality constraints (i.e., rows of  $\mathbf{A} \mathbf{x} \leq \mathbf{b}$ ).

The solution to the linear programming problem is not necessarily unique. In cases where the solution is not unique, the linear programming solver may produce a solution  $\mathbf{x}_0$ . A solution of equal quality (i.e.,  $\mathbf{c}^T \mathbf{x}_0$ ) but with the most balanced elements is preferred because it more accurately reflects the power sharing behavior of generators, converters, etc. Therefore, after solving the linear programming problem, a quadratic problem of the following form is solved:

$$\begin{aligned}
 & \underset{\mathbf{x}}{\text{minimize}} && \frac{1}{2} \mathbf{x}^T \mathbf{H} \mathbf{x} \\
 & \text{subject to} && \mathbf{A} \mathbf{x} \leq \mathbf{b}, \\
 & && \mathbf{A}_{eq} \mathbf{x} = \mathbf{b}_{eq}, \\
 & && \mathbf{c}^T \mathbf{x} = \mathbf{c}^T \mathbf{x}_0, \\
 & && \mathbf{x} \geq \mathbf{0}.
 \end{aligned} \tag{2}$$

The matrix  $\mathbf{H}$  is a diagonal positive semidefinite matrix containing the reciprocals of power ratings of components that are expected to share power (i.e., generators, converters, energy storage, and loads). The power-flow vector  $\mathbf{x}$  represents the instantaneous power flows in the system, and it can be used to update the dynamic state of the system (e.g., generator prime mover dynamics and energy storage state).

### B. Alternative Controller Representation

If an alternative controller representation is to be employed, all of the physical constraints indicated above must be satisfied, but the objective function is not necessarily optimized. Instead, the alternative controller model will establish set points for variables within the power system. The incorporation of the alternative controller model involves attempting to find a power flow solution that is physically feasible while attempting to achieve the set points indicated by the controller model (which may themselves not even be feasible).

This is accomplished by recognizing that the alternative controller model establishes set points related to the power flow variables in the following manner:

$$\mathbf{y} = \mathbf{M} \mathbf{x}, \tag{3}$$

where  $\mathbf{y}$  represents the set points provided by the controller and  $\mathbf{M}$  is a selector matrix that selects the corresponding elements from the power-flow vector.

To incorporate the set points from the controller model, the following quadratic programming problem is solved in each time step:

$$\begin{aligned}
 & \underset{\mathbf{x}}{\text{minimize}} && \frac{1}{2} (\mathbf{y} - \mathbf{y}^*)^T \mathbf{H}_M (\mathbf{y} - \mathbf{y}^*) + \frac{1}{2} \mathbf{x}^T \mathbf{H} \mathbf{x} \\
 & \text{subject to} && \mathbf{A} \mathbf{x} \leq \mathbf{b}, \\
 & && \mathbf{A}_{eq} \mathbf{x} = \mathbf{b}_{eq}, \\
 & && \mathbf{x} \geq \mathbf{0},
 \end{aligned} \tag{4}$$

where  $\mathbf{y}^*$  represents the set points provided by the controller model in the given time step and  $\mathbf{H}_M$  is a diagonal positive definite matrix that indicates the relative weighting of each element of the set-point vector to the controller. The resulting power-flow vector  $\mathbf{x}$  represents the instantaneous power flows in the system, which will be physically feasible and maximally match the set points provided by the controller model.

### C. Compromised Controller Model

The approach described in the subsection above can be used to represent a compromised control system, an example of a nonideal controller model. In particular, the effects of false set point attacks are studied herein. The compromised controller is represented as behaving as the idealized controller until the moment of the attack. The  $\mathbf{M}$  matrix is set up to select the generator output powers, energy storage charging and discharging powers, and load powers. The compromised controller solves the linear programming problem in (1) and the quadratic programming problem in (2) to establish the ideal power-flow vector  $\mathbf{x}^*$ . The ideal power-flow vector is translated into an ideal set-point vector  $\mathbf{y}^* = \mathbf{M} \mathbf{x}^*$ . An attack

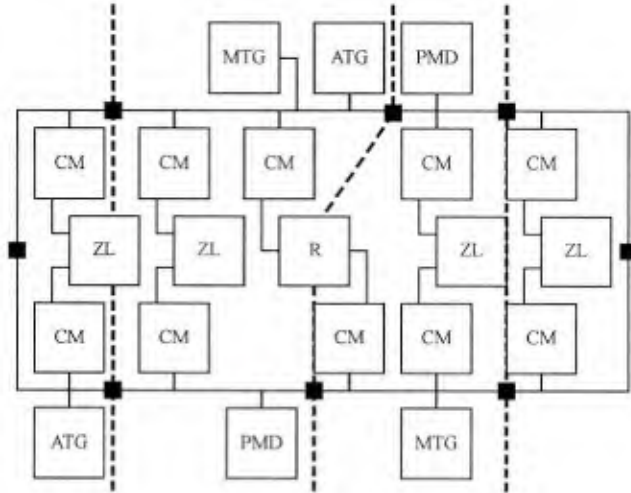


Fig. 2. Notional MVDC system. MTG signifies main generator, ATG signifies auxiliary generator, PMD signifies propulsion, CM signifies converter, R signifies radar, and ZL signifies zonal load.

is characterized by a time of inception  $t_a$ , a set-point index  $i_a$  (representing the component being attacked), and a false set point  $v$ . Once the attack has started, the element of  $\mathbf{y}^*$  corresponding to index  $i_a$  is set to its false set point of  $v$ . The corresponding element on the diagonal of  $\mathbf{H}_M$  is increased to model the failure of the compromised component to participate effectively in power sharing. The set-point vector  $\mathbf{y}^*$  is then passed to the power system model, where it is used to solve the quadratic programming problem in (4) to determine the physical behavior of the power system in response to the compromised control set point.

### III. EXAMPLE SYSTEM AND VIGNETTE

The notional medium-voltage dc (MVDC) system shown in Fig. 2 is used to illustrate the proposed approach. The MVDC system is based on the notional MVDC system developed by the Electric Ship Research and Development Consortium [8]. Parameters for the system are shown in Table I. The four-zone system consists of two main generators and two auxiliary generators. There are two propulsion drives that operate at power levels corresponding with the desired speed. There is a radar that operates at different points during the vignette. A high-power load in Zone 1 and associated energy storage is used to engage in the mission. The zonal loads are fed through converters, and each zone contains some vital and some nonvital load. A representative operational vignette based on [6] is selected. This vignette is described in Table II.

To determine the effectiveness of the power system during the vignette, a metric called operability will be observed. Operability is a measure of the degree to which the performance of the power system contributes to mission effectiveness in a particular scenario  $\theta$ . Operability can be expressed as

$$O(\theta) = \frac{\int_{t_0}^{t_{end}} \sum_{i=1}^I w_i P_i(t) dt}{\int_{t_0}^{t_{end}} \sum_{i=1}^I w_i P_{max,i}(t) dt}, \quad (5)$$

TABLE I  
PARAMETERS OF NOTIONAL MEDIUM-VOLTAGE DC SYSTEM

Rating of main generators	36 MW
Rating of auxiliary generators	5 MW
Total rated propulsion load	60.4 MW
Radar load	3.8 MW
Vital load per zone	0.9 MW
Nonvital load per zone	0.8 MW
Zone 1 mission load	13 MW
Zone 1 energy storage	780 MJ
Zone 1 energy storage rate	13 MW
Zone 1 power conversion capacity	2.6 MW

TABLE II  
REPRESENTATIVE VIGNETTE

Time (s)	Action
0	Cruise at 20 knots with radar and mission load off
30	Decrease to 10 knots and turn on mission load
75	Turn on radar
100	Increase to 20 knots and turn off mission load
135	Increase to 30 knots
180	End of vignette

where  $w_i$  is the weighting of load  $i$  in the system,  $I$  is the number of loads in the system,  $P_i(t)$  is the power consumption of load  $i$  at time  $t$ , and  $P_{max,i}$  is the maximum power that load  $i$  should consume at time  $t$ .

Average system dependability is the expected value of the operability over a distribution of events that the power system could face. If the support of the distribution of events is  $\mathcal{E}$  and a probability density function  $f_\Theta$  is established such that

$$\int_{\mathcal{E}} f_\Theta(\theta) d\theta = 1, \quad (6)$$

then the average system dependability is the expected value of operability:

$$\bar{D}_s = E[O(\Theta)]. \quad (7)$$

Average system dependability is an important property, but it does not indicate the risk of unacceptable performance caused by fairly rare but highly consequential events. Minimum system dependability is another form of dependability that describes the worst-case operability of the system over the set of possible events:

$$D_{s,min} = \min_{\theta \in \mathcal{E}} O(\theta). \quad (8)$$

## IV. SIMULATION STUDIES

### A. Baseline Performance

The performance of the ideal (uncompromised) system is shown in Fig. 3. In the vignette, a mission load situated in Zone 1 is operated. The zonal power conversion equipment in Zone 1 is not sufficiently large to operate the mission load, so it is primarily served from energy storage situated in this zone. It can be seen that the propulsion and generation powers are reduced at 30 s and that the mission load power is increased. The stored energy begins to decrease as the energy storage serves the mission load. The non-vital load in this zone is shed

in order to serve the vital and mission loads with the zonal power conversion equipment and the energy storage. At 75 s, the radar load and generator powers increase. At nearly 100 s, the energy storage is exhausted, and the vital load in the zone is shed briefly in order for all zonal power conversion capability to serve the mission load. At 100 s, the mission load is turned off and the propulsion and generation powers increase. Both the vital and non-vital loads are restored to service and the energy storage begins to charge with remaining zonal power conversion capability. At 135 s, the propulsion and generation powers increase further, but this increase is limited by the ramping limits of the generation. Because of the exhausted energy storage and the ramping limits, the operability for this vignette is calculated as 98.97%.

### B. Example Compromised Performance

It is assumed that a cyber disruption is characterized by a time of inception  $t_a$ , a set-point index  $i_a$  (representing the component being attacked), and a false set point  $v$ . An example disruption occurring at 90 s and setting the output power set point of one of the main turbine generators to zero is simulated. The performance of the system under this disruption is shown in Fig. 4. It can be seen that the performance is identical to the uncompromised controller before the disruption. Following the disruption, there is some load shedding of vital, non-vital, and radar loads. This load shedding increases at 135 s, when the propulsion power is to be increased. The most noticeable difference is that the final propulsion power is approximately 40% lower than in the uncompromised case, resulting in a final speed of approximately 26.5 knots compared to the desired value of 30 knots. The operability for this vignette is calculated as 95.51%.

### C. Average System Dependability

The average system dependability is evaluated using a Monte Carlo approach with 10,000 randomly generated disruptions. The time of inception  $t_a$  is assumed to be uniformly distributed on the interval  $[0, 180]$  s. The set-point index is assumed to be uniformly distributed across the set of set points (in this case,  $\{1, 2, \dots, 33\}$ ). The false set point is assumed to be uniformly distributed on the interval  $[0, 1]$  pu. These random variables are also assumed to be independent. The system is simulated for each disruption and the operability is calculated. The average system dependability is determined to be 98.43%, which seems relatively high compared to the baseline operability of 98.97%. A histogram of the operability is shown in Fig. 5. It is observed that the vast majority of single-point cyber disruptions have little to no effect on the operability of the power system. Of the 10,000 cases observed, only 841 resulted in an operability below 98%, and only 47 cases resulted in operability values below 70%. The worst-case operability observed using the Monte Carlo approach is 69.46%.

In each of the 47 cases with operability values less than 70%, the set-point index corresponds to the charging power of the energy storage in Zone 1. If the average system

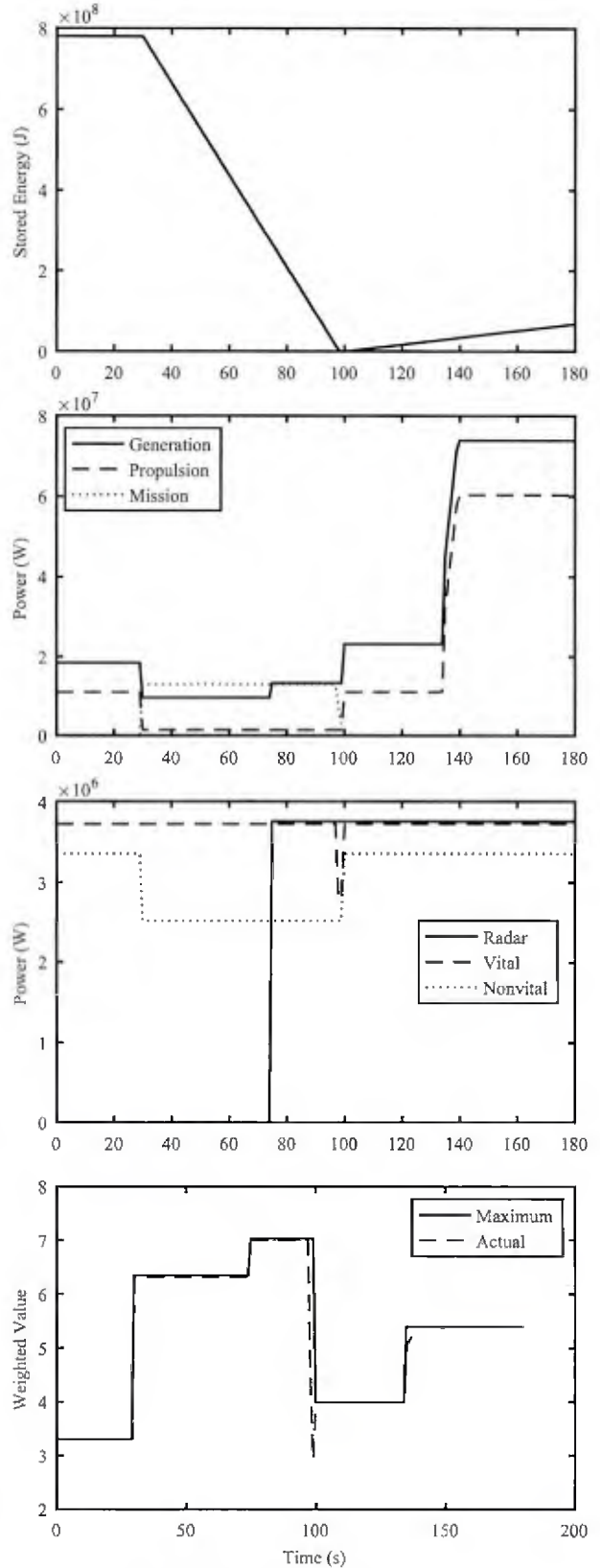


Fig. 3. Ideal system vignette performance.

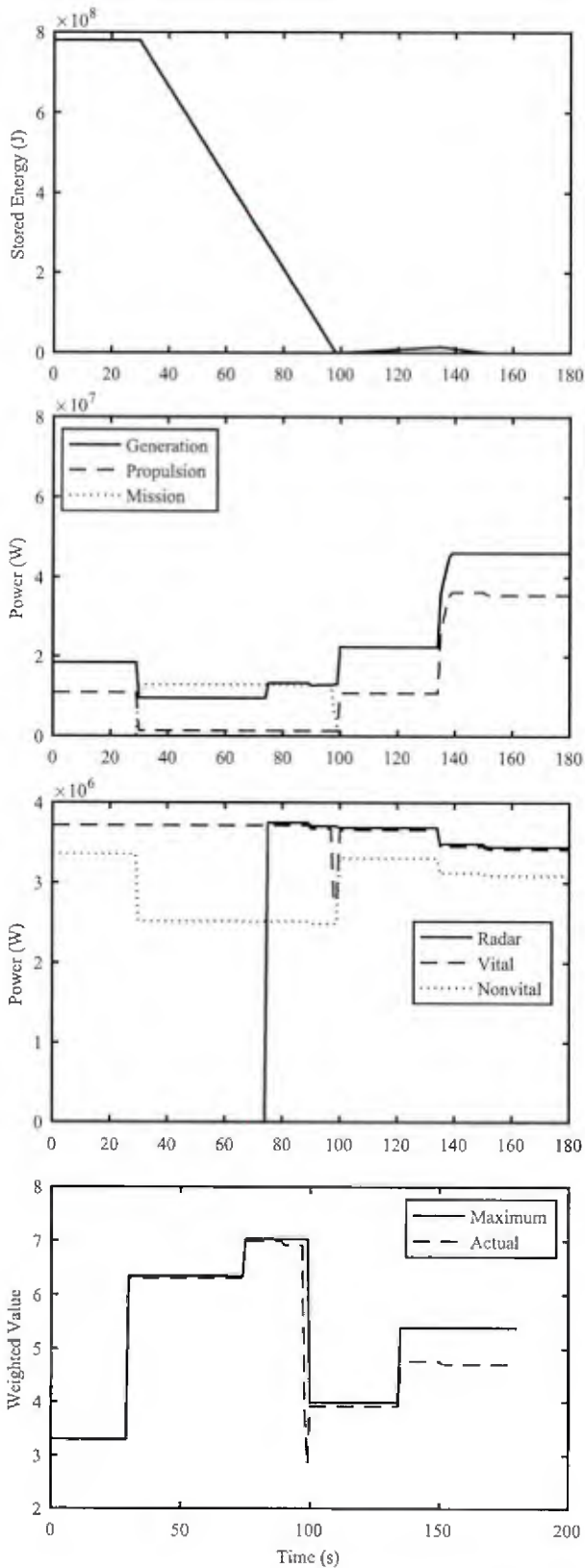


Fig. 4. Example compromised system vignette performance.

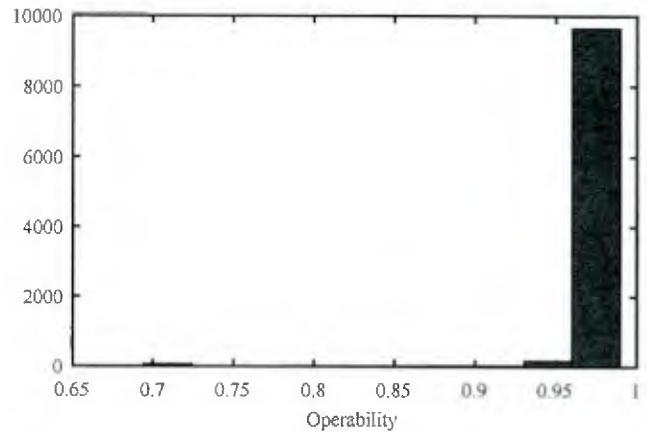


Fig. 5. Histogram of operability.

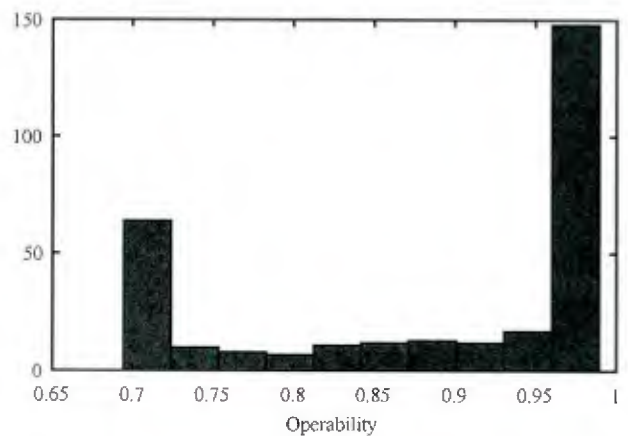


Fig. 6. Histogram of operability conditioned on attacking charging power of Zone 1 energy storage.

dependability is calculated conditioned on attacking this set point, the average system dependability is determined to be 88.39%. A histogram of these operability values is shown in Fig. 6. It can be seen that there is a much stronger probability of a low operability value if the correct component is targeted for the vignette in question.

#### D. Minimum System Dependability

A genetic algorithm is used to determine the minimum system dependability as described in [2] and the corresponding worst-case cyber disruption. MATLAB's `ga` function with default parameters is used for this purpose. Using approximately 2,200 operability evaluations, the worst-case disruption is determined to be an attack commencing at time 0.28 s, attacking the charging power of the energy storage in Zone 1, and attempting to set the charging power to 0.48 pu (compared to the maximum charging rate of this component of 0.16 pu). The performance of the system for this disruption is shown in Fig. 7. By setting the charging power set point for this component to such a high value, the energy storage

is essentially prohibited from discharging. As the mission load requires power from this component to operate, this severely limits the power consumption of the mission load because it can only be served by the zonal power conversion equipment. The remainder of the vignette is basically similar to the baseline case. The minimum system dependability is determined to be 69.46%, which corresponds to the worst-case observed using the Monte Carlo approach. However, only 22% of the number of operability evaluations were required to evaluate the minimum system dependability using the genetic algorithm.

## V. CONCLUSION

An approach for representing a controller model within mathematical-programming-based simulation approaches for shipboard power systems is presented. It separates the physics of the power system from the representation of the controller and permits the inclusion of nonideal controller models, eliminating two of the remaining challenges associated with mathematical-programming-based simulation models. This approach is demonstrated using a compromised control system model in which false set points can be injected, representing a cyber attack. Using a notional MVDC system and a representative operational vignette, the performance of the uncompromised system is compared with the performance of the compromised system over a set of potential cyber disruptions. The average and minimum system dependability is calculated, and it is shown that the system can be vulnerable to specific disruptions even if its average system dependability remains high.

## ACKNOWLEDGMENT

This work was supported by the Office of Naval Research (ONR) through the ONR Young Investigator Program N00014-15-1-2475.

## REFERENCES

- [1] J. P. Walks and J. F. Mearman, "Integrated engineering plant," in *American Society of Naval Engineers Reconfiguration Survivability Symp.*, Atlantic Beach, FL, 2005.
- [2] A. M. Cramer, S. D. Sudhoff, and E. L. Zivi, "Performance metrics for electric warship integrated engineering plant battle damage response," *IEEE Trans. Aerosp. Electron. Syst.*, vol. 47, no. 1, pp. 634–646, Jan. 2011.
- [3] M. G. Richard, D. E. Hastings, D. H. Rhodes, and A. L. Weigel, "Defining survivability for engineering systems," in *Proc. 5th Annu. Conf. Systems Engineering Research*, 2007.
- [4] A. M. Cramer, S. D. Sudhoff, and E. L. Zivi, "Metric optimization-based design of systems subject to hostile disruptions," *IEEE Trans. Syst., Man, Cybern. A, Syst., Humans*, vol. 41, no. 5, pp. 989–1000, Sep. 2011.
- [5] J. D. Stevens, A. M. Cramer, D. Opila, and E. L. Zivi, "Operational vignette-based electric warship load demand," in *American Society of Naval Engineers Reconfiguration Survivability Symp.*, Alexandria, VA, Jun. 2015, pp. 213–218.
- [6] A. M. Cramer, X. Liu, Y. Zhang, J. D. Stevens, and E. L. Zivi, "Early-stage shipboard power system simulation of operational vignettes for dependability assessment," in *2015 IEEE Electric Ship Technologies Symp.*, Jun.
- [7] R. R. Chan, S. D. Sudhoff, Y. Lee, and E. L. Zivi, "A linear programming approach to shipboard electrical system modeling," in *2009 IEEE Electric Ship Technologies Symp.*, pp. 261–269.

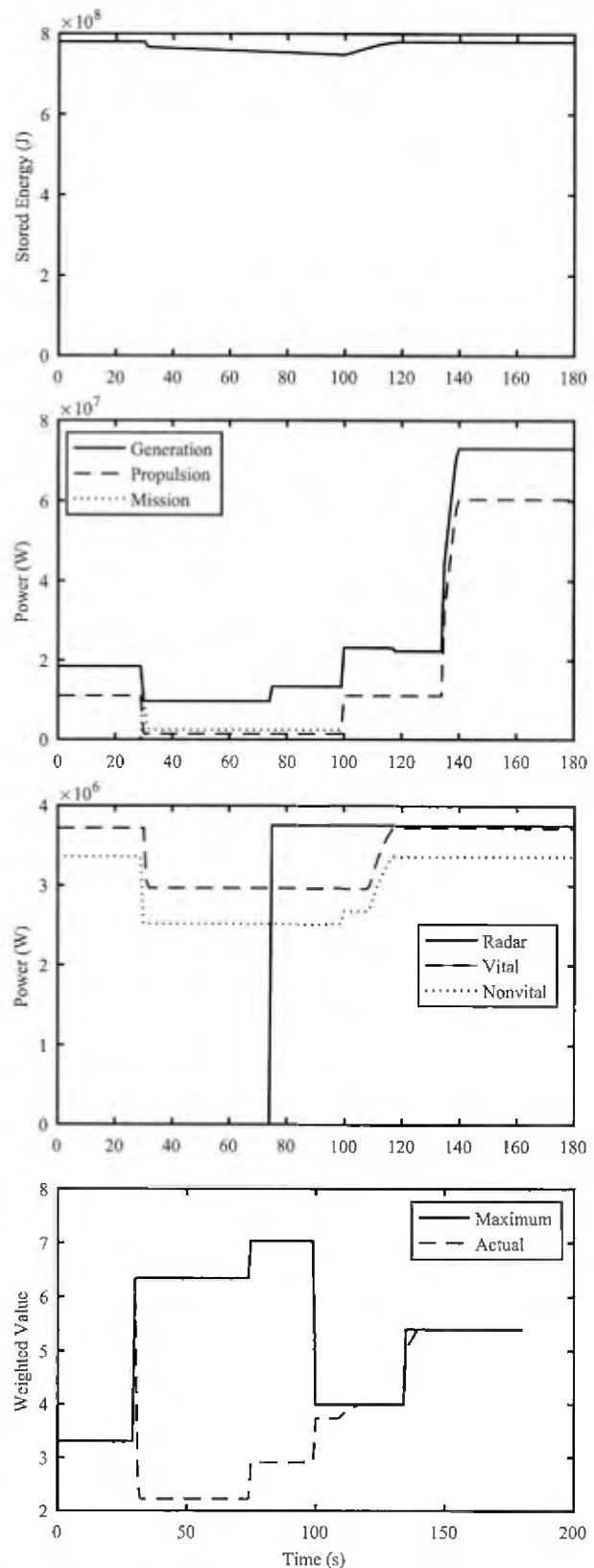


Fig. 7. Example worst-case system vignette performance.

- [8] J. S. Chalfant and C. Chrysostomidis, "Analysis of various all-electric-ship electrical distribution system topologies," in *2011 IEEE Electric Ship Technologies Symp.*, pp. 72–77.
- [9] A. M. Cramer, H. Chen, and E. L. Zivi, "Shipboard electrical system modeling for early-stage design space exploration," in *2013 IEEE Electric Ship Technologies Symp.*, pp. 128–134.
- [10] A. M. Cramer, E. L. Zivi, and J. D. Stevens, "Light-weight, early-stage power system model for time-domain simulation," in *Advanced Machinery Technology Symp.*, Philadelphia, PA, May 2016.
- [11] S. Amini, F. Pasqualetti, and H. Mohsenian-Rad, "Dynamic load altering attacks against power system stability: attack models and protection schemes," *IEEE Trans. Smart Grid*.

# Market-Based Control of Electric Ship Power Systems

YuQi Zhang, Aaron M. Cramer

Department of Electrical and Computer Engineering

University of Kentucky

Lexington, Kentucky 40506

Email: yuqi.zhang@uky.edu, aaron.cramer@uky.edu

**Abstract**—A market-based control approach is presented for the control of power flow within an electric ship. The proposed control method consists of an artificial market in which various actors (a consumer and firms) behave according to microeconomic principles. Each piece of equipment within the engineering plant will behave as a firm, attempting to maximize its profit. The commanding officer will behave as a consumer, attempting to maximize his or her utility. By proper market design, the control system allocates resources within the system efficiently to meet the objectives of the commanding officer. This control strategy does not inherently depend on the mode of operation. If objectives change (e.g., cruising vs. battle), the market reacts, prices shift, and resources are allocated to new purposes. If the structure of the system changes (e.g., due to a change in plant lineup or due to battle damage), the prices will change to reflect the new conditions, and the market will attempt to meet the objectives in the most efficient manner under the new configuration. In this way, a unified control strategy can be applied to achieve various objectives, such as fuel efficiency, continuity of service, and survivability.

## I. INTRODUCTION

Naval ships are evolving from efficient transport platforms to mobile power stations for advanced sensors and weaponry supporting diverse missions ranging from littoral strike to ballistic missile defense. These advanced mission systems will require power of the same order of magnitude as propulsion. Simultaneously, technology and affordability are creating a trend toward more automated ships with reduced crew sizes. These conflicting requirements and constraints provide a compelling need to consider new control system paradigms. Future electric warship engineering plants must provide the escalating electric power required by emerging mission systems. Ongoing developments in power system design and technology are improving power density and efficiency but they are also increasing system complexity. Integration of ship and mission power systems and energy storage require a new control paradigm to effectively manage the ship energy bank account. Other key emergent challenges include increasing dynamic interdependence between ship and mission systems and the emergence of large load transients and cyber threats.

The development of a market-based control method for agile, resilient, effective, and efficient control of progressively more complex electric warship engineering plants is presented herein. Market-based control is an approach in which resources are artificially priced according to laws of supply and demand

and the operation of equipment is governed by profit-seeking behavior [1]. The prices of goods in the system reach equilibrium values when the demand for resources is equal to the supply of those resources. Market-based control is commonly used for resource allocation within communication networks (e.g., [1]), but it has also been applied to building climate control systems [2], the control of structures [3], and other areas [4]–[6].

Market principles are formally applied to the development of the control method, explicitly linking the economic behavior of the actors in the system (the commanding officer and the equipment in the plant) with the physical behavior of the equipment in the system. As mission priorities change, prices in the system will adjust automatically to reach the optimal allocation of resources, resulting in an agile system. The resulting plant will be an engineered resilient system, and the proposed control method will also be applicable to multiple classes of ship, which is a marked departure from existing power control design approaches.

Market-based control algorithms can maximize resource management under highly dynamic and uncertain conditions. These attributes are critical to the success of complex, dynamically interdependent distributed combat systems. The proposed market-based control method provides a mathematical foundation for distributed control systems which are agile, resilient, dependable, effective, and efficient. Herein, a market-based control approach is presented for the control of power flow within an electric ship. The proposed control method consists of an artificial market in which various actors (a consumer and firms) behave according to microeconomic principles. Examples of such actors include generation, distribution, conversion, energy storage, and the commanding officer. Each piece of equipment within the engineering plant will behave as a firm, attempting to maximize its profit. The commanding officer will behave as a consumer, attempting to maximize his or her utility. By proper market design, the control system allocates resources within the system efficiently to meet the objectives of the commanding officer. This control strategy does not inherently depend on the mode of operation. If objectives change (e.g., cruising vs. battle), the market reacts, prices shift, and resources are allocated to new purposes. If the structure of the system changes (e.g., due to a change in plant lineup or due to battle damage), the prices will change

to reflect the new conditions, and the market will attempt to meet the objectives in the most efficient manner under the new configuration. In this way, a unified control strategy can be applied to achieve various objectives, such as fuel efficiency, continuity of service, and survivability.

The remainder of this paper is organized as follows. In Section II, the method for reformulating the power system allocation problem as a market-clearing problem is presented. An illustrative example is described in Section III. A notional medium-voltage dc (MVDC) system and the decision functions for its components are described in Section IV, and the performance of the market-based control is compared with the performance of an idealized controller under both an ordinary operational vignette and a fault scenario.

## II. MARKET-BASED CONTROL

The shipboard power system can be understood as consisting of  $n$  resources (e.g., power at a given bus). Each component  $i$  in the system can be thought to consume a bundle of resources represented as  $\mathbf{Q}_i = [Q_1 \ Q_2 \ \dots \ Q_n]^T$ , in which resources produced by the component are represented with negative numbers. The physical constraints of each component are represented by two constraints that  $\mathbf{g}_i(\mathbf{Q}_i) \leq \mathbf{0}$  and  $\mathbf{h}_i(\mathbf{Q}_i) = \mathbf{0}$ .

The bundle of resources that can be thought to be consumed by the commanding officer in order to meet mission requirements can be represented by  $\mathbf{Q}_c$ , and it is likewise subject to two constraints that  $\mathbf{g}_c(\mathbf{Q}_c) \leq \mathbf{0}$  and  $\mathbf{h}_c(\mathbf{Q}_c) = \mathbf{0}$ . Also, a function  $f_c(\mathbf{Q}_c)$  represents the utility derived from a given bundle of consumed resources, a value that the commanding officer would like to maximize. Conservation laws require that

$$\mathbf{Q}_c + \sum_{\forall i} \mathbf{Q}_i = \mathbf{0}. \quad (1)$$

**Problem 1.** The allocation problem is to find  $\mathbf{Q}_c$  and  $\mathbf{Q}_i \ \forall i$  that solve

$$\max_{\mathbf{Q}_c, \mathbf{Q}_i \ \forall i} f_c(\mathbf{Q}_c) \quad (2)$$

$$\text{subject to } \mathbf{g}_c(\mathbf{Q}_c) \leq \mathbf{0} \quad \mathbf{g}_i(\mathbf{Q}_i) \leq \mathbf{0} \quad \forall i \quad (3)$$

$$\mathbf{h}_c(\mathbf{Q}_c) = \mathbf{0} \quad \mathbf{h}_i(\mathbf{Q}_i) = \mathbf{0} \quad \forall i \quad (4)$$

$$\mathbf{Q}_c + \sum_{\forall i} \mathbf{Q}_i = \mathbf{0}. \quad (5)$$

Necessary conditions for  $\mathbf{Q}_c$  and  $\mathbf{Q}_i \ \forall i$  to be a solution to Problem 1 are that (3)–(5) are satisfied and that  $\exists \mu_c \geq \mathbf{0}$ ,  $\exists \mu_i \geq \mathbf{0} \ \forall i$ ,  $\exists \lambda_c$ ,  $\exists \lambda_i \ \forall i$ , and  $\exists \bar{\lambda}$  such that

$$\nabla f_c = \left( \frac{\partial \mathbf{g}_c}{\partial \mathbf{Q}_c} \right)^T \mu_c + \left( \frac{\partial \mathbf{h}_c}{\partial \mathbf{Q}_c} \right)^T \lambda_c + \bar{\lambda} \quad (6)$$

$$\mathbf{0} = \left( \frac{\partial \mathbf{g}_i}{\partial \mathbf{Q}_i} \right)^T \mu_i + \left( \frac{\partial \mathbf{h}_i}{\partial \mathbf{Q}_i} \right)^T \lambda_i + \bar{\lambda} \quad \forall i \quad (7)$$

$$\mu_{cj} g_{cj}(\mathbf{Q}_c) = 0 \quad \forall j \quad (8)$$

$$\mu_{ij} g_{ij}(\mathbf{Q}_i) = 0 \quad \forall i, j. \quad (9)$$

It is proposed herein to represent the shipboard power system using an artificial market-based economy in which the

components in the system act as firms and the commanding officer acts as a consumer. In this economy, the price of all the goods can be expressed as  $\mathbf{\Pi} = [\Pi_1 \ \Pi_2 \ \dots \ \Pi_n]^T$ . A firm  $i$ , consuming a bundle of resources  $\mathbf{Q}_i$  will receive a profit given by

$$\text{Profit}_i = -\mathbf{\Pi}^T \mathbf{Q}_i. \quad (10)$$

Therefore, the consumption decision for firm  $i$  is

$$\mathbf{Q}_i = \arg \max_{\hat{\mathbf{Q}}_i} -\mathbf{\Pi}^T \hat{\mathbf{Q}}_i \quad (11)$$

$$\text{subject to } \mathbf{g}_i(\hat{\mathbf{Q}}_i) \leq \mathbf{0} \quad (12)$$

$$\mathbf{h}_i(\hat{\mathbf{Q}}_i) = \mathbf{0}. \quad (13)$$

The consumer will attempt to maximize utility by solving the following optimization problem:

$$\mathbf{Q}_c = \arg \max_{\hat{\mathbf{Q}}_c} f_c(\hat{\mathbf{Q}}_c) \quad (14)$$

$$\text{subject to } \mathbf{g}_c(\hat{\mathbf{Q}}_c) \leq \mathbf{0} \quad (15)$$

$$\mathbf{h}_c(\hat{\mathbf{Q}}_c) = \mathbf{0} \quad (16)$$

$$\mathbf{\Pi}^T \hat{\mathbf{Q}}_c = \sum_{\forall i} \text{Profit}_i. \quad (17)$$

**Problem 2.** The market-clearing problem is to find  $\mathbf{\Pi}$  such that

$$\mathbf{Q}_c + \sum_{\forall i} \mathbf{Q}_i = \mathbf{0}. \quad (18)$$

**Proposition 1.** A solution to Problem 2 satisfies the necessary conditions for a solution to Problem 1.

*Proof.* If  $\mathbf{\Pi}$  is a solution to Problem 2, (3)–(5) are satisfied. Also, from the necessary conditions for  $\mathbf{Q}_c$  to be a solution to  $\exists \mu_c \geq \mathbf{0}$  and  $\exists \lambda_c$  such that

$$\nabla f_c = \left( \frac{\partial \mathbf{g}_c}{\partial \mathbf{Q}_c} \right)^T \mu_c + \left( \frac{\partial \mathbf{h}_c}{\partial \mathbf{Q}_c} \right)^T \lambda_c + \mathbf{\Pi} \quad (19)$$

$$\mu_{cj} g_{cj}(\mathbf{Q}_c) = 0 \quad \forall j. \quad (20)$$

Also,  $\exists \mu_i \geq \mathbf{0} \ \forall i$  and  $\exists \lambda_i \ \forall i$  such that

$$-\mathbf{\Pi} = \left( \frac{\partial \mathbf{g}_i}{\partial \mathbf{Q}_i} \right)^T \mu_i + \left( \frac{\partial \mathbf{h}_i}{\partial \mathbf{Q}_i} \right)^T \lambda_i \quad (21)$$

$$\mu_{ij} g_{ij}(\mathbf{Q}_i) = 0 \quad \forall i, j. \quad (22)$$

Thus, (6)–(9) are satisfied with  $\bar{\lambda} = \mathbf{\Pi}$ .  $\square$

*Remark 1.* Under stronger conditions, stronger statements relating Problem 1 and 2 can be made.

## III. ILLUSTRATIVE EXAMPLE

In this section, market-based control will be demonstrated on a simple example in which it is possible to calculate the solution analytically. The example involves a generator, an interconnect, a nonlinear load, and a consumer arranged as shown in Fig. 1. The generator, the interconnect, and the load will behave as firms. Because of the structure of the system, the power provided to Bus 1 by the generator must correspond to the power transferred from Bus 1 to Bus 2 by

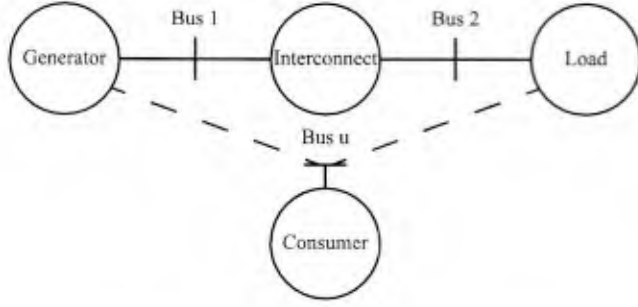


Fig. 1. Illustrative example. The generator, interconnect, and load act as firms.

the interconnect and to the power consumed from Bus 2 by the load. The utility function is expressed as

$$U = -w_g P + w_l \sqrt{P}, \quad (23)$$

where  $P$  is the consumed power and  $w_g \geq 0$  and  $w_l \geq 0$  are the weighting factors for the generator and the load, respectively. The generator, interconnect, and load have maximum powers  $P_{gmax} \geq 0$ ,  $P_{imax} \geq 0$ , and  $P_{lmax} \geq 0$ , respectively.

For this system, it is known that the optimal power is

$$P^* = \min \left\{ \frac{w_l^2}{4w_g^2}, P_{gmax}, P_{imax}, P_{lmax} \right\}. \quad (24)$$

This solution can be compared with the solution found by solving the market-clearing problem.

For market-based control, this system is considered to have three resources: power at Bus 1, power at Bus 2, and utility with prices  $\Pi_1$ ,  $\Pi_2$ , and  $\Pi_u$ , respectively. The profit of the generator can be expressed as

$$\text{Profit}_g = \Pi_1 P_g - \Pi_u w_g P_g, \quad (25)$$

where  $P_g$  is the output power of the generator. The generator will attempt to maximize its profit under given prices  $\Pi_1$  and  $\Pi_u$ . The maximum profit can be reached when

$$P_g = \begin{cases} P_{gmax} & \Pi_1 > \Pi_u w_g \\ 0 & \Pi_1 < \Pi_u w_g. \end{cases} \quad (26)$$

The profit of the interconnect can be expressed as

$$\text{Profit}_i = \Pi_2 P_i - \Pi_1 P_i, \quad (27)$$

where  $P_i$  is the power transferred from Bus 1 to Bus 2. The interconnect will attempt to maximize its profit under given prices  $\Pi_2$  and  $\Pi_1$ . The maximum profit can be reached when

$$P_i = \begin{cases} P_{imax} & \Pi_2 > \Pi_1 \\ -P_{imax} & \Pi_2 < \Pi_1. \end{cases} \quad (28)$$

The profit of the load can be expressed as

$$\text{Profit}_l = \Pi_u w_l \sqrt{P_l} - \Pi_2 P_l, \quad (29)$$

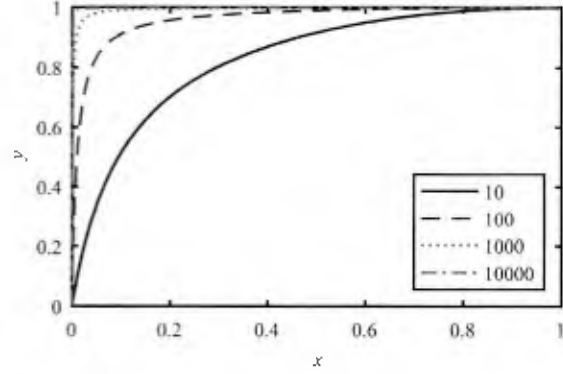


Fig. 2. Plots of the step approximation function for several values of  $m$ .

where  $P_l$  is the power consumed by the load. The load will attempt to maximize its profit under given prices  $\Pi_u$  and  $\Pi_2$ . The maximum profit can be reached when

$$P_l = \begin{cases} \min \left\{ \frac{w_l^2}{4} \left( \frac{\Pi_u}{\Pi_2} \right)^2, P_{lmax} \right\} & \Pi_2 > 0 \\ 0 & \Pi_2 < 0 \text{ and} \\ & \Pi_u > \frac{w_l}{\sqrt{P_{lmax}}} \Pi_2 \\ P_{lmax} & \Pi_2 < 0 \text{ and} \\ & \Pi_u \leq \frac{w_l}{\sqrt{P_{lmax}}} \Pi_2. \end{cases} \quad (30)$$

The consumer consumes the amount of utility available to it from the profits of the components:

$$U = \frac{\text{Profit}_g + \text{Profit}_i + \text{Profit}_l}{\Pi_u}. \quad (31)$$

The discontinuities in the decision functions of the components create numerical challenges for solving the market-clearing problem. These challenges are magnified by the fact that the solution to the problem often lies at the point of discontinuity. To address this challenge throughout, a continuously differentiable approximation of a step function is used throughout. In particular, for a step function passing through zero at  $x = 0$  and having a value of unity at  $x = 1$ , an approximation with a slope of  $m$  at  $x = 0$  and a slope of zero at  $x = 1$  is given by

$$y = \frac{mx + (3x^2 - 2x^3)}{mx + 1}. \quad (32)$$

Plots of this function for several values of  $m$  are shown in Fig. 2. It can be seen that by increasing the value of  $m$ , this function more closely approximates a step function.

The problem is considered with  $P_{gmax} = P_{imax} = P_{lmax} = 1$  pu and with  $w_l = 1$ . The utility function is plotted versus the power for different values of  $w_g$  in Fig. 3. It can be seen that different values of  $w_g$  result in different optimal values of power. Some of these values are internal to the interval  $[0, 1]$  pu, and some lie on the upper limit.

The market-clearing problem is solved for the different values of  $w_g$  using MATLAB's `fsolve`. The results are shown in

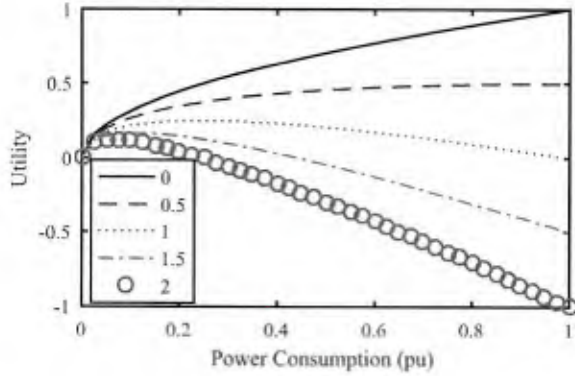


Fig. 3. Relationship between power consumption and utility for different generator weights ( $w_i = 1$ ).

TABLE I  
COMPARISON OF ANALYTICAL AND MARKET-BASED SOLUTIONS FOR DIFFERENT GENERATOR WEIGHTS

Generator weight	Analytical solution	Market-based solution
0	1	1.0000
0.5	1	0.9999
1	0.25	0.2504
1.5	0.1111	0.1111
2	0.0625	0.0625

Table I. It can be seen that the solution to the market-clearing problem (even with the introduced continuously differentiable approximation) corresponds to the analytical solution for cases both internal to and on the boundary of the interval.

#### IV. SHIPBOARD EXAMPLE

In this section, the market-based approach will be demonstrated on a larger system, the notional medium-voltage dc (MVDC) system shown in Fig. 4. The MVDC system is based on the notional MVDC system developed by the Electric Ship Research and Development Consortium [7]. Parameters for the system are shown in Table II. The four-zone system consists of two main generators and two auxiliary generators. There are two propulsion drives that operate at power levels corresponding with the desired speed. There is a radar and a high-power load in Zone 1 and associated energy storage that are used to engage in the mission. The zonal loads are fed through converters, and each zone contains some vital and some nonvital load.

The MVDC system has a variety of different component types: interconnects, generators, converters, energy storage, and loads. Each of these component types will act as firms in the artificial market-based economy and will require a decision function that specifies its profit-maximizing operation for a given set of prices. The decision functions for each of the components under representative conditions are shown in the figures described below. The interconnect decision function is shown in Fig. 5. The decision function for the generator is shown in Fig. 6. The generator decision function is based on

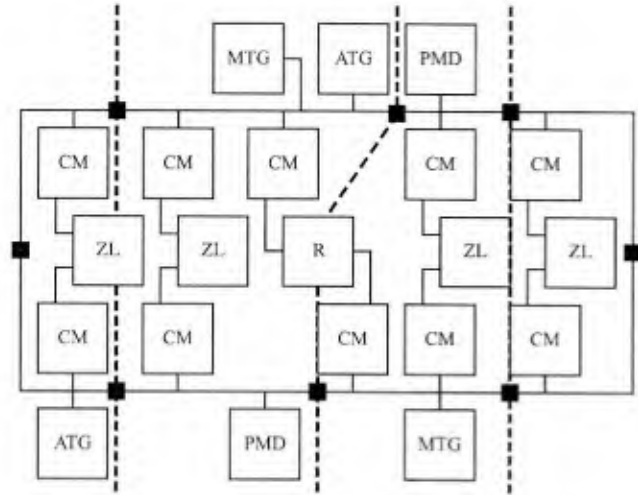


Fig. 4. Notional MVDC system. MTG signifies main generator, ATG signifies auxiliary generator, PMD signifies propulsion, CM signifies converter, R signifies radar, and ZL signifies zonal load.

TABLE II  
PARAMETERS OF NOTIONAL MEDIUM-VOLTAGE DC SYSTEM

Rating of main generators	36 MW
Rating of auxiliary generators	5 MW
Total rated propulsion load	60.4 MW
Radar load	3.8 MW
Vital load per zone	0.9 MW
Nonvital load per zone	0.8 MW
Zone 1 mission load	13 MW
Zone 1 energy storage	780 MJ
Zone 1 energy storage rate	13 MW
Zone 1 power conversion capacity	2.6 MW

the dynamic state of the generator. At any given moment, the generator has a dynamic maximum and minimum power limit that are functions of the prime mover dynamics. For some sets of prices, the generator should produce its maximum power. For others, it should produce its minimum power. As some sets of prices, the generator should produce zero power (e.g., if no load is operational). If the minimum power is greater than zero, operation at zero power will result in the generator entering an overspeed status and tripping offline. The decision function for the converter is shown in Fig. 7. The energy storage decision function is shown in Fig. 8. Finally, Fig. 9 shows the decision function of the load. The profit of each component is given by 10. The decision function for the consumer is to consume the amount of utility available to it from the profits of the components:

$$U = \frac{\sum_{v_i} \text{Profit}_i}{\Pi_u} \quad (33)$$

Two simulation studies of the MVDC system are performed, representing both normal and abnormal operating conditions. The performance of the market-based controller is compared with the performance of an idealized linear-programming-based control representation, which is seeking to maximize the same utility function.

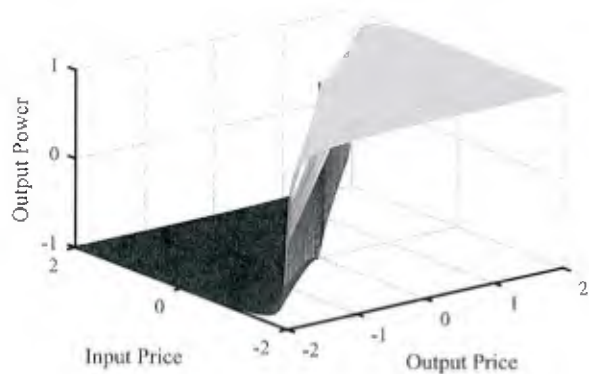


Fig. 5. Interconnect decision function.

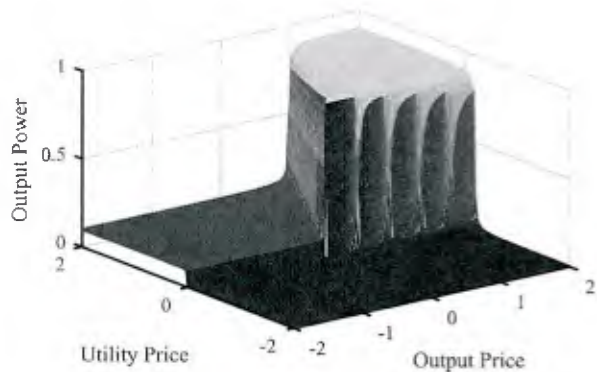


Fig. 6. Generator decision function.

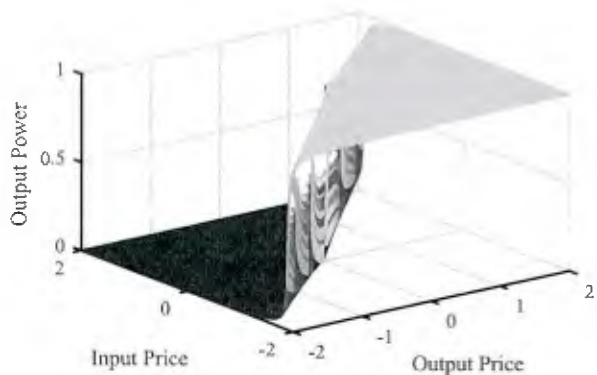


Fig. 7. Converter decision function.

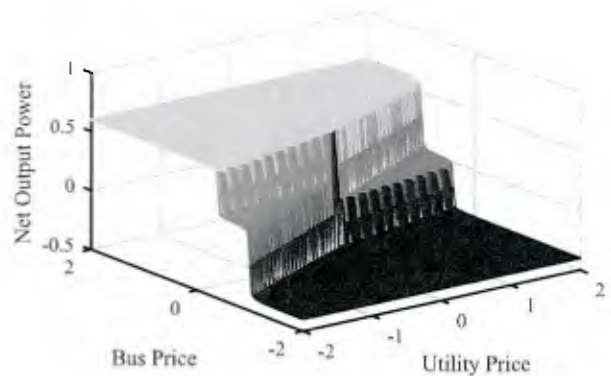


Fig. 8. Energy storage decision function.

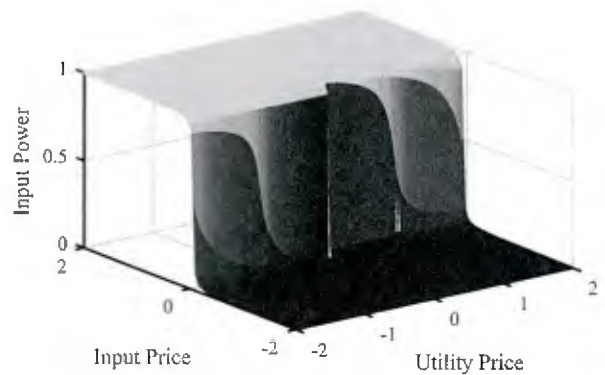


Fig. 9. Load decision function.

In the first scenario, a representative operation vignette based on [8] is studied. In this vignette, the ship cruises at 20 knots with its radar and mission load turned off. At 30 s, the ship reduces speed to 10 knots and turns on the mission load in Zone 1. At 75 s, the radar is turned on. At 100 s, the mission load is turned off, and the ship increases speed to 20 knots. At 135 s, the ship increases speed further to 30 knots. The vignette ends at 180 s.

The performance of the system with an idealized linear-programming-based controller representation is shown in Fig. 10. It can be seen that the propulsion and generation powers are reduced at 30 s and that the mission load power is increased. The zonal power conversion equipment in Zone 1 is not sufficiently large to operate the mission load, so it is primarily served from energy storage situated in this zone. The stored energy begins to decrease as the energy storage serves the mission load. The non-vital load in this zone is shed in order to serve the vital and mission loads with the zonal power conversion equipment and the energy storage. At 75 s, the radar load and generator powers increase. At nearly 100 s, the energy storage is exhausted, and the vital load in the zone is shed briefly in order for all zonal power conversion capability to serve the mission load. At 100 s, the mission

load is turned off and the propulsion and generation powers increase. Both the vital and non-vital loads are restored to service and the energy storage begins to charge with remaining zonal power conversion capability. At 135 s, the propulsion and generation powers increase further, but this increase is limited by the ramping limits of the generation. The results from the market-based controller are shown in Fig. 11 and match the results from the idealized linear-programming based control representation perfectly. The prices of main-bus power, propulsion power, radar power, and power within Zone 1 are also shown in Fig. 11. It can be seen that the price of the power in Zone 1 increases when the mission load in that zone is turned on at 30 s. At 75 s, the price of the radar load changes from a negative value to a positive value when the radar is turned on. At nearly 100 s, the price of power in Zone 1 increases dramatically because the energy storage is exhausted. At 100 s, the price of power in Zone 1 decreases since the mission load is turned off. Because the energy storage is recharging at this time, the price of power in Zone 1 is higher than its initial value. At 135 s, all the prices ramp up because the power required by the propulsion increases and the generators cannot initially meet the increased demand. When the generation ramps up to meet the power demand, all the prices return to their previous values.

In the second scenario, a single-bus fault is studied. In this scenario, the ship cruises at 30 knots with its mission load turned off and its radar turned on. At 15 s, a main-bus fault occurs in the port side of Zone 3 and lasts for 2 s. The vignette ends at 60 s.

The performance of the system with an idealized linear-programming-based controller representation is shown in Fig. 12. It can be seen that the propulsion and generation powers are reduced when the fault occurs since the main generator and auxiliary generator connected to the faulted bus are tripped offline. The non-vital load is shed in order to serve the vital load with the unaffected zonal power conversion equipment in the zone. The remaining generation operates at full power. When the fault clears at 17 s, some of the power being used for propulsion is reallocated to the non-vital load in Zone 3. At 19 s, the two tripped generators recover and begin increasing their output, which goes to serve propulsion load. The results from the market-based controller, shown in Fig. 13, are consistent with the results from the idealized linear-programming based control representation. At 15 s, all the prices go up because of the insufficient power supply. The radar power price increases the most because it must now be served entirely through the starboard side of Zone 2. When the fault is cleared at 17 s, the prices of the main bus, propulsion and radar load drop down to a lower value, reflecting the improved availability of power in Zone 3. When the two tripped generators recover and ramp up to meet the full propulsion load, the prices return to their original levels.

## V. CONCLUSION

The proposed market-based control of electric ship power systems applies market principles to the control method and

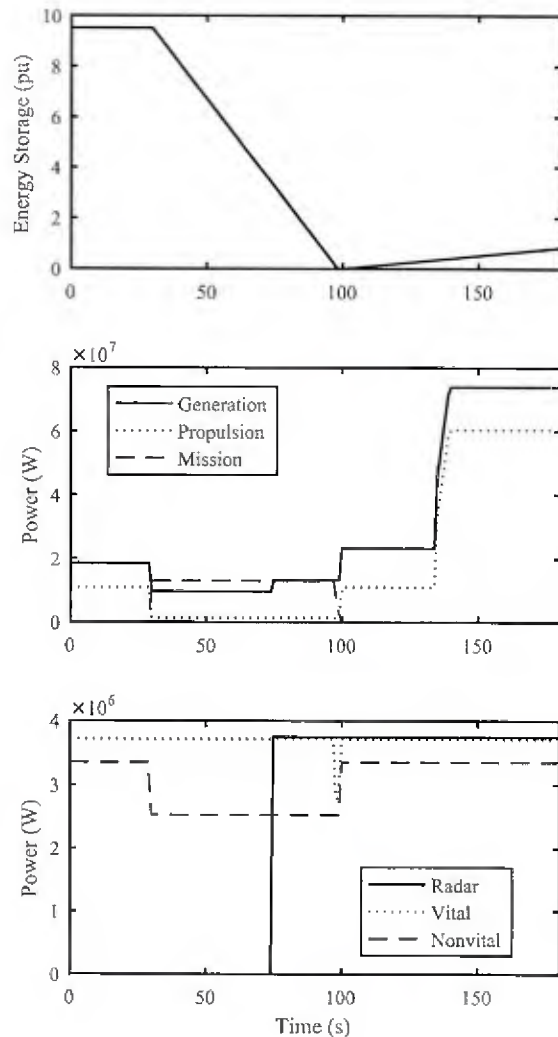


Fig. 10. Load changing vignette performance of idealized linear-programming based control representation.

explicitly links the economic behavior of the actors in the system (a consumer and firms) with the physical behavior of the equipment in the system. It can optimize resource allocation under highly dynamic and uncertain conditions. As objectives change, prices in the system will adjust automatically, and the consumer (commanding officer) will attempt to maximize his or her utility while firms (each piece of equipment) attempt to maximize its profit. In this way, the optimized resources allocation under the new configuration is achieved. Simulation studies of a notional electric power system in both ordinary and faulty conditions are performed and demonstrate that the proposed market-based control system results in performance

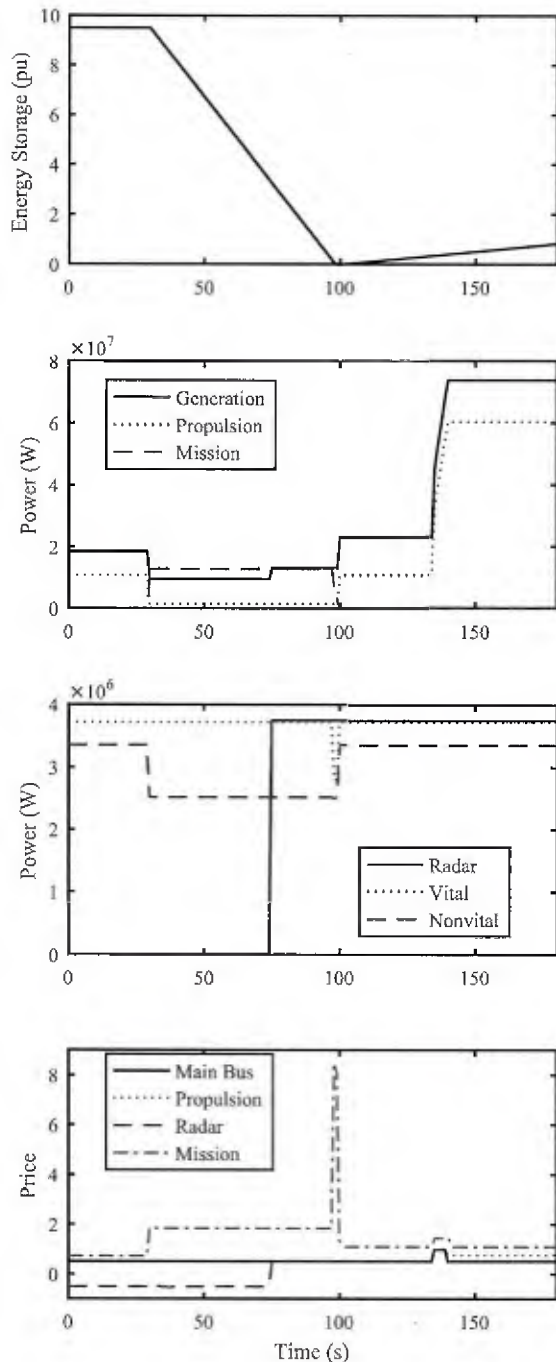


Fig. 11. Load changing vignette performance of market-based controller.

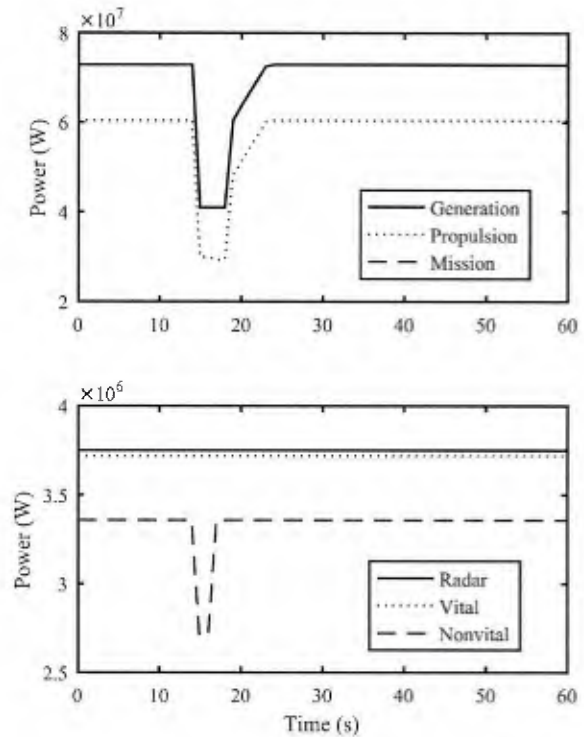


Fig. 12. Fault scenario performance of idealized linear-programming based control representation.

equal to that of an idealized controller.

#### ACKNOWLEDGMENT

This work was supported by the Office of Naval Research (ONR) through the ONR Young Investigator Program N00014-15-1-2475.

#### REFERENCES

- [1] S. H. Clearwater, Ed., *Market-based Control: A Paradigm for Distributed Resource Allocation*. River Edge, NJ, USA: World Scientific Publishing Co., Inc., 1996.
- [2] S. H. Clearwater, "Auction-based control system for energy resource management in a building," U.S. Patent 5 394 324, Feb. 18, 1995.
- [3] J. P. Lynch and K. H. Law, "A market-based control solution for semi-active structural control," in *Proc. 8th Int. Conf. Computing in Civil and Building Eng.*, Stanford, CA, 2000, pp. 588–595.
- [4] J. G. Gomez-Gualdron, M. Velez-Reyes, and L. J. Collazo, "Self-reconfigurable electric power distribution system using multi-agent systems," in *2007 IEEE Electric Ship Technologies Symp.*, May 2007, pp. 180–187.
- [5] A. Feliachi, K. Schoder, S. Ganesh, and H.-J. Lai, "Distributed control agents approach to energy management in electric shipboard power system," in *2006 IEEE Power Eng. Soc. General Meeting*, Montreal, Que., 2006, p. 6.
- [6] A. Deshmukh, F. Ponci, A. Monti, M. Riva, and L. Cristaldi, "Multi-agent system for diagnostics, monitoring and control of electric systems," in *Proc. 13th Int. Conf. Intelligent Syst. Applicat. to Power Syst.*, Nov. 2005, p. 6.
- [7] J. S. Chalfant and C. Chrysostomidis, "Analysis of various all-electric-ship electrical distribution system topologies," in *2011 IEEE Electric Ship Technologies Symp.*, April 2011, pp. 72–77.

- [8] A. M. Cramer, X. Liu, Y. Zhang, J. D. Stevens, and E. L. Zivi, "Early-stage shipboard power system simulation of operational vignettes for dependability assessment," in *2015 IEEE Electric Ship Technologies Symp.*, Jun. 2015, pp. 382–387.

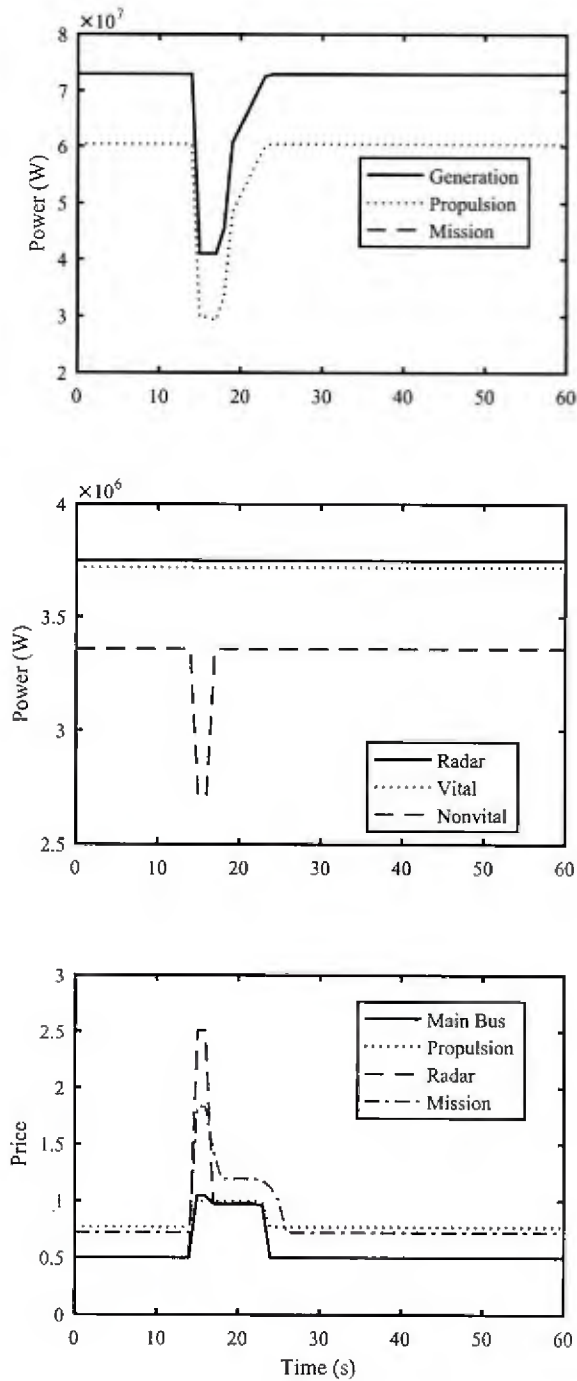


Fig. 13. Fault scenario performance of market-based controller.

# Early Stage Design Evaluation of Shipboard Power Systems Using Multi-Period Power Flow

Eun Oh<sup>1</sup>, Daniel F. Opila<sup>1</sup>, John Stevens<sup>1</sup>, Edwin Zivi<sup>1</sup>, and Aaron Cramer<sup>2</sup>

**Abstract**—Future shipboard power system architectures are designed to service high-power pulsed loads through a combination of generators and energy storage for volume and weight considerations. Optimal control solutions therefore depend on both past and future events. This complicates evaluation of the relative performance of different architectures due to dependence on controller strategies and algorithms. Herein, we introduce a technique for early stage evaluation of the relative performance of various ship power system designs by assuming a known future and calculating the best-case performance of any possible controller design. We demonstrate this technique using 6 mission scenarios on a representative multi-bus power system architecture. The controller has perfect future knowledge of the loads on each 10 minute mission, which provides an upper bound on performance for a given architecture. While not usually achievable in practice, this technique allows a fair early stage comparison of multiple architectures regardless of controller type.

## I. INTRODUCTION

Shipboard power system design and analysis has become much more challenging due to increasing power demands from various mission loads, combined with new generation and storage technologies. Early-stage design studies are critical in designing an effective system. Previous study in this area includes general system arrangement and zones [1], [2], metrics and methods to understand power system resilience [3]–[5], evolutionary algorithms to design a power system or subsystems [6], [7], and numerous controller designs to operate such systems [8].

As power systems have become more complex, they require controllers to regulate component behavior. This implies that the performance of a given design cannot be evaluated without also designing a relevant controller. A linear programming approach was used in [9]–[11] to determine what a controller should do at each instant in time, without designing the controller itself. Automated design methods are then feasible because each candidate power system can be automatically evaluated.

The addition of energy storage in the system has made this problem much more complex in both the design and control of the power system. Energy storage capacity, power rating, and location is a critical question facing ship designers [12]. Storage may be located at the loads, distributed throughout the ship, or in one central location. Storage devices and fast-ramping loads require analysis that considers the dynamic

behavior of the system, rather than the quasi-static analysis that has been sufficient in the past. System control decisions now depend on past and future events, rather than just the current system state as in a traditional power system [13], [14]. Controlling the system based solely on the current time step will yield sub-optimal solutions.

In this paper we propose a method for early stage design evaluation for power systems that include energy storage and dynamic loads. An optimization-based algorithm considers a set of possible mission scenarios with known future loads, and produces a best-case upper bound for any controller's performance. A given controller can potentially reach this limit, but not exceed it. Thus the power system can be analyzed without manually creating a controller for each candidate design, which allows fast, automated system evaluation before controller design. The method also provides a fair comparison; performance is evaluated based on the architecture itself rather than a particular controller design. We are primarily concerned with the feasibility of serving various missions load requirements, rather than optimizing fuel consumption or some other metric, as in [15].

In some sense, our evaluation method to determine this upper-bound control performance is similar to model predictive control [16]–[18], with a prediction horizon of the whole mission, rather than the typical horizons of a few seconds. When we consider the various system power flows, it is equivalent to solving the multi-period optimal power flow (MPOPF) problem [19]–[22].

The end goal is automatic early stage power system evaluation that can predict the feasibility of many possible mission scenarios [11], [23] independent of specific controller design. For each scenario, the algorithm identifies if it is physically possible to serve the required load, and if not, how much power and energy shortfall exists. The result can provide an early insight into the selection of generator and energy storage ratings.

The paper is organized as follows: Section II describes the algorithm, while Section III presents an example power system, mission profiles, and numerical solver details. Results are presented in Section IV, and conclusions in Section V.

## II. ALGORITHM FORMULATION

For early stage design evaluation, the primary concern is the feasibility of solutions, rather than fuel burn, losses, etc. We wish to identify which missions can be accomplished with a given power system architecture, and the remaining under-served load for infeasible cases. This feasibility study can be reformulated as an optimization problem where the

<sup>1</sup>Oh, Opila, Stevens, and Zivi are with Faculty of Electrical and Computer Engineering, United States Naval Academy, Annapolis, MD 21402 oh@usna.edu

<sup>2</sup>Aaron Cramer is with the Department of Electrical Engineering, University of Kentucky, Lexington, KY, USA

original system is augmented with one or more infinite generators ( $\infty$ Gen) that can provide unlimited power, but at very high cost. This will guarantee that all solutions mathematically converge, but if the chosen solution accesses the infinite generator it is not feasible in reality. The problem mathematically starts with a single-period general form,

$$\min_{x, p_g, p_{es}} f_{gen}(x, p_g) + f_{es}(x, p_g, p_{es}) + f_{\infty}(x, p_g) \quad (1)$$

such that

$$g(x, p_g, p_{es}) = 0 \quad (2)$$

$$h(x, p_g, p_{es}) = 0 \quad (3)$$

$$x_{min} \leq x \leq x_{max} \quad (4)$$

$$p_{min} \leq p_{gen} \leq p_{max} \quad (5)$$

$$p_{es, min} \leq p_{es} \leq p_{es, max} \quad (6)$$

$$l \leq A \begin{bmatrix} x \\ p_g \\ p_{es} \end{bmatrix} \leq u. \quad (7)$$

TABLE I: Single-Period Variables and Terms

$x$	Vector of bus voltages and angles
$p_g$	Vector of real outputs for generating units
$p_{es}$	Vector of real outputs for Energy Storage units
$f_{gen}(x, p_g)$	Cost function for generating units
$f_{es}(x, p_g, p_{es})$	Cost function for Energy Storage units
$f_{\infty}(x, p_g)$	Cost function for infinite generator
$g(x, p_g, p_{es})$	Set of equality constraints
$h(x, p_g, p_{es})$	Set of inequality constraints
$A$	Matrix of additional constraints
$l$	Lower limit for additional constraints
$u$	Upper limit for additional constraints

The variables in the single-period equations are defined in Table I. We also add one fictional ‘‘infinite generator’’ ( $\infty$ Gen) which engages the network when all available power resources are exhausted to avoid non-convergence. Hence, accessing the infinite generator equates to inadequate power availability for a given mission. Typically the cost functions  $f(\cdot)$ , in cost-increasing order are: energy storages, conventional generators, and infinite generator.

#### A. Multi-Period Optimal Power Flow

Unlike a single-period optimal power flow which solves for power flow at each time step, the MP-OPF optimizes power and energy management for the entire mission at once by assuming perfect past and future knowledge. It simultaneously considers past, present, and future demand at all times. Conceptually, the MP-OPF is constructed by considering copies of the candidate power system at each of  $T$  time steps. The decision variables  $x, p_g, p_{es}$  have a representation at each time step that combine to create the extended MP-OPF decision variables  $\bar{x} = \{x(1), x(2), \dots, x(T)\}$ ,  $\bar{p}_g = \{p_g(1), p_g(2), \dots, p_g(T)\}$ , and  $\bar{p}_{es} = \{p_{es}(1), p_{es}(2), \dots, p_{es}(T)\}$ . For a power architecture with  $n_b$  buses,  $n_g$  generators, and  $n_{es}$  ES, the new decision variables  $\bar{x}, \bar{p}_g, \bar{p}_{es}$  now have  $2n_b T, n_g T$ , and  $n_{es} T$  elements

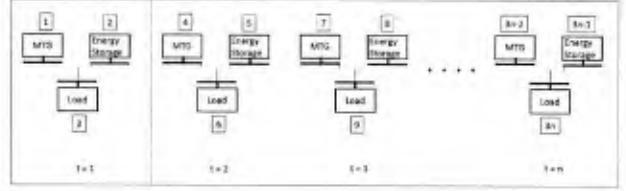


Fig. 1: Conceptual representation of multi-period power flow.

respectively. The vector  $x$  contains real values for bus voltage and angle, so has two values for each bus. The multi-period variables are defined in Table II.

As an example, consider a simple three-bus power architecture consisting of a Main Turbine Generator (MTG), an Energy Storage (ES) unit, and a Load (LD) as shown in Fig. 1. We replicate this three-bus micro-grid, constructing an instance for each of  $T$  mission scenario time steps, but with different bus and branch numbers accordingly.

Then, for each time step, we allocate time-dependent mission loads and apply power and energy storage capacity constraints. The solver can therefore make dispatch decisions considering conditions throughout the planning horizon which best utilize the dynamic interdependence of generators, energy storage, and loads.

TABLE II: Multi-Period Variables and Terms

$\bar{x}$	$x$ in multiple periods $T$
$\bar{p}$	$p$ in multiple periods $T$
$\bar{p}_{es}$	$p_{es}$ in multiple periods $T$
$f_{gen}(x, p_g)$	$f_{gen}$ in multiple periods $T$
$f_{es}(x, p_g, p_{es})$	$f_{es}$ in multiple periods $T$
$f_{\infty}(x, p_g)$	$f_{\infty}$ in multiple periods $T$

#### B. Energy Storage

The energy available in energy storage system evolves over time, so this optimization becomes a multi-period power flow problem. More specifically, energy storage units cannot provide power in the long run, so constraints are added to reflect their storage capacity. As we desire the minimum generator cost-function subject to a time constraint of energy capacity limit in an AC/DC power system. We use a relatively simple model for energy storage that is agnostic to the storage technology or hybrids thereof and provides bidirectional power flow.

Each energy storage unit has a maximum and a minimum power limit (e.g.  $\pm 10$  MW) and an energy capacity (e.g.  $\pm 30$  MJ). The storage is approximated as lossless, so the power output is integrated to determine the energy storage state,

$$E_{min} \leq \sum_{t=0}^{\tau} p_{es_i}(t) \Delta t \leq E_{max} \quad \forall \tau \in (0, T) \quad (8)$$

where  $p_{es_i}(t)$  is power from the energy storage  $i$ ,  $\Delta t$  is time step, and  $E_{min}$  and  $E_{max}$  are minimum and maximum energy capacities, respectively.

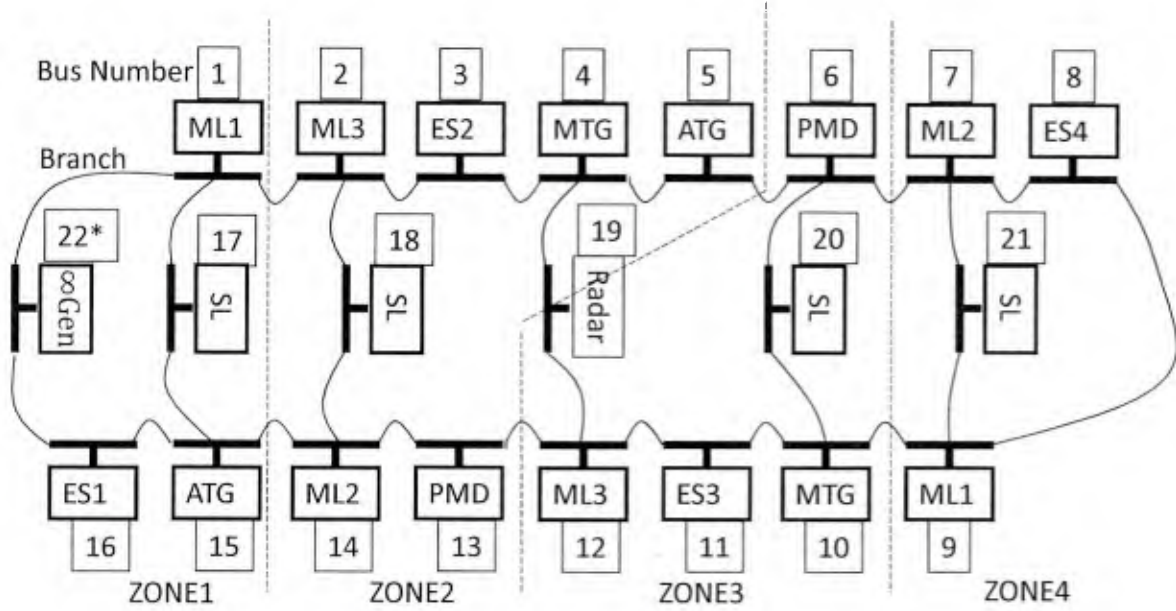


Fig. 2: 21 Bus system (thick lines) and interconnecting transmission lines.

The cumulative sum of energy is set as

$$\sum_t p_{es_i}(t) \Delta t = 0. \quad (9)$$

This is a trans-diachronic condition that the initially half-charged state of energy storage is returned at the end of the mission. We assume that there is no degradation of the energy storage and also that cost for accessing it is virtually zero. The enforcing constraints above are implemented in linear constraints of the type (7). At the end, the final formulation for multi-period optimal power flow is modified from (1) as,

$$\min_{\bar{x}, \bar{p}_g, \bar{p}_{cs}} \sum \bar{f}(\bar{x}, \bar{p}_g) + \bar{f}_{p_{cs}}(\bar{x}, \bar{p}_g, \bar{cs}) + \bar{f}_{\infty}(\bar{x}, \bar{p}_g) \quad (10)$$

where the bar on top of variables include vectors of entire multi-period as oppose to a single-period.

### III. EXAMPLE POWER SYSTEM EVALUATION

#### A. Power System Architecture

For the power system under this study we reproduce and augment the power network proposed by [23]. The system is a 21-bus network with distinct bus/branch elements, as shown in Fig. 2.

This is a 4-zone power architecture with two MTGs noted by bus numbers 4 and 10, and two ATGs noted by bus numbers 5 and 15. There is one energy storage in each zone with bus numbers 3, 8, 11, and 16, respectively. There are 6 main loads distributed throughout the ship: 4 Service Loads (SL) in which each respective bus shares 1/4 of the total service load, two Propulsion Motor Drive (PMD) loads in which each respective bus shares 1/2 of the total PMD load, 1 Radar (R) load, and 3 distinguishable Mission Loads (ML1,

ML2, ML3) split 1/2 load in different zones each sharing 1/2 of the MLx, respectively. We omit power conversion modules as they simply mimic a small line-loss through conversion (or consider a very highly efficient converters). We add one fictional “infinite generator” (bus number 22) for simulation purposes only, as previously mentioned. Total power generation on-board is 82 MW which is comprised of two MTGs at 35 MW each, two ATGs at 6 MW each. The infinite generator is accessed when there is insufficient power available to meet mission load, however, due to its extremely high cost it is only accessed after all available power sources have been exhausted. Power drawn from the virtual infinite generator indicates a power deficit implying a mission failure for that specific system and mission profile. The amount of virtual power required indicates the gap between mission failure and success.

#### B. Operational Vignette Mission Profile

This particular 21-bus ship system is evaluated for its ability to supply power for six missions developed in previous work [23]. We would like to identify which scenarios fail, and to what extent. A failed scenario demonstrates that the system is physically incapable of supplying the load, regardless of the controller selected.

A brief description of each mission is given below. The maximum available generator power is 82 MW, not including energy storage.

**Mission 1:** Constant slow speed. Peak loads are well below the maximum generator power.

**Mission 2:** Moderate ship maneuver. Peak loads are below maximum generator power.

**Mission 3:** Aggressive ship maneuver. Although the main propulsion and other loads fall within the 82 MW, pulsed

loads exceed maximum generation at three different times during the mission.

**Mission 4:** Constant slow speed. Heavy load demand sometimes exceeds maximum generation.

**Mission 5:** Moderate ship maneuver. Total ship power demand often exceeds maximum generation. We expect full usage of generators and energy storage units as well as the possibility of accessing the fictional infinite generator.

**Mission 6:** Aggressive ship maneuver. The majority of the mission exceeds peak generation. It is highly unlikely that there is sufficient power to meet this mission.

### C. Solution method

We use the general purpose power system solver MATPOWER [24], which accepts problems in standard form (1)-(7). By using the extended MP-OPF variables (10), we can use this standard solver for the MP-OPF problem. We select  $\Delta t$  in (8) and (9) as 1 second.

For simplicity, we restrict our simulation to a DC power flow approximation without line-limits, and ramp-rates. This is not required, the formulation and the MATPOWER solver support the full nonlinear power flow equations.

## IV. RESULTS

The results for each 10 minute mission (600 s) are shown in figure 3 and described below for each mission, along with the time required to compute the solution. The key takeaways are to identify which missions failed, and how close they were to success.

**Mission 1 (Fig. 3a):** The two MTGs and two ATGs share significant portion of slowly varying load demands, whereas the rapidly changing pulsed loads are supplied from the 4 energy storage units. We note that the energy storage units are pre-emptively charged to full capacity (+30 MJ), held, then discharged to supply high rep-rate pulsed load at 120 seconds, demonstrating anticipation of future loads. There was sufficient mix of power generation and energy storage capacity to support the mission demand. Computation time was 86 seconds.

**Mission 2 (Fig. 3b):** The two MTGs and two ATGs asymmetrically share power load demand, supplying up to 10 MW and 6 MW, respectively. Again, pulsed loads were provided from the pre-charged energy storage at appropriate times. Computation time was 99 seconds.

**Mission 3 (Fig. 3c):** Total load demand exceeds the installed 82 MW capacity at 120, 240, and 360 seconds. These transient overages are successfully serviced from the four pre-charged energy storage units. Even though the total mission demand exceeds 82 MW in three different instances, total power delivered by the generators and energy storage satisfied the mission requirements so that the virtual infinite generator was never needed. Computation time was 103 seconds.

**Mission 4 (Fig. 3d):** Similar to Mission 3, the peak pulsed load demand exceeded peak generation, but was provided from energy storage discharging at appropriate times. Computation time was 110 seconds.

**Mission 5 (Fig. 3e):** Unlike missions 1-4, this mission consistently demands much greater than 82 MW, sometimes peaking up to 123 MW. The infinite generator is accessed on two different occasions, providing 3.83 MW from 239 to 284 s and 11 MW from 358 to 375 s. Some of this behavior has a simple explanation; the balance of power at  $t = 360$  seconds reveals total generator power is 82 MW and total energy storage provides 30 MW ( $35+35+6+6+30=112$  MW). Overall, there is insufficient mix of power for this mission, thus it fails. Computation time was 117 seconds.

**Mission 6 (Fig. 3f):** This most demanding mission scenario fully engages all 4 generators for the majority of the time. The mission far exceeds ship capability as the infinite generator provides up to 42 MW between 240 to 280 seconds. For about 50 percent of the mission, the generators and energy storage fail to sufficiently satisfy the power demand. The total energy demand for the mission is 40.5 GJ whereas the total available energy generation is 49.2 GJ over the 600s mission. The total energy required is less than the total available generation, implying that larger energy storage could improve performance. Computation time was 130 seconds.

This early stage design evaluation indicates that the power system considered cannot provide sufficient power for 2 of 6 missions, although mission 5 is close. This result is an upper bound on performance regardless of controller type or architecture. It is theoretically possible to complete 4 of the load profiles, but a controller must be designed to achieve that performance. This may not be practical given that the analysis in this paper represents a known future, thus the successful missions are an upper bound on controller performance.

The system behavior exhibits future planning, as expected given the assumption that the future is known to the controller. For example, the start of all 6 missions exhibits generation in excess of load. More specifically, Fig. 4 shows that for mission 1 the difference in the total load demand and total generator output of +2 MW for the first 60 seconds is preemptively being stored for delayed use during a high rep-rate pulsed demand starting at 120 seconds. Furthermore, this pre-allocation of energy is why missions 3 and 4 do not access the infinite generator even though the total demand temporarily exceeds the maximum generation.

As a general trend, generators supply constant power loads, while pulsed loads are supplied by the energy storage units, as shown in Fig. 5. This is intuitive behavior and numerically occurs because of super-linear(quadratic) generator costs. However, in special cases when the generators are at or near their maximum power, a constant load is supplied from both the generators and energy storage units simultaneously, as shown in Figs. 3(d-f) between 420 and 450 seconds.

To verify enforcement of the end-user defined constraints (7), we observe in the bottom subfigures of Fig. 3 that the energy storage unit capacities of  $\pm 30$  MJ and power ratings of  $\pm 10$  MW are upheld throughout the 6 missions. Concurrently, the trans-diachronic constraint of cumulative sum of energy returning to its original state is also upheld.

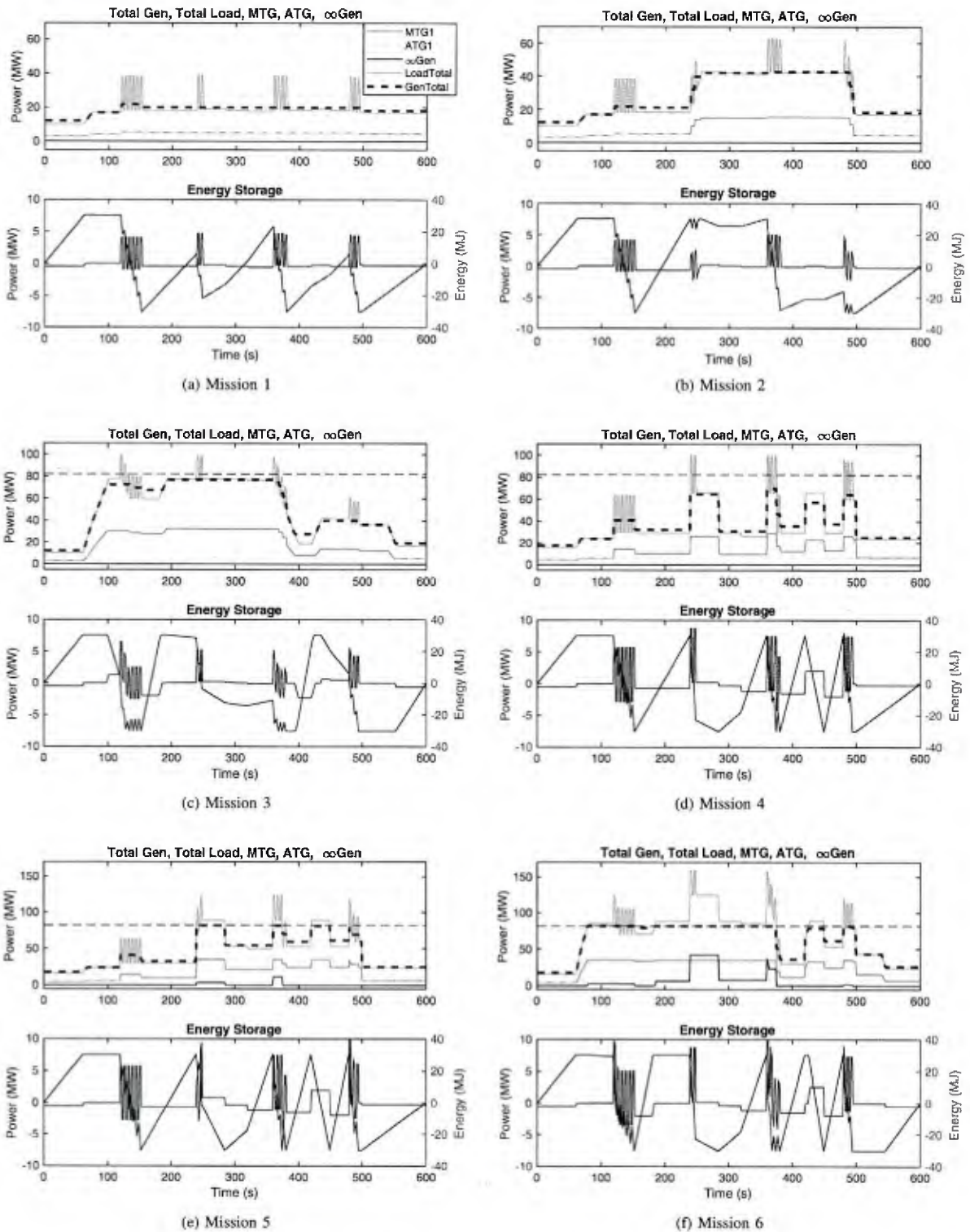


Fig. 3: For each mission, top plot contains total load (blue), total generator (dash-red), MTGs (green), ATGs (yellow), infinite generator (black) outputs, and installed power limit (dash-black). Bottom plot shows energy storage power output (blue) and cumulative sum of energy (red).

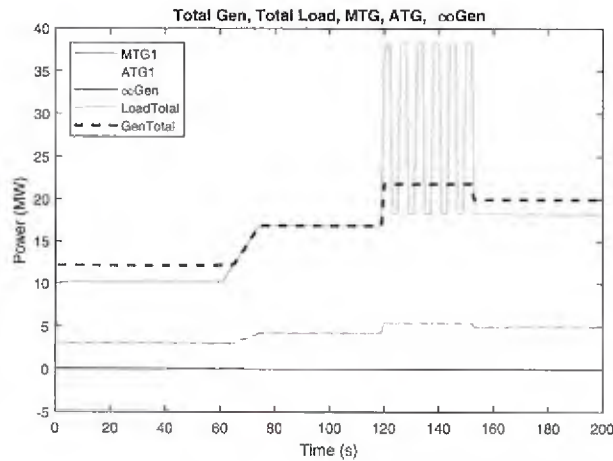


Fig. 4: The excess power from the beginning of the mission 1 is being stored in for later use.

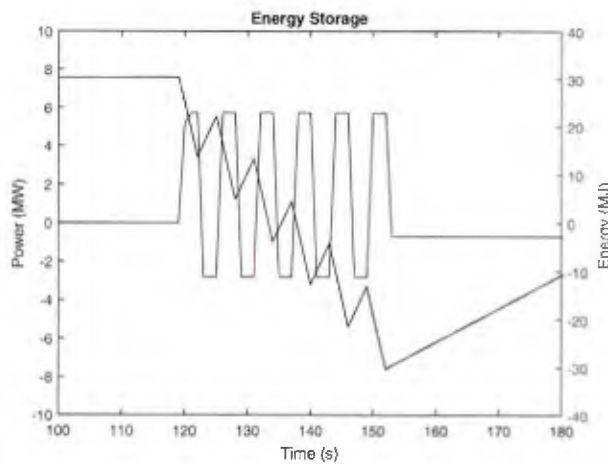


Fig. 5: An example from mission 4 shows pulse loads are served using previously stored energy.

For generators, the ATG and MTG's 6 MW and 35 MW ratings, respectively, have been well preserved in all our results.

The inclusion of the fictional infinite generator is a numerical technique for detecting power insufficiency. Not only does it identify infeasible missions, but quantifies the power shortfall. For example, mission 5 has a power shortfall of only 3.83 MW for 45 seconds and 11 MW for 17 seconds. Minor increases in storage capacity or generator power could make this mission feasible. Conversely, mission 6 has a major power shortfall and would require a large equipment improvements, as visible in Fig. 3(f) which shows 42 MW provided by the infinite generator. Quantitatively identifying energy shortfall provides design intuition in early system evaluation.

## V. CONCLUSIONS

This paper develops a method to evaluate shipboard power architectures early in the design process, before the de-

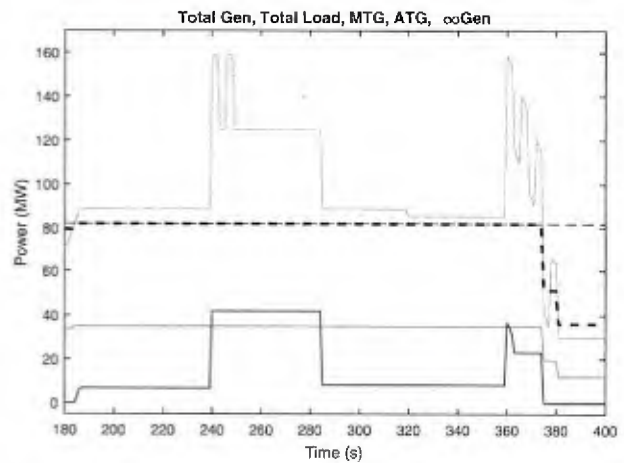


Fig. 6: In mission 6, the infinite generator supplies power to meet the load demand when all available generators and energy storage are exhausted. The amount of power supplied by the infinite generator indicates the severity of unserved load.

sign of specific system controllers. This method produces a provable upper bound on the best case performance of any possible controller, and indicates fundamental limitations of the architecture itself. Real controllers may not achieve this upper limit as the analysis here assumes perfect future knowledge. The power shortfall in a given mission scenario is also numerically quantified, which can assist in identifying possible capability improvements for generators and energy storage units. Future work will include evaluation of large numbers of stochastically generated mission scenarios.

## ACKNOWLEDGMENT

This work was supported by the Office of Naval Research as part of the Electric Ship Research and Development Consortium (ESRDC).

## REFERENCES

- [1] N. Doerry, "Zonal ship design," *Naval engineers journal*, vol. 118, no. 1, pp. 39–53, 2006.
- [2] N. Doerry and K. McCoy, "Next generation integrated power system: Ngips technology development roadmap," *DTIC Document*, 2007.
- [3] A. M. Cramer, S. D. Sudhoff, and E. L. Zivi, "Performance metrics for electric warship integrated engineering plant battle damage response," in *Proc. IEEE Electric Ship Technologies Symp*, May 2007, pp. 22–29.
- [4] —, "Metric optimization-based design of systems subject to hostile disruptions," and *Cybernetics-Part A: Systems and Humans IEEE Transactions on Systems, Man*, vol. 41, no. 5, pp. 989–1000, Sep. 2011.
- [5] —, "Performance metrics for electric warship integrated engineering plant battle damage response," *IEEE Transactions on Aerospace and Electronic Systems*, vol. 47, no. 1, pp. 634–646, Jan. 2011.
- [6] —, "Evolutionary algorithms for minimax problems in robust design," *IEEE Transactions on Evolutionary Computation*, vol. 13, no. 2, pp. 444–453, Apr. 2009.
- [7] R. R. Chan, Y. Lee, S. D. Sudhoff, and E. L. Zivi, "Evolutionary optimization of power electronics based power systems," *IEEE Transactions on Power Electronics*, vol. 23, no. 4, pp. 1907–1917, Jul. 2008.

- [8] H. Park, J. Sun, S. Pekarek, P. Stone, D. Opila, R. Meyer, I. Kolmanovsky, and R. DeCarlo, "Real-time model predictive control for shipboard power management using the IPa-sqp approach," *IEEE Transactions on Control Systems Technology*, vol. 23, no. 6, pp. 2129–2143, Nov. 2015.
- [9] R. R. Chan, S. D. Sudhoff, Y. Lee, and E. L. Zivi, "A linear programming approach to shipboard electrical system modeling," in *Proc. IEEE Electric Ship Technologies Symp.*, Apr. 2009, pp. 261–269.
- [10] A. M. Cramer, H. Chen, and E. L. Zivi, "Shipboard electrical system modeling for early-stage design space exploration," in *Proc. IEEE Electric Ship Technologies Symp. (ESTS)*, Apr. 2013, pp. 128–134.
- [11] A. M. Cramer, X. Liu, Y. Zhang, J. D. Stevens, and E. L. Zivi, "Early-stage shipboard power system simulation of operational vignettes for dependability assessment," in *Proc. IEEE Electric Ship Technologies Symp. (ESTS)*, Jun. 2015, pp. 382–387.
- [12] R. R. Chan, S. D. Sudhoff, and E. L. Zivi, "An approach to optimally allocate energy storage in naval electric ships," in *Proc. IEEE Electric Ship Technologies Symp.*, Apr. 2011, pp. 402–405.
- [13] D. Gayme and U. Topcu, "Optimal power flow with large-scale storage integration," *IEEE Transactions on Power Systems*, vol. 28, no. 2, pp. 709–717, May 2013.
- [14] K. M. Chandy, S. H. Low, U. Topcu, and H. Xu, "A simple optimal power flow model with energy storage," in *Proc. 49th IEEE Conf. Decision and Control (CDC)*, Dec. 2010, pp. 1051–1057.
- [15] A. Anvari-Moghaddam, T. Dragicevic, L. Meng, B. Sun, and J. M. Guerrero, "Optimal planning and operation management of a ship electrical power system with energy storage system," in *IECON 2016 - 42nd Annual Conference of the IEEE Industrial Electronics Society*, Oct 2016, pp. 2095–2099.
- [16] T. V. Vu, D. Gonsoulin, F. Diaz, C. S. Edrington, and T. El-Mezyani, "Predictive control for energy management in ship power systems under high-power ramp rate loads," *IEEE Transactions on Energy Conversion*, vol. 32, no. 2, pp. 788–797, June 2017.
- [17] T. V. Vu, S. Paran, F. Diaz, T. E. Mezyani, and C. S. Edrington, "Model predictive control for power control in islanded dc microgrids," in *IECON 2015 - 41st Annual Conference of the IEEE Industrial Electronics Society*, Nov 2015, pp. 001 610–001 615.
- [18] S. Paran, T. V. Vu, T. E. Mezyani, and C. S. Edrington, "Mpc-based power management in the shipboard power system," in *2015 IEEE Electric Ship Technologies Symposium (ESTS)*, June 2015, pp. 14–18.
- [19] A. J. Lamadrid, T. D. Mount, and C. Shoemaker, "Dynamic optimization for the management of stochastic generation and storage," in *2010 IEEE/PES Transmission and Distribution Conference and Exposition: Latin America (T D-LA)*, Nov 2010, pp. 860–866.
- [20] J. F. Marley and I. A. Hiskens, "Multi-period ac-qo optimal power flow including storage," in *2016 Power Systems Computation Conference (PSCC)*, June 2016, pp. 1–7.
- [21] A. J. Lamadrid, D. L. Shawhan, C. E. Murillo-Sanchez, R. D. Zimmerman, Y. Zhu, D. J. Tylavsky, A. Kindle, and Z. Dar, "Economic cost-benefit analysis for power system operations with environmental considerations," in *2015 IEEE Eindhoven PowerTech*, June 2015, pp. 1–6.
- [22] A. Gopalakrishnan, A. U. Raghunathan, D. Nikovski, and L. T. Biegler, "Global optimization of multi-period optimal power flow," in *Proc. American Control Conf.*, Jun. 2013, pp. 1157–1164.
- [23] J. D. Stevens, D. F. Opila, A. M. Cramer, and E. L. Zivi, "Operational vignette-based electric warship load demand," in *Proc. IEEE Electric Ship Technologies Symp. (ESTS)*, Jun. 2015, pp. 213–218.
- [24] R. D. Zimmerman, C. E. Murillo-Sanchez, and R. J. Thomas, "Matpower: Steady-state operations, planning, and analysis tools for power systems research and education," *IEEE Transactions on Power Systems*, vol. 26, no. 1, pp. 12–19, Feb. 2011.

# Early-Stage Shipboard Power System Simulation of Operational Vignettes for Dependability Assessment

Aaron M. Cramer, Xiao Liu, Yuqi Zhang  
Department of Electrical and Computer Engineering  
University of Kentucky  
Lexington, KY, USA

John D. Stevens\*, Edwin L. Zivi†  
\*Electrical and Computer Engineering Department  
†Weapons and Systems Engineering Department  
United States Naval Academy  
Annapolis, MD, USA

**Abstract**—A principle motivation for the development of early-stage shipboard power system simulation techniques is the need to perform time-domain simulation during the early design stage. In particular, there is a need to understand the performance of a candidate system during challenging situations involving dynamic load profiles and disruptive conditions in order to assess the system dependability. An early-stage simulation technique is applied to simulate the performance of a candidate system for given operational vignettes. Using this early-stage approach allows simulations to be performed very quickly, allowing many vignettes to be considered and the overall system dependability to be assessed.

**Index Terms**—energy storage, linear programming, military equipment, modeling

## I. INTRODUCTION

It has been argued that the power system of an electric warship should be viewed as a service provider, responsible for providing electric power to the mission loads that it serves [1]–[3]. By virtue of this argument, assessment of the power system should be performed by considering its dynamic ability to deliver this power across the range of vignettes for which it must operate [2], [4]. Time-domain performance metrics have been proposed for performing this assessment [2], [4]. One of these metrics is operability, which quantifies the performance of a shipboard power system in a particular scenario. Operability is a measure of the degree to which the performance of the shipboard power system contributes to mission effectiveness in that scenario, or operational vignette. As the system must perform well over a broad range of operational vignettes, dependability metrics have been proposed that aggregate the operability values over distributions of operational vignettes. The calculation of these dependability metrics requires many time-domain simulations in order to quantify the systems performance over the distribution of vignettes. This is motivation for the development of modeling and simulation techniques that minimize the computational burden of these simulations and allow the use of such techniques during the early design stage. It has been found that fast electrical dynamics can be neglected with relatively little influence on the performance of the system [4]–[7]. Therefore, the computational burden of the

simulations can be reduced and the system can be simulated at an earlier design stage because less detailed information about the system is required to construct its simulation model [4], [5], [8]. Linear programming approaches have previously been proposed and successfully demonstrated in [5], [8], [9]. In these approaches, the mechanical dynamics associated with prime movers and energy storage dynamics are retained, but the electrical power flow is modeled statically. Using this approach, it becomes feasible to perform computationally inexpensive time-domain simulations of candidate systems in given operational vignettes at an early design stage.

Herein, a complicated distribution of operational vignettes representing a given mission profile is considered. In this set of vignettes, the ship is engaged in a given mission while reacting to threats and possible disruptions. This set represents significantly more complicated vignettes than were considered in previous proof-of-concept work in dependability calculation, and the application of early-stage simulation techniques to the simulation of these vignettes represents an improved capability for trade space exploration.

The remainder of the paper is organized as follows. In Section II, the notional power system studied herein is described. The set of operational vignettes considered is discussed in Section III. In Section IV, a series of simulation studies are presented and analyzed. Conclusions are drawn in Section V

## II. NOTIONAL POWER SYSTEM

A notional medium-voltage dc system (MVDC) shown in Fig. 1 is studied. This system has the arrangement shown in Fig. 2 and is based on the notional MVDC system developed by the Electric Ship Research and Development Consortium [7]. Parameters for system are shown in Table I. The four-zone system consists of two main generators and two auxiliary generators. There are two propulsion drives that operate at power levels corresponding with the desired speed. There is a radar that can operate in two modes, a low-power mode and a high-power mode, at different points during the vignettes. A high-power load is used to engage in the mission. A centralized energy storage module can compensate for load dynamics and provide backup power. The zonal loads are fed through converters, and each zone contains some vital and some nonvital load.

This work was supported by the Office of Naval Research through the United States Naval Academy N00189-14-P-1197.

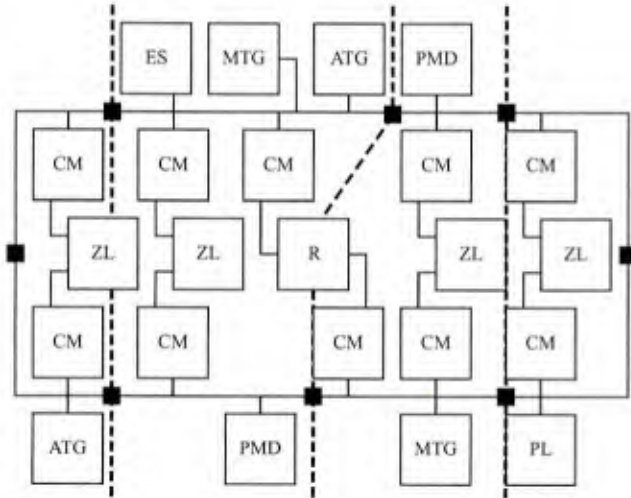


Fig. 1. Notional medium-voltage dc system: MTG signifies main generator, ATG signifies auxiliary generator, PMD signifies propulsion drive, R signifies radar, PL signifies high-power load, ES signifies energy storage, CM signifies converter, ZL signifies zonal load

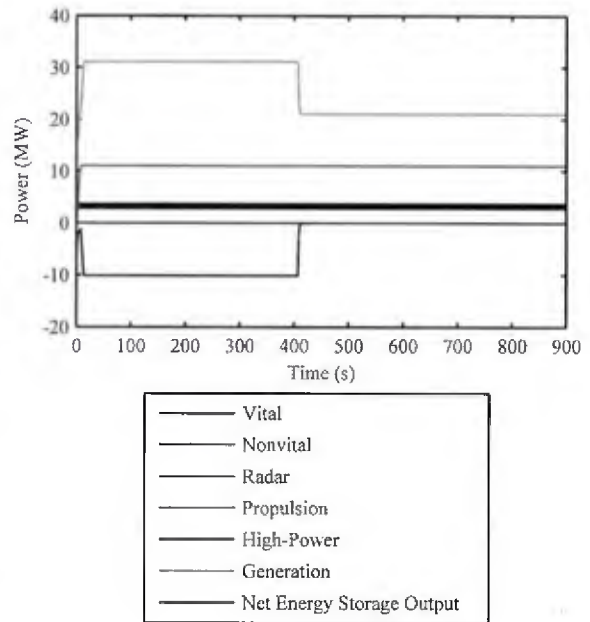


Fig. 3. Startup transient

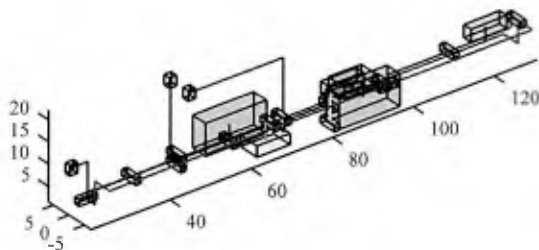


Fig. 2. Arrangement of notional medium-voltage dc system

TABLE I  
PARAMETERS OF NOTIONAL MEDIUM-VOLTAGE DC SYSTEM

Rating of main generators	36 MW
Rating of auxiliary generators	5 MW
Total rated propulsion load	60.4 MW
Radar low-power load	2.9 MW
Radar high-power load	3.8 MW
High-power load	10 MW
Energy storage capacity	4 GJ
Energy storage rating	10 MW
Zonal converter rating	0.9 MW
Vital load per zone	0.9 MW
Nonvital load per zone	0.8 MW

The system is modeled using the techniques described in [8], [9]. These techniques entail representing the power system using a linear program. In the linear program, power control is modeled using weights assigned to each load, which indicates its general importance. In this system, the weights of the vital and nonvital loads are 25 and 3, respectively. The weight of the radar and high-power loads are both 15. Levels of propulsion power associated with speeds of 5 knots, 10 knots, 15 knots, 20 knots, 25 knots, and 30 knots are weighted at 26, 18, 16, 14, 6, and 1, respectively. These weights are also used to determine the operability of the system during an event. In particular, the operability is calculated as

$$O = \frac{\int_{t_0}^{t_f} \sum_{i=1}^I w_i P_i(t) dt}{\int_{t_0}^{t_f} \sum_{i=1}^I w_i P_{max,i}(t) dt}, \quad (1)$$

where  $t_0$  and  $t_f$  are the initial and final times, respectively,  $I$  is the number of loads,  $w_i$  is the weight of the  $i$ th load, and  $P_i(t)$  and  $P_{i,max}(t)$  are the power and the maximum power consumption of load  $i$  at time  $t$ , respectively.

Each vignette starts from steady state. The startup transient of the system from zero-initial conditions is shown in Fig. 3. As the generator output power and propulsion demand increase, the loads are handled in order of priority and the energy storage is charged.

### III. OPERATIONAL VIGNETTES

A set of operational vignettes is considered. These vignettes correspond to a given mission profile. The temporal progress

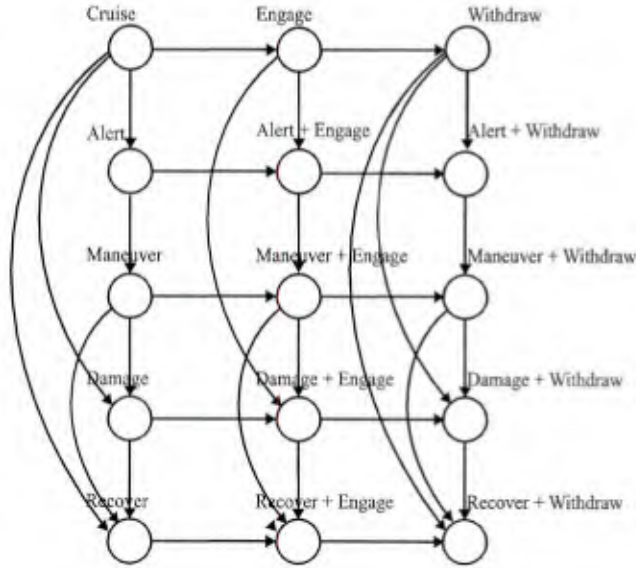


Fig. 4. Finite state machine describing operational vignettes

of the ship through the vignettes can be represented using a finite state machine as shown in Fig. 4. In the course of the mission, the ship must cruise to a given station. It is assumed that the ship attempts to cruise at 20 knots during the cruise interval. After the cruise interval, the duration of which is determined by an exponential distribution with mean time of 5 minutes, the ship reaches the station and engages in the mission. During this engage interval, the ship attempts to move at 10 knots and engages with the high-power load. The duration of this interval is determined by a uniform distribution from 5 minutes to 10 minutes. After the engage interval, the ship withdraws, attempting to cruise at 20 knots.

Concurrently with the mission, the ship may become damaged at some point during the vignette. The moment at which damage may occur is determined by an exponential distribution with mean time of 6 minutes shifted by 2 minutes. The probability that damage occurs is 0.5, and the damage is represented by a spherical region of disruption with radius 5.2 m [7] uniformly located within the bounding box of the shipboard power system. Before the ship is possibly damaged, it may enter a state of alert. The time at which the ship enters a state of alert is determined by an exponential distribution with mean time of 5 minutes. If the ship is in a state of alert during the 2 minutes before damage may occur, it begins maneuvering by increasing its speed to 30 knots. After the moment at which damage may occur, the power to the radar is reduced. If the ship is damaged, it reduces speed to an attempted 5 knots and pauses providing ground support. After 2 minutes, the ship will attempt to resume its mission. All vignettes last for 15 minutes.

A set of random variables can be used to describe these vignettes. In particular, the duration of the cruise interval can be described as

$$\Delta T_{cruise} \sim \text{Exp}(300 \text{ s}). \quad (2)$$

Likewise, the duration of the fire interval can be described as

$$\Delta T_{fire} \sim \text{Unif}(300 \text{ s}, 600 \text{ s}). \quad (3)$$

The time at which damage may occur is represented by

$$T_{damage} \sim \text{Exp}(360 \text{ s}) + 120 \text{ s}. \quad (4)$$

Whether damage occurs or not has the following representation

$$D \sim \text{Bern}(0.5). \quad (5)$$

If damage occurs, the centroid of the region of disruption is distributed according to

$$X_{damage} \sim \text{Unif}(20.5 \text{ m}, 130.6 \text{ m}) \quad (6)$$

$$Y_{damage} \sim \text{Unif}(-7.2 \text{ m}, 6.7 \text{ m}) \quad (7)$$

$$Z_{damage} \sim \text{Unif}(1.6 \text{ m}, 22.2 \text{ m}). \quad (8)$$

The time at which the ship may become alert is distributed according to

$$T_{alert} \sim \text{Exp}(300 \text{ s}). \quad (9)$$

Given random variates from these distributions, the time to enter the fire interval is given by

$$t_{fire} = \Delta t_{cruise}. \quad (10)$$

The time to enter the withdraw interval is

$$t_{withdraw} = t_{fire} + \Delta t_{fire}. \quad (11)$$

If  $t_{alert} < t_{damage}$ , then

$$t_{maneuver} = \max\{t_{alert}, t_{damage} - 120 \text{ s}\}. \quad (12)$$

Otherwise, the ship never enters the alert or maneuver intervals. Finally, the ship enters the recover interval immediately if no damage occurs or 120 s after the damage occurs:

$$t_{recover} = \begin{cases} t_{damage} & \bar{d} \\ t_{damage} + 120 \text{ s} & d. \end{cases} \quad (13)$$

Having established the distribution of the operational vignettes to be considered, 1000 sample vignettes are drawn from the distribution and used to demonstrate the approach in the simulation studies below.

#### IV. SIMULATION STUDIES

The performance of the notional system is considered for two particular configurations. These configurations are differentiated by the manner in which the energy storage module is controlled. In the first configuration, the energy storage is configured so that it is normally full and is discharged as needed to provide backup power. In the second configuration, 90% of the energy storage capacity is normally full as in the first configuration. However, 10% of the capacity is reserved to absorb power during load shedding events.

The operability of each configuration is evaluated for each of the 1000 sample operational vignettes. The sorted operability values for both configurations are plotted in Fig. 5. It can be seen that most of the time, both configurations result in perfect performance (100% operability). The disruption caused

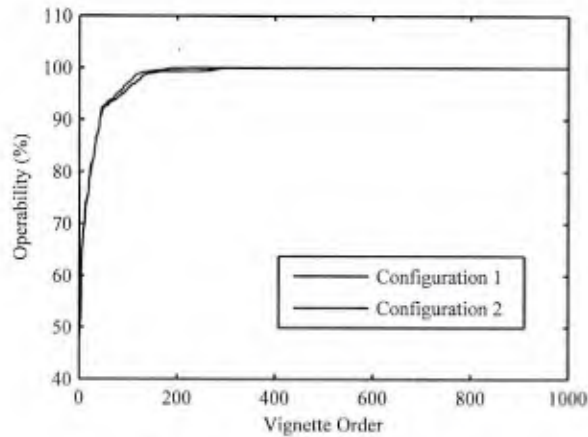


Fig. 5. Distribution of operability values

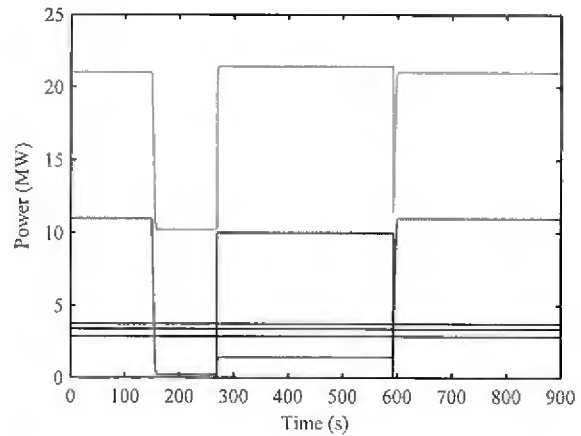


Fig. 7. Performance during unchallenging vignette

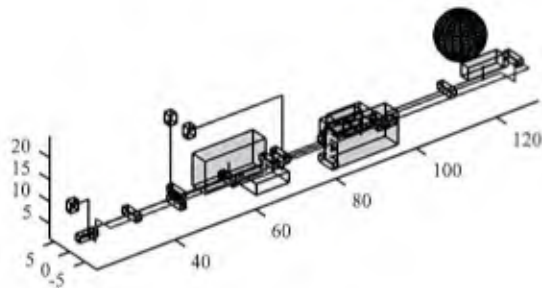


Fig. 6. Disruption from unchallenging vignette

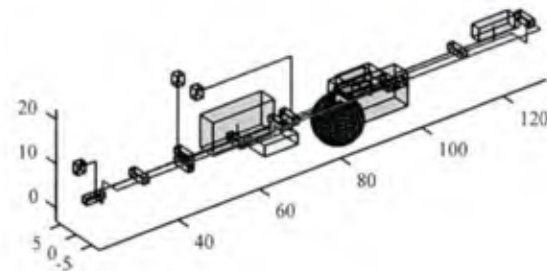


Fig. 8. Disruption from challenging vignette

by such an unchallenging vignette is shown in Fig. 6. The disruption misses the power system components; nothing is damaged. The performance of the first configuration is shown in Fig. 7, and the performance of the second configuration is identical. It can be seen that the disruption occurs at 149 s. The ship never enters the alert of maneuver intervals. The ship slows down for 120 s to assess the disruption. The ship resumes the engage interval at 269 s before proceeding to the withdraw interval at 592 s. The power system is able to deliver the desired power to each load at all times during the vignette.

At the other end of the performance spectrum are vignettes for which the operability was very low. The disruption associated with one of these challenging vignettes is shown in Fig. 8. The performance of the first configuration is shown in Fig. 9. Again, the performance of the second configuration is identical. In this vignette, the ship is damaged at 143 s, and the damage affects generation, propulsion, and energy storage. The power system serves loads in order of priority, but its capability of serving loads is significantly reduced. After 120 s, the ship

attempts to resume the cruise interval, but it can only provide approximately 20% of the propulsion power. The operability in this case is 48.3%.

In the middle of the distribution shown in Fig. 5 are a subset of operational vignettes in which the second configuration performs better than the first configuration. The disruption associated with one such middle vignette is shown in Fig. 10, and it damages one of the auxiliary generators, one of the propulsion drives, and one zone of one of the main buses. In this vignette, the ship becomes alert at 62 s and begins to maneuver at 95 s. It commences the engage interval at 190 s before being damaged at 215 s. In the first configuration, the performance of which is shown in Fig. 11, the damage combined with sudden load shedding causes some generators to go offline. The energy storage provides power during the transient, but it cannot provide all the power required when the system resumes the engage interval at 335 s. At 574 s, the generation that had tripped offline recovers, and the ship commences the withdraw interval at 604 s. The operability for

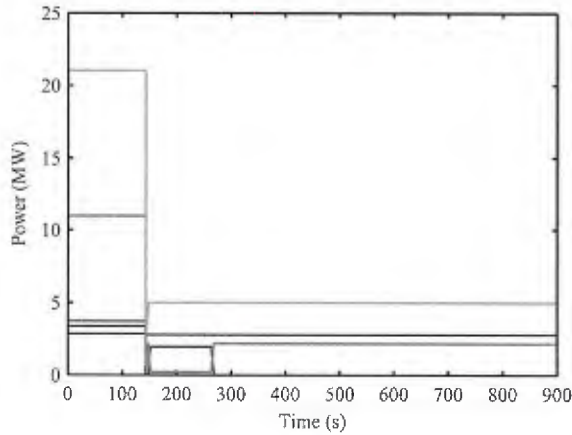


Fig. 9. Performance during challenging vignette

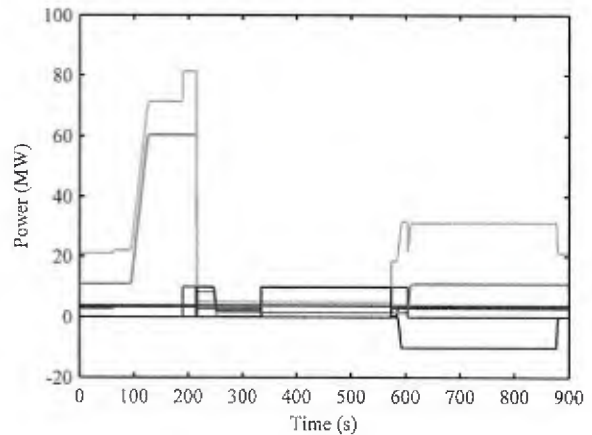


Fig. 11. Performance of configuration 1 during middle vignette

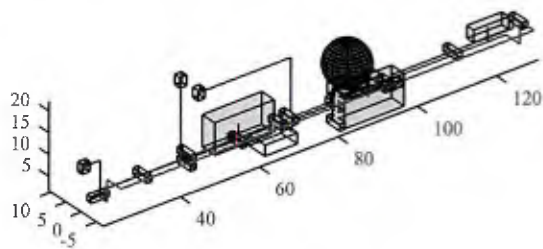


Fig. 10. Disruption from middle vignette

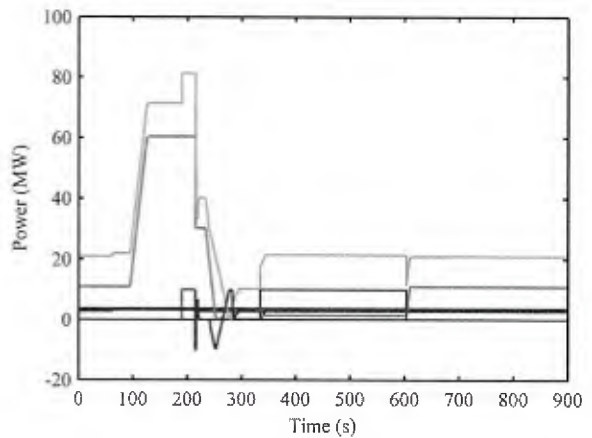


Fig. 12. Performance of configuration 2 during middle vignette

this vignette is 93.7%.

In contrast to the performance of the first configuration, the performance of the second configuration is shown in Fig. 12. In this case, the energy storage attempts to absorb power that was shed from propulsion. It cannot absorb sufficiently quickly to prevent a generator from tripping offline, but the generator is able to recover much more quickly than in the previous case. Energy storage is able to provide backup power while the auxiliary generator recovers. When the engage interval begins, sufficient generation is available to serve each load. The operability for this vignette is 99.9%, 6.2% better than the first configuration.

The mean operability values, or average system dependability, for the first and second configurations are 98.5% and 98.6%, respectively. This suggests that mean value as a metric is not particularly sensitive to these changes in performance. On the other hand, risk metrics may be better able to quantify these differences. For example, value-at-risk is a commonly used metric in financial risk modeling. It

represents a given percentile of the performance. The values-at-risk at the 10th percentile are 96.0% and 97.1% for the first and second configurations, respectively. Another measure is the probability that the performance is less than a given threshold. The probabilities that the operability values are less than 98% are 12.5% and 10.9%, respectively. These risk metrics are more sensitive by approximately an order of magnitude to the performance differences of these two configurations. The results also suggest that improving the control of energy storage or the management of the shipboard "energy bank account" is unlikely to significantly improve performance for unchallenging or very challenging situations, but it may create significant improvements to performance during situations falling between these extremes.

## V. CONCLUSION

Previous proof-of-concept research showed how time-domain performance metrics can be used to quantify the performance of shipboard systems, but this work focused

on relatively simple disruptive scenarios. Herein, these approaches are extended to more complicated distributions of operational vignettes, including mission and situational dynamics in addition to potential disruption. The ability to quantify the performance over such distributions represents an improved capability for trade space exploration. The application of these techniques is demonstrated using a notional shipboard power system, a representative set of operational vignettes, and two system configurations.

#### REFERENCES

- [1] J. P. Walks and J. F. Mearman, "Integrated engineering plant," in *American Society of Naval Engineers Reconfiguration Survivability Symp.*, Atlantic Beach, FL, 2005.
- [2] A. M. Cramer, S. D. Sudhoff, and E. L. Zivi, "Performance metrics for electric warship integrated engineering plant battle damage response," *IEEE Trans. Aerosp. Electron. Syst.*, vol. 47, no. 1, pp. 634–646, Jan. 2011.
- [3] M. G. Richard, D. E. Hastings, D. H. Rhodes, and A. L. Weigel, "Defining survivability for engineering systems," in *Proc. 5th Annu. Conf. Systems Engineering Research*, 2007.
- [4] A. M. Cramer, S. D. Sudhoff, and E. L. Zivi, "Metric optimization-based design of systems subject to hostile disruptions," *IEEE Trans. Syst., Man, Cybern. A, Syst., Humans*, vol. 41, no. 5, pp. 989–1000, Sep. 2011.
- [5] R. R. Chan, S. D. Sudhoff, Y. Lee, and E. L. Zivi, "A linear programming approach to shipboard electrical system modeling," in *2009 IEEE Electric Ship Technologies Symp.*, pp. 261–269.
- [6] R. R. Chan, S. D. Sudhoff, and E. L. Zivi, "An approach to optimally allocate energy storage in naval electric ships," in *2011 IEEE Electric Ship Technologies Symp.*, pp. 402–405.
- [7] J. S. Chalfant and C. Chrysostomidis, "Analysis of various all-electric-ship electrical distribution system topologies," in *2011 IEEE Electric Ship Technologies Symp.*, pp. 72–77.
- [8] A. M. Cramer, H. Chen, and E. L. Zivi, "Shipboard electrical system modeling for early-stage design space exploration," in *2013 IEEE Electric Ship Technologies Symp.*, pp. 128–134.
- [9] A. M. Cramer, F. Pan, H. Chen, and E. L. Zivi, "Modeling and simulation for early-stage quantitative assessment of medium-voltage dc power system protection schemes," in *Electric Machines Technology Symp. 2014*.

## Light-Weight, Early-Stage Power System Model for Time-Domain Simulation

### ABSTRACT

During the early stage, it is desirable to assess the ship impact of various technology alternatives. For example, the sizing, placement, and control of energy storage within the system can significantly affect the performance of the system in situations involving challenging loading or disruptive conditions. To understand these effects, it is necessary to perform time-domain simulation of the power system over the course of the scenario. In such cases, it may be necessary to perform many such simulations. Simultaneously, limited information about the power system design (including control) is available at this early stage. To address these dual concerns, a light-weight power system model can be employed to evaluate these scenarios. The model is light weight in two respects. First, the computational burden associated with the model is low, allowing many simulations to be performed in a reasonable amount of time. Second, the model requires relatively little information about the power system in order to parameterize it. The explanation of how the light-weight model differs from other types of power system models, the rationale for using such models, and discussion of applications is provided.

### INTRODUCTION

Modern trends in electric warship power system design are creating new challenges at the early stage. These trends include the introduction of high-power, pulsed mission loads and the system-level integration of energy storage within the power system [1], [2]. The unique challenges posed by these trends originate from their highly dynamic nature. In the past, it was sufficient to perform static analysis of the power system in a given number of fixed operational conditions in order to ensure that system was properly sized

and to assess performance metrics such as fuel consumption.

In order to assess dynamic performance, it is necessary to perform time-domain simulations. However, traditional models for performing such simulations require long simulation run times and require extensive parameter data that may not be available at the early stage.

In order to fill the requirement for time-domain simulation at the early stage without introducing high computational or data requirements, a light-weight power system model is described. This model has been developed over time, motivated by the observation that certain dynamics of the system will not have an appreciable effect on the system-level performance at the early stage. By neglecting these dynamics, it becomes possible to accelerate simulation speed and to characterize the system without a high level of parameter details.

The remainder of this paper is organized as follows. First, the principle of the light-weight power system model is described. Then, the modeling approach is outlined generally, and recent improvements to the approach are presented. A discussion of the relationship of the simulation model to power system control follows. Finally, some example simulation results are shown to illustrate the performance of the method.

### PRINCIPLE

The underlying principle to the light-weight, early-stage power system model is to locate a level of fidelity and computational efficiency between that of static models and dynamic electrical models. The static models, while fast to analyze, cannot provide details on dynamic behavior. The electrical models, which can provide very detailed predictions of the time-

domain response of the system, are very computationally intense to simulate. It can also be difficult to gather the data required to simulate an electrical model during the early stage. For example, the power rating of a generator may be known, but it is unlikely that the machine inductances are known. This principle is illustrated in Figure 1.

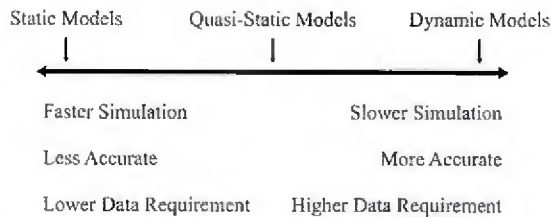


Figure 1: Spectrum of Simulation Models

In order to use this approach, information about the components and their ratings and interconnections must be imported from an appropriate database. When this data is imported, it can be used to form a light-weight simulation model as described herein. The model can be combined with a description of operational vignettes to perform time-domain simulation. The results of the simulation are used to evaluate relevant performance metrics (e.g., how well did the power system provide power to loads during a challenging vignette). When many such operational vignettes are to be considered or when many potential systems are to be considered, this process must be repeated many times, creating a requirement for computationally efficient simulation. This process is shown in Figure 2.

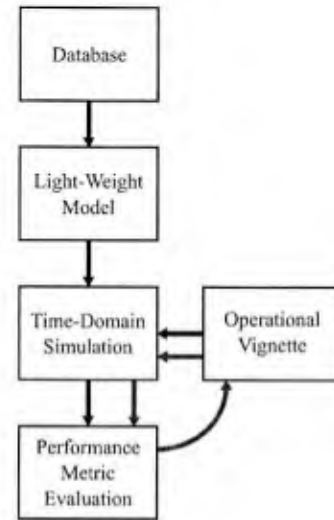


Figure 2: Light-Weight Simulation Process

## MODELING APPROACH

The particular modeling approach has been developed over a number of years. It was recognized that the exact electrical dynamics had limited impact on early-stage metrics. For example, in [3], it was found that the operability [4] of a given candidate power system for a given operational vignette could be calculated accurately while neglecting electrical dynamics. This idea was formalized in [5], where a linear programming model of the electrical power system was proposed for light-weight simulation studies. This idea was further advanced in [6] where computational challenges associated with the linear program were addressed, resulting in a 99.8% reduction in required simulation run time and in [7] where the approach was extended to include effects associated with fault protection in medium-voltage dc systems.

In the linear programming approach, the power system is represented as a linear program:

$$\begin{aligned}
 \max_{\mathbf{x}} \quad & \mathbf{c}^T \mathbf{x} \\
 \text{subject to} \quad & \mathbf{A} \mathbf{x} \leq \mathbf{b} \\
 & \mathbf{A}_{eq} \mathbf{x} = \mathbf{b}_{eq} \\
 & \mathbf{x} \geq \mathbf{0}.
 \end{aligned} \tag{1}$$

In this linear program,  $\mathbf{x}$  is a vector representing the nonnegative decision variables. For this model, the elements of  $\mathbf{x}$  are typically power

flows through different power system components, from generation, distribution, conversion, energy storage, and loads. The vector  $\mathbf{c}$  represents the weights associated with each decision variable. For example, the weight of more important loads would be set accordingly to indicate that the power system should prioritize delivery of power to these loads. The matrices  $\mathbf{A}$  and  $\mathbf{A}_{eq}$  and the vectors  $\mathbf{b}$  and  $\mathbf{b}_{eq}$  are used to represent the linear inequality and equality constraints that govern the problem. For example, these constraints are used to limit the output power of a device by its rated power and to ensure that power conservation occurs at each bus.

The structure of the required linear program has been described in [5]-[7]. This linear program is solved at each time step of the system simulation, its solution representing the quasi-static response of the electrical system. Efficient solvers for linear programs exist, including both simplex and interior point methods (e.g., [8]).

While the structure has been described, there are two aspects to the structure that are improved. The first is the representation of limits associated with the dynamic loading and unloading of generators. In particular, each generator has at each moment a dynamic minimum and maximum power limit,  $P_{min}$  and  $P_{max}$ , respectively. These limits are functions of the generator state [7], and operation outside of these limits will cause a generator rotor speed to exceed its limits. However, it is necessary for the generator to be able to output zero in order to ensure that the linear program has a feasible solution. In order to implement this, there are two decision variables associated with each generator:  $P_{out}$  and  $\hat{P}_{out}$ . The generator output power  $P_{out}$  is bounded above by  $P_{max}$ :

$$P_{out} < P_{max}. \quad (2)$$

However, it is only bounded below by zero. Instead, the dynamic minimum limit is accounted for by requiring

$$P_{out} - \hat{P}_{out} \leq P_{min}. \quad (3)$$

In this way,  $\hat{P}_{out}$  represents the degree to which  $P_{out}$  does not exceed the dynamic minimum limit. The linear inequality constraints are included in  $\mathbf{Ax} \leq \mathbf{b}$  for each generator. Likewise, in the weight vector  $\mathbf{c}$ , the element associated with  $P_{out}$  is assigned a relatively low positive value (indicating a cost associated with the required fuel consumption). The element associated with  $\hat{P}_{out}$  is assigned a large positive value to penalize generator operation that will lead to overspeed tripping of the generator.

The other aspect of the linear program structure that has been improved is the representation of load sharing. There are sets of components that would normally operate by sharing load proportionally. The use of weights in the linear program does not ensure that a given solution of the linear program will exhibit this load sharing behavior. This has been considered in [5] by examining many linear programs in each time step, which proved very computationally expensive. It was addressed in [6] by adding additional decision variables. It has been found that there are situations in which the existing load sharing models do not result in linear program solutions with the expected behavior. Herein, an alternative approach is described.

For two components,  $i$  and  $j$ , with rated powers  $P_{rated,i}$  and  $P_{rated,j}$ , respectively, it is expected that their output powers,  $P_{out,i}$  and  $P_{out,j}$ , respectively, are related by

$$\frac{P_{out,i}}{P_{rated,i}} = \frac{P_{out,j}}{P_{rated,j}}. \quad (4)$$

This could be represented as an equality constraint in  $\mathbf{A}_{eq} \mathbf{x} = \mathbf{b}_{eq}$ , but there are situations in which the equality should not hold. For example, if one of the components was damaged, such a constraint would require that the other component should also not operate. Instead, two decision variables are added to represent the relationship between the two output powers:

$$\frac{P_{rated,j}}{P_{rated,i} + P_{rated,j}} P_{out,i} - \frac{P_{rated,i}}{P_{rated,i} + P_{rated,j}} P_{out,j} + P_{\alpha} - P_{\beta} = 0. \quad (5)$$

This equality constraint is added to the set of equality constraints  $\mathbf{A}_{eq}\mathbf{x} = \mathbf{b}_{eq}$  for each pair of components within the load sharing group. The elements of the weight vector  $\mathbf{c}$  corresponding to the decision variables  $P_{\alpha}$  and  $P_{\beta}$  are assigned small positive weights to slightly penalize solutions in which load is not shared proportionally. For a load sharing group with  $N$  components, this approach involves the introduction of  $N(N-1)/2$  equality constraints and  $N(N-1)$  decision variables. The each scale quadratically, but the values of  $N$  are generally small.

## RELATIONSHIP TO CONTROL

There is some relationship between the simulation model and power system control. In particular, the linear program combines both a representation of the power system physics, i.e., where power will flow, with a representation of the power system controller. By formulating the system model as a linear program, it is assuming that the controller will act to maximize the weighted function given in (1). This approximation is both optimistic in certain situations and can be misleading in other situations. By assuming the controller to be capable of optimal operation, practical effects associated with the controller's ability to do this are ignored. While this is a reasonable approximation at the early stage, it represents an upper bound on the achievable controller performance. The controller representation also represents a simplification of the power control problem. By representing this problem as an optimization problem that should be solved at each moment in time (compared with e.g., [9], [10]), it neglects the temporal effects associated with the problem. For example, energy stored within an energy storage device can be used now or later. By not treating the future value of the stored energy, the linear programming method does not fully solve the optimal control problem.

There has been recent discussion as to whether it is necessary to represent the controller at the early stage. This discussion remains open, but it seems that there may be value in doing so when dynamics associated with loading and energy storage are considered and can have a significant ship impact.

There are presently efforts to separate the representation of the power system physics from the power system control representation to allow alternative control representations to be used with the light-weight model. There are also possibilities of using the linear program directly for control purposes. Finally, because of the relationship between optimization problems and Lagrange multipliers, there is a duality between this modeling approach and market-based control approaches. These represent areas of future development for the light-weight model.

## SIMULATION RESULTS

In order to demonstrate the light-weight simulation model, a notional medium-voltage dc power system is considered. This system is shown in Figure 3. The arrangement of the power system is shown in Figure 4. This system is a four-zone system. Each zone features both vital and nonvital load. Each zone also includes some higher power mission load and some local energy storage that is intended to supply the higher power requirements of the mission load.

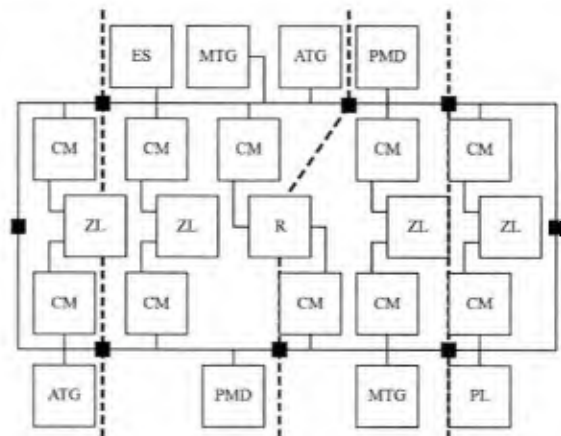


Figure 3: Notional Medium-Voltage DC System (MTG is Main Generator, ATG is Auxiliary Generator, PMD is Propulsion Load, ES is Centralized Energy Storage, PL

is Pulsed Load, CM is Converter, ZL is Zonal Load, and R is Radar Load)

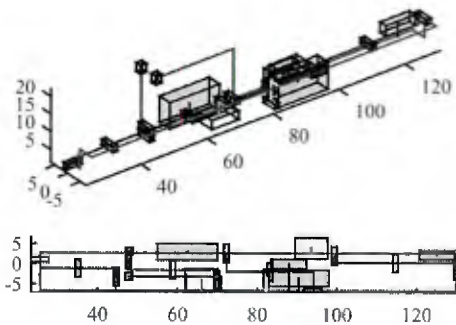


Figure 4: Notional Power System Arrangement

The system is first simulated from zero initial conditions (cold iron startup) for 30 minutes to establish initial conditions. This process is shown in Figure 5. As the generation ramps up, the power system serves loads in priority order and begins to fill the energy storage devices. After about 15 minutes, the energy storage devices are filled, and generation continues to serve all loads. This simulation requires approximately 2.6 s of run time on an i7 2.79-GHz processor with 16 GB of memory. The simulation runs nearly 700 times faster than realtime speed.

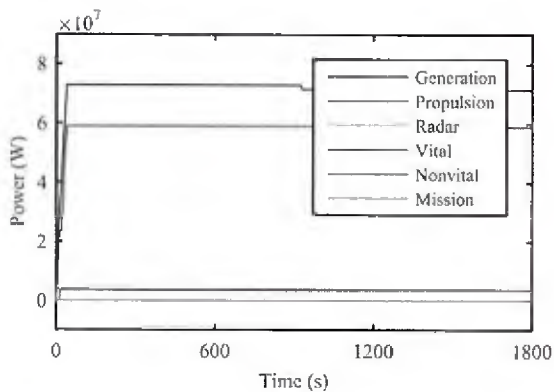


Figure 5: Startup Response of System

In the second simulation, which commences from the steady-state conditions reached at the end of the previous simulation, one of the zonal mission loads is engaged. This load is fed primarily from the local energy storage because

the zonal power conversion equipment is not sized sufficiently to handle the full load. At 15 s, one of the main buses is faulted for 0.15 s. This faults the output of one of the main generators and one of the auxiliary generators. The response of the system in this scenario is shown in Figure 6. It can be seen that there is a small dip in the nonvital load consumption corresponding to the temporary fault. It can also be seen that both of the affected generators enter an overspeed condition and trip offline. The auxiliary generator recovers within a few seconds. However, the local energy storage is depleted after about 75 s and the mission load ceases operation. After about 250 s, the main generator recovers from the overspeed condition and resumes providing power. This simulation requires approximately 3.2 s of run time. While this is more than 100 times faster than realtime speed, it can be seen that the simulation run time required is not proportional to the duration of time simulated. For such models, the required run time is related to the complexity of the scenario being simulated.

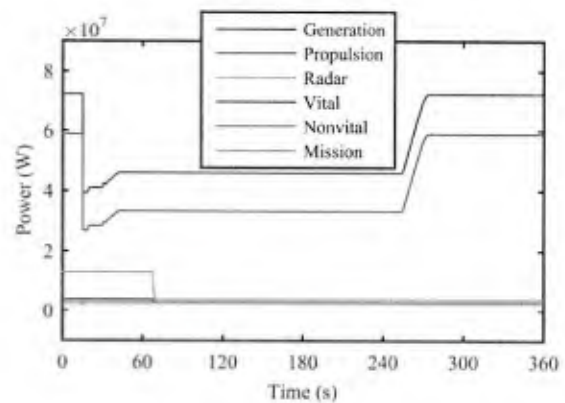


Figure 6: Response of System to Operational Vignette

## CONCLUSION

A light-weight power system model can be employed to evaluate dynamic performance at the early stage. In this context, light weight means both that the computational burden associated with the model is low and that the model requires relatively little information about the power system in order to parameterize it. The guiding principle for such models, a description of the model itself, the relationship

of the model to ongoing research, and demonstration simulation results are presented.

## REFERENCES

- [1] N. Doerry, "Next generation integrated power system: NGIPS technology development roadmap," Naval Sea Systems Command, Washington, DC, Nov. 2007.
- [2] J. Kuseian, "Naval power systems technology development roadmap," Naval Sea Systems Command, Washington, DC, May 2013.
- [3] A. M. Cramer, S. D. Sudhoff, and E. L. Zivi, "Metric optimization-based design of systems subject to hostile disruptions," *IEEE Trans. Systems, Man, and Cybernetics, Part A: Systems and Humans*, vol. 41, no. 5, pp. 989–1000, Sep. 2011.
- [4] A. M. Cramer, S. D. Sudhoff, and E. L. Zivi, "Performance metrics for electric warship integrated engineering plant battle damage response," *IEEE Trans. Aerospace and Electronic Systems*, vol. 47, no. 1, pp. 634–646, Jan. 2011.
- [5] R. R. Chan, S. D. Sudhoff, Y. Lee, and E. L. Zivi, "A linear programming approach to shipboard electrical system modeling," in *IEEE Electric Ship Technologies Symp., 2009*, Baltimore, MD, pp. 261–269, 20–22 Apr. 2009.
- [6] A. M. Cramer, H. Chen, and E. L. Zivi, "Shipboard electrical system modeling for early-stage design space exploration," in *2013 IEEE Electric Ship Technologies Symp.*, Arlington, VA, pp. 128–134, 22–24 Apr. 2013.
- [7] A. M. Cramer, F. Pan, H. Chen, and E. L. Zivi, "Modeling and simulation for early-stage quantitative assessment of medium-voltage dc power system protection schemes," in *Electric Machines Technology Symp. 2014*, Philadelphia, PA, 28–29 May 2014.
- [8] E. K. P. Chong and S. H. Zak, *An Introduction to Optimization*, 4th ed. Hoboken, NJ: Wiley, 2013.
- [9] P. Stone, D. F. Opila, H. Park, J. Sun, S. Pekarek, R. DeCarlo, E. Westervelt, J. Brooks, and G. Seenumani, "Shipboard power management using constrained nonlinear model predictive control," in *2015 IEEE Electric Ship Technologies Symp.*, Alexandria, VA, pp. 1–7, 21–24 Jun. 2015.
- [10] S. Parvan, T. V. Vu, T. El Mezyani, C. S. Edrington, "MPC-based power management in the shipboard power system," in *2015 IEEE Electric Ship Technologies Symp.*, Alexandria, VA, pp. 14–18, 21–24 Jun. 2015.

# Operational Vignette-based Electric Warship Load Demand

John D. Stevens and Daniel F. Opila  
Department of Electrical and Computer  
Engineering  
U.S. Naval Academy  
Annapolis, MD  
{stevens, opila}@usna.edu

Aaron M. Cramer  
Department of Electrical and Computer  
Engineering  
University of Kentucky  
Lexington, KY  
aaron.cramer@uky.edu

Edwin L. Zivi  
Department of Weapons and Systems  
Engineering  
U.S. Naval Academy  
Annapolis, MD  
zivi@usna.edu

**Abstract**—The design and control of electric warship power systems is a complex, challenging problem and numerous power system architectures, technologies, algorithms, and control schemes have been proposed. Instead of a quantitative assessment of these ideas based on ideal, steady-state conditions, a set of representative operational vignettes that span the entire electric warship mission package is introduced in order to obtain true results. This paper describes a set of realistic test cases that provide load demand dynamics based on a variety of unique scenarios, mission load characteristics, and human-in-the-loop decision-making. Stochastic and deterministic power profiles are established for individual ship systems and mission loads, which are then combined together for a particular scenario. These test cases can be applied to early-stage design trade studies as well as design tool development. For example, various control methods can be benchmarked against the same test cases. In addition to the established test cases, the method used here enables operators to communicate to design engineers how they intend to use the ship (not the other way around).

**Keywords**—naval power systems; electric ship design; dynamic loads; stochastic loads

## I. INTRODUCTION

Multi-mission high energy weapons and sensors on electric warships represent game-changing capabilities to the warfighter [1]. A common challenge to realize this future capability is designing a system architecture that reliably delivers power under potentially disruptive conditions to all loads, including pulse-power mission loads and propulsion [2]-[4]. Adding to the complexity is the nearly stochastic behavior of the aggregate load demand, where the magnitude of a single load can rival a single generation source and significant load variations can occur within very short time durations. During intense operational engagements, electric warships will experience the most demanding and dynamic load behavior – when reliability and resiliency is needed the most.

These load requirements are unique to Naval integrated power systems, and designing a suitable architecture using traditional design methods is not adequate. New metric-based methods and tools have been introduced to address these challenges. Recent results have shown valuable insight into various system architectures under disruptive conditions based

This work was supported by the Office of Naval Research under the United States Naval Academy N00189-14-P-1197.

on these dynamic mission loads [5]-[8] and the computationally low-cost modeling and simulation techniques they use [9] and [10]. Building on this body of work, a complementary approach for analyzing candidate electrical distribution topologies is introduced in [11] where a representative all-electric-ship load model is proposed.

This paper develops a systematic method for generating appropriately-scaled load demand profiles based on the ship's intended operational use. By factoring in the operational environment and mission capability of the ship, specific scenario-driven vignettes can be mapped to unique ship-level dynamic load profiles. In this manner, the ship load demand profiles are ideally suited for the early design trade study tools. Herein, a representative power system architecture is proposed with locations for the various generators and loads, so the load profiles also introduce a spatial component to the simulation. With this tool, design studies on power system topology, architecture, dynamic load flow, control, and protection such as in [12] become more realistic and actionable for the early design trade space.

## II. LOAD DEMAND GENERATOR FRAMEWORK AND FEATURES

The electric ship load demand assumes realistic operational scenario-driven episodes reflecting actual human-in-the-loop decisions. All loads are characterized and modeled, resulting in a complete set of independent load demand profiles in a given time frame. A principle advantage of this framework is that it focuses on accurate ship-level load dynamics without the need for architecture-specific characteristics, making it ideal for a wide variety of early design trade space studies. In developing the load demand, several key features were considered:

- **Scalable:** Individual load models can either be lumped-parameter or physics-based, depending on the appropriate trade-off between model fidelity and computation speed. At a minimum, lumped-load parameters include maximum and minimum power ratings for peacetime cruising and battle posture, ramp rates, pulse widths and repetitions.

- Tunable: The load sampling frequency can be changed for adjustable model fidelity. Twenty samples per second are used for the lumped-parameter ship load model test case herein.
- Stochastic: Load parameters often behave as random variables. The model can introduce randomness to maximum ratings, pulse widths, pulse repetitions, and ship speed. For example, the propulsion load can be mapped to a random speed based on a probability density function of ship speed-time profile collected from actual U.S. Navy destroyer operations [13]. In the same manner, histogram data can be used to predict the number of times a pulse load will cycle.
- Expandable: The model is modular, making it easy to add or remove loads to define a new set of ship loads or include battle damage to the scenario.

### III. NOTIONAL NAVAL POWER SYSTEM BASELINE

The notional all-electric ship baseline developed by the Electric Ship Research and Development Consortium (ESRDC) is a medium-voltage dc (MVDC) topology shown in [11] and re-envisioned in [12]. It features a 4-zone, 2-bus dc distribution system fed by two main turbine generators (MTG) and two auxiliary turbine generators (ATG). The complete load set consists of propulsion, service, radar, and three high-energy mission loads spatially separated throughout the ship for increased survivability as shown in Fig. 1. Zonal loads (ZL) and the Radar (R) are fed from the main buses by converter modules (CM).

To demonstrate the scalability of the load generation model, a comparison between two ships is presented with the same set of mission loads, but a different scaling of power requirements. Ship A is a notional near-term platform described in [9], with a total installed power of 82 MW. By comparison, Ship B is smaller in displacement, total propulsion power, and total installed power (48 MW), but its mission loads are representative higher-power, far-term, multi-mission pulse loads similar to those described in [14].

#### A. Service and Radar Loads

The topology in [11] contains 22 lumped-parameter loads spread proportionally throughout each zone, representing a full composition of ship-wide ac and dc service loads. The conversion modules (CM) shown in Fig. 1 are converting the dc bus voltage to the appropriate load voltage (ac or dc) in each zone. There are two states in the service load model. The “cruise” state represents the load demand during peaceful transit, while “battle” represents an increase in service load demand due to the need for added redundancy and survivability. For example, all firemain, seawater, and chill water pumps will be operating and cross connect valves closed during battle conditions. The service load model can add random fluctuations for lumped-parameter models or specific load profiles for detailed models if greater detail is needed. Herein, the service load demand is modeled as the aggregate of the 22 lumped loads in [11].

The radar model is similar to the service load model in that it operates at a “cruise” level when in a peacetime transit

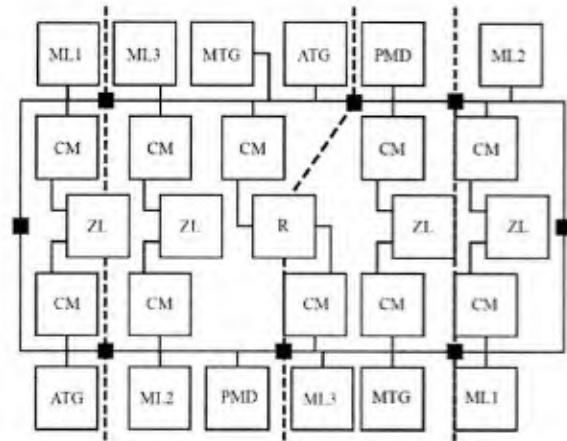


Fig. 1: Notional naval power system baseline

condition. Then, the load demand increases for “battle” condition where backup systems are energized for maximum redundancy and operating at full capacity.

#### B. Mission Loads

There are three high power mission loads in the ship set that are directly fed from the bus and identified as “ML1”, “ML2”, and “ML3” in Fig. 1. They are characterized by peak power, pulse duration, and slew rate as shown in Table I. The mission loads are shown in two locations to represent the physical layout, but the power level shown represents the total of each mission load in both locations; the power could go to either location or be split between the two.

Another characteristic of the mission load model is that the power and duration of each mission load can be modeled stochastically. Mission load 1 has a defined pulse duration (3s), and these pulses occur in sequential groups. The number of pulses in a group can be represented using the binominal distribution for the number of sequential pulses  $N$ ,

TABLE I.

THREE MISSION LOADS (MLX) FOR NOTIONAL SHIPS A AND B

		Peak (pu %)	Duration (sec)	Slew (pu/sec)
ML1	Ship A	24.4	3	$\pm 1.22$
	Ship B	41.7	3	$\pm 2.50$
ML2	Ship A	0.9	Various	$\pm 1.22$
	Ship B	43.8	Various	$\pm 2.50$
ML3	Ship A	0.6	Various	$\pm 1.22$
	Ship B	4.2	Various	$\pm 2.50$

$$\Pr(N = k) = \frac{n!}{k!(n-k)!} p^k (1-p)^{n-k} \quad (1)$$

The parameters for ML1 are  $n=10$  and  $p = 0.45$ . This distribution is shown in the top of Fig. 2. For each operation, the power of each mission load can vary. As ML1 operates using groups of pulses, each pulse is assumed to be at the same power level. ML1 and ML2 exhibit similar characteristics in the power they use in that they typically operate near their max power (1.0 pu). The probability of operating at a given per-unit power level  $Pwr$ , termed the probability density function, is modeled with the Beta distribution,

$$\Pr(Pwr = x) = \frac{x^{\alpha-1} (1-x)^{\beta-1}}{B(\alpha, \beta)} \quad (2)$$

where  $B(\alpha, \beta)$  is a normalization constant to ensure the total probability integrates to 1. The parameters  $(\alpha, \beta)$  characterize the distribution and are 2 and 0.2 respectively.

The length of each pulse for ML 2 and 3 is represented by a truncated version of the Gaussian normal distribution. We assume there is some minimum practical activation time, as well as a maximum operational time due to cooling or other limitations.

The probability of a given operating duration  $D$  is

$$\Pr(D = x) = \frac{\frac{1}{\sigma} \phi\left(\frac{x-\mu}{\sigma}\right)}{\Phi\left(\frac{b-\mu}{\sigma}\right) - \Phi\left(\frac{a-\mu}{\sigma}\right)} \quad (3)$$

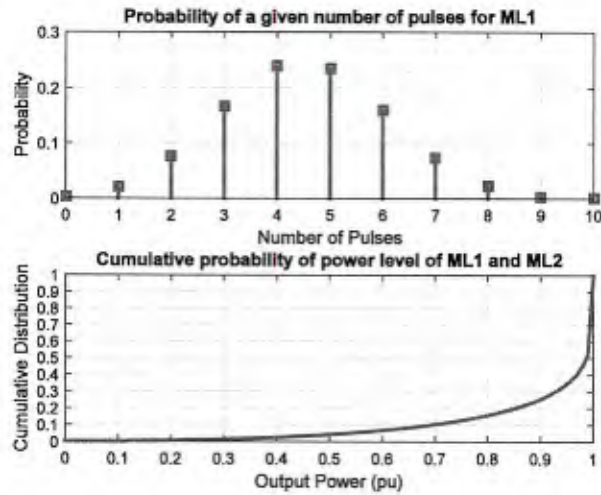


Fig. 2: Pulse load characteristics of ML1. The load operates with groups of pulses. The probability distribution for the number of pulses in a group is shown in the top plot. The power of the pulses in a given group is the same, but can vary for each group of pulses. The cumulative probability distribution for the pulse power is shown in the bottom plot. One can interpret this plot as the probability the pulses have a given output power or less. For example, there is only a 25% probability the power will be less than 0.9 pu.

where  $\phi$  is the standard normal Gaussian distribution and  $\Phi$  is its cumulative distribution. The mean and variance are  $\mu$  and  $\sigma$  respectively, while  $[a, b]$  is the valid interval. ML2 has mean 30, variance 20, and operates between 2 and 60 s. ML3 has mean 120, variance 150, and operates between 5 and 300 s. These distributions are shown in Fig. 3.

### C. Propulsion Load

The propulsion system consists of two propeller shafts connected to two spatially-separated motor and motor drive systems. The system interface to the power distribution system is shown as the Propulsion Motor Drive (PMD) interface off the port and starboard dc buses in Fig. 1. The total notional ship power versus speed curve is found in [11] and is a nearly cubic curve with 73.7% (pu %) at a max speed of 30 knots. Note that for Ship A and Ship B, the propulsion load characteristic is assumed to be similarly scaled and therefore maintains the same per-unit values. Additional parameter settings, such as slew rate for modeling increasing and decreasing speed, are nominally set to  $\pm 1.5$  MW/sec for Ship A and  $\pm 2.0$  MW/sec for Ship B.

## IV. OPERATIONAL VIGNETTES

Six variants of a notional 10-minute operational vignette were considered to simulate the ship's multi-mission capability and to severely – realistically – stress the integrated power system. The sequence of service, radar, mission, and propulsion load levels are shown in Table II. Here, service and radar loads begin at cruise-level and then transition to battle condition in support of an imminent operational threat engagement. Through a series of simulated detect-to-engage sequences and human-in-the-loop responses, the ship then initiates a series of pulse power multi-mission loads. Mission load characteristics in Table I are identified as a number of pulse repetitions shown in Table II and based on the density function equation (1). The pulse duration of Mission Load 1 is set to 3s, while Mission Load Two varies as a probability density function described in equation (3) and are set at 45, 15, 30, and 20 s.

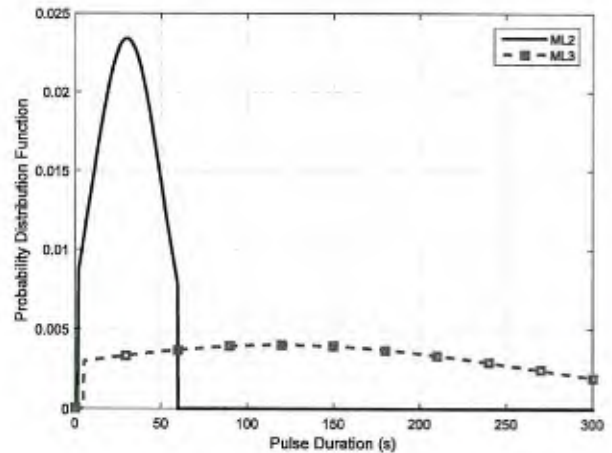


Fig. 3: Probability distribution of operating time for ML2 and ML3. Both distributions follow a Truncated Gaussian Normal distribution with different parameters.

TABLE II.

LOAD SEQUENCE DECOMPOSITION FOR NOTIONAL SHIPS A AND B (% PU)

		Time (min)										
		0	1	2	3	4	5	6	7	8	9	10
Ship A Load	Service	7.50	15.7	15.7	15.7	15.7	15.7	15.7	15.7	15.7	15.7	15.7
	Radar	3.50	3.50	4.60	4.60	4.60	4.60	4.60	4.60	3.50	3.50	3.50
Ship B Load	Service	9.0	18.8	18.8	18.8	18.8	18.8	18.8	18.8	18.8	18.8	18.8
	Radar	8.9	8.9	11.7	11.7	11.7	11.7	11.7	11.7	8.9	8.9	8.9
Mission Load (# pulse)												
	ML1	0	0	6X	0	2X	0	4X	0	3X	0	0
	ML2	0	0	0	0	1X	0	1X	1X	1X	0	0
	ML3	0	0	1X	0	0	0	1X	0	0	0	0
Speed												
	Constant	1.38	1.38	1.38	1.38	1.38	1.38	1.38	1.38	1.38	1.38	1.38
	Moderate	1.38	1.38	1.38	1.38	30.2	30.2	30.2	30.2	30.2	1.38	1.38
	Aggressive	1.38	76.0	52.0	73.6	73.6	73.6	73.6	1.73	30.2	25.1	1.38

Likewise, Mission Load Three pulse durations are set to 200 s and 120 s based on the same density function.

Propulsion power is the largest single load demand, so three degrees of propulsion maneuvering were used for comparison, as shown in Table II and in Fig. 4. From this plot, the impact ship speed has on available power can be readily seen. Ships A and B undergo the same operational scenario with constant, moderate, and aggressive propulsion load dynamics for a total of six variants based on the same operational vignette. The individual service, radar, mission, and propulsion load sequences are added, resulting in the total ship load demand profile for each variation.

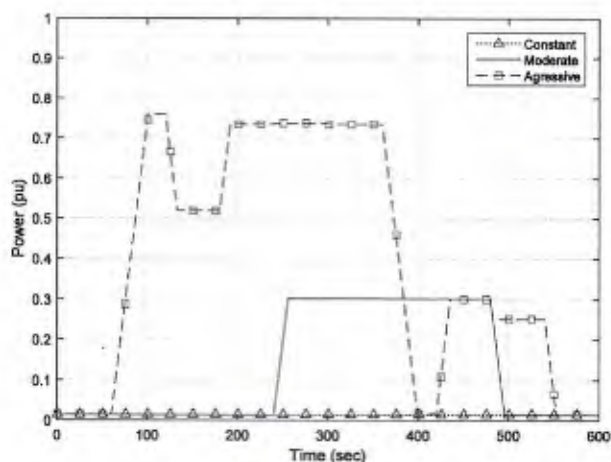


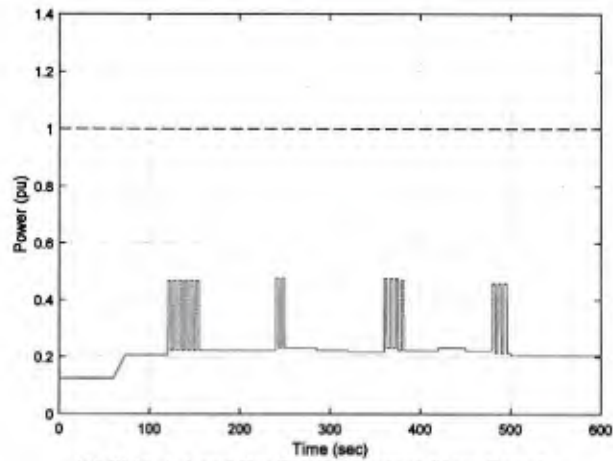
Fig 4: Ship propulsion power demand for increasing ship maneuvering.

## V. RESULTS

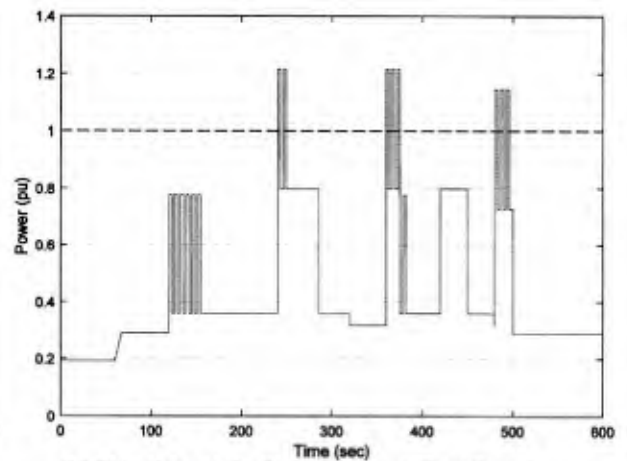
The total load demand profile for six operational vignette variants described in Table II is shown in Fig. 5. Ship A, the electric ship with near-term mission loads and 82 MW of total installed power, is in the first column of results while Ship B, the smaller displacement and smaller installed power (48 MW) with higher pulse loads is shown in the second column. From the left column to the right in each row, the dashed line across the unity per unit power indicates the total installed power (1.0 pu) for Ships A and B. The rows of load profiles from top to bottom indicate the propulsion load dynamics of increasing ship maneuvering speeds.

For Ship A, the total peak load demand is well within the total installed power envelope at most speeds and only just begins to exceed it at its top speed (maximum propulsion load). If historical speed-time profiles are used, then probabilities can be quantified and speed envelopes can be established to mitigate the risk of exceeding the power generation capability of the ship. Localized energy storage can also be added to buffer the pulse loads from the bus and allow for ideal generator loading.

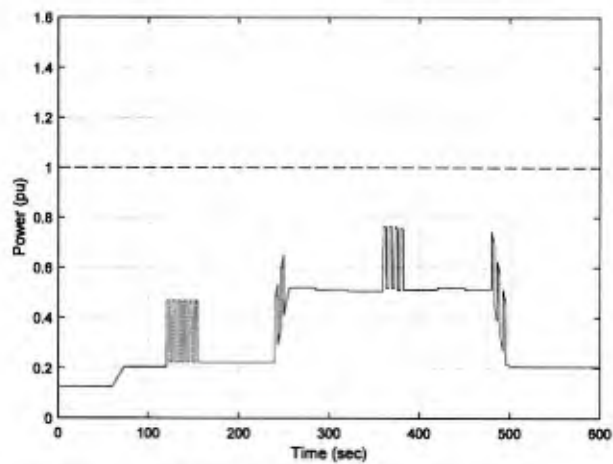
For Ship B, the total peak load demand begins to exceed the total installed power even at a low, constant speed. In order to realize this ship's power system architecture, energy storage is not only necessary to buffer the pulse loads from the bus as discussed for Ship A, but also to store large quantities of energy to support the total ship load demand. By integrating the power profile, these results can be interpreted as an energy management problem, where storage capacity, type, and location can be studied.



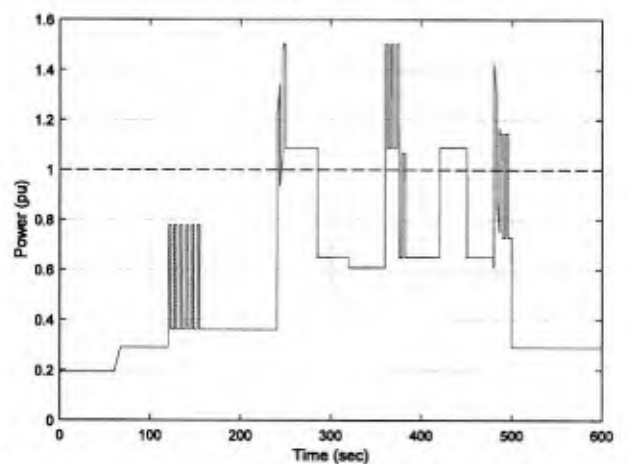
(a) Ship A Load Profile at Constant Slow Speed



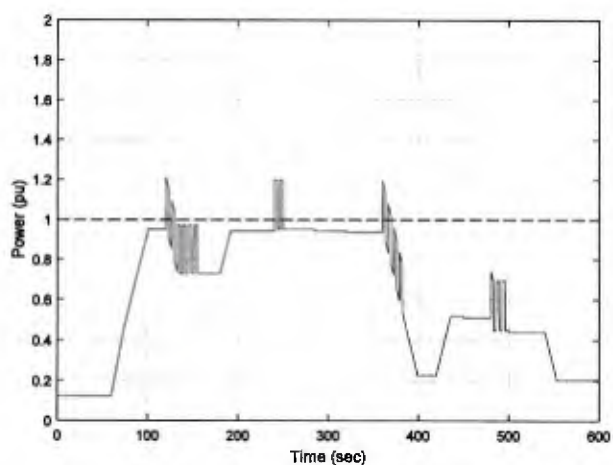
(b) Ship B Load Profile at Constant Slow Speed



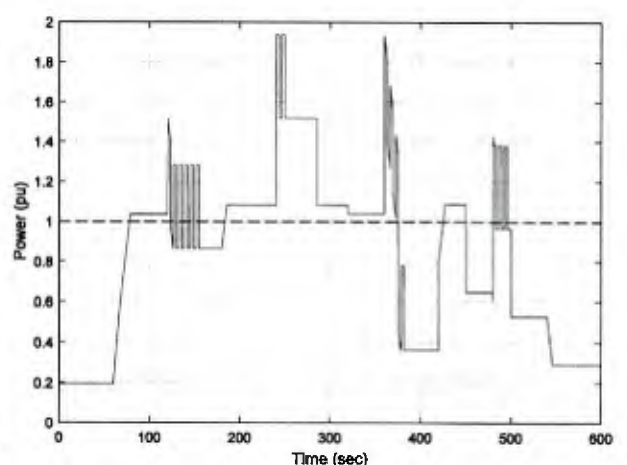
(c) Ship A Load Profile with Moderate Ship Maneuver



(d) Ship B Load Profile with Moderate Ship Maneuver



(e) Ship A Load Profile with Aggressive Ship Maneuver



(f) Ship B Load Profile with Aggressive Ship Maneuver

Fig. 5: Total Load Demand Profiles for Ships A (left column) and B (right column) under constant speed (a,b) and moderate (c,d) or aggressive (e,f) maneuvering. Note the vertical axis values are the same for both columns, but change with each row. A dashed horizontal line indicates 1.0 pu generation power. Exceeding this threshold requires either more installed generation capacity or energy storage.

## VI. CONCLUSIONS AND FUTURE WORK

In the larger body of work on developing early design tools for power system architecture assessment such as in [5]-[12], the premise that early design trade space studies should not assume a constant steady state condition is established. Rather, basing assessments on realistic dynamic loading under potentially disruptive conditions is most appropriate.

In this paper, a systematic method for generating total ship load demand profiles based on its intended operational use is introduced through a representative test case of six variants. The operational vignette represents a multi-mission situation where human-in-the-loop decisions drive the dynamic sequencing of service, radar, mission, and propulsion loads. Stochastic models are presented for various mission load power demands and durations. In so doing, the full ship load set spans the overall load demand profile. One advantage of this framework is that it focuses on accurately capturing ship load dynamics while severely stressing the power system. Since the notional power system baseline architecture is generally defined, it does not assume vendor-specific characteristics or point design solutions, which makes it ideal for early design trade space studies on architecture or control [15].

The set of load profiles are specified here as raw power demand from the perspective of the dc bus without considering the buffering effects of local energy storage. When viewed this way, integrating the total power profile provides insight into understanding energy storage characteristics such as capacity, charge rates, discharge rates, and power interconnect ratings. For future work, we anticipate a major area of research will develop around the best locations for energy storage units and the topology of the power system. As part of the system analysis and tradeoff studies, one can add energy storage to the model at will. For example, adding localized storage at each mission load will limit the impact on the main bus, while adding centralized storage will require high-capacity interconnects.

## REFERENCES

- [1] D. Majumdar. (2013, May 7). *Work and Roughtend Talk Fleet Protection* [Online]. Available: <http://www.news.usni.org>
- [2] A. M. Cramer, S. D. Sudhoff, and E. L. Zivi, "Performance metrics for electric warship integrated engineering plant battle damage response," *IEEE Trans. Aerosp. Electron. Syst.*, vol. 47, no. 1, pp. 634-646, 2011.
- [3] Ciezki, John G., and Robert W. Ashton. "Selection and stability issues associated with a navy shipboard DC zonal electric distribution system." *Power Delivery, IEEE Transactions on* 15, no. 2 (2000): 665-669.
- [4] Amy Jr, J. V. "Considerations in the design of naval electric power systems." In 2002 IEEE Power Engineering Society Summer Meeting, , vol. 1, pp. 331-335. IEEE, 2002.
- [5] A. M. Cramer, S. D. Sudhoff, and E. L. Zivi, "Metric optimization-based design of systems subject to hostile disruptions," *IEEE Trans. Syst., Man, Cybern. A, Syst., Humans*, vol. 41, no. 5, pp. 989-1000, 2011.
- [6] R. R. Chan, S. D. Sudhoff, Y. Lee, and E. L. Zivi, "A linear programming approach to shipboard electrical system modeling," in *IEEE Electric Ship Technologies Symp.*, 2009, Baltimore, MD, pp. 261-269.
- [7] R. R. Chan, S. D. Sudhoff, and E. L. Zivi, "An approach to optimally allocate energy storage in naval electric ships," in 2011 IEEE Electric Ship Technologies Symp., Alexandria, VA, pp. 402-405.
- [8] Butler-Purry, Karen L., and N. D. R. Sarma. "Self-healing reconfiguration for restoration of naval shipboard power systems." *IEEE Transactions on Power Systems*, 19, no. 2 (2004): 754-762.
- [9] A. M. Cramer, H. Chen, and E. L. Zivi, "Shipboard electrical system modeling for early-stage design space exploration," in *IEEE Electric Ship Technologies Symp.*, 2013, Arlington, VA.
- [10] A. M. Cramer, F. Pan, H. Chen, and E. L. Zivi, "Modeling and simulation for early-stage quantitative assessment of medium-voltage dc power system protection schemes," in *Electric Machines Technology Symp.* 2014, Philadelphia, PA, 28-29 May 2014.
- [11] J. S. Chalfant and C. Chryssostomidis, "Analysis of various all-electric ship electrical distribution system topologies," in 2011 IEEE Electric Ship Technologies Symp., Alexandria, VA, pp. 72-77.
- [12] A. M. Cramer, Xiao Liu, Yuqi Zhang, J. D. Stevens, and E. L. Zivi, "Early-Stage Shipboard Power System Simulation of Operational Vignettes for Dependability Assessment," in 2015 IEEE Electric Ship Technologies Symp., Alexandria, VA. Submitted.
- [13] S. Surko and M. Osborne, "Operating Speed Profiles and the Ship Design Cycle," *Naval Engineers Journal*, pp. 79-85, 2005.
- [14] N. Doerry. Peachman Lecture Series, Topic: "Medium voltage dc power for the future fleet." University of Michigan, Ann Arbor, MI, April 15, 2015.
- [15] H. Park, J. Sun, S. Pekarek, P. Stone, D.F. Opila, R. Meyer, I. Kolmanovsky, R. DeCarlo, "Real-Time Model Predictive Control for Shipboard Power Management Using the IPA-SQP Approach," *IEEE Transactions on Control Systems Technology*, Preprint, Vol. PP (99), 2015.

# The role of future information in control system design for shipboard power systems

D. F. Opila<sup>a\*</sup>, J. D. Stevens<sup>a</sup>, A. Cramer<sup>b</sup>

<sup>a</sup>United States Naval Academy; <sup>b</sup>University of Kentucky

\*Corresponding author. Email: opila@usna.edu

## Synopsis

Both naval and commercial shipboard power systems are incorporating new technologies to improve fuel economy and performance. Adding to this challenge, load demands can now rival a single generator's capacity and ramp rate. Devices with limited ramp rates or those with energy storage capacity are time dependent and have capabilities that depend on their current state, like stored energy or present operating point. This means that future information can be useful to prepare the system to service future loads in some conditions. Obtaining these future forecasts and designing a controller can be difficult, so this paper develops a method to quantify the potential value of the future information depending on the system characteristics. This quantitative value allows designers to decide whether or not to pursue future forecasting and a controller that can use it. Two optimization-based control methods are developed. One uses only current information, while the other has an exact forecast of the future. The difference between the two is the potential value of the information. As examples, the method is applied to a notional naval ship and drill platform service vessel with representative power and energy system architectures under indicative operational load demands.

## 1 Introduction: Dynamic Power systems

New technologies are being deployed in marine power systems including batteries, fuel cells, integrated electric propulsion, and standby generators. These systems can improve fuel economy, performance, and service more exotic loads. Many of these system elements are time dependent and their current state depends on past actions, like stored energy or fuel cells with slow power ramp rates. Even traditional generators have finite ramp rates that cannot serve some modern pulse-power loads.

Traditionally, power systems could be analysed in steady state to determine if the generation was sufficient to meet loads, but as the system elements become time dependent they become much more difficult to analyse and control. This control is critical to realizing the benefits of the new components [Kankanala et al. (2012); Hossain and Ginn (2017)]. For example, energy storage devices should be charged in anticipation of large loads [Chan et al. (2011)], and standby generators should be started in advance. Rapid decreases in load can be equally problematic. Numerous proposed control architectures explicitly consider the system dynamics.

When discussing control of these dynamic systems, for clarity we use the terminology of "predictions" and "forecasts." The generation system dynamics can be modeled, so it is often possible to predict the future system state based on the control inputs - the known system commands determined by the controller. The un-modeled changes are considered disturbances to the system and often arise from changing loads. This is the general form of model predictive control (MPC) in which a plant model is used to predict the effects of possible control actions over a fixed time horizon. Here, the controller selects the best input choice, applies that command at the current time step, and repeats the process at the next time step. There are both linear and nonlinear versions [Zohrabi and Abdelwahed (2017); Zhu et al. (2017)] and they can be centralized or distributed [Banaei and Alizadeh (2016)]. These controllers set the power levels of the various generators, sometimes curtail loads, and can be used for system breaker configuration [Zohrabi et al. (2017)]. In all of these works, the controller does not have advanced knowledge of changes in load, but it can predict the results of its own actions on the plant.

By contrast, a forecast is an estimate of future disturbances that the controller cannot change, but may have some knowledge of it. For more aggressive and rapidly changing loads, the controller may receive a forecast of future loads to better prepare for fast transients [Gonsoulin et al. (2017); Vu et al. (2017); Stone et al. (2015); Park et al. (2015)]. The controller then incorporates this forecast as it makes its predictions for the effects of the control actions. This type of control is also typically called MPC.

This paper considers the control and analysis challenges of using time-dependent power system elements and the relative importance of future forecasts to mission success. In some cases this future information is critical, while in other cases it provides no benefit. Specifically, even if a controller uses a prediction model like MPC, it has no explicit future forecast and could be compared with a more typical PID or other standard controller. Adding an explicit future load forecast is often difficult and inaccurate, so it is useful to quantify the potential benefits of this approach. For example, future load information is critical to a drill platform servicing a vessel attempting to temporarily shut down engines, while the information is irrelevant when the ship is at steady state cruise. Naval vessels servicing rapid pulse loads also benefit from forecasts.

To quantify this difference, this paper compares the unserved load with and without future knowledge. Power systems require some form of controller [Paran et al. (2015); Vu et al. (2017)], but rather than design a controller for every case an optimization process is used that mimics the behaviour of an ideal controller. Herein, two types of

optimization methods are used to generate controller behavior. The first optimization algorithm is described as an “instantaneous” because it only has knowledge at the present time. The second algorithm is called a “multi-period” controller because it has exact future knowledge of load demands, which essentially can consider many actions at many different times. Practically speaking, the tradeoff between the two methods is the value of future knowledge at an additional computational cost. The multi-period controller is very difficult to fully implement in practice as it assumes exact future knowledge on a long horizon, but it provides an upper bound on the system performance given a specific system architecture. These two controller types have been proposed separately before, where the instantaneous version was discussed in [Chan et al. (2009); Cramer et al. (2013, 2015)] and the multi-period version was shown in [Oh et al. (2017)]. The goal here is to compare the two and rigorously quantify the value of the forecasts.

When using MPC, the advanced knowledge given to the controller depends on the application and it is a design decision. The multi-period controller in this paper has exact future knowledge for the whole simulation horizon, so a more practical controller like MPC with a limited lookahead capability should exhibit performance somewhere between the instantaneous and multi-period optimizations. As the MPC horizon gets longer its performance should approach the ideal multi-period case assuming the forecast is accurate.

The sections that follow first present some limited conditions when future forecasts are not useful, then develops the two control methods for comparison. The ship architectures are then described, followed by results and conclusions.

## 2 Analysis

Providing sufficient overall power for dynamic load demands is a primary consideration in ship power system design and the focus of this paper. Fuel economy is not directly studied, but it does have a strong secondary effect in that correct system control can allow generation assets to be turned off rather than left idling.

This section first proposes some simple conditions to quantify when future information is not useful, and then establishes that even minor system complexity requires more advanced analysis to understand the value of a forecast. The instantaneous and multi-period optimization based control algorithms are then described.

### 2.1 Relevant Operating Conditions

Load shortfalls can occur when power ramp rates exceed capacity, or if there is insufficient total generation. Power plant lineups are often optimized for fuel economy, which implies that offline generators will need time to start up in order to serve the maximum load. To formulate the problem, each generator  $i$  has maximum and minimum power limits such that

$$p_{min}^i \leq p_{gen}^i \leq p_{max}^i \quad (1)$$

Both gas turbine and diesel generators have positive and negative rate limits  $r_+^i$  and  $r_-^i$  that are significantly less than ramp rates of newer system loads. Assuming these ramp rates do not depend on operating condition, they can be defined as

$$r_-^i \leq \frac{p_t^i - p_{t-1}^i}{\Delta t} \leq r_+^i \quad (2)$$

where  $p_t^i$  and  $p_{t-1}^i$  represent the  $i$ th generator power at time  $t$  and  $t - 1$ .

The total generation capacity is simple to check, but ramp rates require more analysis to account for the dynamics involved. If we assume  $n$  generators have identical ramp rates and capacities, and share power equally, then the total system ramp rates are  $n * r_-^i$  and  $n * r_+^i$  across the full range from zero to full system capacity. If the load ramp rate stays within these bounds, the system is able to provide sufficient power even without future predictions. However, if the generators differ in either their specifications or operating conditions, then more detailed analysis is required. For example, one generator may hit its maximum power limit before the others and thus be unable to contribute to total system ramp rate.

Even analyzing the startup of idle generators requires significant simplification. Let us assume an offline generator requires some time to start, synchronize, and come online at zero load. It can then respond to a load based on its ramp rate. Even if the next generator is assumed to be online before the existing generators reach capacity, this condition is not sufficient because the existing generators no longer contribute to the power ramp once they reach their maximum. These dynamic factors drive the need for automated methods to analyze and control the power system, even without the addition of energy storage.

### 2.2 Optimization-based analysis

To study the relative value of this future information, two control methods are used. One considers only current information, and the other has full future knowledge. Many methods exist to mathematically formulate the problem, for example linear vs nonlinear models, and whether decision variables should be generator powers or line flows. This section focuses on the overall optimization goals rather than the details of the numerical solution.

### 2.2.1 Instantaneous optimization

The general form for an instantaneous single-period optimization is a minimization of some cost function subject to constraints defined as

$$\min_{p_g, p_{es}} c_{gen}(p_g) + c_{es}(p_{es}) + c_z(p_g, p_{es}) \quad (3)$$

such that

$$g(p_g, p_{es}) = 0 \quad (4)$$

$$h(p_g, p_{es}) \leq 0 \quad (5)$$

$$p_{min} \leq p_{gen} \leq p_{max} \quad (6)$$

$$p_{esmin} \leq p_{es} \leq p_{esmax} \quad (7)$$

$$l \leq A \begin{bmatrix} p_g \\ p_{es} \end{bmatrix} \leq u. \quad (8)$$

The basic costs are associated with generator  $c_{gen}$  and energy storage usage  $c_{es}$ . The functions  $g$  and  $h$  represent equality and inequality constraints on the system like power flow and line limits. The generic cost function  $c_z$  includes any other design attributes like a desire for generator balancing. Some portion of the problem may be linear, and those constraints are often represented separately in (8) to simplify the solution. This setup is generic and admits a variety of optimization setups from linearized DC systems with direct control of line flows to full nonlinear AC power flow equations.

### 2.2.2 Multi-Period Optimization

The multi-period control optimizes power and energy management for the entire scenario at once by assuming perfect knowledge of all loads. It simultaneously considers past, present, and future demand at all times. This is distinctly different than a single-period controller, which optimizes commands only at each time step.

Conceptually, the optimization simultaneously analyzes copies of the power system at each of  $T$  time steps. The decision variables  $p_g, p_{es}$  have a representation at each time step that combine to create the extended multi-period decision variables  $\bar{p}_g = \{p_g(1), p_g(2), \dots, p_g(T)\}$ , and  $\bar{p}_{es} = \{p_{es}(1), p_{es}(2), \dots, p_{es}(T)\}$ . For a power architecture with  $n_g$  generators and  $n_{es}$  ES, the new decision variables  $\bar{p}_g, \bar{p}_{es}$  now have  $n_g T$  and  $n_{es} T$  elements, respectively.

### 2.2.3 Energy Storage

The energy available in energy storage system evolves over time and the units cannot provide sustainable power, so constraints are added to reflect their storage capacity. We use a relatively simple model for energy storage that is agnostic to the storage technology or hybrids thereof and provides bidirectional power flow.

Each energy storage unit has a maximum and a minimum power limit (e.g.  $\pm 10$  MW) and an energy capacity (e.g. 60 MJ). The storage is approximated as lossless, so the power output is integrated to determine the energy storage state,

$$E_{min} \leq E_{start} - \sum_{t=0}^{\tau} p_{es_i}(t) \Delta t \leq E_{max} \quad \forall \tau \in \{0, T\} \quad (9)$$

where  $p_{es_i}(t)$  is power from the energy storage  $i$  (positive for output power),  $\Delta t$  is time step, and  $E_{min}$  and  $E_{max}$  are minimum and maximum energy capacities, respectively. Example capacity ranges can be 0-60 MJ with 30 MJ starting point, or equivalently  $\pm 30$  MJ with a 0 MJ start.

### 2.2.4 Multi-Period Objective Function

After adding the multi-period constraints on energy storage capacity and ramp rates, the final formulation for multi-period optimal power flow is modified from (3) as

$$\min_{\bar{p}_g, \bar{p}_{es}} \bar{c}_{gen}(\bar{p}_g) + \bar{c}_{es}(\bar{p}_{es}) + \bar{c}_z(\bar{p}_g, \bar{p}_{es}) \quad (10)$$

where the bar on top of variables include vectors of entire multi-period as suppose to a single-period. The constraints are similarly modified with the extended decision variables.

## 3 Ship Architectures

To illustrate this phenomenon, consider two applications: a drill support ship and a naval vessel, both with high power dynamic loads and multiple generators. The naval vessel also has energy storage. The drill ship power system shown in figure 1 does not contain energy storage and is less complex, so it will be considered first.

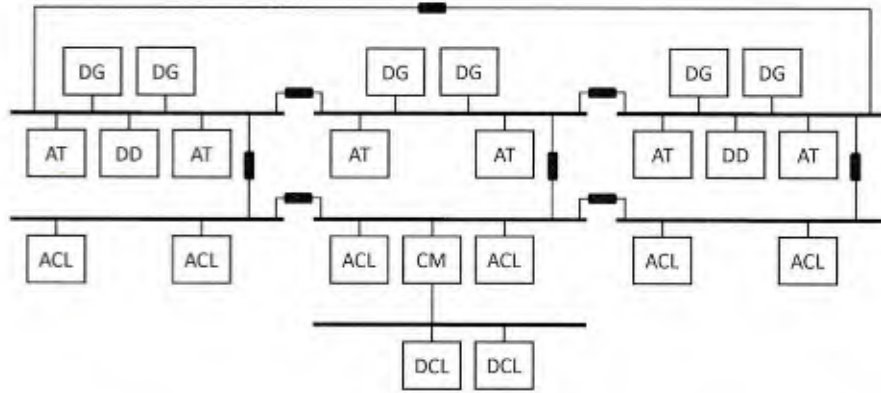


Figure 1: Notional drilling vessel power system as described in [Anvari-Moghaddam et al. \(2016\)](#). DG signifies diesel generator, AT signifies Azimuth Thruster Load, DD signifies Drilling Drive, CM signifies converter, ACL signifies general AC Load, and DCL signifies general DC Load.

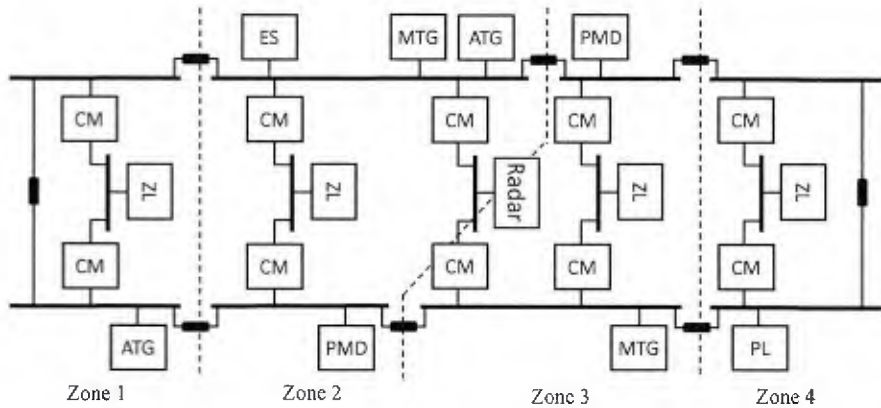


Figure 2: Notional shipboard MVDC system. MTG signifies main generator, ATG signifies auxiliary generator, PMD signifies propulsion, CM signifies converter, R signifies radar, and ZL signifies zonal load.

### 3.1 Drill Ship

We consider the architecture studied in [Anvari-Moghaddam et al. \(2016\)](#) with the energy storage element removed, shown in figure [1](#). The drill ship has 6 generators with a maximum power of 7 MW each. The analysis considers two cases, one where all the generators have slow ramp limits of 0.117 MW/s (1 p.u./min), and the second where three of the generators are replaced with faster versions with 1 MW/s ramp rates.

### 3.2 Naval Vessel

The naval vessel under consideration is shown in figure [2](#). The system has 82 MW of installed generation that can absorb a step load change of 22.2 MW and has a response time constant of approximately 2.9 s. The maximum propulsion load is 60.4 MW. Distributed through the four zones is a total of 3.4 MW of non-vital load and 3.7 MW of vital load. The radar load is 3.8 MW. There are three mission loads. In zone 1, there is a 13-MW mission load and accompanying 13-MW, 780-MJ energy storage. In zone 2, there is a 5-MW mission load and accompanying 5-MW, 50-MJ energy storage. In zone 3, there is a 7-MW mission load and accompanying 7-MW, 420-MJ energy storage.

## 4 Simulation Results

In this section, we present the simulation results for the two different ships under various load demands during representative operational missions.

#### 4.1 Drill Support Ship

The drill support ship load profile is a simple combination of two steps from 50% to 100% of rated total generation (21 - 42 MW). The first step occurs slowly at positive and negative ramp rates of 0.6 MW/s. The second step is more rapid with a rate of 3.3 MW/s.

The energy storage units are not used in the drill ship model to provide simple examples when future forecasting is not helpful. Forecasts are almost always helpful when energy storage is included.

##### 4.1.1 All slow generators

The drill ship is first studied assuming all the generators have slow ramp rates of 0.117 MW/s, for a total ramp rate of up to 0.7 MW/s. With these rates, the first step load is within the generator ramp rate limits, but the second load step exceeds the total ramp limits. The results are shown in figure 3 for both the instantaneous and multi-period optimization.

The generators have identical power ratings and ramp limits but slightly different costs, so they do not share power equally but their operating points are very similar. The maximum generator power is sufficient to serve the load, and the first ramp rates are within the system capability. This satisfies the assumptions of Section 2.1, so we should expect that future forecasts do not help and the instantaneous and multi-period control should yield similar results. This can be seen in the first load step from 25-125 s when both control methods generally serve the load during transients. However, the instantaneous version has a slight power shortfall as it reaches a peak at 70s. This occurs because the generator operating points are different. Generators 4-6 start at a higher operating point than the others, and thus saturate sooner leaving only 3 generators to provide the ramp rate during the end of the ramp from 60-70 s.

During the second power step increase at 150 s, the ramp rate exceeds the installed capacity. It is physically impossible to serve the load, and both controller types fail.

##### 4.1.2 Half fast, half slow generators

The drill ship is next studied assuming three of the generators are replaced with faster versions with 1 MW/s ramp rates. This means the total ramp rate is 3.3 MW/s when no generators are saturated, derived from  $3 \times 1 \text{ MW/s} + 3 \times 0.167 \text{ MW/s}$ . With these rates, both load steps are within the total ramp limits, but only with no saturation. The results are shown in figure 4 for both the instantaneous and multi-period optimization. With different generator ratings, one of the assumptions of Section 2.1 is clearly violated and it is possible that forecasts may help.

The second load step is a change of 21 MW which represents the full capacity of the 3 fast generators, meaning they are likely to saturate. The multi-period control successfully tracks the fast ramp at 150 s by changing the generator operating points in anticipation of the ramp. The load is transferred to the slow generators (1-3) so that the fast generators can operate lightly loaded and be ready to provide the fast ramping power to track the step. The instantaneous optimization does not show this characteristic. The fast generators start at about 50% load and quickly saturate, meaning the load is under-served.

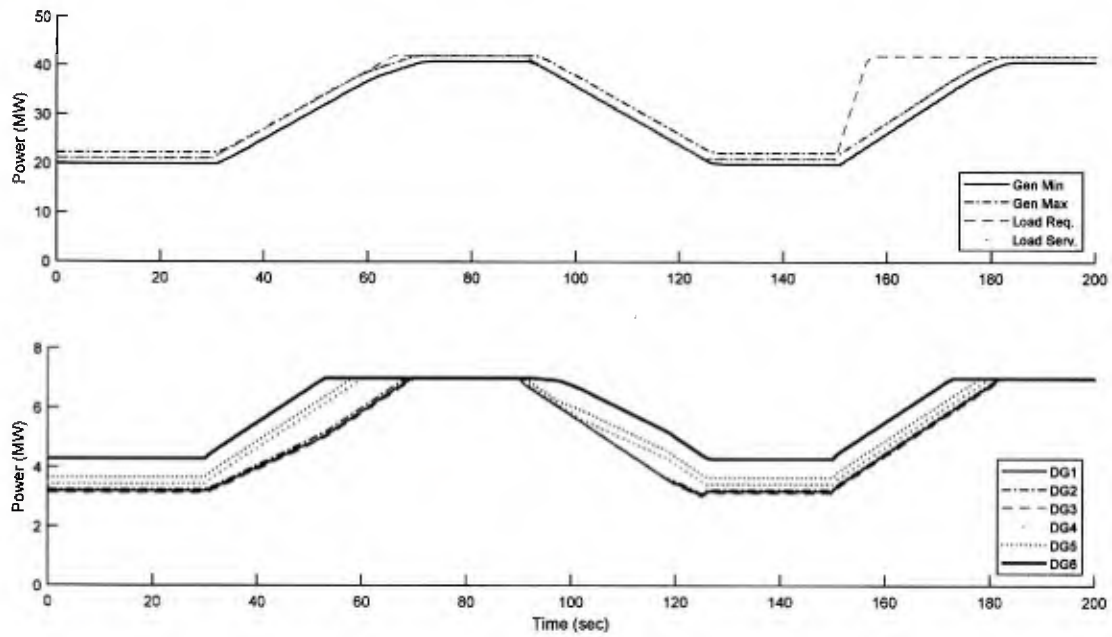
#### 4.2 Naval Vessel

As an example scenario the system is initially operating with full energy storage, cruising at 20 knots, and radar and mission loads off. At 30 s, speed is reduced to 10 knots, and the mission load in zone 1 (13 MW) is turned on. At 75 s, the radar (3.8 MW) is turned on. At 100 s, speed is increased to 20 knots, and the mission load is turned off. At 135 s, speed is increased to 30 knots. The vignette ends at 180 s. For this mission, the performance of the single-period instantaneous optimization method is shown in figure 5. The same mission using the multi-period optimization is shown in figure 6.

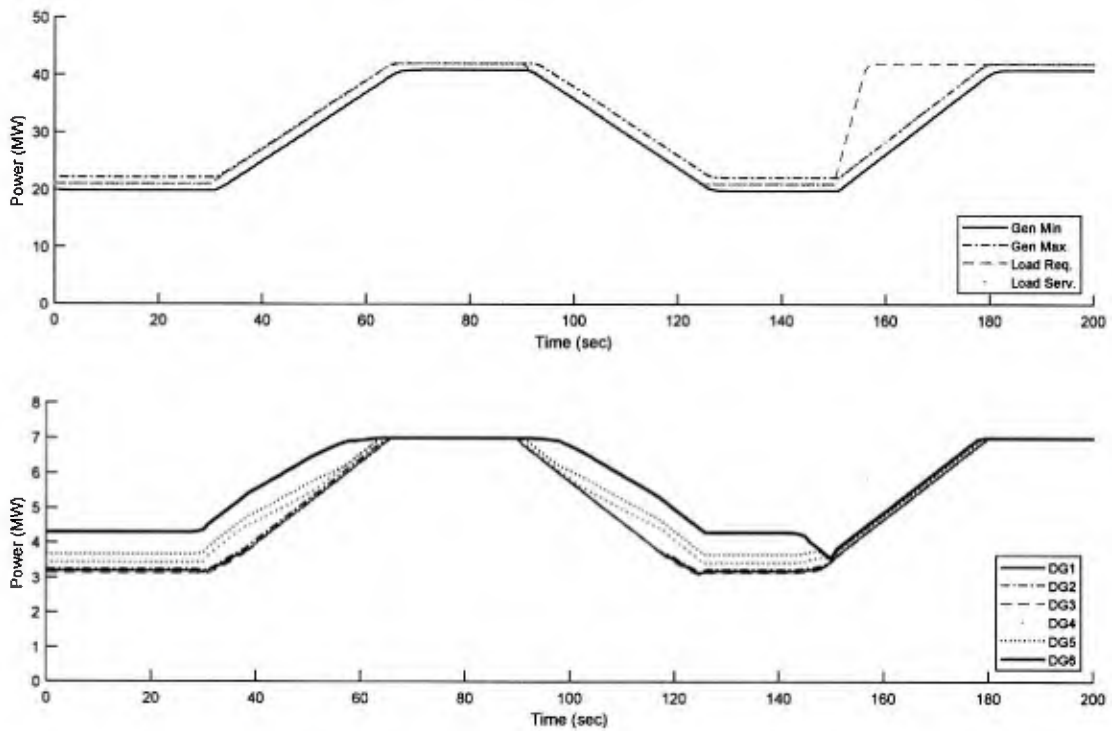
It can be seen that the multi-period approach is generally using less generation to satisfy the load, although during the challenging propulsion transient at 135 s, it has more instantaneously available generation. The multi-period approach actually serves slightly less load during the mission load operation time in order to improve the endurance of the mission load. This is reflected in the load difference just before 100 s. Also, the improved capability of the multi-period approach to serve the propulsion load can be seen at 135 s.

### 5 Discussion

As expected, future information becomes more valuable for systems with time dependent features. Forecasts do not help in some limited conditions, but as shown in the earlier examples even a set of conventional generators can benefit if they do not have identical power limits, ramp rates, and operating conditions. Aggressive loads combined with limited generator ramp rates and startup time is a typical example of a system that can benefit from forecasts. Adding Energy storage to the power system can provide performance benefits, but the control of these devices significantly improves with future forecasting. This implies that systems without forecasting may not realize the full benefits of the storage devices.

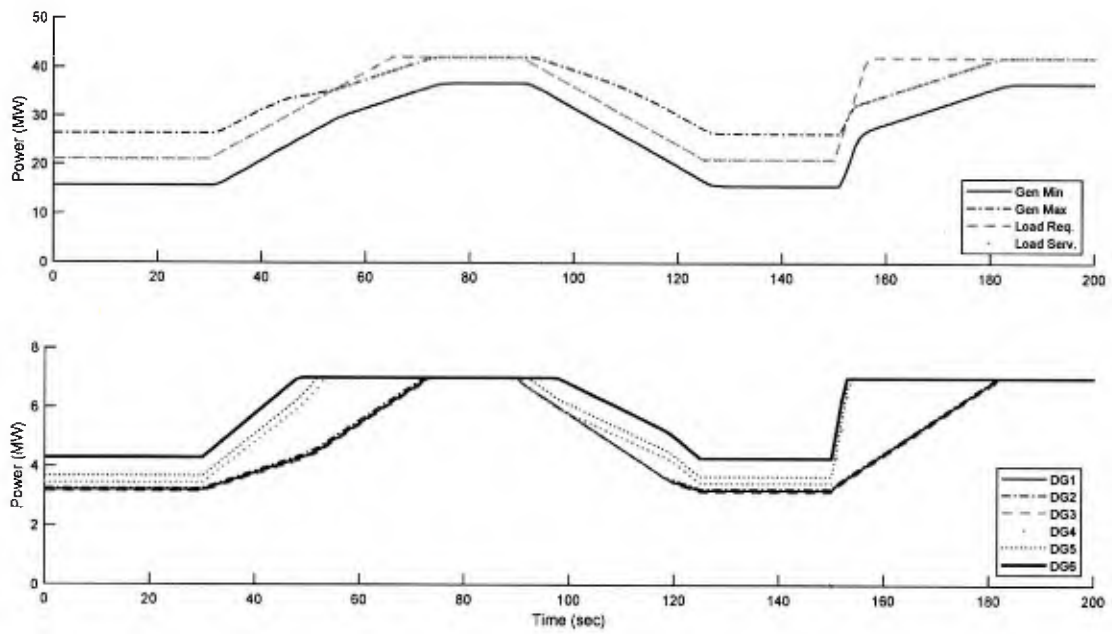


(a) Instantaneous

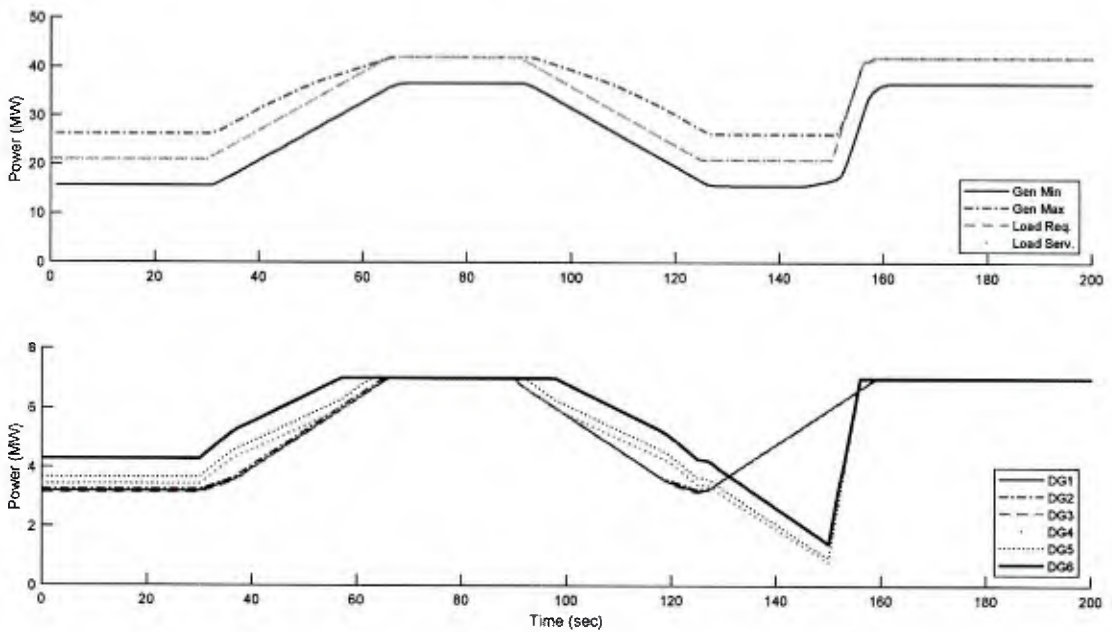


(b) Multi-period

Figure 3: Drill Ship with all slow generators



(a) Instantaneous



(b) Multi-period

Figure 4: Drill Ship with half fast, half slow generators

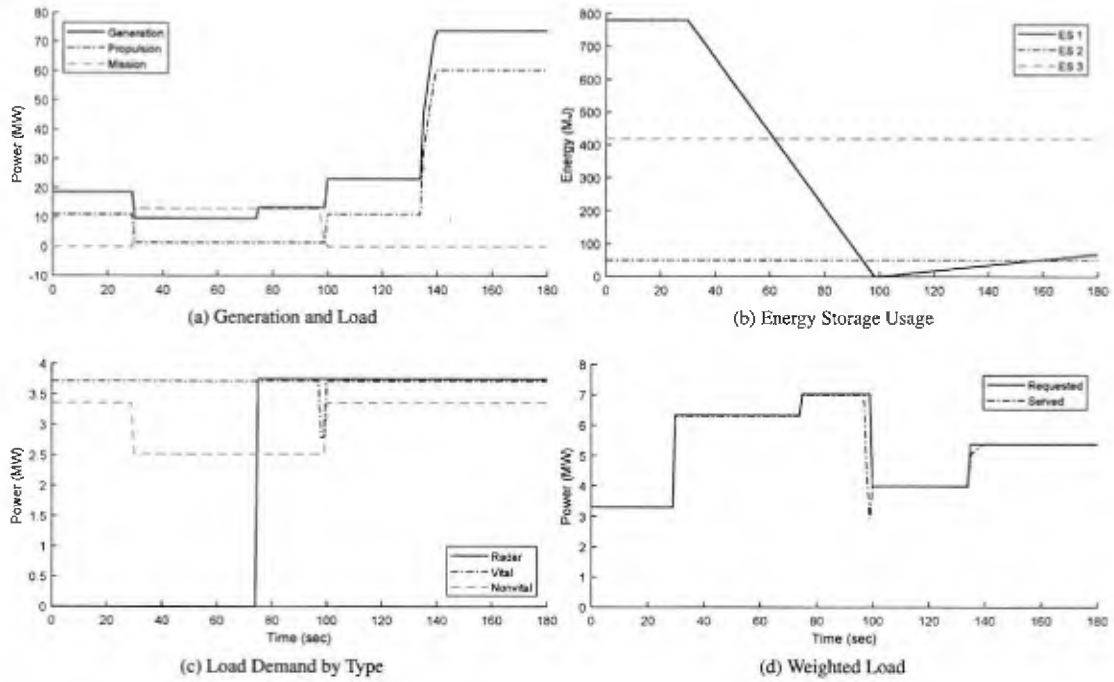


Figure 5: Instantaneous control for the naval vessel.

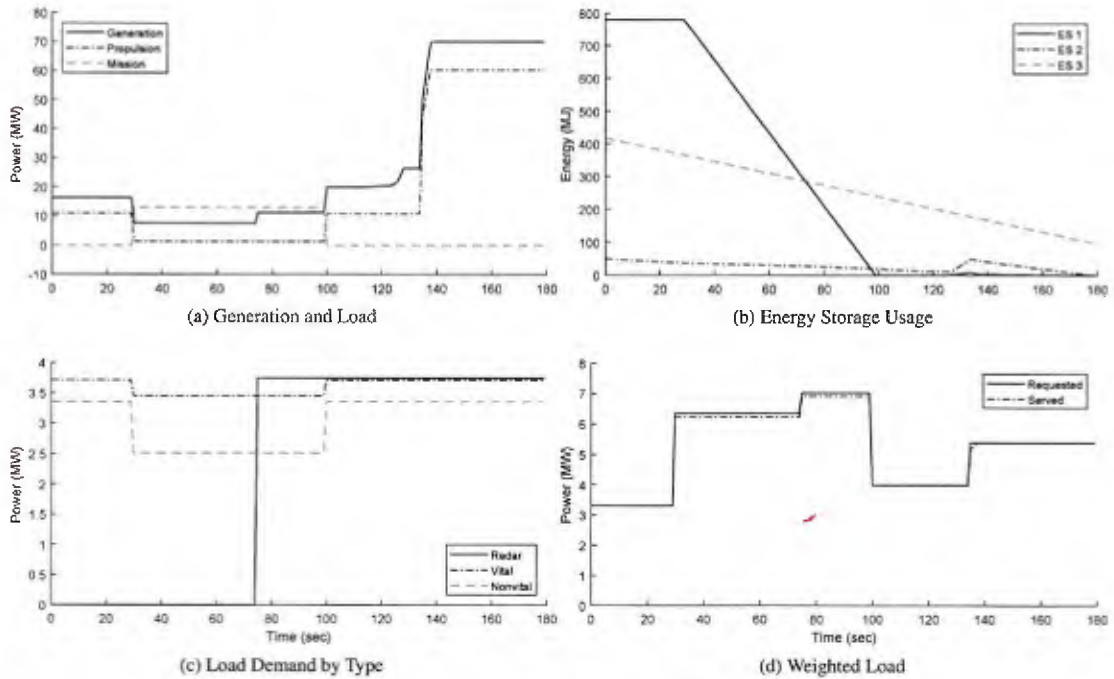


Figure 6: Multi-period control for the naval vessel.

The difference in performance between the instantaneous and multi-period controllers provides the quantifiable benefit of future forecasts. However, this metric must be evaluated with caution as it represents a hard upper bound on that performance. If the future forecast or the dynamic models are incorrect, that maximum performance will not be achieved and the controller may actually do worse than one without forecasting.

## 6 Conclusions

Modern marine power systems increasingly incorporate new technologies and service fast ramping loads. The time-dependent nature of these systems indicate that they can benefit from forecasts of future load demand, but implementing such a system is difficult. This paper presents a method to quantify the benefit of this future information. Some power systems may see no value in future forecasting, but systems with load ramp rates approaching generator limits or those with energy storage generally benefit.

Two optimization based controllers were developed, one with only current instantaneous information, and the other with full future knowledge of load. Each represents an upper-bound performance given the information available, so the difference between the two reflects the value of that information. Implementing a real controller with exact load forecasts is very difficult, but the methods here allow a rigorous quantification of the potential benefits to determine if such an idea is worth pursuing.

These ideas were demonstrated on a drill platform service vessel with both slow- and fast-ramping generator lineups, and on a naval vessel with electric propulsion and demanding mission loads.

## References

- Anvari-Moghaddam, A., Dragicevic, T., Meng, L., Sun, B., Guerrero, J. M., Oct 2016. Optimal planning and operation management of a ship electrical power system with energy storage system. In: IECON 2016 - 42nd Annual Conference of the IEEE Industrial Electronics Society. pp. 2095–2099.
- Banaei, M. R., Alizadeh, R., 2016. Simulation-based modeling and power management of all-electric ships based on renewable energy generation using model predictive control strategy. *IEEE Intelligent Transportation Systems Magazine* 8 (2), 90–103.
- Chan, R. R., Sudhoff, S. D., Lee, Y., Zivi, E. L., Apr. 2009. A linear programming approach to shipboard electrical system modeling. In: Proc. IEEE Electric Ship Technologies Symp. pp. 261–269.
- Chan, R. R., Sudhoff, S. D., Zivi, E. L., Apr. 2011. An approach to optimally allocate energy storage in naval electric ships. In: Proc. IEEE Electric Ship Technologies Symp. pp. 402–405.
- Cramer, A. M., Chen, H., Zivi, E. L., Apr. 2013. Shipboard electrical system modeling for early-stage design space exploration. In: Proc. IEEE Electric Ship Technologies Symp. (ESTS). pp. 128–134.
- Cramer, A. M., Liu, X., Zhang, Y., Stevens, J. D., Zivi, E. L., Jun. 2015. Early-stage shipboard power system simulation of operational vignettes for dependability assessment. In: Proc. IEEE Electric Ship Technologies Symp. (ESTS). pp. 382–387.
- Gonsoulin, D. E., Vu, T. V., Diaz, F., Vahedi, H., Perkins, D., Edrington, C. S., Aug. 2017. Coordinating multiple energy storages using MPC for ship power systems. In: Proc. IEEE Electric Ship Technologies Symp. (ESTS). pp. 551–556.
- Hossain, M. R., Ginn, H. L., Jun. 2017. Real-time distributed coordination of power electronic converters in a DC shipboard distribution system. *IEEE Transactions on Energy Conversion* 32 (2), 770–778.
- Kankanala, P., Srivastava, S. C., Srivastava, A. K., Schulz, N. N., May 2012. Optimal control of voltage and power in a multi-zonal mvdc shipboard power system. *IEEE Transactions on Power Systems* 27 (2), 642–650.
- Oh, E., Opila, D. F., Stevens, J., Zivi, E., Cramer, A., Aug. 2017. Early stage design evaluation of shipboard power systems using multi-period power flow. In: Proc. IEEE Electric Ship Technologies Symp. (ESTS). pp. 225–231.
- Paran, S., Vu, T. V., Mezyani, T. E., Edrington, C. S., June 2015. Mpc-based power management in the shipboard power system. In: 2015 IEEE Electric Ship Technologies Symposium (ESTS). pp. 14–18.
- Park, H., Sun, J., Pekarek, S., Stone, P., Opila, D., Meyer, R., Kolmanovsky, J., DeCarlo, R., Nov. 2015. Real-time model predictive control for shipboard power management using the IPa-sqp approach. *IEEE Transactions on Control Systems Technology* 23 (6), 2129–2143.
- Stone, P., Opila, D. F., Park, H., Sun, J., Pekarek, S., DeCarlo, R., Westervelt, E., Brooks, J., Seenumani, G., Jun. 2015. Shipboard power management using constrained nonlinear model predictive control. In: Proc. IEEE Electric Ship Technologies Symp. (ESTS). pp. 1–7.
- Vu, T. V., Gonsoulin, D., Diaz, F., Edrington, C. S., El-Mezyani, T., June 2017. Predictive control for energy management in ship power systems under high-power ramp rate loads. *IEEE Transactions on Energy Conversion* 32 (2), 788–797.
- Zhu, W., Wang, W., Fu, L., Aug. 2017. System-level dynamic power management for islanded DC microgrid with pulse load. In: Proc. IEEE Int. Conf. Mechatronics and Automation (ICMA). pp. 1204–1209.
- Zohrabí, N., Abdelwahed, S., Aug. 2017. On the application of distributed control structure for medium-voltage

DC shipboard power system. In: Proc. IEEE Conf. Control Technology and Applications (CCTA). pp. 1201–1206.

Zohrabi, N., Abdelwahed, S., Shi, J., Aug. 2017. Reconfiguration of mvdc shipboard power systems: A model predictive control approach. In: Proc. IEEE Electric Ship Technologies Symp. (ESTS). pp. 253–258.

## Market-Based Control as a Paradigm for Power System Control

### ABSTRACT

Market-based control has previously been proposed as an option for the control of shipboard power systems. Such an approach consists of an artificial market for power in which various actors (a consumer and firms) behave according to microeconomic principles. With each piece of equipment operating through laws of supply and demand, a system that is agile, resilient, effective, and efficient can be obtained. If objectives change or the system configuration is altered, prices shift, and resources are automatically reallocated to their most productive uses. This behavior arises because it has been shown that there is a fundamental equivalence between the solution to the market-based control approach and the underlying optimal control problem involved in controlling the shipboard power system. Formulating the problem in this way is not fundamentally necessary, but market principles will be at work in any solution to the problem. Herein, advancements in the control method as applied to time-dependent elements such as energy storage are presented. Methods of operating equipment in which future operation is limited by present choices are discussed. These methods allow for optimal control over a dynamic and uncertain future. Extensions of this work into the joint control of electric power and thermal management systems are also presented.

### INTRODUCTION

Energy storage in power systems must be considered in order to achieve an optimal decision-making process when faced with shifting objectives and system states. When posing the problem in terms of market-based control, this is essentially formulating how the energy storage will react to known market conditions and predictable future market conditions that can affect the optimal decision. Ideally, the most potentially valuable choice, whether to charge or to discharge, will always be chosen to reach optimal system behavior.

Generators and loads are both more straightforward to consider - they respectively generate or consume power only as needed to achieve optimal performance and their

behavior is not time dependent. However, the optimal performance of the power system overall has been shown to rely heavily on the charging and discharging behavior of energy storage. For example, a ship needing to fire an advanced high-performance weapon system may require more power than the installed generators can provide, so the energy storage is required to have a substantial capacity of charge to adequately meet the power demand of the system's objectives.

Great advances have been made in the modeling and simulation of electric shipboard power systems such as those explored in [1] [2], which feature mathematical programming-based approaches. However, these advances have relied on a very limiting view of the energy storage in the system - one that forces a static, unchanging weight on charging or discharging energy. For truly optimal control, the control element of the energy storage must be able to evaluate the conditions of the current market, and then determine the optimal price of energy storage and release. Then, an optimal decision can be reached. This is a challenging dynamic problem. It is very intuitive to imagine that the optimal price of energy in a storage element should not be static - it should be changing depending on the energy demands that the storage element is expected to serve. For a simple example, imagine a typical mobile phone battery. As time progresses and the battery discharges over time, the mobile phone continually experiences a decrease in available time before the battery must be charged, or else the system will cease to function in a useful manner. It is then useful to formulate the situation as remaining charge being more valuable than dispensed charge, because the implied time limit to charge the battery to keep the system operational is always decreasing. Once the phone does not have sufficient energy to operate, it must be connected to a nominal wall-charger as a source of power. It is helpful to conceptualize the system powering on as the moment when energy in the battery is the most valuable. Then, as time progresses the battery gains more charge, and the effective time that the system could stay operational while away from the power source increases. Thus, it is reasonable to say that more charge becomes less valuable, becoming completely

worthless when the battery is fully charged. This is a simple enough cycle to automatically control with no complications, but for the problem at hand, it is imperative to consider the more complex situation where the energy storage must decide to purchase excess energy from generators (power sources that are typically always connected to the system) and sell stored energy to the loads when deemed optimal.

At some level, the problem is that of quantifying the opportunity costs faced by the system at any moment in time, and an optimal approach to evaluating opportunity costs is not an intuitive process. The controller must be able to consider the possible impact on future value given the recommended actions in each time step. There are also considerations that elements of the electrical power system may be compromised or effectively neutralized. In the interest of making a survivable system, two immediate barriers exist: it is important to evaluate the economic value of restoring service to a faulted component, and to determine the appropriate effect of this loss of a component's capability on the value of energy in the energy storage units.

From [3], it has been found that the market-based control problem is fundamentally the same as the underlying constrained optimization problem. Thus, any solution to such a constrained optimization problem may reasonably be expressed in terms of a market-based control problem and would be solvable using similar techniques. Furthermore, the optimal state of the power system is analogous to the artificially constructed market reaching equilibrium – when supply of resources is equal to the demand of resources.

Possible approaches to achieving market equilibrium, and thus the optimal state of the power system, are discussed herein. In particular, the alternating direction method of multipliers (ADMM) and existing issues with distributed control approaches are explored.

Solving how energy storage can be optimally controlled in this manner can also have immediately useful results for other subsystems found in the naval ship environment. Shipboard power systems are always accompanied by a cooling system, in order to maintain acceptable temperature levels so that no equipment is exposed to unrated conditions for any significant amount of time. Acknowledging heat dynamics, the electrical components being serviced can be treated as “heat capacitors”, or another form of energy storage. This makes any solution to the optimal control of electrical energy storage applicable to the control of the cooling system. Consequently, the cooling system can also be modeled and controlled as another artificial market with analogous constraints, and solutions for optimal control, as the electrical power system.

Any implications of this solution affecting the thermal management subsystem will rely on the two artificial markets being connected, but the true nature of these systems will certainly demand that the two markets operate on two different time-scales. The electrical power system practically functions as an instantaneous market - but there is a slight delay between power and energy transactions in the order of nanoseconds. The thermal management system cannot operate at these speeds, so it must be able to anticipate the expected demands of the electric power system and respond appropriately.

This paper will proceed to go into more detail on current approaches to modeling and simulation of naval shipboard power systems. The market-based control approach will be explained, and the exact problem formulation will be used for illustration. Mathematical programming will be briefly explained and illustrated, as it is the basis of many different proposed simulation approaches in the field as it exists today. The equivalence of the market-based approach and the underlying optimization problem will be highlighted. Then, different approaches for achieving market equilibrium will be discussed, with a focus on existing issues and barriers currently facing the practice. Future opportunities are then explored, such as methods to improve the robustness of simulation once the microeconomic decisions of the individual components are settled, and the expansion of such solutions to other analogous systems.

## MARKET-BASED CONTROL

In [3], a market-based control approach is presented for the control of power flow within an electric ship. The control method consists of an artificial market in which various actors (a consumer and firms) behave according to microeconomic principles. Each piece of equipment within the engineering plant will behave as a firm, attempting to maximize its profit. The commanding officer (CO) will behave as a consumer, attempting to maximize their utility. By properly designing the market, the control system allocates resources within the system efficiently to meet the current objectives of the CO. However, this control strategy does not inherently depend on the mode of operation. If objectives change, the market will react and experience price shifts, causing resources to be allocated to their new desired purposes. If the structure of the system changes (e.g., due to a change in plant lineup or due to battle damage), the prices will change to reflect the new conditions, and the market will attempt to meet the objectives in the most efficient manner under the new configuration. In this way, a unified control strategy can be applied to achieve various objectives such as fuel efficiency, continuity of service, and survivability.

The shipboard power system can be understood as a market consisting of  $n$  resources, when defining power at a given node as the resource being traded. Each component  $i$  in the system can be thought to consume a bundle of resources represented as  $\mathbf{Q}_i = [Q_1 \ Q_2 \ \dots \ Q_n]^T$ , in which resources produced by the component are represented with negative numbers, representing power generation or energy storage discharging. The physical constraints of each component are represented by two constraints that  $g_i(\mathbf{Q}_i) \leq 0$  and  $h_i(\mathbf{Q}_i) = 0$ . The bundle of resources that could be consumed by the commanding officer to meet mission requirements can be represented by  $\mathbf{Q}_c$ , and this is likewise subject to two constraints such that  $g_c(\mathbf{Q}_c) \leq 0$  and  $h_c(\mathbf{Q}_c) = 0$ . Also, a function  $f_c(\mathbf{Q}_c)$  represents the utility achieved from consuming a given bundle of resources, a value that the commanding officer would like to maximize.

**Problem 1.** The allocation problem can be expressed as finding  $\mathbf{Q}_c$  and  $\mathbf{Q}_i \forall i$  that solve

$$\begin{aligned} & \max_{\mathbf{Q}_c, \mathbf{Q}_i \forall i} && f_c(\mathbf{Q}_c) \\ \text{subject to} & && g_c(\mathbf{Q}_c) \leq 0, g_i(\mathbf{Q}_i) \leq 0 \forall i \\ & && h_c(\mathbf{Q}_c) = 0, h_i(\mathbf{Q}_i) = 0 \forall i \\ & && \mathbf{Q}_c + \sum_{\forall i} \mathbf{Q}_i = 0, \end{aligned}$$

which is just maximizing the utility, given the resources consumed by the commanding officer. Necessary conditions for  $\mathbf{Q}_c$  and  $\mathbf{Q}_i \forall i$  to be a solution to Problem 1 are that the constraint equations and inequalities are satisfied.

It is also possible to represent the shipboard power system using an artificial market-based economy in which the components in the system act as firms and the commanding officer acts as a consumer. In this economy, the price of all the goods can be expressed as  $\mathbf{\Pi} = [\Pi_1 \ \Pi_2 \ \dots \ \Pi_n]^T$ . A firm  $i$ , consuming a bundle of resources  $\mathbf{Q}_i$  will receive a profit given by

$$Profit_i = -\mathbf{\Pi}^T \mathbf{Q}_i$$

Then, the consumption decision is simply finding the bundle of resources  $\mathbf{Q}_i$  that maximizes the profit function, and the consumer will attempt to maximize utility by finding the bundle of resources  $\mathbf{Q}_c$  that maximizes the utility of the system.

Therefore, the consumption decision for firm  $i$  is

$$\begin{aligned} \mathbf{Q}_i = & \operatorname{argmax}_{\widehat{\mathbf{Q}}_i} && -\mathbf{\Pi}^T \widehat{\mathbf{Q}}_i \\ \text{subject to} & && g_i(\widehat{\mathbf{Q}}_i) \leq 0 \\ & && h_i(\widehat{\mathbf{Q}}_i) = 0. \end{aligned}$$

The consumer will attempt to maximize utility by solving the following optimization problem:

$$\begin{aligned} \mathbf{Q}_c = & \operatorname{argmax}_{\widehat{\mathbf{Q}}_c} && f_c(\widehat{\mathbf{Q}}_c) \\ \text{subject to} & && g_c(\widehat{\mathbf{Q}}_c) \leq 0 \\ & && h_c(\widehat{\mathbf{Q}}_c) = 0 \\ & && \mathbf{\Pi} \widehat{\mathbf{Q}}_c = \sum_{\forall i} Profit_i. \end{aligned}$$

**Problem 2.** The market-clearing problem is to find  $\mathbf{\Pi}$  such that

$$\mathbf{Q}_c + \sum_{\forall i} \mathbf{Q}_i = 0.$$

An interesting observation is that the solutions of Problems 1 and 2 are equivalent under many conditions. Thinking about the problem in terms of market-based control (i.e., Problem 2) results in the solution to the desired allocation problem (i.e., Problem 1).

The market-based control technique applies market principles to the control method and explicitly links the economic behavior of the actors in the system with the physical behavior of the equipment in the system. As mission priorities change, prices in the system will adjust automatically to reach the optimal allocation of resources, resulting in an agile system. Simulation studies of a notional electric power system in both ordinary and faulty conditions are performed and demonstrate that the proposed market-based control system results in performance equal to that of an idealized controller, illustrating the property that the market-based control problem is equivalent to the underlying optimal-control problem. The proposed market-based control method can therefore provide a mathematical foundation for distributed control approaches which are agile, resilient, dependable, effective, and efficient.

## MODELING & SIMULATION

The modeling approach, shown in Figure 1, involves the embedding of a mathematical programming problem within the solution for each time step of the simulation. Specifically, the system has dynamic state that is updated from time step to time step. Within the calculations of a given time step, this dynamic state is used to establish a mathematical programming problem that represents the characteristics of the system at that time. By solving the optimization problem, the state of the power system at that time is calculated. This is used to update the dynamic state of the system and to advance time.

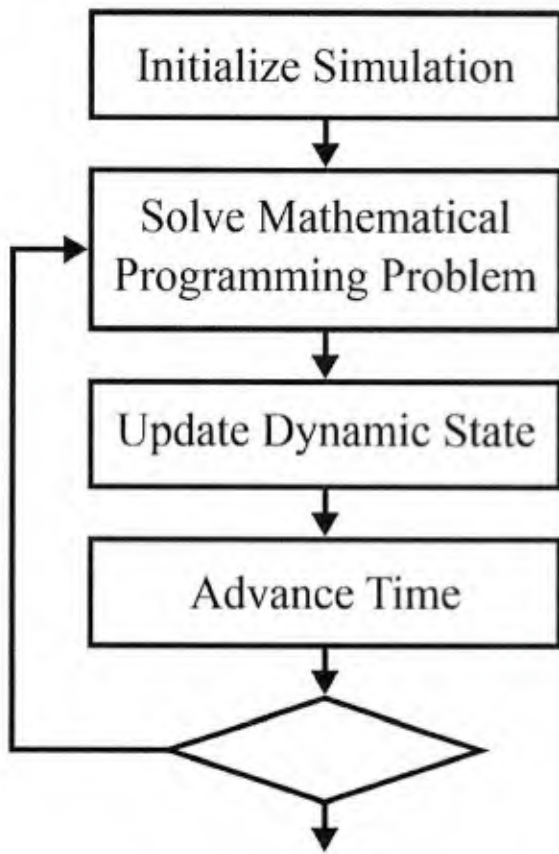


Figure 1. Simulation approach

Mathematical programming is a form of optimization, in which the best element from some set of available alternatives is determined. In its simplest form, the maximum or minimum possible result of a real function is determined. It is possible to model the behavior of a shipboard power system by determining the minimum cost of such a system when operating under nominal mission conditions. This is directly solving the underlying constrained optimization problem, without framing the problem in terms of an artificial market. This formulation is subject to additional constraint equations to ensure the satisfaction of mission objectives, the conservation of energy, etc. Linear programming is a mathematical programming problem in which the requirements are expressed as linear relationships.

The physical behavior of the power system (with an idealized controller representation) in a given time step is approximated using a linear programming problem with the following structure:

$$\begin{aligned}
 & \max_{\mathbf{x}} && \mathbf{c}^T \mathbf{x} \\
 & \text{subject to} && \mathbf{A} \mathbf{x} \leq \mathbf{b} \\
 & && \mathbf{A}_{eq} \mathbf{x} = \mathbf{b}_{eq} \\
 & && \mathbf{x} \geq 0.
 \end{aligned}$$

The vector  $\mathbf{x}$  contains the decision variables of the optimization problem, which represent the various power flows in the system in a given time step. The vector  $\mathbf{c}$  represents the weights of different power flows in the objective function of the controller. The matrix  $\mathbf{A}$  and the vector  $\mathbf{b}$  represent inequality constraints associated with each component (e.g., maximum power ratings). The matrix  $\mathbf{A}_{eq}$  and the vector  $\mathbf{b}_{eq}$  represent the conservation of power at each bus. Each component in the system contributes decision variables (i.e., elements of  $\mathbf{x}$ ), terms in the objective function (i.e., linear terms appearing in  $\mathbf{c}^T \mathbf{x}$ ), and inequality constraints (i.e., rows of  $\mathbf{A} \mathbf{x} \leq \mathbf{b}$ ). This is a programming problem that can result in non-unique solutions, or multiple feasible power-flow configurations that achieve the same maximum value. In the cases where multiple feasible solutions are found, it is more physically realistic if the most balanced solution is dictated by the model. This is meant to show the power-sharing behavior exhibited by generators, converters, and the other electrical components comprising an electrical power system.

The results of the linear programming problem are then subjected to a quadratic programming problem, which differs from a linear programming problem since a quadratic function is the real function being optimized, in order to determine the most balanced solution.

The results from [2] demonstrated a functionality to change the dictated weight of a component in the system during simulation due to a randomized cyber disruption. This same functionality can be used to dictate the weights of components in the system during simulation in order to satisfy mission objectives, thus proving the feasibility of a market-based control approach in which the weights of the system can function as shifting prices in a market, thus directing the power system to achieve market equilibrium. Observing results from both the constrained optimization approach and the market-based control approach when faced with the exact same simulated operating conditions, it is evident that both are solving the same problem, as shown in Figure 2 and Figure 3.

Optimization problems of increasing scale become exponentially more time consuming to solve, as it takes increasingly long computation times in order to converge to an acceptably accurate result. It is a common approach in most math problems to break down complicated problems into smaller ones. Simply put, this can have the benefit of turning one computationally expensive problem into two insignificantly expensive problems. The alternating direction method of multipliers (ADMM) is a mathematical algorithm that solves convex optimization problems by splitting the problem into smaller sub-problems. This is a widely

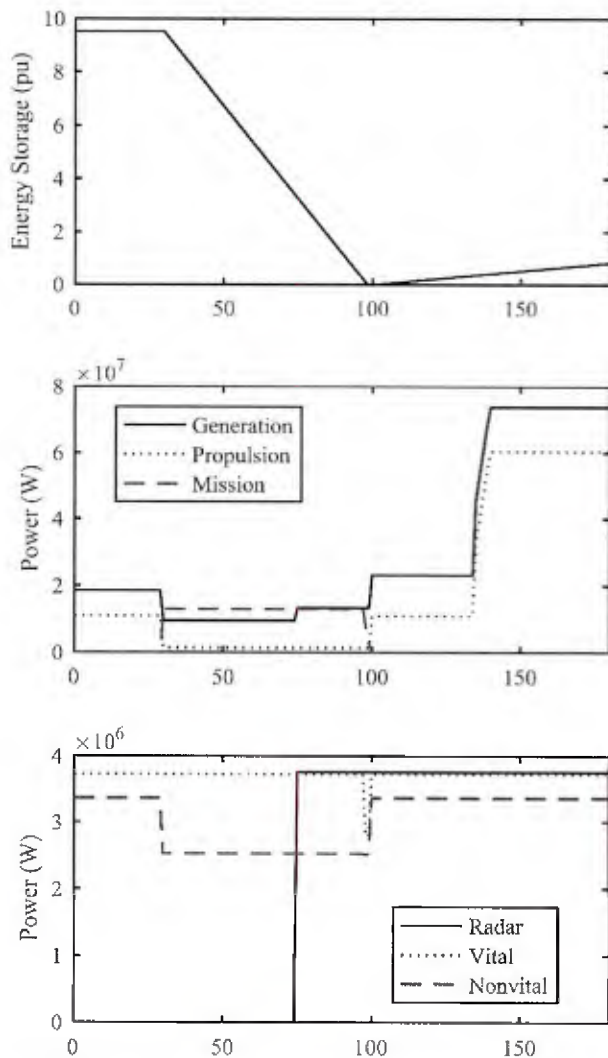


Figure 2. Constrained optimization results

used technique in many areas and is thoroughly discussed in [4]. ADMM converges exceptionally well onto an optimal solution when two assumptions are satisfied. First, the objective function being optimized, and its associated dual function, must both be closed, proper, and convex functions. Second, the unaugmented lagrangian associated with the problem must have a saddle point. When these assumptions are met, the process of ADMM experiences residual, objective, and dual-variable convergence. Residual convergence implies that the iterate results approach feasibility, which means that the final solution will be a feasible state to impose on the system. Objective convergence implies that the objective function of the iterates approach the optimal value for the power system. Dual variable convergence implies that as the iteration count approaches infinity, the solution is a dual-optimal point. ADMM generally is slow to converge to high accuracy. However, most cases result in a moderately accurate result in a few tens of iterations. Considering the application, it is reasonable to surmise that a moderate level of accuracy is preferable when the reward is shorter

computation time. In a combat-environment, a slow control element can become a huge drawback that is obviously preferable to avoid as opposed to a slight decrease in accuracy. Another limitation of ADMM is the sheer amount of knowledge that is required of the system to reach a reasonable result. This is achievable in very strict design environments where as much detail about a system and its components is determined and logged for future reference. The more data involved in the process, the longer it will take to process, and the slower it will be to converge to a reasonable result, thus reinforcing the tradeoff between accuracy and computation time.

## OPPORTUNITIES FOR GROWTH

New solution methods for the optimal control of shipboard power systems should focus on improving the robustness of such systems. This generally refers to the system's ability to remain viable in the face of uncertainty. For naval shipboard power systems, such uncertainty is represented by disruptions, and the possible loss of component capability due to malfunction or direct enemy interference with the power system. The robustness of new methods could be expanded in a few ways. Experimenting with different system layouts could result in limiting the susceptibility of particularly vulnerable components, thus protecting the viability of the system. Improving the decision making around restarting faulted components may be a difficult problem to solve, but this is possible to automate once a solution is determined.

Any exhaustive modeling approach that fully encompasses the knowledge of the system, and thus provides the greatest possible accuracy in the optimization process, must also realize the physical consequences of the communication devices connecting the components of the system together. This introduces the concept of propagation in the system, where a command is issued with known current conditions, only to impose an actual change in the system that will occur in the future, with possibly different conditions than when the "optimal choice" was made.

The optimal path of control for a shipboard power system is intuitively time-dependent. A weapon that must fire at specific time must be supplied enough available power, in enough time to ensure that the weapon can be fired. Referencing opportunity cost again, it is reasonable to surmise that an energy storage component should decide to store energy when future load demands require more power than all available generation can supply. The tricky part is determining the optimal time to perform this charging. It is easy to imagine that there will be many theoretical situations where a shipboard power system simply would not have

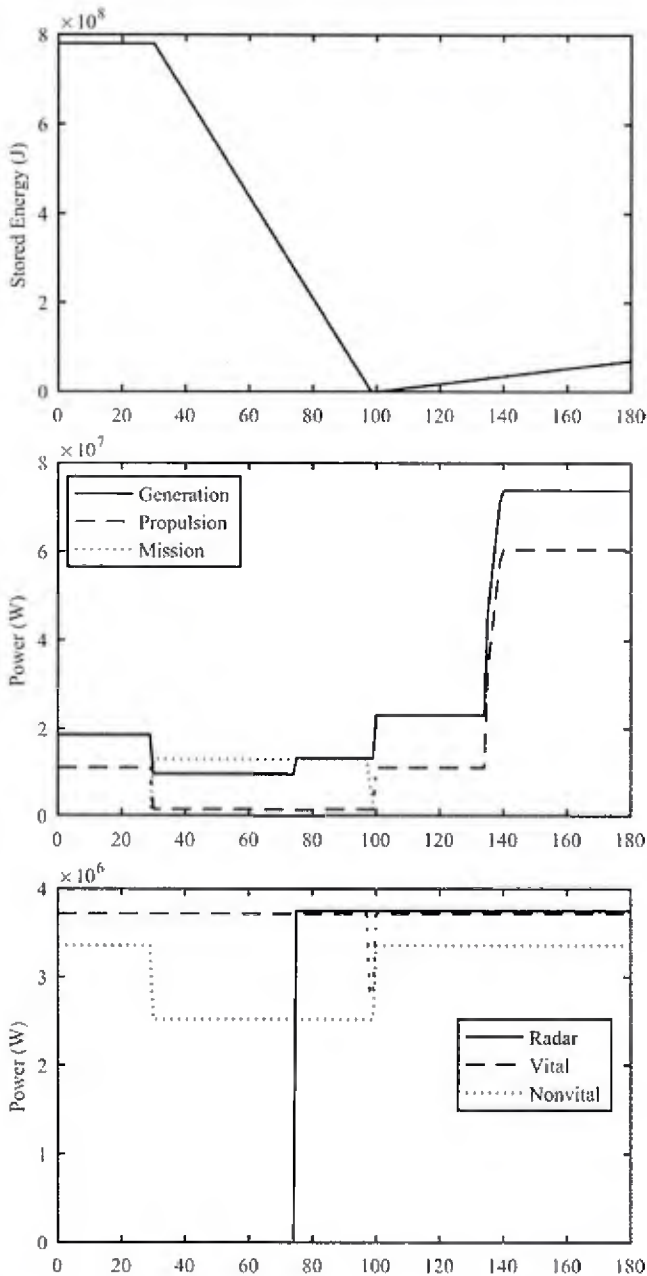


Figure 3. Market-based control model results

the chance, or may be rendered incapable, of storing the necessary amount of energy stored required to meet load demands before it is must attempt to meet them anyway. Approaches that can reasonably evaluate the most effective way to handle such a shortage of energy are particularly of value. Approaches such as these have the capability of making the most out of a bad situation, so even if the required load demands cannot be fully met, the system will still attempt to meet them in the most effective way possible within the limited time constraints.

In general, the actual control elements dictating the component behavior will be localized to that component, only seeking weighting information and data about the

rest of the system from some central computing element. It should be noted that all prior optimization approaches discussed herein have been posed from a centrally controlled perspective, maximizing value from the system as defined from a broad scope of the total specified mission and the system's ideal capability of meeting the objectives of that specified mission. Thus, to alleviate this limitation and more accurately present the behavior of a practical control system, it is proposed to determine the optimal behavior of each type of component in the system utilizing the prior discussed optimization model to account for the current state of the system and the opportunity cost presented by future mission objectives. It is theorized that when each individual component is making the best decisions for its own maximum value, this will result in the system experiencing the maximum possible utility over-all. Centralized measures can still be sought and applied, and the different approaches may have a different optimal approach depending on the current priorities of the mission. For example, a focus on survivability may be more effectively handled from a centrally controlled perspective, whereas a focus on performance may be more effectively handled from a more distributed approach. Regardless, once the distributed allocation problem is solved, the dynamic case of the same problem will need to be solved. As the existing distributed allocation problem is already expensive to solve, the dynamic case cannot possibly be easier to solve. This additionally suggests that the accuracy-computation time tradeoff will need to be carefully balanced in order to maintain the viability of the approach.

Classical simulation approaches are focused on optimizing the state of the model at each individual time step over the course of the simulated vignette. This simply updates the power flows of the system according to achieve maximum utility, subject to static component weights that do not reflect changes in mission objectives, and the current or future states of system components. This is a fundamental limitation, as discriminating opportunity costs is practically impossible to do with an unknown future. Therefore, a more effective market-based approach is possible when considering the expected possible future. This should also positively affect the robustness of the system. In order to address this limitation, the system can be expressed in similar mathematical structures as that of a multi-period model commonly used in economic studies [5]. Multi-period models are able to address intertemporal preferences desired from the model. Intuitively, this is a powerful tool that can address the opportunity cost problem. A system of matrix equations can be defined to represent the electrical characteristics, physical constraints, state variable dynamics, and decision variables of the system. The final system of equations will contain a set of every

constraint the system will face for every second the simulation is to be run.

Prior discussed optimization techniques can be applied to the new constraint equations. Whereas in classical approaches, these optimizations are performed at each time step as the power system progresses through the simulated mission, the optimization process can be performed once on the multi-period model. This will yield the desired result of the prior simulation process, with an added benefit of making decisions that consider the opportunity cost over the course of the entire mission. This also vastly improves simulation run time, as the model is now executing the optimization process one time, and not once for every time-step. The value of this is two-fold, as freeing up as much computation as possible will allow for even more accuracy to be attained through the previously define trade-off with computation time.

Since a reasonable set of solutions are being derived for the operation of electric power systems, it is desirable to evaluate these solutions for their possible applications in other physical domains of the naval shipboard environment. The nature of electrical current makes all forms of electrical transfer of energy prone to the loss of energy in the form of heat. The amount of heat output is equivalent to the power input if there are no other energy interactions going on. So, it can be seen as anytime a component in the electrical market transfers resources, the associated components generate heat. Excess heat can wreak havoc on the behavior of any electrical system, and any substantially large electrical system can generate excess heat. Thermal management of a shipboard electrical power system is usually handled by an accompanying cooling system, and effective thermal management is crucial to improving reliability and preventing premature component failure.

A heatsink's thermal mass can be considered as another type of energy storage, storing heat instead of charge. A heatsink has a thermal resistance analogous to electrical resistance, giving a metric describing how fast the stored heat can be dissipated from the heatsink. Thus, every electrical component in the system is also functioning as an RC circuit with an associated time constant resulting from the capacitive nature of the heatsink and the resistive nature of heat dissipation. Thus, any thermal management system can be thought of properly allocating the heat (the newly defined resource of the thermal management market), among the electrical heatsinks (the newly defined market firms) to meet the objective of keeping each heatsink below a threshold that would significantly hinder, and possibly shut down, the electrical component.

The electrical power system in [2] is modeled as a layered simulation consisting of two layers. One is a spatial layer defining rough geometric profiles and relative locations of each component in the naval shipboard power system. The second is the electrical layer, which defines the electrical metrics associated with the components in the power system, and the processes dictating the conditions of the electrical power system. It is proposed to add another layer, an auxiliary layer, that represents the thermal management system's dynamics in the model. Whereas it is simple to connect the impacts of the spatial layer and component destruction or damage, to the associated components in the electrical or auxiliary layer, it seems much more difficult to properly connect the impacts of the electrical layer to the auxiliary layer, and vice versa. If the control of both systems is desired to operate in conjunction, with the same control elements, these relationships must be properly accounted for. The different timing dynamics inherent in the two physically different layers must be separated yet connected, in order to evaluate optimal control behavior of the naval shipboard power system. The thermal management system is limited to dictating a new configuration in the span of seconds, while the electrical system can impose a new system configuration as quickly as the ramping limits of the individual components, if there are any, will allow. This means that the simulation will move forward at the rate of the practically instant electrical layer, but must also evaluate and update the thermal management system according to the feasible processing speed of the auxiliary system, hence the need for a level separation between the two processes. It is a waste of computation time to evaluate the states of the thermal management system for time-steps that cannot feasibly impact the decision of the thermal management system.

## CONCLUSION

The optimal control of electrical storage elements within a naval shipboard power system is explored using a philosophy of market-based control. Existing simulation and modeling efforts are explained, with a description of possible mathematical tools that can be used to improve the accuracy and convergence of the existing model. New priorities for future solutions are proposed as increasing the robustness of the system, as well as realizing the limitations that necessary communication systems present to the power system. The time-dependence of the optimal path of control is explained as being a consequence of the energy storage elements in the system, and the effects this has on the optimization process have been illustrated. A multi-period market approach is explained to formally provide a realization of opportunity cost as it is faced by the decision makers in the system. Two new challenges are identified as posing the control problem as a distributed allocation

problem, and then expanding this problem to the dynamically changing case. Finally, the possibility of controlling the shipboard systems across multiple domains is provided, with a focus on the analogous nature between electrical energy storage components, and the heat-energy storage dynamics that are exhibited by all significantly large components in the power system.

## REFERENCES

- [1] A. M. Cramer, X. Liu, Y. Zhang, J. D. Stevens and E. L. Zivi, "Early-Stage Shipboard Power System simulation of operational vignettes for dependability assessment," in *2015 IEEE Electric Ship Technologies Symp.*, Alexandria, VA, 2015.
- [2] A. W. Flath, III, A. M. Cramer and X. Liu, "Control System Modeling in Early-Stage Simulation for Cyber Vulnerability Assessment," in *2017 IEEE Electric Ship Technologies Symposium*, Arlington, VA, 2017.
- [3] Y. Zhang and A. M. Cramer, "Market-Based Control of Electric Ship Power Systems," in *2017 IEEE Electric Ship Technologies Symposium*, Arlington, VA, 2017.
- [4] S. Boyd, N. Parikh, E. Chu, B. Peleato and J. Eckstein, "Distributed Optimization and Statistical," *Foundations and Trends in Machine Learning*, vol. 3, no. 1, pp. 1-122, 2010.
- [5] E. Oh, D. F. Opila, J. Stevens, E. Zivi and A. M. Cramer, "Early stage design evaluation of shipboard power systems using multi-period power flow," in *2017 IEEE Electric Ship Technologies Symposium*, Arlington, VA, 2017.

## ACKNOWLEDGEMENTS

This work was supported by the Office of Naval Research (ONR) through the ONR Young Investigator Program N00014-15-1-2475

## BIOGRAPHIES

Allen W. Flath, III  
University of Kentucky, Lexington, KY, USA

Allen W. Flath, III, received the B.S. degree (magna cum laude) in electrical engineering from the University of Kentucky, Lexington, KY, USA, in 2017. He is currently pursuing the M.S. degree in electrical engineering from the same institution with a focus on power electronics, while working as a research assistant.

Mr. Flath received the Space Grant Graduate Fellowship from NASA Kentucky in 2018 and is currently working on a research effort to improve the design efforts of small spacecraft power systems, in addition to his work on the simulation and modeling of shipboard electric power systems.

Aaron M. Cramer  
University of Kentucky, Lexington, KY, USA

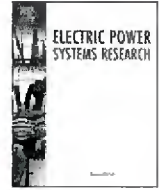
Aaron M. Cramer received the B.S. degree (summa cum laude) in electrical engineering from the University of Kentucky, Lexington, KY, USA, in 2003, and the Ph.D. degree from Purdue University, West Lafayette, IN, USA, in 2007.

From 2007 to 2010, he was a Senior Engineer with P C Krause and Associates, West Lafayette. In 2010, he joined the University of Kentucky, where he is currently an Associate Professor. His research interests include modeling, simulation, and control of power and energy systems. Dr. Cramer received the ONR Young Investigator Program Award in 2015.

YuQi Zhang  
University of Kentucky, Lexington, KY, USA

YuQi Zhang received the B.S. degree in electrical engineering from Harbin Institute of Technology, Harbin, China, in 2005, and the M.S.E.E. degree from the University of Kentucky, Lexington, KY, USA, in 2014, where she is currently working toward the Ph.D. degree in electrical engineering.

Her research interests include electric machine modeling and simulation, power electronics, and power systems.



## Reactive power control methods for photovoltaic inverters to mitigate short-term voltage magnitude fluctuations



Xiao Liu, Aaron M. Cramer\*, Yuan Liao

University of Kentucky, Lexington, KY 40506, USA

### ARTICLE INFO

#### Article history:

Received 6 March 2015

Received in revised form 7 May 2015

Accepted 4 June 2015

Available online 24 June 2015

#### Keywords:

Distributed power generation

Photovoltaic systems

Power quality

Voltage control

Reactive power control

Three-phase inverter

### ABSTRACT

Variations in the output power of intermittent renewable sources can cause significant fluctuations of distribution system voltage magnitudes. Reactive power control methods that employ the reactive power capability of photovoltaic three-phase inverters to mitigate these fluctuations are proposed. These control methods cause the three-phase inverters to substitute reactive output power for real output power when fluctuations in the solar power are experienced, allowing the fluctuations to be controlled. Performance metrics for assessing the ability of these controllers to perform this mitigation are defined. The controllers are examined using the IEEE 123-bus feeder distribution system, and it is found that the controllers can effectively mitigate voltage magnitude fluctuations and that the appropriate choice of controller depends on the performance metrics of interest.

© 2015 Elsevier B.V. All rights reserved.

### 1. Introduction

There are significant technical challenges at every level associated with the integration of renewable energy sources. One significant challenge is managing variations in distribution system voltage magnitudes caused by fluctuations in the output power of intermittent sources such as photovoltaic (PV) generation. Distributed generation can cause the voltage magnitudes in distribution systems to rise. However, the output power of these sources can fluctuate rapidly. For example, PV sources use maximum power point tracking (MPPT) to make most effective use of the incident sunlight. Consequently, the output power of such sources can vary rapidly in response to passing clouds. Irradiance changes of as much as 60%/s have been observed during such cloud transients [1,2]. These transients can have significant impacts on the voltage magnitudes in distribution systems, and these impacts can be expected to increase with increasing renewable penetration. Such transients also occur too rapidly for traditional distribution system regulation equipment, such as tap changing transformers and switched capacitor banks, to respond to them in an appropriate manner.

Herein, various reactive power control methods are studied in which the PV inverter responds to variations in its real power output by varying its reactive power output. The control methods

involve the inverter substituting reactive power production for real power production when solar power changes. It is well understood that the reactive power capability of inverter-based distributed generation can be used to improve distribution system operation (e.g., [3–7]). In [8–11], the integration of MPPT with real and reactive power control of the PV inverter is discussed. In [12,13], the control of reactive power is optimized to reduce the system losses. Reactive power can be dispatched as part of the volt/var control strategy of the distribution system [14–20]. In [21], both real and reactive power are controlled to keep the voltage magnitude in the acceptable range. In [22], a local linear controller is used to inject balanced three-phase reactive power into the grid.

In this paper, several reactive power control methods of the form proposed in [22] are proposed. In these methods, the reactive power output is a linear function of the instantaneous solar power. Each method is defined by a scope, an objective, and a domain, which describe the manner of selecting the control parameters used by the reactive power controller. Unlike methods in other studies [23–28], the reactive power controller does not require high-bandwidth communication to improve voltage quality. These methods only require local information in order to function. To quantify and compare the performance of the different control methods, voltage magnitude violation and variation performance metrics are defined. Finally, the performance of these control methods is demonstrated with the IEEE 123-bus feeder distribution system [29] with three different cases. The primary developments of this paper with respect to [22] are (1) the consideration of unbalanced reactive power injection, (2) the demonstration of the

\* Corresponding author. Tel.: +1 8592579113.

E-mail address: [aaron.cramer@uky.edu](mailto:aaron.cramer@uky.edu) (A.M. Cramer).

proposed methods with a more complex system (123 buses vs. 5 buses), and (3) the demonstration of the proposed reactive power control methods with multiple PV sources.

The contributions of this work are (1) the proposal of various reactive power control methods for mitigation of short-term voltage magnitude fluctuations, (2) the definition of performance metrics to assess the performance of the reactive power control methods, and (3) the demonstration of the reactive power control methods over several cases on a well-defined test system. The remainder of this paper is organized as follows. The reactive power control methods are described in Section 2. In Section 3, performance metrics are defined for assessment of the reactive power controller performance. The controllers are demonstrated and their performance is assessed in the presence of single and multiple PV sources in Section 4. Finally, conclusions are presented in Section 5.

## 2. Reactive power control methods

At a given bus, various reactive power control methods are proposed to allow a three-phase PV inverter to adjust its three-phase reactive power injections in response to fluctuations in solar power. These controllers can be expressed in the form

$$\mathbf{Q} = \mathbf{Q}^* + \beta \Delta P_s, \quad (1)$$

where

$$\Delta P_s = P_s - P_s^*, \quad (2)$$

$P_s$  is the solar power,  $P_s^*$  is the reference solar power,  $\mathbf{Q} \in \mathbb{R}^3$  is a vector of the three-phase reactive power injections of the PV inverter,  $\mathbf{Q}^* \in \mathbb{R}^3$  is a vector of the three-phase reference reactive power injections of the PV inverter, and  $\beta \in \mathbb{R}^3$  is a vector containing control parameters, which are called the substitution rates, that are specific to the given reactive power control method. The objective of this controller is to mitigate against system voltage magnitude variations caused by fluctuating PV real power injection. Alternative methods of choosing the control parameters contained in  $\beta$  are studied herein.

All else being equal, the magnitudes of the system voltages can be expressed as a function of the three-phase PV real and reactive power injections at a given bus:

$$\mathbf{V} = \mathbf{f}(\mathbf{P}, \mathbf{Q}), \quad (3)$$

where  $\mathbf{V} \in \mathbb{R}^m$  is a vector containing bus voltage magnitudes,  $m$  is equal to the number of system buses, and  $\mathbf{P} \in \mathbb{R}^3$  is a vector containing the three-phase real power injections of the PV inverter. Herein, each phase of a polyphase bus is treated as a separate bus. If Taylor series expansion is performed about the operating point  $(\mathbf{P}^*, \mathbf{Q}^*)$ , (3) can be approximated as

$$\Delta \mathbf{V} \approx \alpha_P \Delta \mathbf{P} + \alpha_Q \Delta \mathbf{Q}, \quad (4)$$

where

$$\Delta \mathbf{V} = \mathbf{V} - \mathbf{V}^* = \mathbf{f}(\mathbf{P}, \mathbf{Q}) - \mathbf{f}(\mathbf{P}^*, \mathbf{Q}^*) \quad (5)$$

$$\Delta \mathbf{P} = \mathbf{P} - \mathbf{P}^* \quad (6)$$

$$\Delta \mathbf{Q} = \mathbf{Q} - \mathbf{Q}^* = \beta \Delta P_s \quad (7)$$

$$\alpha_P = \left. \frac{\partial \mathbf{f}}{\partial \mathbf{P}} \right|_{(\mathbf{P}, \mathbf{Q})=(\mathbf{P}^*, \mathbf{Q}^*)} \quad (8)$$

$$\alpha_Q = \left. \frac{\partial \mathbf{f}}{\partial \mathbf{Q}} \right|_{(\mathbf{P}, \mathbf{Q})=(\mathbf{P}^*, \mathbf{Q}^*)} \quad (9)$$

The partial derivative terms  $\alpha_P$  and  $\alpha_Q$  are called sensitivity factors which can be estimated using small perturbations [22] or calculated by the power flow algorithm at the operating point. The

real power injections of the PV inverter are assumed to be balanced. Furthermore, it is assumed that a sufficiently fast MPPT algorithm is applied that the three-phase real power injections can be expressed as

$$\mathbf{P} = \frac{1}{3} [1 \ 1 \ 1]^T P_s, \quad (10)$$

Similarly, the three-phase reference real power injections are expressed as

$$\mathbf{P}^* = \frac{1}{3} [1 \ 1 \ 1]^T P_s^*, \quad (11)$$

and substitution of (10) and (11) into (6) yields the following expression for the three-phase incremental real power injections:

$$\Delta \mathbf{P} = \frac{1}{3} [1 \ 1 \ 1]^T \Delta P_s. \quad (12)$$

By substitution of (7) and (12) into (4), the incremental magnitudes of the system voltages can be approximated as

$$\Delta \mathbf{V} \approx \left( \frac{1}{3} \alpha_P [1 \ 1 \ 1]^T + \alpha_Q \beta \right) \Delta P_s. \quad (13)$$

It can be seen that choice reactive power control method, i.e., choice of  $\beta$ , can influence the response of the system voltage magnitudes to solar power fluctuations. Each reactive power control method discussed herein is defined by selecting a scope, an objective, and a domain. The possible scopes, objectives, and domains are described below.

### 2.1. Local vs. global scope

The scope of a method indicates the buses at which the voltage magnitudes are considered by the method. Each of the methods can be applied with respect to either the local bus voltage (i.e., the bus at which the PV inverter is located) or across all of the bus voltages in the system. Without loss of generality, it is assumed that the PV inverter is located at buses  $n$ ,  $n+1$ , and  $n+2$ , the three phases of the three-phase bus. If the local scope is used, only the voltage magnitudes at these three buses are considered. A selector matrix  $\mathbf{S} \in \mathbb{R}^{3 \times m}$  is constructed such that all elements are zero except for the  $(1, n)$ ,  $(2, n+1)$ , and  $(3, n+2)$  elements, which are unity. A local bus voltage magnitude vector is then constructed as

$$\mathbf{V}_l = \mathbf{S} \mathbf{V}. \quad (14)$$

Similarly, local sensitivity factors can be calculated:

$$\alpha_{Pl} = \mathbf{S} \alpha_P \quad (15)$$

$$\alpha_{Ql} = \mathbf{S} \alpha_Q. \quad (16)$$

A method with local scope uses the local bus voltage magnitude vector and the local sensitivity factors, while a method with global scope uses the global bus voltage magnitude vector and the global sensitivity factors.

### 2.2. Sensitivity minimization vs. violation optimization objective

The objective of a method indicates what criterion is used to select  $\beta$ . The sensitivity minimization objective is to minimize the response of the considered bus voltage magnitudes to solar power perturbations. From (13), this can be accomplished by selecting

$$\beta = \underset{\beta}{\operatorname{argmin}} \left\| \frac{1}{3} \alpha_P [1 \ 1 \ 1]^T + \alpha_Q \beta \right\|. \quad (17)$$

The violation optimization objective is to maximize the magnitude of solar power perturbation for which none of the considered

bus voltage magnitudes leaves its acceptable range. The considered bus voltage magnitudes are required to fall within a range:

$$\mathbf{V}_- \leq \mathbf{V} \leq \mathbf{V}_+, \quad (18)$$

where  $\mathbf{V}_-$  is a vector containing the voltage magnitude lower limits of the considered buses and  $\mathbf{V}_+$  is a vector containing the voltage magnitude upper limits of the considered buses. It is assumed that this requirement is satisfied at the operating point  $(\mathbf{P}^*, \mathbf{Q}^*)$ . The voltage magnitude constraint corresponds to a requirement on the incremental bus voltage magnitudes:

$$\Delta \mathbf{V}_- \leq \Delta \mathbf{V} \leq \Delta \mathbf{V}_+, \quad (19)$$

where

$$\Delta \mathbf{V}_- = \mathbf{V}_- - \mathbf{V}^* \quad (20)$$

$$\Delta \mathbf{V}_+ = \mathbf{V}_+ - \mathbf{V}^*. \quad (21)$$

The voltage optimization objective can be accomplished by substituting (13) into (19):

$$\begin{aligned} \beta &= \operatorname{argmax}_{\beta} |\Delta P_s| \\ \text{such that } \Delta \mathbf{V}_- &\leq \left( \frac{1}{3} \alpha_P [\mathbf{1} \quad \mathbf{1} \quad \mathbf{1}]^T + \alpha_Q \beta \right) \Delta P_s \leq \Delta \mathbf{V}_+. \end{aligned} \quad (22)$$

### 2.3. Balanced vs. unbalanced domain

The domain of a method indicates what values of  $\beta$  are considered in meeting the objective of the method. The balanced domain allows for injection of equal amounts of reactive power into each of the PV inverter's phases. In this case, the vector of substitution rates can be expressed as

$$\beta = \beta [\mathbf{1} \quad \mathbf{1} \quad \mathbf{1}]^T. \quad (23)$$

The unbalanced domain allows for unbalanced injection of reactive power, so the vector of substitution rates to be arbitrary. It should be noted that three-phase, four-wire inverters are assumed throughout. This permits either balanced or unbalanced reactive power injection despite voltage imbalances.

### 2.4. Method integration

Each of the methods below is described in terms of global vectors (e.g.,  $\mathbf{V}$ ) and sensitivity factors ( $\alpha_P$  and  $\alpha_Q$ ), which is appropriate for methods with a global scope. If a method has a local scope, the selector matrix  $\mathbf{S}$  is used, and all global vectors and sensitivity factors are replaced with local vectors (e.g.,  $\mathbf{V}_i$ ) and local sensitivity factors ( $\alpha_{P_i}$  and  $\alpha_{Q_i}$ ).

For a method with the sensitivity minimization objective and the balanced domain, substitution of (23) into (17) yields the following substitution rate:

$$\beta = \operatorname{argmin}_{\beta} \left\| \frac{1}{3} \alpha_P [\mathbf{1} \quad \mathbf{1} \quad \mathbf{1}]^T + \beta \alpha_Q [\mathbf{1} \quad \mathbf{1} \quad \mathbf{1}]^T \right\| \quad (24)$$

$$\beta = -\frac{1}{3} \left( \alpha_Q [\mathbf{1} \quad \mathbf{1} \quad \mathbf{1}]^T \right)^\dagger \alpha_P [\mathbf{1} \quad \mathbf{1} \quad \mathbf{1}]^T, \quad (25)$$

where  $\dagger$  denotes the Moore–Penrose pseudoinverse.

For a method with the sensitivity minimization objective and the unbalanced domain, the vector of substitution rates is determined from (17):

$$\beta = -\frac{1}{3} \alpha_Q^\dagger \alpha_P [\mathbf{1} \quad \mathbf{1} \quad \mathbf{1}]^T. \quad (26)$$

For a method with the violation optimization objective and the balanced domain, substitution of (23) into (22) yields the following problem:

$$\begin{aligned} \beta &= \operatorname{argmax}_{\beta} |\Delta P_s| \\ \text{such that } \Delta \mathbf{V}_- &\leq \left( \frac{1}{3} \alpha_P [\mathbf{1} \quad \mathbf{1} \quad \mathbf{1}]^T + \beta \alpha_Q [\mathbf{1} \quad \mathbf{1} \quad \mathbf{1}]^T \right) \Delta P_s \leq \Delta \mathbf{V}_+. \end{aligned} \quad (27)$$

This problem can be solved using a line search method.

For a method with the violation optimization objective and the unbalanced domain, (22) can be solved using grid-based search techniques.

The methods herein are denoted using three letters. The first letter indicates the scope: 'L' is local, and 'G' is global. The second letter indicates the objective: 'S' is sensitivity minimization, and 'V' is violation optimization. The third letter indicates the domain: 'B' is balanced, and 'U' is unbalanced. For example, the global, sensitivity minimization, balanced method is denoted by GSB. As a benchmark, the method 0 indicates that no reactive power control is performed, i.e.,  $\beta = \mathbf{0}$ .

For the LSU method, there is generally a unique solution to

$$\frac{1}{3} \alpha_P [\mathbf{1} \quad \mathbf{1} \quad \mathbf{1}]^T + \alpha_Q \beta = \mathbf{0}. \quad (28)$$

If (4) remains a good approximation of the bus voltage magnitudes under changing solar power, the local bus voltage magnitudes will not change for any solar power variation. This means that the same value of  $\beta$  would result in the allowable  $\Delta P_s$  being infinite in the LVU method. Therefore, the solutions to the LSU and LVU methods are identical, and the performance of both of these methods is identical as well.

## 3. Performance metrics

To study the performance of the PV reactive power control methods on distribution system voltages, several performance metrics are employed. The performance metrics are calculated for buses in the set  $M = \{1, 2, \dots, m\}$  over the time interval  $[0, T]$ . All of the performance metrics are calculated with voltage magnitudes converted to a 120-V scale. To aid in defining the performance metrics, some functions are defined below. The absolute voltage magnitude violation of bus  $i$  at time  $t$  is

$$V_{vi}(t) = \max\{V_i(t) - V_{+i}, V_{-i} - V_i(t), 0\}, \quad (29)$$

where  $V_i(t)$  is the voltage magnitude of bus  $i$  at time  $t$  and  $V_{+i}$  and  $V_{-i}$  are the upper and lower voltage magnitude limits of bus  $i$ , respectively. The violation indicator function for bus  $i$ , which is 1 if bus  $i$  is experiencing a voltage magnitude violation at time  $t$  and 0 otherwise, is defined as

$$q_i(t) = \begin{cases} 0 & \text{if } V_{vi}(t) = 0 \\ 1 & \text{if } V_{vi}(t) > 0 \end{cases}. \quad (30)$$

The global violation indicator function can be expressed as

$$q(t) = 1 - \prod_{i=1}^m (1 - q_i(t)), \quad (31)$$

is 1 if any bus is experiencing a voltage magnitude violation at time  $t$ , and is 0 otherwise.

The performance metrics can be divided into two classes: those related to system voltage magnitude violations, violation metrics, and those related to system voltage magnitude deviations from the reference system voltage magnitudes, sensitivity metrics.

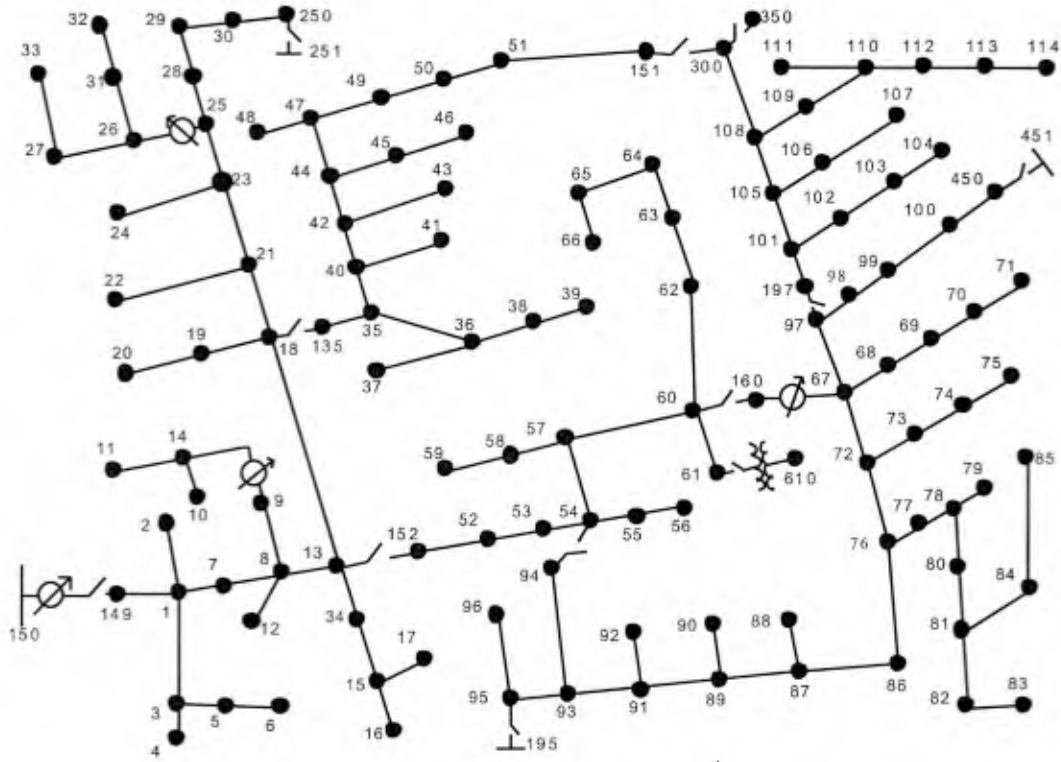


Fig. 1. IEEE 123 node test feeder [29].

The following global violation metrics are employed in this study. The number of violated buses is the number of buses that experience a voltage magnitude violation, i.e.,

$$|\{i \in M : \exists t(i) \in [0, T] \text{ such that } q_i(t) = 1\}|. \tag{32}$$

The violation time is the time during which at least one bus experiences a voltage magnitude violation, i.e.,

$$\int_0^T q(t) dt. \tag{33}$$

The mean violation time indicates the mean over the buses of the time during which each bus experiences a voltage magnitude violation, i.e.,

$$\frac{1}{m} \sum_{i=1}^m \int_0^T q_i(t) dt. \tag{34}$$

The mean violation refers to the mean over the buses of the mean absolute voltage magnitude violation experienced by each bus, i.e.,

$$\frac{1}{m} \sum_{i=1}^m \frac{1}{T} \int_0^T V_{vi}(t) dt. \tag{35}$$

The maximum violation indicates the maximum absolute voltage magnitude violation experienced at any time by any bus, i.e.,

$$\max_{i \in \{1, 2, \dots, m\}} \max_{t \in [0, T]} V_{vi}(t). \tag{36}$$

Two global sensitivity metrics are defined below for use in this study. The mean variation is given by

$$\frac{1}{T} \int_0^T \sqrt{\frac{1}{m} \sum_{i=1}^m (V_i(t) - V_i^*)^2} dt, \tag{37}$$

where  $V_i^*$  is the reference voltage magnitude of bus  $i$ . The maximum variation is given by

$$\max_{t \in [0, T]} \sqrt{\frac{1}{m} \sum_{i=1}^m (V_i(t) - V_i^*)^2}. \tag{38}$$

Each of the performance metrics described above are global metrics, which means that they consider each of the bus voltage magnitudes in the system. It is also possible to consider the performance at only a given local bus. Two local sensitivity metrics are defined for analyzing the local performance. The local mean variation is given by

$$\frac{1}{T} \int_0^T \sqrt{\frac{1}{3} \sum_{i=1}^3 (V_{li}(t) - V_{li}^*)^2} dt. \tag{39}$$

where  $V_{li}(t)$  is the voltage magnitude of local bus  $i$  at time  $t$  and  $V_{li}^*$  is the reference voltage magnitude of local bus  $i$ . The local maximum variation is given by

$$\max_{t \in [0, T]} \sqrt{\frac{1}{3} \sum_{i=1}^3 (V_{li}(t) - V_{li}^*)^2}. \tag{40}$$

The local mean and maximum variations are local analogs to the mean and maximum variation global sensitivity metrics.

#### 4. Simulation results

In order to investigate the performance of the various reactive power control methods, three cases based on the IEEE 123-bus feeder distribution system [29] are studied. The structure of IEEE 123-bus feeder distribution system is shown in Fig. 1 [29]. The system nominal voltage is 4.16kV, and it contains four voltage

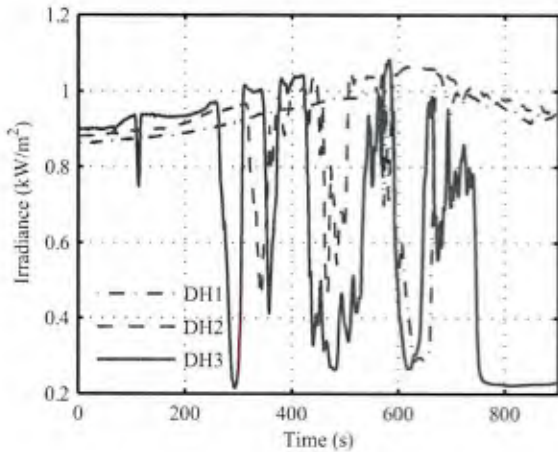


Fig. 2. Sample irradiance data from studied interval.

regulators, four capacitor banks, and unbalanced loads [29]. It is also known to have voltage drop problems that must be carefully managed [29]. A number of buses associated with open and closed switchgear are excluded from the global bus voltage magnitude vector  $\mathbf{V}$  because the buses are unloaded or have identical characteristics to adjacent buses. These buses are 135, 149, 152, 160, 197, 251, 350, 451, and 610. The three cases involve various levels of PV penetration located at various locations within the system. In the first case, a large PV source is concentrated at a single three-phase bus. In the second case, ten smaller PV sources are distributed in a fairly uniform manner throughout the system. In the final case, the ten smaller PV sources are more concentrated.

The system is simulated for 15 min using PV output power derived from the global horizontal irradiance data collected at the National Renewable Energy Laboratory Solar Measurement Grid in Oahu, Hawaii. This measurement grid collects data at various nearby locations at 1-s intervals. The various sites at which data are collected are labeled DH1 through DH10, each corresponding to a different irradiance sensor placed in a different position. For the studies described herein, data from March 1, 2011 between 11:00 am and 11:15 am are used. The irradiance from several of the sites is shown in Fig. 2. It can be seen that the irradiance at these sites exhibits varying degrees of correlation on different time scales, and this correlation is expected in distribution systems in which the PV sources are near each other. It can also be seen that the irradiance can exhibit very rapid fluctuations due to cloud transients. This is consistent with previous observations of nearly 60%/s changes in irradiance [2]. Because MPPT algorithms are capable of converging to the correct maximum power point very quickly [30], it is appropriate to consider the effect of such rapid transients on distribution system voltages.

The parameters of the PV sources for the three cases are listed in Table 1. The solar power of a PV source is modeled by

$$P_s = \frac{S}{1000 \text{ W/m}^2} P_r \tag{41}$$

where  $S$  is the irradiance and  $P_r$  is the rated solar power of the PV source when the irradiance is equal to  $1000 \text{ W/m}^2$ . The rated solar power for each PV source is listed in Table 1. During the 15-min interval, the reference solar power  $P_r^*$  is taken to be the average solar power. This means that the reference solar power is assumed to be correct over the interval and that any deviations  $\Delta P_s$  are due solely to rapid solar fluctuations during the interval. By (11), the reference real power injection in each phase is one third of the reference PV solar power. While injecting reactive power on slower time scales has been proven to improve distribution system

Table 1  
Photovoltaic source parameters.

Case	Source number	Bus location	Rated solar power	Irradiance data source
1	1	100	600 kW	DH3
	1	1	200 kW	DH1
	2	21	200 kW	DH2
	3	35	200 kW	DH3
	4	49	200 kW	DH4
2	5	55	200 kW	DH5
	6	63	200 kW	DH6
	7	76	200 kW	DH7
	8	82	200 kW	DH8
	9	93	200 kW	DH9
	10	101	200 kW	DH10
3	1	1	200 kW	DH1
	2	7	200 kW	DH2
	3	8	200 kW	DH3
	4	13	200 kW	DH4
	5	18	200 kW	DH5
	6	52	200 kW	DH6
	7	53	200 kW	DH7
	8	54	200 kW	DH8
	9	55	200 kW	DH9
	10	56	200 kW	DH10

performance [14–20], the reference reactive power  $Q^*$  is assumed to be zero for these studies.

The upper and lower voltage limits are assumed to be 126 V and 118 V, respectively, on a 120-V scale. Because PV sources are added in the distribution system, the tap settings of the voltage regulators must be adjusted to ensure that the system voltages are acceptable at the reference operating point. There are four voltage regulators in the distribution system. One of the regulators, at bus 150, regulates each of the three phases in a ganged manner. The other regulators control each phase independently. The regulators at buses 9, 25, and 160, affect one, two, and three phases, respectively. They are capable of 0.625% steps. The tap settings for the different regulators and the different cases are listed in Table 2. The reference voltages are calculated by using a modified version of the ladder iterative technique [31] and by assuming that the injected real and reactive power of PV sources are  $P^*$  and  $Q^*$ , respectively. The sensitivity factors at the operating point are also calculated by using a modified version of the ladder iterative technique. When calculating the sensitivity factors for one phase of a PV source, the other two phases and the remaining PV sources are treated as constant (negative) PQ loads at the operating point. It is noted that the sensitivity factors and  $\mathbf{V}^*$  are only calculated once for each of the 15 min simulations.

For each of the three cases, the system is simulated using the data given in Table 1. The solar power is calculated according to (41). The real and reactive power injections of each PV source are calculated using (10) and (1), respectively. The substitution rates  $\beta$  are calculated using each of the methods described above. The voltages at each time step are determined using a modified version of the ladder iterative technique [31]. Each of the global performance metrics defined above are calculated for each method. For Case 1, the local sensitivity performance metrics defined above are also calculated. The results from the cases are described in detail below.

Table 2  
Voltage regulator tap settings.

Bus	150	9		25		160		
	Phase	a,b,c	a	a	c	a	b	c
Case 1	7	--2	0	--1		8	2	3
Case 2	6	--3	0	--2		7	0	4
Case 3	5	0	1	0		8	3	5

**Table 3**  
Simulation results for Case 1.

Method	Number of violated buses	Violation time (s)	Mean violation time (s)	Mean violation (mV)	Maximum violation (mV)	Mean variation (mV)	Maximum variation (mV)	Mean local variation (mV)	Maximum local variation (mV)
0	5	522	8.98	1.46	448	201	330	343	562
LSB	1	520	2.16	$7.15 \times 10^{-2}$	49.0	25.7	43.8	25.7	42.5
LSU	1	519	2.15	$4.35 \times 10^{-2}$	29.0	20.9	36.1	3.36	7.53
LVB	1	519	2.15	$6.23 \times 10^{-2}$	42.4	25.2	42.3	26.1	41.9
LVS	1	519	2.15	$4.35 \times 10^{-2}$	29.0	20.9	36.1	3.36	7.53
GSB	1	519	2.15	$5.48 \times 10^{-2}$	37.1	25.0	41.6	27.4	42.8
GSU	1	110	0.456	$2.16 \times 10^{-4}$	0.671	13.0	21.7	27.7	44.6
GVB	1	155	0.643	$1.58 \times 10^{-3}$	3.41	32.8	51.3	54.1	86.2
GVU	0	0	0	0	0	13.2	22.9	25.5	40.5

#### 4.1. Case 1

In Case 1, only one large PV source exists in the system. The performance metrics for this case are shown in Table 3. It can be seen that without the reactive power controller, the solar power variations cause significant effects in the distribution system. These effects include both significant voltage magnitude violations and significant deviations from the reference voltage magnitudes. Five buses experience voltage magnitude violations, and at least one bus experiences a voltage magnitude violation during more than half of the duration of the study. In terms of the violation performance metrics, it can be seen that the GVU method has the greatest improvement in performance, preventing any voltage magnitude violations from occurring. In terms of the sensitivity performance metrics, it can be seen that the GSU method performs the best; it reduces both the mean and maximum variations by more than 93%. For this case, which only has one PV source, the local sensitivity metrics described above are also calculated at the local three-phase bus associated with the PV source. For the local sensitivity metrics, the LSU method, which has identical performance to the LVU method as described above, is best. These methods reduce the mean local variation by more than 99% and the maximum local variation by more than 98%.

#### 4.2. Case 2

In Case 2, there are ten PV sources distributed throughout the system. When the substitution rates  $\beta$  for one of the PV sources are calculated, the other PV sources are treated as negative constant PQ loads at the operating point. The performance metrics for this case are shown in Table 4. It can be seen that without the reactive power controller three buses experience voltage magnitude violations and at least one bus experiences a voltage magnitude violation during more than 64% of the duration of the study. In terms of the violation performance metrics, the four violation optimization methods have good performance. For these methods, no voltage violation is experienced by any bus. In terms of the sensitivity performance metrics, the GSU method has the best performance; it reduces the

**Table 4**  
Simulation results for Case 2.

Method	Number of violated buses	Violation time (s)	Mean violation time (s)	Mean violation (mV)	Maximum violation (mV)	Mean variation (mV)	Maximum variation (mV)
0	3	578	4.00	$5.30 \times 10^{-1}$	376	172	605
LSB	1	1	0.00415	$2.51 \times 10^{-6}$	0.545	26.7	90.7
LSU	0	0	0	0	0	15.9	49.6
LVB	0	0	0	0	0	26.9	91.9
LVS	0	0	0	0	0	15.9	49.6
GSB	1	2	0.00830	$6.27 \times 10^{-6}$	0.764	25.7	90.7
GSU	1	3	0.0124	$4.45 \times 10^{-6}$	0.648	9.77	29.5
GVB	0	0	0	0	0	38.6	114
GVU	0	0	0	0	0	24.8	74.8

mean variation by more than 94% and the maximum variation by more than 95%.

#### 4.3. Case 3

There are also ten PV sources in Case 3, but they are concentrated within the distribution system. As before, the other PV sources are treated as PQ loads when the substitution rates  $\beta$  for a given PV source are calculated. The performance metrics are shown in Table 5. Without the reactive power controller, 14 buses experience voltage magnitude violation. In terms of the violation performance metrics, it can be seen that the two global violation methods have good performance. For the global violation methods, only one bus experiences a voltage magnitude violation. Also, the violation time is reduced by nearly 50%. The GVU method has the best performance for the violation metrics, reducing the maximum violation by more than 99% and the mean violation by more than 99.9%. The mean variation is reduced by the sensitivity minimization methods. The GSU method has the least mean variation, which is less than 3% of mean variation without reactive power control. The maximum variation is reduced by more than 98% by the GSU method.

The voltage variation of the  $a$  phase of three-phase bus 65 with three different methods is shown in Fig. 3(a). Without reactive power control, the  $a$  phase of bus 65 has the largest maximum violation, dipping significantly below the 118-V lower limit. It can be seen that both the GVU and GSU methods keep the voltage magnitude very close to 118 V. Fig. 3(b) shows the voltage magnitude variation of these two methods more closely. It can be seen that the GSU method exhibits more frequent and more severe voltage magnitude violations, which corresponds to the results in Table 5. It can also be seen that the GSU actually increases the violation time, which is also consistent with Table 5.

#### 4.4. Analysis

Several trends exist among the performance of the different reactive power control methods with respect to the various performance metrics. For the global violation performance metrics, i.e., number of violated buses, violation time, mean violation

**Table 5**  
Simulation results of Case 3.

Method	Number of violated buses	Violation time (s)	Mean violation time (s)	Mean violation (mV)	Maximum violation (mV)	Mean variation (mV)	Maximum variation (mV)
0	14	305	6.54	1.27	542	111	385
LSB	4	306	2.62	$1.36 \times 10^{-1}$	137	25.3	89.5
LSU	1	374	1.55	$1.31 \times 10^{-2}$	13.8	4.49	8.80
LVB	3	327	1.98	$7.38 \times 10^{-2}$	90.5	27.4	93.8
LVU	1	374	1.55	$1.31 \times 10^{-2}$	13.8	4.49	8.80
GSB	4	305	2.49	$1.23 \times 10^{-1}$	129	25.2	89.0
GSU	1	374	1.55	$6.63 \times 10^{-3}$	5.89	3.17	5.04
GVB	1	155	0.643	$1.07 \times 10^{-3}$	3.77	41.8	141
GVU	1	146	0.606	$9.41 \times 10^{-4}$	3.55	18.1	30.1

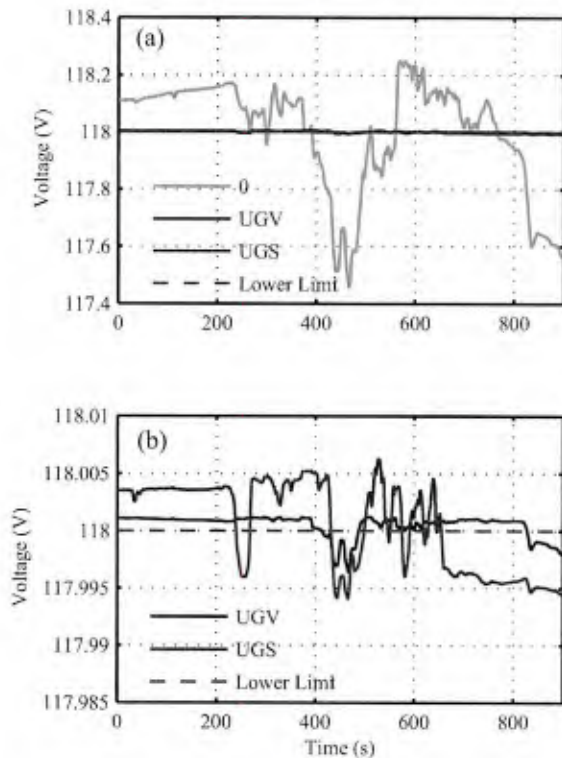


**Fig. 3.** Case 3 bus 65 a-phase voltage magnitude. (a) 0, GVU and GSU methods; (b) GVB and GSU methods.

time, mean violation, and maximum violation, the methods with global scope and violation optimization objective outperform the corresponding methods with either local scope or sensitivity minimization objective. Furthermore, GVU outperforms GVB. These relationships are illustrated in Fig. 4. In this and the subsequent figures, an arrow indicates that the method at the origin outperforms

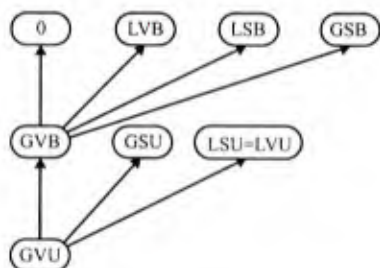


**Fig. 4.** Global violation performance metrics relationships.

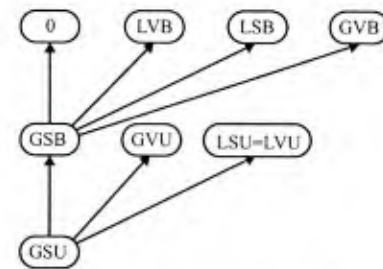


**Fig. 5.** Global sensitivity performance metrics relationships.

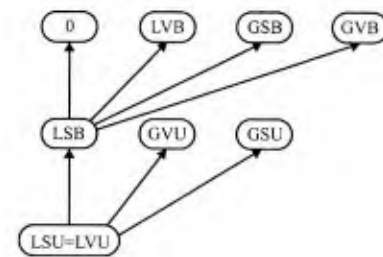


**Fig. 6.** Local sensitivity performance metrics relationships.

the method at the destination. These relationships hold for each of the global violation performance metrics in each of the three cases as seen in Tables 3–5.

When the global sensitivity metrics, i.e., mean variation and maximum variation, are considered, the methods with global scope and sensitivity minimization objective outperform the corresponding methods with either local scope or the violation optimization objective. Once again, the method with unbalanced domain (GSU) exceeds the performance of the method with balanced domain (GSB). The relationships of the methods for the global sensitivity metrics are shown in Fig. 5. These relationships also hold for both of the global sensitivity performance metrics in each of the three cases as seen in Tables 3–5.

For the local sensitivity metrics, i.e., local mean variation and local maximum variation, the methods with local scope and sensitivity minimization objective outperform the corresponding methods with either global scope or the violation optimization objective. This excludes the relationship between the LSU and LVU methods, which are equal and have equal performance. The performance of the unbalanced LSU method is better than that of the balanced LSB method. The relationships for these metrics are presented in Fig. 6. The local sensitivity metrics are not evaluated in Cases 2 and 3 because these cases have multiple PV sources. However, it can be seen in Table 3 that these relationships hold for both local sensitivity metrics in Case 1.

## 5. Conclusion

Various reactive power control methods that substitute reactive power output for real power output during solar power fluctuation are presented. These methods are intended to mitigate against voltage magnitude fluctuations due to short-term solar power variability. These methods are characterized by local or global scope, sensitivity minimization or violation optimization objective, and balanced or unbalanced domain. The various controllers are studied using the IEEE 123-bus feeder distribution system with three different cases, involving different degrees and distributions of PV penetration. Various global violation, global sensitivity, and local sensitivity metrics are considered. It is found that the reactive power control methods can effectively reduce voltage magnitude violation frequency and severity and voltage magnitude variation. Furthermore, it is seen that the best choice of reactive power control method depends on the choice of performance metric. Improvement of global violation performance metrics requires the use of global, violation optimization methods. If global sensitivity performance metrics are chosen, the use of global, sensitivity minimization methods are recommended. If only local sensitivity performance metrics are considered, local methods can be used. In all cases, it is found that the methods with unbalanced domain have better performance than the methods with balanced domain. Overall, it is found that the use of the proposed reactive power control methods can mitigate distribution system voltage magnitude fluctuations.

## Acknowledgements

This work was supported in part by the Office of Naval Research through the United States Naval Academy, N00189-14-P-1197 and in part by the Southeastern Center for Electrical Engineering Education, SCEEE-14-003.

## References

- [1] M. Lave, J. Kleissl, E. Arias-Castro, High-frequency irradiance fluctuations and geographic smoothing, *Solar Energy* 86 (8) (2012) 2190–2199.
- [2] W. Jewell, T. Unruh, Limits on cloud-induced fluctuation in photovoltaic generation, *IEEE Trans. Energy Convers.* 5 (1) (1990) 8–14.
- [3] J. Smith, W. Sunderman, R. Dugan, B. Seal, Smart inverter volt/var control functions for high penetration of PV on distribution systems, in: 2011 IEEE/PES Power Syst. Conference and Exposition, 2011, pp. 1–6.
- [4] D. Rizy, Y. Xu, H. Li, F. Li, P. Irminger, Volt/var control using inverter-based distributed energy resources, in: 2011 IEEE Power and Energy Soc. General Meeting, 2011, pp. 1–8.
- [5] P. Jahangiri, D. Aliprantis, Distributed volt/var control by PV inverters, *IEEE Trans. Power Syst.* 28 (3) (2013) 3429–3439.
- [6] G.E.M. Aly, A.A. El-Zeftawy, A.A. El-Hefanwy, S.A. Eraky, Reactive power control on residential utility-interactive PV power systems, *Electr. Power Syst. Res.* 51 (3) (1999) 187–199.
- [7] R. Yan, B. Marais, T.K. Saha, Impacts of residential photovoltaic power fluctuation on on-load tap changer operation and a solution using DSTATCOM, *Electr. Power Syst. Res.* 111 (2014) 185–193.
- [8] H. Li, Y. Xu, S. Adhikari, D. Rizy, F. Li, P. Irminger, Real and reactive power control of a three-phase single-stage PV system and PV voltage stability, in: 2012 IEEE Power and Energy Soc. General Meeting, 2012, pp. 1–8.
- [9] N. Shah, R. Chudamani, Single-stage grid interactive PV system using novel fuzzy logic based MPPT with active and reactive power control, in: 2012 7th IEEE Conference on Ind. Electron. and Applications, 2012, pp. 1667–1672.
- [10] S. Adhikari, F. Li, Coordinated V-f and P-Q control of solar photovoltaic generators with MPPT and battery storage in microgrids, *IEEE Trans. Smart Grid* 5 (3) (2014) 1270–1281.
- [11] G. Tsengenes, G. Adamidis, Investigation of the behavior of a three phase grid-connected photovoltaic system to control active and reactive power, *Electr. Power Syst. Res.* 81 (1) (2011) 177–184.
- [12] A. Cagnano, E. De Tuglie, M. Liserre, R. Mastromauro, Online optimal reactive power control strategy of PV inverters, *IEEE Trans. Ind. Electron.* 58 (10) (2011) 4549–4558.
- [13] R. Aggarwal, Y. Pan, Minimization of real power losses using reactive power control, *Electr. Power Syst. Res.* 17 (2) (1989) 153–157.
- [14] T. Niknam, A. Ranjbar, A.R. Shirani, Impact of distributed generation on volt/var control in distribution networks, in: 2003 IEEE Bologna PowerTech. Conference Proc., vol. 3, 2003, p. 7.
- [15] T. Niknam, A. Ranjbar, A.R. Shirani, A. Ostadi, A new approach based on ant algorithm for volt/var control in distribution network considering distributed generators, *Iran. J. Sci. Technol. Trans. B: Eng.* 29 (B4) (2005) 385–398.
- [16] T. Senjyu, Y. Miyazato, A. Yona, N. Urasaki, T. Funabashi, Optimal distribution voltage control and coordination with distributed generation, *IEEE Trans. Power Deliv.* 23 (2) (2008) 1236–1242.
- [17] T. Niknam, A new approach based on ant colony optimization for daily volt/var control in distribution networks considering distributed generators, *Energy Convers. Manag.* 49 (12) (2008) 3417–3424.
- [18] T. Niknam, B.B. Firouzi, A. Ostadi, A new fuzzy adaptive particle swarm optimization for daily volt/var control in distribution networks considering distributed generators, *Appl. Energy* 87 (6) (2010) 1919–1928.
- [19] S. Deshmukh, B. Natarajan, A. Pahwa, Voltage/var control in distribution networks via reactive power injection through distributed generators, *IEEE Trans. Smart Grid* 3 (3) (2012) 1226–1234.
- [20] K. Turitsyn, P. Šulc, S. Backhaus, M. Chertkov, Distributed control of reactive power flow in a radial distribution circuit with high photovoltaic penetration, in: 2010 IEEE Power and Energy Soc. General Meeting, 2010, pp. 1–6.
- [21] S. Weckx, C. Gonzalez, J. Driesen, Combined central and local active and reactive power control of PV inverters, *IEEE Trans. Sustain. Energy* 5 (3) (2014) 776–784.
- [22] X. Liu, A.M. Cramer, Y. Liao, Reactive-power control of photovoltaic inverters for mitigation of short-term distribution-system voltage variability, in: 2014 IEEE PES T & D Conference and Exposition, 2014, pp. 1–5.
- [23] M. Farivar, C. Clarke, S. Low, K. Chandy, Inverter var control for distribution systems with renewables, in: 2011 IEEE Int. Conference on Smart Grid Commun., 2011, pp. 457–462.
- [24] M. Farivar, R. Neal, C. Clarke, S. Low, Optimal inverter var control in distribution systems with high PV penetration, in: 2012 IEEE Power and Energy Soc. General Meeting, 2012, pp. 1–7.
- [25] G. Pyo, H.W. Kang, S. Moon, A new operation method for grid-connected PV system considering voltage regulation in distribution system, in: 2008 IEEE Power and Energy Soc. General Meeting – Conversion and Del. of Elect. Energy in the 21st Century, 2008, pp. 1–7.
- [26] K. Turitsyn, P. Šulc, S. Backhaus, M. Chertkov, Local control of reactive power by distributed photovoltaic generators, in: 2010 First IEEE Int. Conference on Smart Grid Commun., 2010, pp. 79–84.
- [27] K. Turitsyn, P. Šulc, S. Backhaus, M. Chertkov, Options for control of reactive power by distributed photovoltaic generators, *Proc. IEEE* 99 (6) (2011) 1063–1073.
- [28] W. Xiao, K. Torchyian, M. El Moursi, J. Kirtley, Online supervisory voltage control for grid interface of utility-level PV plants, *IEEE Trans. Sustain. Energy* 5 (3) (2014) 843–853.
- [29] W. Kersting, Radial distribution test feeders, in: IEEE Power Eng. Soc. Winter Meeting, vol. 2, 2001, pp. 908–912.
- [30] E. Bianconi, J. Calvente, R. Giral, E. Mamarelis, G. Petrone, C. Ramos-Paja, G. Spagnuolo, M. Vitelli, A fast current-based MPPT technique employing sliding mode control, *IEEE Trans. Ind. Electron.* 60 (3) (2013) 1168–1178.
- [31] W. Krause, *Distribution System Modeling and Analysis*, CRC Press, Boca Raton, FL, 2001.

# Generalized Average Method for Time-Invariant Modeling of Inverters

Xiao Liu, *Student Member, IEEE*, Aaron M. Cramer, *Senior Member, IEEE*, and Fei Pan

**Abstract**—Models of inverters and other converters based on averaging have been widely used in numerous simulation applications. Generalized averaging can be applied to model both average and switching behavior of converters while retaining the faster run times associated with average-value models. Herein, generalized average models for single- and three-phase pulse width modulation inverters are proposed. These models are based on a quasi-Fourier series representation of the switching functions that includes fundamental and switching frequency components as well as sideband components of the switching frequency. The proposed models are demonstrated both in simulation and experimentally and are found to accurately portray both the fundamental and the switching behavior of the inverter. In particular, the use of sideband components allows accurate representation of the variation in switching ripple magnitude that occurs in the steady state. The generalized average models are found to have simulation run times that are significantly faster than those associated with detailed models. Therefore, the proposed generalized average models are suitable for simulation applications in which both accuracy (including the switching behavior) and fast run times are required (e.g., long simulation times, systems with multiple converters, and repeated simulations).

**Index Terms**—DC-AC power converters, mathematical model, pulse width modulation inverters.

## I. INTRODUCTION

THE PULSE width modulation (PWM) inverter has been widely used in renewable energy integration [1], [2], motor drive [3]–[5], and other applications (e.g., [6]). Models are necessary for analyzing the dynamic behavior of inverters in many different simulation applications. Detailed models represent every switching action of an inverter, resulting in very accurate simulation results. However, the simulation of such models is time consuming because the simulation time step is limited by the switching period of the inverter. This can be particularly problematic when systems require long simulation times, contain large numbers of power converters, and/or require many repeated simulations with different parameters, e.g., simulating a photovoltaic inverter system over the

interval of a cloud transient [7], simulating multi-converter systems such as electrical railway systems [8], shipboard power systems [9], distribution systems with high penetrations of renewable energy generation [10], and microgrids with many power converters [11], or parameter tuning by genetic algorithm [12]. Furthermore, the detailed models of power converter are time-varying systems without stationary equilibrium points, which makes them generally unsuitable for controller design.

Models based on state-space averaging (SSA) [13] can reduce the run time of the simulation by replacing the switching function with its fast average. SSA is a very common approach for modeling power electronic circuits and is a useful tool for controller design. However, the improved run times available from SSA models come at the cost of reduced model accuracy. In particular, such models are incapable of representing the switching ripple present in the inverter.

Models based on the generalized averaging method (GAM) use a quasi-Fourier series (QFS) representation of waveforms in order to represent both the fundamental behavior and the switching harmonics. GAM models represent a compromise between the high model fidelity available from detailed models and the fast simulation run times available with SSA models. Such models make it possible to investigate the steady-state and dynamic characteristics of the switching ripple without incurring the runtime penalty associated with detailed models, making them particularly appropriate in the cases mentioned above (i.e., long simulation times, systems with multiple converters, and repeated simulations).

Herein, the GAM is extended to model PWM inverters including both their fundamental and switching behavior. QFS representations for the switching functions of PWM inverters are used to construct GAM models of single- and three-phase inverters. In the proposed GAM models, the state variables are represented using not only the fundamental component of the modulation signal and components corresponding to multiples of the switching frequency, but also sideband components of multiples of the switching frequency. The proposed models are demonstrated both in simulation and experimentally and are found to accurately portray both the fundamental and the switching behavior of the inverter. Furthermore, the proposed GAM models are time invariant, resulting in state variables that are constant in the steady state and simulation run times that are considerably smaller than those that can be achieved with a detailed model. The contributions of this work are the application of QFS representations of the switching functions in PWM inverters for constructing GAM models of PWM single- and three-phase inverters and

Manuscript received July 11, 2016; revised September 7, 2016; accepted October 13, 2016. Date of publication November 15, 2016; date of current version February 23, 2017. This work was supported in part by the Southeastern Center for Electrical Engineering Education, SCEEE-14-003, and the Office of Naval Research (ONR) through the ONR Young Investigator Program, N00014-15-1-2475. This paper was recommended by Associate Editor K.-H. Chen.

X. Liu and A. M. Cramer are with the University of Kentucky, Lexington, KY 40506 USA (e-mail: xiao.liu@uky.edu; aaron.cramer@uky.edu).

F. Pan is with Yaskawa - Solectria Solar, Lawrence, MA 01843 USA (e-mail: fei.pan@solectria.com).

Color versions of one or more of the figures in this paper are available online at <http://ieeexplore.ieee.org>.

Digital Object Identifier 10.1109/TCSI.2016.2620442

the demonstration of the proposed GAM models in simulation and experimentally.

The remainder of this paper is organized as follows. Previous work on inverter modeling and its relationship to the present work is discussed in Section II. The general approach to construct GAM inverter models and the QFS representation of the switching functions of PWM inverters are described in Section III. In Section IV, the GAM models for single- and three-phase inverters are proposed, and an estimation technique for assessing the accuracy of such models is discussed. The proposed models are compared with detailed and SSA inverter models in Section V. In Section VI, the GAM models are demonstrated by comparing their simulation results with experimentally measured waveforms. Finally, conclusions are drawn in Section VII.

## II. INVERTER MODELING BACKGROUND

Different inverter models have been developed for different circuit topologies and simulation applications [14]–[17]. These models are useful tools for analyzing and predicting the dynamic behavior of the inverter. Examples include using models to analyze inverter power loss [14] and to design feedback controllers for grid-tie inverters [15]. To overcome the difficulties associated with detailed models (i.e., slower run times and lack of stationary equilibrium points), SSA models have been applied for a variety of types of converters [18]–[20]. Such an approach has its limitations with respect to inverter modeling. The cross-coupling effect of the switching ripple can cause offsets in the lower frequency components of state variables [21], [22], and it is possible that the switching ripple can be resonantly amplified in the LCL filter of a grid-tie inverter system. Furthermore, the effect of the PWM is not considered in SSA models, e.g., a low-order harmonic can be produced in the inverter with uniformly sampled PWM [23]. In [24], an average-value model with switching ripple estimation is discussed. However, the switching ripple must be calculated by an iterative algorithm for each switching cycle, and the time step of this average-value model is still limited by the switching frequency.

The GAM has been developed broadly [21], [25]–[28] with wide application in dc-dc converters. The GAM encompasses conceptually similar ideas, sometimes referred to as generalized SSA and multifrequency averaging, but it can not be applied to model inverters directly. Unlike GAM models for dc-dc converters, the switching functions for the inverters involve two frequencies: the frequency of the sinusoidal modulation signal and the switching frequency associated with the carrier signal. In order to find the GAM model of the inverter, the QFS representation of the switching function for sinusoidal modulation signal is necessary. The Fourier series representation for periodic switching functions of PWM inverter is discussed in [23] and used herein. A GAM-like model for three-phase inverters is proposed in [29], but this model uses a QFS representation for only the fundamental components, neglecting the switching harmonics and producing results analogous to an SSA model. A GAM model for class-E inverters is proposed in [30], but the switching duty cycle is a constant in steady state for this topology, and,

as a result, the state variables in the GAM model only represent the switching harmonics. In [31], a model of a naturally sampled PWM modulator with non-periodical modulation signal is proposed to reduce simulation run time. In each sampling period, the switching function is represented by a Fourier series approximation based on the sampled modulation signal. However, the sampling frequency of the modulation signal must be much larger than the PWM carrier signal frequency to achieve an accurate result.

## III. GENERALIZED AVERAGING METHOD FOR INVERTERS

The general approach for constructing GAM models is as follows. Starting with a system of ordinary differential equations representing a detailed model, a new system of ordinary differential equations is constructed wherein the instantaneous state variables are represented using a QFS representation. In particular, for a PWM inverter, a waveform  $x(t)$  is represented as

$$x(t) = x_{0,0} + x_{0,1c} \cos(\bar{\omega}t) + x_{0,1s} \sin(\bar{\omega}t) + \sum_{n=1}^{\infty} \sum_{i=-\infty}^{\infty} x_{n,ic} \cos(n\hat{\omega}t + i\bar{\omega}t) + \sum_{n=1}^{\infty} \sum_{i=-\infty}^{\infty} x_{n,is} \sin(n\hat{\omega}t + i\bar{\omega}t), \quad (1)$$

where  $\bar{\omega}$  is the angular frequency of the fundamental component and  $\hat{\omega}$  is the angular switching frequency. While the waveform  $x(t)$  varies with time, each of the coefficients of the QFS representation (e.g.,  $x_{0,0}$ ,  $x_{n,ic}$ , and  $x_{n,is}$ ) are constant in steady state. It is assumed that the waveform can be approximated by index-0, index- $n_1i_1c$ , index- $n_1i_1s$ , index- $n_2i_2c$ , index- $n_2i_2s$ , ..., index- $n_o i_o c$ , and index- $n_o i_o s$  QFS components, where  $n_k$  is the order of the  $k$ th selected  $\hat{\omega}$  component and  $i_k$  is the corresponding order of  $k$ th selected  $\bar{\omega}$  component for  $k \in \{1, 2, \dots, o\}$  and that the unselected harmonic components are negligible. In this case, the waveform  $x(t)$  can be represented by an average vector of length  $2o+1$  that is constructed from the QFS coefficients:

$$\mathbf{x} = [x_{0,0} \ x_{n_1,i_1c} \ x_{n_1,i_1s} \ \dots \ x_{n_o,i_o c} \ x_{n_o,i_o s}]^T. \quad (2)$$

The instantaneous value of the waveform can be approximated as

$$x(t) \approx \mathbf{C}(t)\mathbf{x}, \quad (3)$$

where

$$\mathbf{C}(t) = \begin{bmatrix} 1 \\ \cos(n_1\hat{\omega}t + i_1\bar{\omega}t) \\ \sin(n_1\hat{\omega}t + i_1\bar{\omega}t) \\ \vdots \\ \cos(n_o\hat{\omega}t + i_o\bar{\omega}t) \\ \sin(n_o\hat{\omega}t + i_o\bar{\omega}t) \end{bmatrix}^T. \quad (4)$$

A GAM model is a system of ordinary differential equations constructed in terms of these average vectors and their time derivatives.

Certain mathematical properties of signals approximated by QFS representations are straightforward. One necessary

TABLE I  
RELEVANT QUASI-FOURIER SERIES RELATIONSHIPS

Instantaneous signal	Average vector
$x(t)$	$\mathbf{x}$
$\frac{dx(t)}{dt}$	$\frac{d\mathbf{x}}{dt}$
$x(t) + y(t)$	$\mathbf{x} + \mathbf{y}$
$\frac{dx(t)}{dt}$	$(\mathbf{T}\mathbf{x} + \frac{d\mathbf{x}}{dt})$

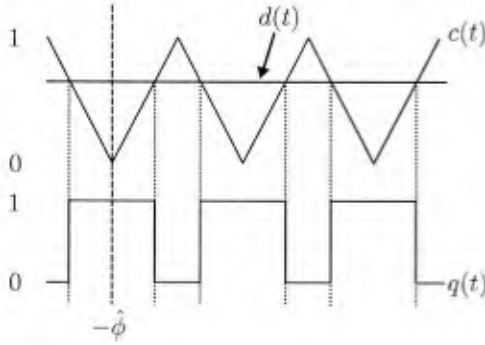


Fig. 1. Relationship of the PWM carrier, the duty cycle and the switching function.

property for constructing GAM models is the relationship between the QFS representation of a signal's time derivative and the time derivative of the QFS representation of the signal. The derivative with respect to time of a QFS-approximated signal can be given by

$$\begin{aligned} \frac{dx(t)}{dt} &\approx \frac{d}{dt}(\mathbf{C}(t)\mathbf{x}) \\ &= \frac{d\mathbf{C}(t)}{dt}\mathbf{x} + \mathbf{C}(t)\frac{d\mathbf{x}}{dt} \\ &= \mathbf{C}(t)\left(\mathbf{T}\mathbf{x} + \frac{d\mathbf{x}}{dt}\right), \end{aligned} \quad (5)$$

where  $\mathbf{T}$  is a  $(2o + 1) \times (2o + 1)$  matrix that is constructed such that all elements are zero except for the  $(2k, 2k + 1)$  elements with values  $n_k\hat{\omega} + i_k\bar{\omega}$  and the  $(2k + 1, 2k)$  elements with values  $-(n_k\hat{\omega} + i_k\bar{\omega})$  for  $k \in \{1, 2, \dots, o\}$ . A summary of relevant QFS relationships is given in Table I.

In order to model PWM inverters, a QFS representation of the switching functions of the inverters is necessary. It is assumed that the inverter modulation signal is a sinusoidal waveform without high order harmonics. The modulation signal can be expressed by

$$m(t) = m_{0,1c} \cos(\bar{\omega}t) + m_{0,1s} \sin(\bar{\omega}t), \quad (6)$$

where  $m_{0,1c}$  and  $m_{0,1s}$  are real-valued QFS coefficients. The instantaneous duty cycle can be expressed as

$$d(t) = \frac{1}{2}(m(t) + 1). \quad (7)$$

The relationship among the PWM carrier  $c(t)$ , the duty cycle  $d(t)$ , and the switching function  $q(t)$  is shown in Fig. 1. Whenever the value of  $d(t)$  is larger than the PWM carrier signal, the switching function is equal to 1; otherwise, the switching function is equal to 0.

It has been shown in [25] that for relatively slowly varying duty cycle, the general periodic switching function can be expressed as the following Fourier series:

$$q(t) = d(t) + \frac{2}{\pi} \sum_{n=1}^{\infty} \frac{\sin(n\pi d(t))}{n} \cos(n\hat{\omega}t + n\hat{\phi}), \quad (8)$$

where  $\hat{\phi}$  is the switching function phase as shown in Fig. 1. It is assumed that  $\bar{\omega} \ll \hat{\omega}$ , i.e., that modulation signal changes slowly with respect to the switching frequency. By expanding (8), the general QFS representation of the switching function for sinusoidal modulation signals can be expressed by

$$\begin{aligned} q(t) &= q_{0,0} + q_{0,1c} \cos(\bar{\omega}t) + q_{0,1s} \sin(\bar{\omega}t) \\ &+ \sum_{n=1}^{\infty} \sum_{i=-\infty}^{\infty} q_{n,ic} \cos(n\hat{\omega}t + i\bar{\omega}t) \\ &+ \sum_{n=1}^{\infty} \sum_{i=-\infty}^{\infty} q_{n,is} \sin(n\hat{\omega}t + i\bar{\omega}t), \end{aligned} \quad (9)$$

where

$$q_{0,0} = \frac{1}{2} \quad (10)$$

$$q_{0,1c} = \frac{1}{2}m_{0,1c} \quad (11)$$

$$q_{0,1s} = \frac{1}{2}m_{0,1s} \quad (12)$$

$$q_{n,ic} = \frac{2}{n\pi} \sin\left(\frac{\pi(n+i)}{2}\right) J_i(y_n) \cos(n\hat{\phi} + i\bar{\phi}) \quad (13)$$

$$q_{n,is} = -\frac{2}{n\pi} \sin\left(\frac{\pi(n+i)}{2}\right) J_i(y_n) \sin(n\hat{\phi} + i\bar{\phi}) \quad (14)$$

$$y_n = \frac{n\pi}{2} \sqrt{m_{0,1c}^2 + m_{0,1s}^2} \quad (15)$$

$$\bar{\phi} = \arg(m_{0,1c} - jm_{0,1s}). \quad (16)$$

The function  $J_i(x)$  is the Bessel function of the first kind of integer order  $i$ . Similar analyses of the spectral content of PWM waveforms can be found in [23]. It is noted that  $\bar{\phi}$  is the modulation signal phase. The coefficients calculated by (10)–(14) have been found to be highly accurate when  $\hat{\omega}/\bar{\omega} \geq 10$ . These expressions are valid for naturally sampled PWM, but other modulation techniques have similar QFS representations of their switching functions.

The most significant components of the Fourier spectrum of two switching functions are shown in Fig. 2. These switching functions, produced when a 10-kHz carrier signal is modulated by two different 60-Hz modulation signals, are sampled at 30 MHz, and discrete Fourier transforms are performed. It can be seen that the high-order harmonic amplitudes change when the magnitude of the modulation signal changes. It is observed from (13) and (14) that the  $q_{n,ic}$  and  $q_{n,is}$  terms vanish when the sum  $n+i$  is even. As a result, no components at 9.94 kHz, 10.06 kHz, 20 kHz, 19.88 kHz, and 20.12 kHz are present in Fig. 2. The magnitudes of the components shown in Fig. 2 correspond to those calculated using (10)–(14). The relative magnitudes of the components at different frequencies are used to determine which components are most significant to include in a GAM model.

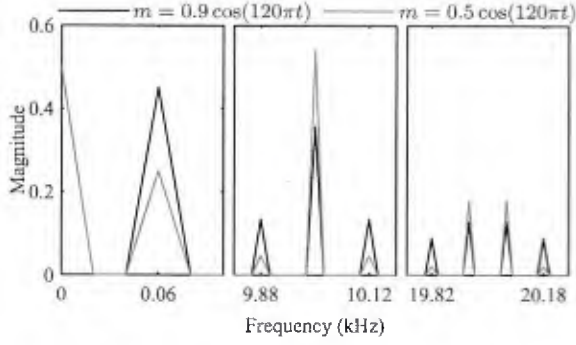


Fig. 2. Discrete Fourier transform of switching functions.

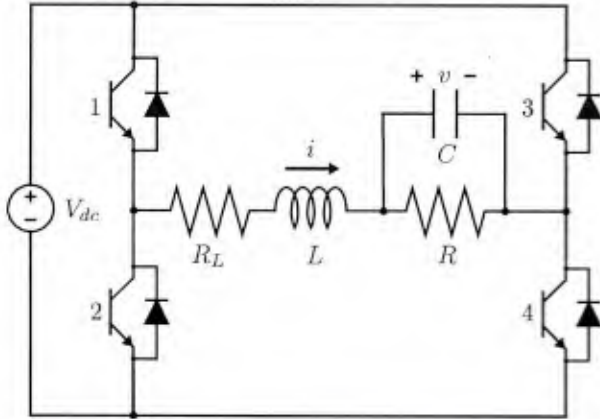


Fig. 3. Single-phase inverter.

By combining the properties of QFS-represented signals with the QFS representation of inverter switching functions, it is possible to construct GAM models for various PWM inverter systems as shown in the following section.

#### IV. INVERTER GENERALIZED AVERAGING METHOD MODELS

The inverter topologies considered herein are described in the subsections below. The topologies span single-phase and three-phase and grid-connected and standalone, and each topology has an output filter. It is noted that the particular filter is not a limiting characteristic of the modeling approach, and GAM models can be easily described for other types of output filter.

##### A. Single-Phase Inverter

The single-phase full bridge inverter with LC filter and resistive load is shown in Fig. 3. For each switch branch, either the upper or lower switch can be on. The state equations for the detailed model are given by

$$\frac{di(t)}{dt} = \frac{V_{dc}}{L} (q_+(t) - q_-(t)) - \frac{R_L}{L} i(t) - \frac{1}{L} v(t) \quad (17)$$

$$\frac{dv(t)}{dt} = \frac{1}{C} i(t) - \frac{1}{RC} v(t), \quad (18)$$

where  $q_+(t)$  is equal to 1 when switch 1 is on and switch 2 is off and equal to 0 when switch 1 is off and switch 2 is

on and where  $q_-(t)$  is equal to 1 when switch 3 is on and switch 4 is off and equal to 0 when switch 3 is off and switch 4 is on. By representing  $i(t)$  with  $\mathbf{i}$ ,  $v(t)$  with  $\mathbf{v}$ ,  $q_+(t)$  with  $\mathbf{q}_+$ , and  $q_-(t)$  with  $\mathbf{q}_-$ , the following state equations for the GAM model are found:

$$\frac{d\mathbf{i}}{dt} = \frac{V_{dc}}{L} (\mathbf{q}_+ - \mathbf{q}_-) - \left( \frac{R_L}{L} \mathbf{I} + \mathbf{T} \right) \mathbf{i} - \frac{1}{L} \mathbf{v} \quad (19)$$

$$\frac{d\mathbf{v}}{dt} = \frac{1}{C} \mathbf{i} - \left( \frac{1}{RC} \mathbf{I} + \mathbf{T} \right) \mathbf{v}, \quad (20)$$

where  $\mathbf{I}$  is the identity matrix. If  $q_+(t)$  and  $q_-(t)$  are complementary (as considered herein), (19) can be simplified to

$$\frac{d\mathbf{i}}{dt} = \frac{V_{dc}}{L} (2\mathbf{q}_+ - [1 \ 0 \ 0 \ \dots \ 0]^T) - \left( \frac{R_L}{L} \mathbf{I} + \mathbf{T} \right) \mathbf{i} - \frac{1}{L} \mathbf{v}. \quad (21)$$

From Fig. 2, it can be seen that the important components of the switching function include dc, the fundamental frequency  $\bar{\omega}$  and the switching frequency  $\hat{\omega}$ . It is noted that the component magnitudes shown in Fig. 2 are independent of  $\bar{\omega}$  and  $\hat{\omega}$ . From (10) and (21), it can be seen that the dc components are not excited and can be excluded if their initial values are zero. So, the average vectors can be given by

$$\mathbf{x} = [x_{0,1c} \ x_{0,1s} \ x_{1,0c} \ x_{1,0s}]^T, \quad (22)$$

where  $x \in \{i, v, q_+\}$  and  $\mathbf{x}$  is the corresponding average vector. This representation is referred to as Configuration 1 in Section V-A below.

It is also possible to represent more components in the GAM model. Depending on the magnitude of the modulation signal, the next most significant components shown in Fig. 2 are the second-order sideband components of the switching frequency  $\hat{\omega} \pm 2\bar{\omega}$ . If these components are also included, the average vectors can be given by

$$\mathbf{x} = [x_{0,1c} \ x_{0,1s} \ x_{1,0c} \ x_{1,0s} \ x_{1,-2c} \ x_{1,-2s} \ x_{1,2c} \ x_{1,2s}]^T. \quad (23)$$

This representation is referred to as Configuration 2 in Section V-A below. It could be expected that including more components in the QFS representations will result in more accurate simulation results, and this relationship is described more formally in Section IV-C.

It is possible to generalize the original system of ordinary differential equations in (17) and (18) to include various non-ideal effects (e.g., on-state voltage drop or passive component ESR). Using the properties in Table I, these modifications can also be included in the GAM model in (20) and (21), resulting in improved accuracy (e.g., low-voltage, high-current inversion).

It is noted that other modulation strategies can be considered with the proposed GAM models. For example, the first-order switching harmonic and associated sideband harmonics vanish under three-level modulation [23]. So the first-order sidebands associated with double switching frequency can be selected to construct such inverter GAM models (i.e.,  $2\hat{\omega} \pm \bar{\omega}$  components).

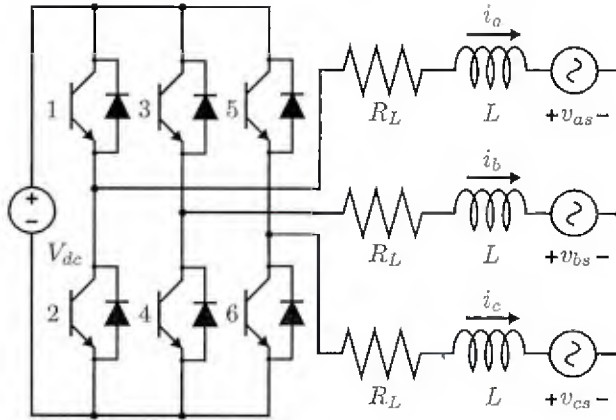


Fig. 4. Three-phase inverter.

### B. Three-Phase Inverter

The three-phase grid-tie inverter is shown in Fig. 4. The state equations for the detailed model are given by

$$\frac{di_a(t)}{dt} = \frac{V_{dc}}{L} \left( \frac{2}{3}q_a(t) - \frac{1}{3}q_b(t) - \frac{1}{3}q_c(t) \right) - \frac{R_L}{L}i_a(t) - \frac{v_{as}}{L} \quad (24)$$

$$\frac{di_b(t)}{dt} = \frac{V_{dc}}{L} \left( \frac{2}{3}q_b(t) - \frac{1}{3}q_a(t) - \frac{1}{3}q_c(t) \right) - \frac{R_L}{L}i_b(t) - \frac{v_{bs}}{L} \quad (25)$$

$$\frac{di_c(t)}{dt} = \frac{V_{dc}}{L} \left( \frac{2}{3}q_c(t) - \frac{1}{3}q_a(t) - \frac{1}{3}q_b(t) \right) - \frac{R_L}{L}i_c(t) - \frac{v_{cs}}{L}, \quad (26)$$

where  $q_a(t)$  is equal to 1 when switch 1 is on and switch 2 is off and equal to 0 when switch 1 is off and switch 2 is on,  $q_b(t)$  is equal to 1 when switch 3 is on and switch 4 is off and equal to 0 when switch 3 is off and switch 4 is on, and  $q_c(t)$  is equal to 1 when switch 5 is on and switch 6 is off and equal to 0 when switch 5 is off and switch 6 is on. By representing  $i_y(t)$  with  $\mathbf{i}_y$ ,  $v_{ys}(t)$  with  $\mathbf{v}_{ys}$ ,  $q_y(t)$  with  $\mathbf{q}_y$ , where  $y \in \{a, b, c\}$ , the following state equations for the GAM model are found:

$$\frac{d\mathbf{i}_a}{dt} = \frac{V_{dc}}{L} \left( \frac{2}{3}\mathbf{q}_a - \frac{1}{3}\mathbf{q}_b - \frac{1}{3}\mathbf{q}_c \right) - \left( \mathbf{T} + \frac{R_L}{L}\mathbf{I} \right) \mathbf{i}_a - \frac{1}{L}\mathbf{v}_{as} \quad (27)$$

$$\frac{d\mathbf{i}_b}{dt} = \frac{V_{dc}}{L} \left( \frac{2}{3}\mathbf{q}_b - \frac{1}{3}\mathbf{q}_a - \frac{1}{3}\mathbf{q}_c \right) - \left( \mathbf{T} + \frac{R_L}{L}\mathbf{I} \right) \mathbf{i}_b - \frac{1}{L}\mathbf{v}_{bs} \quad (28)$$

$$\frac{d\mathbf{i}_c}{dt} = \frac{V_{dc}}{L} \left( \frac{2}{3}\mathbf{q}_c - \frac{1}{3}\mathbf{q}_a - \frac{1}{3}\mathbf{q}_b \right) - \left( \mathbf{T} + \frac{R_L}{L}\mathbf{I} \right) \mathbf{i}_c - \frac{1}{L}\mathbf{v}_{cs}. \quad (29)$$

Again from Fig. 2, it can be seen that the most significant components of the switching function include dc, the fundamental frequency  $\bar{\omega}$ , the switching frequency  $\hat{\omega}$ , and the second-order sideband components of the switching frequency  $\hat{\omega} \pm 2\bar{\omega}$ . It is noted from (13) and (14) that if the three-phase modulation signals are balanced and compared with the same PWM carrier  $c(t)$ , the  $q_{n,0c}$  and  $q_{n,0s}$  components in the three-phase switching functions are equal to each other.

From (27) – (29), it can be seen that the  $x_{n,0c}$  and  $x_{n,0s}$  components are not excited and can be excluded if their initial values are zero. So, the average vector can be given by

$$\mathbf{x} = [x_{0,1c} \ x_{0,1s} \ x_{1,-2c} \ x_{1,-2s} \ x_{1,2c} \ x_{1,2s}]^T, \quad (30)$$

where  $x \in \{i_a, i_b, i_c, v_{as}, v_{bs}, v_{cs}, q_a, q_b, q_c\}$  and  $\mathbf{x}$  is the corresponding average vector. This representation is referred to as Configuration 1 in Section V-B below.

As with the single-phase inverter, it is possible to represent more components in the GAM model. The next most significant components shown in Fig. 2 are the first-order sideband components of double the switching frequency  $2\hat{\omega} \pm \bar{\omega}$ . If these components are also represented, the average vector can be given by

$$\mathbf{x} = [x_{0,1c} \ x_{0,1s} \ x_{1,-2c} \ x_{1,-2s} \ x_{1,2c} \ x_{1,2s} \ x_{2,-1c} \ x_{2,-1s} \ x_{2,1c} \ x_{2,1s}]^T, \quad (31)$$

and this representation is referred to as Configuration 2 in Section V-B below. As with the single-phase inverter, it could be expected that including more components in the QFS representations will result in more accurate simulation results.

If the grid voltages are purely sinusoidal, the grid voltage vectors are given by

$$\mathbf{v}_y = [v_{y,0,1c} \ v_{y,0,1s} \ 0 \ \dots \ 0]^T, \quad (32)$$

where  $y \in \{as, bs, cs\}$ .

In the proposed single- and three-phase GAM models, it can be shown that the real part of the eigenvalues associated with different harmonic components of a state variable are the same, which means that the settling time of high-order switching harmonic components is the same as that of the fundamental component for a given state variable and that the dynamics associated with the switching harmonic components are significant in the transient response.

### C. Accuracy of Generalized Averaging Method Models

A natural question arising from the use of truncated QFS representations for waveforms is that of the accuracy associated with these representations. The various fundamental and switching frequency components and sideband components of the switching frequency arise from the components of the switching function in (9). It can be seen in Fig. 2 that these components have varying magnitudes depending on operating condition. Also, these components will be affected by the system in different ways depending on their frequencies. If a particular signal is of interest (e.g., the inductor current), it is possible to derive the transfer function from the switching function to the signal of interest. For example, in the single-phase inverter model given above, the switching-function-to-inductor-current transfer function is

$$H_{Q+I}(s) = \frac{2V_{dc}}{R_L + sL + \frac{1}{sC} || R} \quad (33)$$

Each component of the switching function (i.e., (9)) can be expressed as

$$q_{+,n,i}(t) = |Q_{+,n,i}| \cos(n\hat{\omega}t + i\bar{\omega}t + \angle Q_{+,n,i}), \quad (34)$$

where  $Q_{+,n,i} = q_{+,n,ic} - jq_{+,n,is}$ . The corresponding steady-state component of the signal of interest can be expressed as

$$i_{n,i}(t) = |I_{n,i}| \cos(n\hat{\omega}t + i\bar{\omega}t + \angle I_{n,i}), \quad (35)$$

where  $I_{n,i} = H_{Q_{+I}}(j(n\hat{\omega} + i\bar{\omega}))Q_{+,n,i}$ .

The instantaneous steady-state deviation associated with excluding some of the infinite terms from the truncated QFS representation can be calculated by

$$\Delta i(t) = \sum_{(n,i) \text{ not selected for QFS}} i_{n,i}(t). \quad (36)$$

As the magnitudes of the switching frequency components rapidly decay with increasing frequency and the transfer function has limited bandwidth, selection of a few relatively low-frequency components can achieve suitable accuracy. The maximum absolute deviation can be estimated by sampling (36) at a sufficiently high sampling rate (1 MHz used herein) over a sufficiently long window (0.05 s used herein) and including a sufficiently large number of terms in the summation ( $n \in \{0, \dots, 20\}$  and  $i \in \{-20, \dots, 20\}$  used herein). Specific examples of these accuracy estimates are provided in the sections below.

## V. SIMULATION RESULTS

In order to examine the proposed inverter GAM models, simulations of single- and three-phase inverters are discussed in this section. All of the models are simulated by the ode32tb Simulink solver with a default relative tolerance of  $10^{-3}$  in MATLAB 2013a. The Bessel function of the first kind is implemented using the MATLAB interpreter. The simulation time for each simulation study is 2 s. In each simulation study, a detailed model, an SSA model, and the configurations of the GAM model are compared. Plots comparing simulation waveforms on the order of the fundamental period and on the order of the switching period are shown. The maximum absolute deviations (with respect to the detailed model) are calculated from the final steady state using a sampling rate of 1 MHz over one period. The run time of the simulation is reported as the mean run time over 100 simulations. The initial values of the state variables in all of the simulations are equal to the corresponding steady state values.

### A. Single-Phase Inverter Simulation Results

The structure of the single-phase inverter for the simulation is shown in Fig. 3. The parameters of the single-phase inverter are listed in the Table II. A step load resistance change is considered. Two configurations of the single-phase inverter GAM model are considered. In Configuration 1, the waveforms of the GAM model are represented using a 60-Hz fundamental component and a 10-kHz switching frequency component. In Configuration 2, the components of Configuration 1 are used as well as 9.88-kHz and 10.12-kHz sideband components. Each of these configurations is compared with a detailed model that models the detailed behavior of each switch.

Figs. 5 (a) and 6 (a) show the inductor current and capacitor voltage during the first two fundamental periods predicted by the detailed model, Configuration 1 of the GAM model, and the SSA model. Figs. 5 (b) and 6 (b) show these waveforms

TABLE II  
SINGLE-PHASE INVERTER SIMULATION PARAMETERS

Input voltage, $V_{dc}$	220 V
Inductance of LC filter, $L$	0.276 mH
Inductor resistance, $R_L$	0.05 $\Omega$
Capacitance of LC filter, $C$	8 $\mu\text{F}$
Switching frequency, $\tilde{f}$	10 kHz
Switching function phase, $\tilde{\phi}$	$\pi/2$ rad
Modulation signal frequency, $\tilde{f}$	60 Hz
Modulation signal magnitude	0.9
Modulation signal phase, $\tilde{\phi}$	1 rad
Initial load resistance, $R$	2 $\Omega$
Final load resistance, $R$	5 $\Omega$
Load resistance step time	16.7 ms

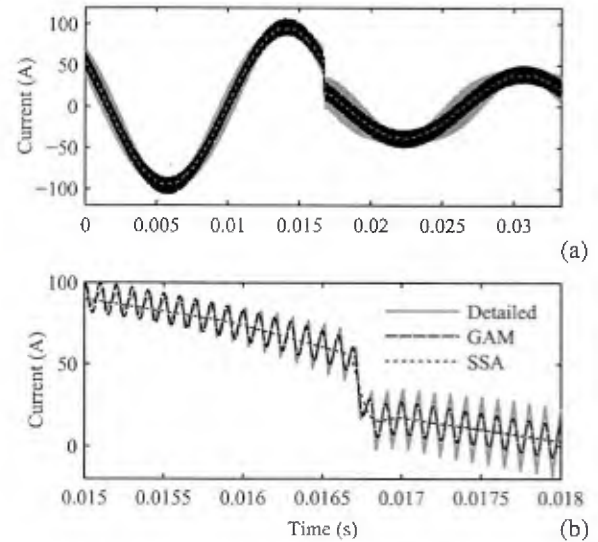


Fig. 5. Configuration 1 (without sidebands) single-phase inverter inductor current.

in closer proximity to the step resistance change. From Fig. 5, it can be seen that the fundamental component of the current waveform matches the detailed model current waveform and the SSA model current waveform. However, the magnitude of the current ripple predicted by Configuration 1 of the GAM model shown in Fig. 5 does not change during steady state. As a result, the current ripple predicted by the GAM model is larger than that predicted by the detailed model when the current is high and smaller than that predicted by the detailed model when the current is near 0 A. It also can be seen that the voltage ripple magnitude predicted by Configuration 1 of the GAM model shown in Fig. 6 does not vary in the same way as that predicted by the detailed model. In the steady state, the average vectors are constant and the switching ripple is represented by a 10-kHz sinusoidal waveform. As a result, the capacitor voltage and inductor current ripple magnitudes predicted by Configuration 1 do not vary as those predicted by the detailed model. It is noted that the change of the load resistance  $R$  affects the transfer functions (e.g., (33)). Thus, the switching ripple magnitudes of the inductor current and the capacitor voltage predicted by the GAM model change after step load change.

Figs. 7 (a) and 8 (a) show the inductor current and capacitor voltage during the first two fundamental periods predicted by

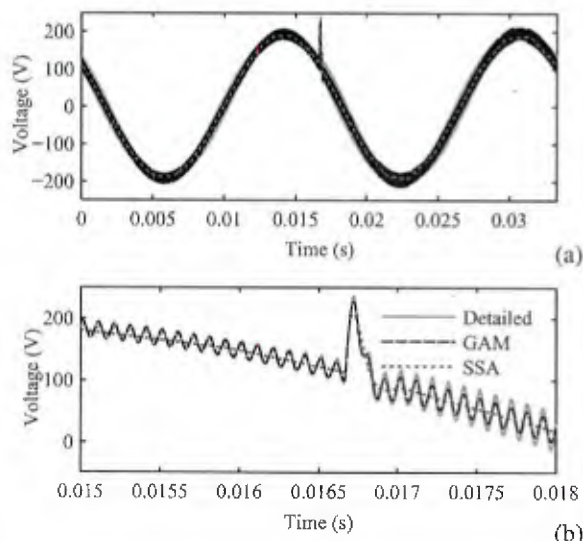


Fig. 6. Configuration 1 (without sidebands) single-phase inverter capacitor voltage.

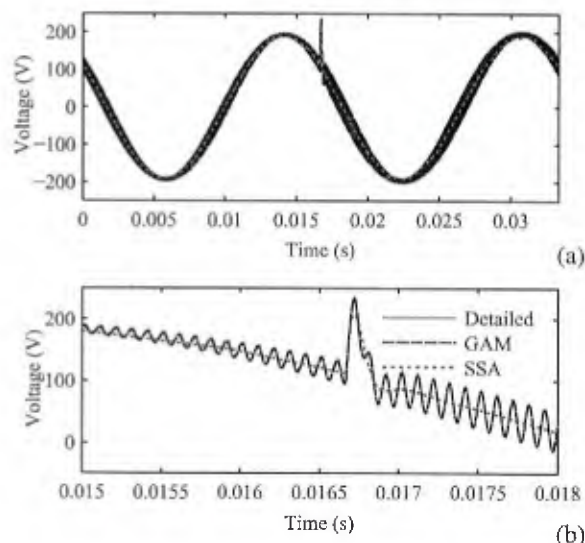


Fig. 8. Configuration 2 (with sidebands) single-phase inverter capacitor voltage.

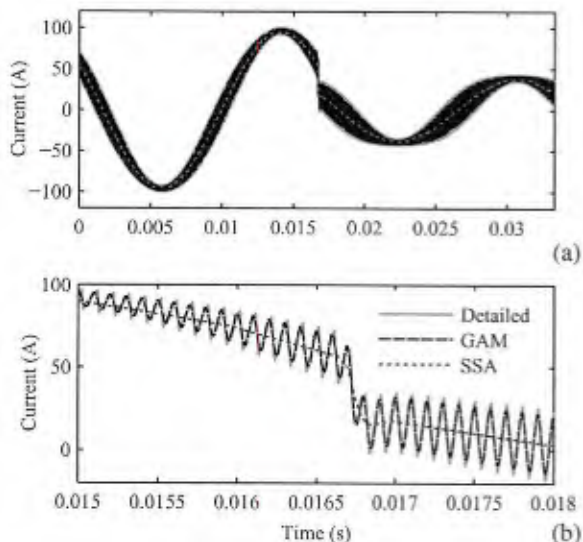


Fig. 7. Configuration 2 (with sidebands) single-phase inverter inductor current.

the detailed model, Configuration 2 of the GAM model, and the SSA model. Figs. 7 (b) and 8 (b) show these waveforms in closer proximity to the step resistance change. From Fig. 7, it can be seen that the magnitude of the inductor current ripple predicted by Configuration 2 of the GAM model follows the variation of that predicted by the detailed model during both steady-state and transient conditions. The voltage ripple magnitude predicted by Configuration 2 of the GAM model also changes in the same manner as that predicted by the detailed model as shown in Fig. 8.

Figs. 5–8 show that the fundamental components of the inductor current and capacitor voltage waveforms always match the corresponding detailed model fundamental components and the corresponding SSA model waveforms. However, the SSA model does not represent the switching ripple.

TABLE III  
SINGLE-PHASE MAXIMUM ABSOLUTE DEVIATION OF STEADY-STATE CAPACITOR VOLTAGE AND INDUCTOR CURRENT

Variable	Model	Maximum absolute deviation	
		Simulation	Estimate
Inductor current	SSA	21.9 A	
	Configuration 1	11.7 A	11.2 A
	Configuration 2	7.13 A	6.70 A
Capacitor voltage	SSA	35.5 V	
	Configuration 1	14.6 V	14.8 V
	Configuration 2	4.49 V	4.54 V

To assess the accuracy of the two configurations, the maximum absolute deviations of the inductor current and the capacitor voltage for the condition following the step load change are determined from the simulation and from the estimation technique presented in Section IV-C. The results are listed in Table III. The maximum absolute deviations of the inductor current and the capacitor voltage between the SSA model and the detailed model from simulation are also listed in Table III. The maximum absolute deviations of the two GAM configurations are significantly smaller than those of the SSA model. It can be seen that the maximum absolute deviations of the GAM model are decreased by including more harmonic components in the waveform representations. It is also observed that the accuracy estimates correspond with the deviations observed in the simulation results.

The run times of the SSA model, Configurations 1 and 2 of the GAM model, and the detailed model are shown in Table IV. The normalized run times of those models are shown in Fig. 9, wherein the run times are normalized by the run time of the detailed model. It can be seen that average simulation speeds of both configurations of the GAM model are more than 100 times faster than that of the detailed model and less than two times slower than that of the SSA model. They each also predict the switching ripple components of the waveforms like the detailed model, but Configuration 2 provides better predictions of

TABLE IV  
SINGLE-PHASE INVERTER SIMULATION RUN TIME

Model	Run time (ms)
SSA	29.8
Configuration 1	33.5
Configuration 2	43.1
Detailed	4590

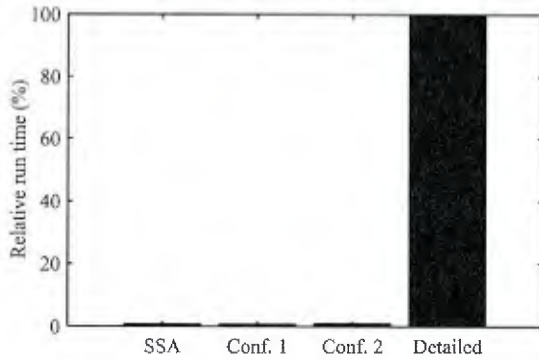


Fig. 9. Normalized single-phase inverter simulation run time. Conf. 1 and Conf. 2 indicate Configuration 1 and Configuration 2 of the single-phase GAM model, respectively.

TABLE V  
THREE-PHASE INVERTER SIMULATION PARAMETERS

Input voltage, $V_{dc}$	220 V
Grid line-to-line rms voltage	120 V
Inductance of L filter, $L$	0.276 mH
Inductor resistance, $R_L$	0.05 $\Omega$
Switching frequency, $f$	10 kHz
Switching function phase, $\phi$	0 rad
Grid voltage frequency, $f$	60 Hz
Initial modulation signal, $m(t)$	$0.911 \cos(\bar{\omega}t + 0.0441)$
Final modulation signal, $m(t)$	$0.875 \cos(\bar{\omega}t + 0.0561)$
Modulation signal step time	16.7 ms

these components; the SSA model does not attempt to represent these components. The run time of Configuration 2 of the GAM model is larger than the run time of Configuration 1 because of the additional complexity associated with including the sideband components. This results in a trade off between simulation run time and accuracy, which should be addressed based on the requirements of a given simulation study.

### B. Three-Phase Inverter Simulation Results

The structure of the three-phase inverter for the simulation is shown in Fig. 4. The parameters of the three-phase inverter are listed in the Table V. The three-phase grid voltages and the three-phase output voltages of the inverter are balanced. The phase angle of the  $a$ -phase line-to-neutral grid voltage  $v_{a5}$  is equal to 0 rad. A step change in modulation signal is studied. Two configurations of the three-phase GAM model are considered. In Configuration 1, the waveforms of the GAM model are represented using 60-Hz components and 9.88-kHz and 10.12-kHz components that are sidebands to the 10-kHz switching frequency. In Configuration 2, the components of Configuration 1 are used as well as 19.94-kHz and 20.06-kHz components that are sidebands to double the

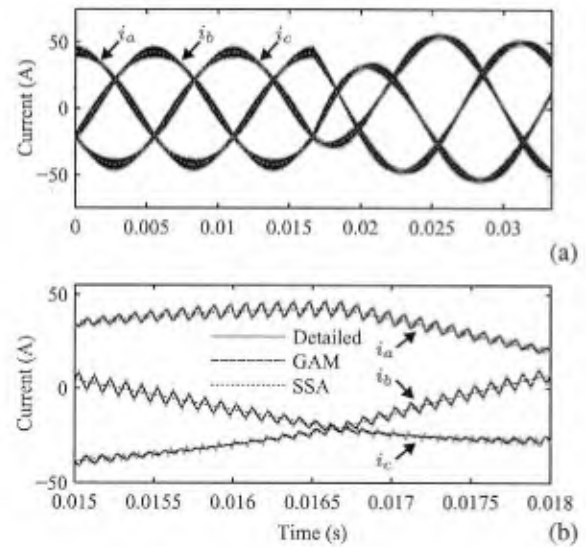


Fig. 10. Configuration 1 (with sidebands of 10 kHz) three-phase inverter inductor currents.

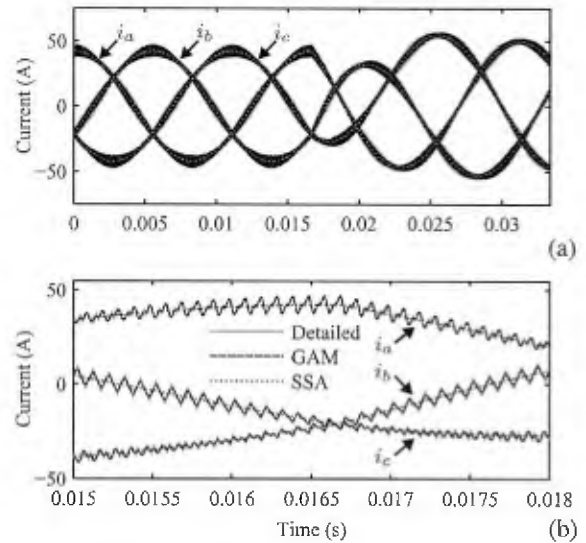


Fig. 11. Configuration 2 (with sidebands of 10 kHz and 20 kHz) three-phase inverter inductor currents.

switching frequency. Each of these configurations is compared with a detailed model that models the detailed behavior of each switch.

Fig. 10 (a) shows the three-phase inductor currents during the first two fundamental periods predicted by the detailed model, Configuration 1 of the GAM model and the SSA model. Fig. 10 (b) shows these waveforms in closer proximity to the modulation signal step change. It can be seen that the current ripple predicted by Configuration 1 of the GAM model matches that predicted by the detailed model during the steady state and transient conditions.

Fig. 11 (a) shows the three-phase inductor currents during the first two fundamental periods predicted by the detailed model, Configuration 2 of the GAM model and the SSA model. Fig. 11 (b) shows these waveforms in closer proximity to the modulation signal step change. It can be seen that

TABLE VI  
THREE-PHASE MAXIMUM ABSOLUTE DEVIATION OF  
STEADY-STATE INDUCTOR CURRENTS

Variable	Model	Maximum absolute deviation	
		Simulation	Estimate
$\alpha$ -phase inductor current	SSA	5.15 A	
	Configuration 1	2.49 A	2.39 A
	Configuration 2	1.78 A	1.62 A
$\beta$ -phase inductor current	SSA	5.24 A	
	Configuration 1	2.50 A	2.39 A
	Configuration 2	1.79 A	1.62 A
$\gamma$ -phase inductor current	SSA	5.24 A	
	Configuration 1	2.50 A	2.39 A
	Configuration 2	1.79 A	1.62 A

TABLE VII  
THREE-PHASE INVERTER SIMULATION RUN TIME

Model	Run time (ms)
SSA	67.0
Configuration 1	246
Configuration 2	612
Detailed	5610

the inductor currents predicted by the Configuration 2 of the GAM model fit inductor currents predicted by detailed model better than those predicted by the Configuration 1 of the GAM model, especially when the current ripple is small (e.g.,  $i_b$  at approximately 16 ms).

Figs. 10 and 11 show the fundamental components of the three-phase inductor currents of both configurations match those of the detailed model and the three-phase inductor currents of the SSA model.

The maximum absolute deviations of the three-phase inductor currents for the condition following the step modulation signal change are determined from the simulation and from the estimation technique, and the results are listed in Table VI. The maximum absolute deviations of the three-phase inductor currents between the SSA model and the detailed model from simulation are also listed in Table VI. It can be seen that the accuracy of the GAM model can be increased by adding more harmonic components in the average vectors, and that the estimates correspond well with the simulation results. Both configurations of the GAM model have better accuracy than the SSA model because of their representation of the switching components.

The run times of the SSA model, the two configurations of the GAM model, and the detailed model are shown in Table VII. The normalized run times of those models are also shown in Fig. 12, wherein the run times are normalized by the run time of the detailed model. It can be seen that the run times of both configurations of the GAM model are much smaller (approximately 10–20 times smaller) than the run time of the detailed model. The run time of Configuration 1 of the GAM model is less than 4 times larger than that of the SSA model. It can be noted that the run-time advantages of the GAM models are less pronounced than those in the single-phase inverter. It can also be noted that the inclusion of more generalized averaging components (i.e., the sidebands of 20 kHz in Configuration 2) has a relatively higher cost compared with including more components in the single-phase inverter GAM models. The source of these differences

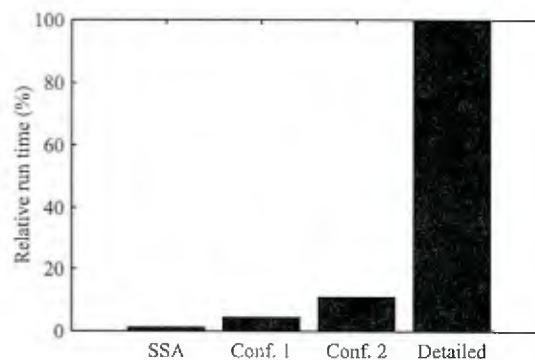


Fig. 12. Normalized three-phase inverter simulation run time. Conf. 1 and Conf. 2 indicate Configuration 1 and Configuration 2 of the three-phase GAM model, respectively.

between the single- and three-phase inverters is related to the dynamics of the grid-tied three-phase inverter system with open-loop control. This system is very lightly damped and causes significantly longer settling times, resulting in longer generalized averaging simulation run times. The open-loop system is considered in simulation to demonstrate the method, but it would be impractical to operate such a system without more damping. In such a more practical situation, simulation run times for the GAM models are expected to decrease further, and the relative run-time penalty of including more generalized averaging components is expected to decrease as well.

## VI. EXPERIMENTAL RESULTS

To demonstrate the proposed GAM model, it is compared with experimental measurements in this section. A flexible prototype inverter is controlled using a TMS320F28335 microcontroller. The sampling rates of the analog-to-digital converter and the controller are 100 kHz. The waveforms are sampled using an oscilloscope with a 20-MHz sampling rate. The experimental setup is shown in Fig. 13. The prototype inverter box contains three IGBT modules (Powerex CM200DY-24A modules) and drives, the microcontroller, sensors, a power supply, and an interface board. The filter box contains two three-phase inductors and a three-phase capacitor. Single- and three-phase experiments are conducted by changing the connections among the IGBT modules, the capacitor, and the inductors.

### A. Single-Phase Experimental Results

For the single-phase inverter experiment, a grid-tied single-phase inverter setup is used. The output of the inverter is connected to the grid through an L filter. This setup corresponds to the circuit shown in Fig. 3 with the parallel capacitor  $C$  and resistor  $R$  replaced by a grid voltage source  $v_g$ . Due to grid voltage distortion, a PI controller is used to ensure that the output current follows the reference current. The control equation is given by

$$m = k_p(i^* - \bar{i}) + k_i \int (i^* - \bar{i}) dt + \frac{L \frac{di^*}{dt} + v_g^*}{V_{dc}}, \quad (37)$$

where  $\bar{i}$  is the output current filtered by a second-order low-pass filter with a time constant of 37.9  $\mu$ s. The parameters

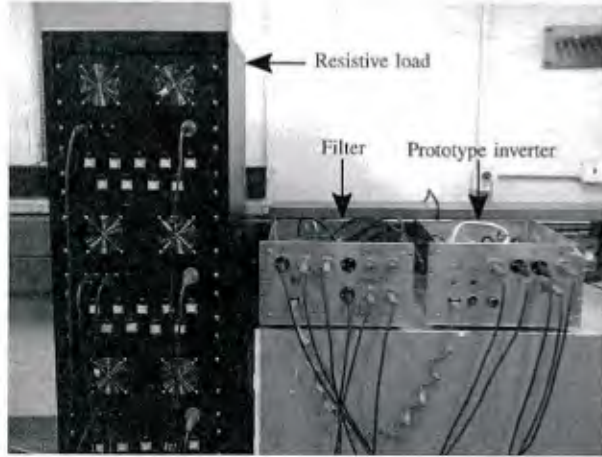


Fig. 13. Experimental setup.

TABLE VIII

SINGLE-PHASE INVERTER EXPERIMENTAL PARAMETERS

Input voltage, $V_{dc}$	220 V
Grid voltage, $v_g$	$\sqrt{2} 125 \cos(\omega t)$ V
Inductance of L filter, $L$	1.352 mH
Inductor resistance, $R_L$	0.05 $\Omega$
Proportional gain, $k_p$	0.05 $A^{-1}$
Integral gain, $k_i$	5 $A^{-1}s^{-1}$
Grid reference voltage, $v_g^*$	$\sqrt{2} 125 \cos(\omega t)$ V
Switching frequency, $f_s$	10 kHz
Grid voltage frequency, $f$	60 Hz
Initial reference current, $i^*$	$\sqrt{2} 25 \cos(\omega t)$ A
Final reference current, $i^*$	$\sqrt{2} 15 \cos(\omega t + \frac{\pi}{8})$ A
Reference current step time	16.7 ms

for the single-phase inverter are listed in Table VIII. The grid phase information is obtained by a phase-locked loop based on a second-order generalized integrator [32]. A step change in reference current  $i^*$  is studied. Because the second-order low-pass filter is used to filter the ripple of the inductor current, the effect of high-frequency inductor current harmonics on the modulation signal is considered negligible. The GAM model of the PI controller only includes the 60-Hz component of the inductor current. The QFS components of the switching function are calculated from the modulation signal output from the PI controller. Fig. 14 (a) shows the inductor current predicted by the GAM model compared with that measured experimentally. Fig. 14 (b) shows these waveforms in closer proximity to the modulation signal step change. The GAM model inductor current shown in Fig. 14 is represented by a 60-Hz fundamental component, a 10-kHz switching frequency component, and 9.88-kHz and 10.12-kHz sideband components, corresponding to Configuration 2 in Section V-A. It can be seen that the magnitude of the inductor current ripple predicted by the GAM model follows the variation that was observed experimentally during the steady state and transient.

The maximum absolute deviation of the inductor current following the step reference signal change is determined from the experimental data, from a detailed simulation, and by estimation. The results are presented in Table IX. It can be seen that the estimate corresponds well with the detailed

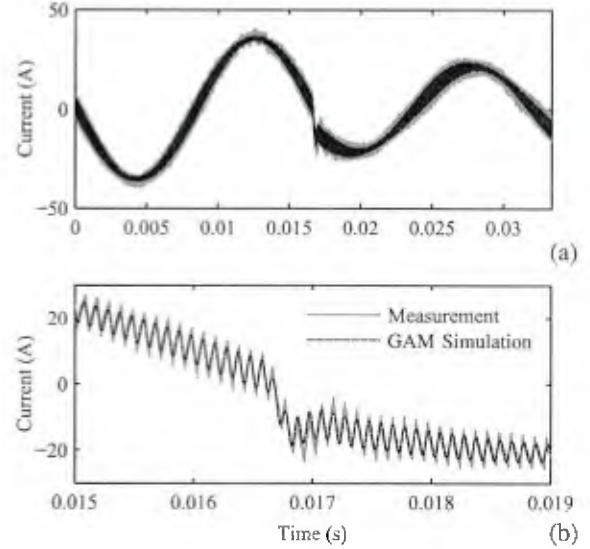


Fig. 14. Single-phase inverter inductor current.

TABLE IX

SINGLE-PHASE MAXIMUM ABSOLUTE DEVIATION OF STEADY-STATE INDUCTOR CURRENT

Variable	Maximum absolute deviation		
	Experiment	Simulation	Estimate
Inductor current	5.49 A	2.23 A	1.89 A

TABLE X

THREE-PHASE INVERTER EXPERIMENTAL PARAMETERS

Input voltage, $V_{dc}$	170 V
Inductance of LC filter, $L$	0.276 mH
Inductor resistance, $R_L$	0.05 $\Omega$
Capacitance of LC filter, $C$	24 $\mu F$
Load resistance, $R$	2.2 $\Omega$
Switching frequency, $f_s$	5 kHz
Modulation signal frequency, $f$	60 Hz
Initial modulation signal of a phase	$0.8 \cos(\omega t)$
Final modulation signal of a phase	$0.5 \cos(\omega t - \pi/6)$
Modulation signal step time	16.7 ms

simulation result. However, it can be seen that measurement noise, unmodeled switching transient behavior, and unmodeled grid voltage harmonics can cause the estimate (and the detailed simulation) to underpredict the maximum absolute deviation.

### B. Three-Phase Experimental Results

For the three-phase experiment, a three-phase inverter setup is connected with a three-phase LC filter to a wye-connected resistive load. This setup corresponds to the circuit shown in Fig. 4 with the three-phase grid voltage sources  $v_{as}$ ,  $v_{bs}$ , and  $v_{cs}$  replaced with three-phase wye-connected parallel capacitors  $C$  and resistors  $R$ . The parameters of the three-phase inverter are listed in Table X. A step change in three-phase modulation signal is studied. Figs. 15 (a) and 16 (a) show the inductor currents and line-to-line capacitor voltages predicted by the GAM model compared with those measured experimentally. Figs. 15 (b) and 16 (b) show these waveforms in closer proximity to the modulation signal step change. It is

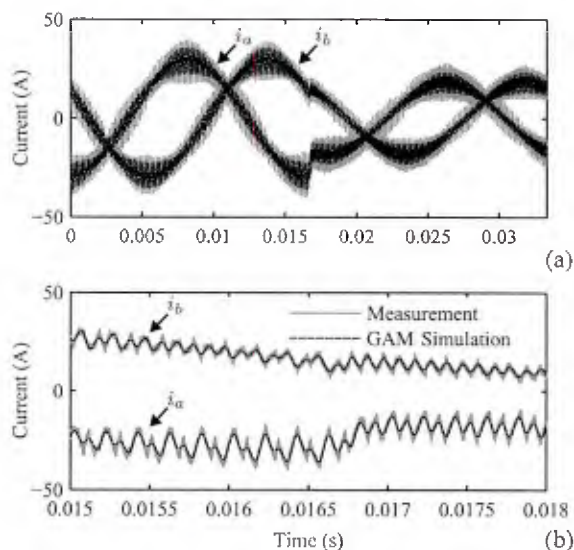


Fig. 15. Three-phase inverter inductor currents.

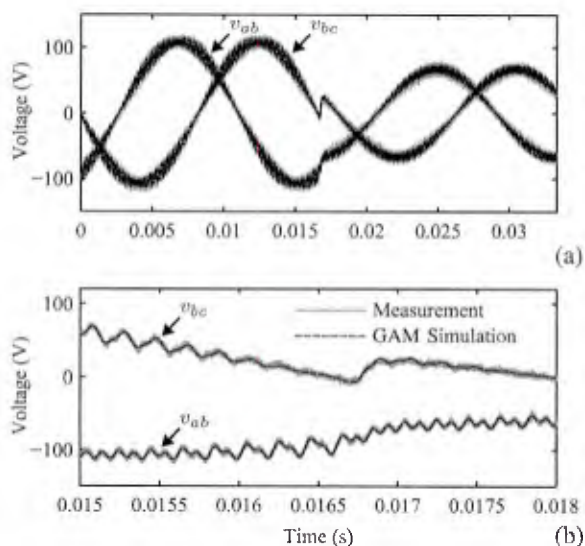


Fig. 16. Three-phase inverter line-to-line capacitor (load) voltages.

noted that the line-to-line capacitor voltage is also the line-to-line load voltage because the three-phase capacitor and three-phase resistor are parallel connected. The GAM model waveforms shown in Figs. 15 and 16 are represented by a 60-Hz fundamental component, 4.88-kHz and 5.12-kHz sideband components of the switching frequency, and 9.94-kHz and 10.06-kHz sideband components of double the switching frequency, corresponding to Configuration 2 in Section V-B. It can be seen that the magnitude of the inductor current ripple predicted by the GAM model follows the variation that was observed experimentally during the steady state and transient. It also can be seen that the line-to-line capacitor voltages predicted by the GAM model match those measured experimentally.

After the step modulation signal change, the maximum absolute deviations of the inductor currents and the line-to-line capacitor voltages are determined from the experimental

TABLE XI  
THREE-PHASE MAXIMUM ABSOLUTE DEVIATIONS OF INDUCTOR CURRENTS AND LINE-TO-LINE CAPACITOR VOLTAGES

Variable	Maximum absolute deviation		
	Experiment	Simulation	Estimate
$a$ -phase inductor current	6.12 A	2.55 A	2.34 A
$b$ -phase inductor current	4.98 A	2.55 A	2.34 A
$a$ -to- $b$ -phase capacitor voltage	8.59 V	1.54 V	1.53 V
$b$ -to- $c$ -phase capacitor voltage	8.52 V	1.54 V	1.53 V

data, a detailed simulation, and the estimation technique, and the results are shown in Table XI. As seen in the single-phase case, the estimates match the deviations observed between the detailed model and the GAM model. However, measurement noise and unmodeled switching dynamics can cause both the estimates and the detailed simulation results to underpredict the maximum absolute deviations.

## VII. CONCLUSION

Herein, GAM models for single- and three-phase PWM inverters are proposed. These models are based on a QFS representation of the switching functions that includes fundamental and switching frequency components as well as sideband components of the switching frequency. These models are compared with the detailed model and the SSA model in simulations, and it is found that the use of sideband components allows accurate representation of the variation in switching ripple magnitude that occurs in the steady state. Furthermore, because the state variables in the GAM models are constant in the steady state, the GAM models are found to have significantly faster simulation speeds than those associated with detailed models and slightly slower simulation speeds than those associated with SSA models. These models are also demonstrated experimentally, and it is found that the simulation results from the GAM models match the experiment measurements in the steady state and transient. Therefore, the proposed GAM models are suitable for simulation applications in which both accuracy (in terms of both fundamental and switching behavior) and fast run times are required (e.g., long simulation times, systems with multiple converters, and repeated simulations).

## REFERENCES

- [1] R.-J. Wai and W.-H. Wang, "Grid-connected photovoltaic generation system," *IEEE Trans. Circuits Syst. I, Reg. Papers*, vol. 55, no. 3, pp. 953–964, Apr. 2008.
- [2] C.-Y. Yang, C.-Y. Hsieh, F.-K. Feng, and K.-H. Chen, "Highly efficient analog maximum power point tracking (AMPPT) in a photovoltaic system," *IEEE Trans. Circuits Syst. I, Reg. Papers*, vol. 59, no. 7, pp. 1546–1556, Jul. 2012.
- [3] D. S. Maric, S. Hiti, C. C. Stancu, J. M. Nagashima, and D. B. Rutledge, "An application of a constrained adaptive lattice-structure allpass-based notch filter for advanced control of surface-mounted permanent-magnet synchronous drives," *IEEE Trans. Circuits Syst. I, Fundam. Theory Appl.*, vol. 46, no. 12, pp. 1513–1516, Dec. 1999.
- [4] J. Zhang, J. Zhao, D. Zhou, and C. Huang, "High-performance fault diagnosis in PWM voltage-source inverters for vector-controlled induction motor drives," *IEEE Trans. Power Electron.*, vol. 29, no. 11, pp. 6087–6099, Nov. 2014.
- [5] G. Liu and K. Mao, "A novel power failure compensation control method for active magnetic bearings used in high-speed permanent magnet motor," *IEEE Trans. Power Electron.*, vol. 31, no. 6, pp. 4565–4575, Jun. 2016.

- [6] R. Gupta and A. Ghosh, "Frequency-domain characterization of sliding mode control of an inverter used in DSTATCOM application," *IEEE Trans. Circuits Syst. I, Reg. Papers*, vol. 53, no. 3, pp. 662–676, Mar. 2006.
- [7] J. D. Mondol, Y. G. Yohanis, and B. Norton, "Comparison of measured and predicted long term performance of grid a connected photovoltaic system," *Energy Convers. Manage.*, vol. 48, no. 4, pp. 1065–1080, 2007.
- [8] E. Mollerstedt and B. Bernhardsson, "Out of control because of harmonics—an analysis of the harmonic response of an inverter locomotive," *IEEE Control Syst.*, vol. 20, no. 4, pp. 70–81, Aug. 2000.
- [9] A. M. Cramer, X. Liu, Y. Zhang, J. D. Stevens, and E. L. Zivi, "Early-stage shipboard power system simulation of operational vignettes for dependability assessment," in *Proc. IEEE Electr. Ship Technol. Symp. (ESTS)*, Jun. 2015, pp. 382–387.
- [10] S. Chiniforoosh *et al.*, "Definitions and applications of dynamic average models for analysis of power systems," *IEEE Trans. Power Del.*, vol. 25, no. 4, pp. 2655–2669, Oct. 2010.
- [11] X. Liu, P. Wang, and P. C. Loh, "A hybrid AC/DC micro-grid," in *Proc. Conf. IPEC*, Oct. 2010, pp. 746–751.
- [12] T. K. Mok, H. Liu, Y. Ni, F. F. Wu, and R. Hui, "Tuning the fuzzy damping controller for UPFC through genetic algorithm with comparison to the gradient descent training," *Int. J. Elect. Power Energy Syst.*, vol. 27, no. 4, pp. 275–283, May 2005.
- [13] R. Middlebrook and S. Cuk, "A general unified approach to modelling switching-converter power stages," in *Proc. IEEE Power Electron. Specialists Conf.*, Jun. 1976, pp. 18–34.
- [14] H. Samago, Ó Lucía, A. Mediano, and J. M. Burdio, "Analytical model of the half-bridge series resonant inverter for improved power conversion efficiency and performance," *IEEE Trans. Power Electron.*, vol. 30, no. 8, pp. 4128–4143, Aug. 2015.
- [15] Z. Zou, Z. Wang, and M. Cheng, "Modeling, analysis, and design of multifunction grid-interfaced inverters with output LCL filter," *IEEE Trans. Power Electron.*, vol. 29, no. 7, pp. 3830–3839, Jul. 2014.
- [16] X. Ding, J. Poon, I. Čelanović, and A. D. Domínguez-García, "Fault detection and isolation filters for three-phase AC-DC power electronics systems," *IEEE Trans. Circuits Syst. I, Reg. Papers*, vol. 60, no. 4, pp. 1038–1051, Apr. 2013.
- [17] T. A. Sakharuk, A. M. Stankovic, G. Tadmor, and G. Eirea, "Modeling of PWM inverter-supplied AC drives at low switching frequencies," *IEEE Trans. Circuits Syst. I, Fundam. Theory Appl.*, vol. 49, no. 5, pp. 621–631, May 2002.
- [18] N. Kroutikova, C. A. Hernandez-Aramburo, and T. C. Green, "State-space model of grid-connected inverters under current control mode," *IET Electr. Power Appl.*, vol. 1, no. 3, pp. 329–338, May 2007.
- [19] A. Davoudi and J. Jatskevich, "Parasitics realization in state-space average-value modeling of PWM DC–DC converters using an equal area method," *IEEE Trans. Circuits Syst. I, Reg. Papers*, vol. 54, no. 9, pp. 1960–1967, Sep. 2007.
- [20] V. Moreno-Font, A. E. Aroudi, J. Calvente, R. Giral, and L. Benadero, "Dynamics and stability issues of a single-inductor dual-switching DC–DC converter," *IEEE Trans. Circuits Syst. I, Reg. Papers*, vol. 57, no. 2, pp. 415–426, Feb. 2010.
- [21] H. Behjati, L. Niu, A. Davoudi, and P. L. Chapman, "Alternative time-invariant multi-frequency modeling of PWM DC–DC converters," *IEEE Trans. Circuits Syst. I, Reg. Papers*, vol. 60, no. 11, pp. 3069–3079, Nov. 2013.
- [22] Z. Mihajlovic, B. Lehman, and C. Sun, "Output ripple analysis of switching DC–DC converters," *IEEE Trans. Circuits Syst. I, Reg. Papers*, vol. 51, no. 8, pp. 1596–1611, Aug. 2004.
- [23] D. Holmes and T. Lipo, *Pulse Width Modulation for Power Converters: Principles and Practice*. New York, NY, USA: Wiley, 2003.
- [24] Y. Xu, Y. Chen, C.-C. Liu, and H. Gao, "Piecewise average-value model of PWM converters with applications to large-signal transient simulations," *IEEE Trans. Power Electron.*, vol. 31, no. 2, pp. 1304–1321, Feb. 2016.
- [25] V. A. Caliskan, O. C. Verghese, and A. M. Stankovic, "Multifrequency averaging of DC/DC converters," *IEEE Trans. Power Electron.*, vol. 14, no. 1, pp. 124–133, Jan. 1999.
- [26] S. R. Sanders, J. M. Noworolski, X. Z. Liu, and G. C. Verghese, "Generalized averaging method for power conversion circuits," *IEEE Trans. Power Electron.*, vol. 6, no. 2, pp. 251–259, Apr. 1991.
- [27] J. Mahdavi, A. Emaadi, M. D. Bellar, and M. Ehsani, "Analysis of power electronic converters using the generalized state-space averaging approach," *IEEE Trans. Circuits Syst. I, Fundam. Theory Appl.*, vol. 44, no. 8, pp. 767–770, Aug. 1997.
- [28] H. Qin and J. W. Kimball, "Generalized average modeling of dual active bridge DC–DC converter," *IEEE Trans. Power Electron.*, vol. 27, no. 4, pp. 2078–2084, Apr. 2012.
- [29] Z. Lin and H. Ma, "Modeling and analysis of three-phase inverter based on generalized state space averaging method," in *Proc. 39th Annu. Conf. IEEE Ind. Electron. Soc. (IECON)*, Nov. 2013, pp. 1007–1012.
- [30] C. Bernal, E. Oyarbide, P. M. Gaudó, and A. Mediano, "Dynamic model of class-E inverter with multifrequency averaged analysis," *IEEE Trans. Ind. Electron.*, vol. 59, no. 10, pp. 3737–3744, Oct. 2012.
- [31] R. A. Guince and C. Lyden, "A novel Fourier series time function for modeling and simulation of PWM," *IEEE Trans. Circuits Syst. I, Reg. Papers*, vol. 52, no. 11, pp. 2427–2435, Nov. 2005.
- [32] M. Ciobotaru, R. Teodorescu, and F. Blaabjerg, "A new single-phase PLL structure based on second order generalized integrator," in *Proc. 37th IEEE Power Electron. Specialists Conf. (PESC)*, Jun. 2006, pp. 1–6.



**Xiao Liu** (S'14) received the B.S. degree in electrical engineering from Yangtze University, Jingzhou, Hubei, China, in 2009 and the M.S. degree in electrical engineering from University of Kentucky, Lexington, KY, USA, in 2013. He is currently working toward the Ph.D. degree in electrical engineering from the University of Kentucky.

His current research interests include power electronics, electrical machines and drives, and power systems.



**Aaron M. Cramer** (S'02–M'07–SM'13) received the B.S. degree (summa cum laude) in electrical engineering from the University of Kentucky, Lexington, KY, USA, in 2003 and the Ph.D. degree from Purdue University, West Lafayette, IN, USA, in 2007.

From 2007 to 2010, he was a Senior Engineer with PC Krause and Associates, West Lafayette. He was an Assistant Professor from 2010 to 2016 at the University of Kentucky, where he is currently as Associate Professor. His research interests include modeling, simulation, and control of power and energy systems.

Dr. Cramer was a recipient of the ONR Young Investigator Program award in 2015. He serves as an Editor of IEEE TRANSACTIONS ON ENERGY CONVERSION.



**Fei Pan** received the B.S. degree in electrical engineering from Southeast University, Nanjing, China, in 2008 and the Ph.D. degree from University of Kentucky, Lexington, KY, USA, in 2014.

He is currently a Scrum Master and Embedded Software Engineer at Yaskawa-Solectria Solar, Lawrence, MA, USA, where he developed and implemented residential solar inverters. His interests include simulation, control, modeling, and optimization of power electronic systems.

# Three-Phase Inverter Modeling using Multifrequency Averaging with Third Harmonic Injection

Xiao Liu, Aaron M. Cramer  
Department of Electrical and Computer Engineering  
University of Kentucky  
Lexington, Kentucky  
Email: xiao.liu@uky.edu, aaron.cramer@uky.edu

*Abstract*—Models of converters based on averaging have been used widely with numerous benefits. Multifrequency averaging (MFA) model can predict both the fundamental and switching behavior of converters and has the faster simulation run times associated with average-value models. Third harmonic injection is commonly used in the modulation signal for three-phase inverters to increase the inverter maximum output voltage while avoiding overmodulation. Herein, an MFA model for three-phase pulse width modulation inverters with third harmonic injection is proposed. The quasi-Fourier-series representation of the switching functions with third harmonic injection is necessary for constructing three-phase inverter MFA model. The third harmonic injection does not change the fundamental and third harmonic components of the state variables in a balanced three-phase system, but it changes the higher-order harmonics. As a result, the quasi-Fourier-series representation of the switching functions for three-phase inverters with third harmonic injection must include the third harmonics. The proposed MFA model is demonstrated in simulation, and the simulation results show that this model has high accuracy (including the switching behavior) and fast run times.

## I. INTRODUCTION

Three-phase pulse width modulation (PWM) inverters have been widely used in motor drives, renewable energy integration, and other applications. Third harmonic injection is used in the modulation signal for the three-phase inverters to increase the inverter maximum output voltage while avoiding overmodulation, which results in undesirable low-frequency harmonics. Third harmonic injection also can be used to reduce the output current harmonics [1].

Multifrequency averaging (MFA) is a generalized averaging method that uses a quasi-Fourier-series (QFS) representation of waveforms in order to represent both the fundamental behavior and the switching harmonics. This idea has been developed broadly [2]–[5] with wide application in dc-dc converters. In the MFA model for inverters with sinusoidal modulation signal, the switching functions are represented using two frequencies: the frequency of the sinusoidal modulation signal and the switching frequency associated with the carrier signal. Third harmonic injection does not change the fundamental component of the state variables in a balanced three-phase system, but it changes the higher-order harmonics.

As a result, the QFS representation of the switching functions for three-phase inverter with third harmonic injection must include the third harmonics.

Herein, the QFS representation for the switching functions of three-phase PWM inverters with third-harmonic injection is provided. This representation is used to construct an MFA model of three-phase inverters with third-harmonic injection. In the proposed MFA model, the state variables are represented using the fundamental and third harmonic components of the modulation signal, the components corresponding to multiples of the switching frequency and the sideband components of multiples of the switching frequency. At the steady state, the state variable switching ripple magnitude in three-phase inverters changes for each switching period. The sideband components of multiples of the switching frequency cause such variations in the state variable switching ripple magnitude. The sideband components can be included in the MFA model for three-phase inverters. The proposed model is demonstrated in simulation and found to accurately predict both the fundamental and the switching behavior of the three-phase inverter. Furthermore, since the proposed MFA model is time invariant, state variables in this model are constant in the steady state and the simulation speed of the MFA model is significantly faster than that of the detailed model. The contributions of this work are (1) the QFS representation of the switching function of three-phase PWM inverters with third harmonic injection, (2) the proposal of an MFA model for PWM three-phase inverters with third harmonic injection, and (3) the demonstration of the proposed MFA model in simulation.

The remainder of this paper is organized as follows. The QFS representation of the switching function of three-phase PWM inverters with third harmonic injection is described in Section II. In Section III, the MFA model for three-phase inverters is proposed. The proposed three-phase inverter MFA model is compared with a detailed model in Section IV. Finally, conclusions are drawn in Section V.

## II. MULTIFREQUENCY AVERAGING MODEL

Herein, the QFS representation of the state variables in three-phase PWM inverters with third harmonic injection is studied. By assuming the modulation signal is a sinusoidal waveform with third harmonic injection, the modulation signal can be expressed by

$$m(t) = m_1 \cos(\bar{\omega}t + \bar{\phi}_0) + m_3 \cos(3\bar{\omega}t + \bar{\phi}_{30}), \quad (1)$$

where  $\bar{\omega}$  is the angular frequency of the modulation signal,  $m_1$  and  $m_3$  are the magnitude of the fundamental modulation signal and third harmonic injection, respectively, and  $\bar{\phi}_0$  and  $\bar{\phi}_{30}$  are the phase angle of the fundamental modulation signal and third harmonic injection, respectively. The instantaneous switch duty cycle can be expressed as

$$D = \frac{1}{2}(m(t) + 1). \quad (2)$$

The instantaneous switching function is generated by comparing the switch duty cycle  $D$  with the double-edge triangular carrier signal  $c(t)$  as in the following relationship:

$$q(t) = \begin{cases} 1, & D \geq c(t) \\ 0, & \text{otherwise} \end{cases}. \quad (3)$$

The general periodic switching function for constant duty cycle  $D$  can be expressed as the following Fourier series:

$$q(t) = D + \frac{2}{\pi} \sum_{n=1}^{\infty} \frac{\sin(n\pi D)}{n} \cos(n\hat{\omega}t + n\hat{\phi}), \quad (4)$$

where  $\hat{\omega}$  is the angular frequency of switching function and  $\hat{\phi}$  is the phase angle of the switching function. In [2], it states that the same switching function expression can be used with the time-varying duty cycle for the slowly varying duty cycle. It is assumed that the modulation signal changes more slowly than the switching signal. By substituting (1) and (2) into (4), it can be shown that the general QFS representation of the switching function for sinusoidal modulation signal with third harmonic injection can be given by

$$\begin{aligned} q(t) = & q_{0,0} + q_{0,1c} \cos(\bar{\omega}t) + q_{0,1s} \sin(\bar{\omega}t) + q_{0,3c} \cos(3\bar{\omega}t) \\ & + q_{0,3s} \sin(3\bar{\omega}t) + \sum_{n=1}^{\infty} \sum_{i=-\infty}^{\infty} q_{n,i,c} \cos(n\hat{\omega}t + i\bar{\omega}t) \\ & + \sum_{n=1}^{\infty} \sum_{i=-\infty}^{\infty} q_{n,i,s} \sin(n\hat{\omega}t + i\bar{\omega}t), \end{aligned} \quad (5)$$

where

$$q_{0,0} = \frac{1}{2} \quad (6)$$

$$q_{0,1c} = \frac{1}{2} m_1 \cos(\bar{\phi}_0) \quad (7)$$

$$q_{0,1s} = -\frac{1}{2} m_1 \sin(\bar{\phi}_0) \quad (8)$$

$$q_{0,3c} = \frac{1}{2} m_3 \cos(\bar{\phi}_{30}) \quad (9)$$

$$q_{0,3s} = -\frac{1}{2} m_3 \sin(\bar{\phi}_{30}) \quad (10)$$

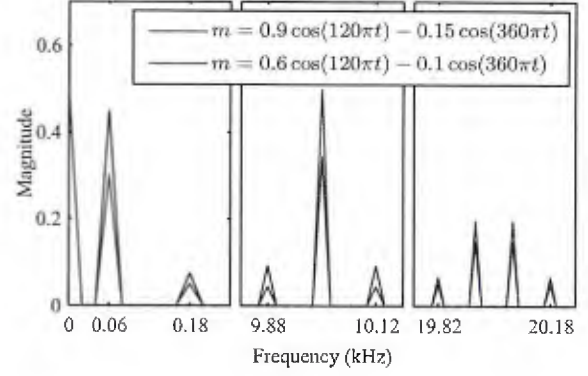


Fig. 1. Discrete Fourier transform of switching functions

$$\begin{aligned} q_{n,i,c} = & \sum_{j=-\infty}^{\infty} \frac{2}{n\pi} J_{i-3j} \left( \frac{n\pi m_1}{2} \right) J_j \left( \frac{n\pi m_3}{2} \right) \\ & \sin \left( \frac{(n+i-2j)\pi}{2} \right) \\ & \cos \left( n\hat{\phi} + (i-3j)\bar{\phi}_0 + j\bar{\phi}_{30} \right) \end{aligned} \quad (11)$$

$$\begin{aligned} q_{n,i,s} = & - \sum_{j=-\infty}^{\infty} \frac{2}{n\pi} J_{i-3j} \left( \frac{n\pi m_1}{2} \right) J_j \left( \frac{n\pi m_3}{2} \right) \\ & \sin \left( \frac{(n+i-2j)\pi}{2} \right) \\ & \sin \left( n\hat{\phi} + (i-3j)\bar{\phi}_0 + j\bar{\phi}_{30} \right) \end{aligned} \quad (12)$$

The function  $J_y(x)$  is the Bessel function of the first kind of integer order  $y$ . The analyses of the harmonic spectrum of PWM waveforms with third harmonic injection can also be found in [6].

Discrete Fourier transformations are used to find the magnitudes of the components of the switching functions. Two switching functions are generated by comparing a 10-kHz carrier signal with two different  $\alpha$ -phase 60-Hz modulation signals which are sampled at 30 MHz. The magnitude of the third harmonic injection  $m_3$  is set to  $-m_1/6$  to allow for a wider voltage range without overmodulation. Fig. 1 shows the most important components of the switching functions. It can be seen that all harmonic amplitudes of the switching functions except for the dc component amplitude change when the magnitudes of the fundamental modulation signal and third harmonic injection change. When the sum  $n+i$  is even, the  $\sin((n+i-2j)\pi/2)$  terms in (11) and (12) are equal to zero, resulting in vanishing of the corresponding components of the switching functions. So, there are no 9.94 kHz, 10.06 kHz, 20 kHz, 19.88 kHz and 20.12 kHz harmonics in Fig. 1. The harmonic amplitudes shown in Fig. 1 can also be calculated by using (5)–(12).

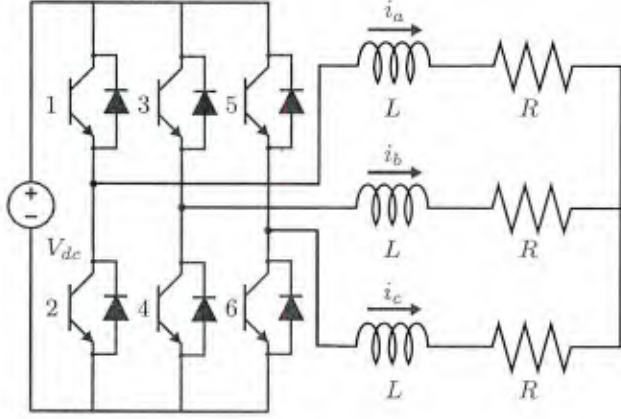


Fig. 2. Three-phase inverter

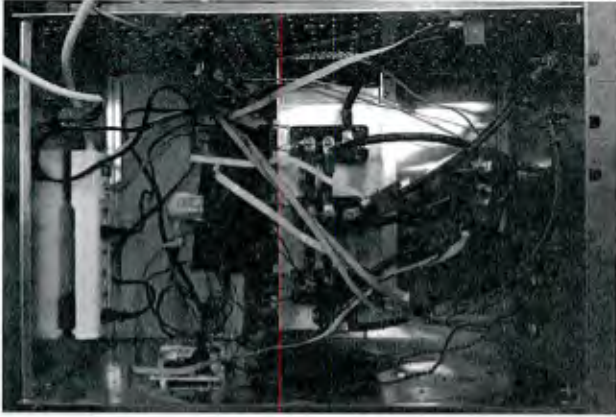


Fig. 3. Three-phase inverter prototype

All of the state variables of the PWM inverter can be expressed using a QFS representation similar to that of the switching function. The instantaneous state variables can be approximated by the QFS representation as

$$x(t) \approx \mathbf{C}(t)\mathbf{x}, \quad (13)$$

where

$$\mathbf{x} = [x_{0,0} \ x_{n_1,i_1c} \ x_{n_1,i_1s} \ \dots \ x_{n_o,i_oc} \ x_{n_o,i_os}]^T, \quad (14)$$

$$\mathbf{C}(t) = \begin{bmatrix} 1 \\ \cos(n_1\bar{\omega}t + i_1\bar{\omega}t) \\ \sin(n_1\bar{\omega}t + i_1\bar{\omega}t) \\ \vdots \\ \cos(n_o\bar{\omega}t + i_o\bar{\omega}t) \\ \sin(n_o\bar{\omega}t + i_o\bar{\omega}t) \end{bmatrix}^T, \quad (15)$$

$x_{0,0}$ ,  $x_{n_1,i_1c}$ ,  $x_{n_1,i_1s}$ ,  $\dots$ ,  $x_{n_o,i_oc}$  and  $x_{n_o,i_os}$  are index-0, index- $n_1i_1c$ , index- $n_1i_1s$ ,  $\dots$  index- $n_oi_oc$ , and index- $n_oi_os$  QFS coefficients of the Fourier series of state variables, respectively, and  $n_k$  is the order of the  $k$ th selected  $\bar{\omega}$  component and  $i_k$  is the corresponding order of  $k$ th selected  $\bar{\omega}$  component for  $k \in \{1, 2, \dots, o\}$ . It can be seen that the average vector  $\mathbf{x}$  is constructed by the QFS coefficients and has  $2o + 1$  elements.

### III. INVERTER MULTIFREQUENCY AVERAGING MODEL

The three-phase grid-tie inverter is shown in Fig. 2. For each branch, the switching function is equal to 1 when the corresponding upper switch is on and is equal to 0 when the corresponding lower switch is on. The state equations for the detailed model are given by

$$\frac{di_a(t)}{dt} = \frac{V_{dc}}{L} \left( \frac{2}{3}q_a(t) - \frac{1}{3}q_b(t) - \frac{1}{3}q_c(t) \right) - \frac{R}{L}i_a(t) \quad (16)$$

$$\frac{di_b(t)}{dt} = \frac{V_{dc}}{L} \left( \frac{2}{3}q_b(t) - \frac{1}{3}q_a(t) - \frac{1}{3}q_c(t) \right) - \frac{R}{L}i_b(t) \quad (17)$$

$$\frac{di_c(t)}{dt} = \frac{V_{dc}}{L} \left( \frac{2}{3}q_c(t) - \frac{1}{3}q_a(t) - \frac{1}{3}q_b(t) \right) - \frac{R}{L}i_c(t). \quad (18)$$

where  $q_a(t)$ ,  $q_b(t)$  and  $q_c(t)$  are the three-phase switching functions. By using average vectors instead of instantaneous values of the state variables and switching functions, (16)–(18) become

$$\frac{d\mathbf{i}_a}{dt} = \frac{V_{dc}}{L} \left( \frac{2}{3}\mathbf{q}_a - \frac{1}{3}\mathbf{q}_b - \frac{1}{3}\mathbf{q}_c \right) - \left( \mathbf{T} + \frac{R}{L}\mathbf{I} \right) \mathbf{i}_a \quad (19)$$

$$\frac{d\mathbf{i}_b}{dt} = \frac{V_{dc}}{L} \left( \frac{2}{3}\mathbf{q}_b - \frac{1}{3}\mathbf{q}_a - \frac{1}{3}\mathbf{q}_c \right) - \left( \mathbf{T} + \frac{R}{L}\mathbf{I} \right) \mathbf{i}_b \quad (20)$$

$$\frac{d\mathbf{i}_c}{dt} = \frac{V_{dc}}{L} \left( \frac{2}{3}\mathbf{q}_c - \frac{1}{3}\mathbf{q}_a - \frac{1}{3}\mathbf{q}_b \right) - \left( \mathbf{T} + \frac{R}{L}\mathbf{I} \right) \mathbf{i}_c, \quad (21)$$

where  $\mathbf{q}_a$ ,  $\mathbf{q}_b$  and  $\mathbf{q}_c$  are the average vectors of the three-phase switching functions, and  $\mathbf{i}_a$ ,  $\mathbf{i}_b$  and  $\mathbf{i}_c$  are the average vectors of the three-phase inductor currents,  $\mathbf{I}$  is the identity matrix and  $\mathbf{T}$  is a  $(2o + 1) \times (2o + 1)$  matrix that is constructed such that all elements are zero except for the  $(2k, 2k + 1)$  elements with values  $n_k\bar{\omega} + i_k\bar{\omega}$  and the  $(2k + 1, 2k)$  elements with values  $-(n_k\bar{\omega} + i_k\bar{\omega})$  for  $k \in \{1, 2, \dots, o\}$ .

To achieve the maximum output voltage without overmodulation [6], the three-phase modulation signals with third harmonic injection are given by

$$m_a = m_1 \cos(\bar{\omega}t + \bar{\phi}_a) - \frac{m_1}{6} \cos(3\bar{\omega}t + 3\bar{\phi}_a) \quad (22)$$

$$m_b = m_1 \cos(\bar{\omega}t + \bar{\phi}_a - \frac{2\pi}{3}) - \frac{m_1}{6} \cos(3\bar{\omega}t + 3\bar{\phi}_a) \quad (23)$$

$$m_c = m_1 \cos(\bar{\omega}t + \bar{\phi}_a + \frac{2\pi}{3}) - \frac{m_1}{6} \cos(3\bar{\omega}t + 3\bar{\phi}_a). \quad (24)$$

where  $\bar{\phi}_a$  is the phase angle of the  $\alpha$ -phase fundamental modulation signal. It is noted that if such three-phase modulations are compared with the same PWM carrier, the components corresponding to multiples of the switching frequency (i.e.,  $q_{n,0c}$  and  $q_{n,0s}$ ) for the three-phase switching functions are equal. These components can be canceled in (19)–(21). As a result, no components corresponding to multiples of the switching frequency exist in the inductor currents. It can be seen from (6)–(10) that the magnitudes of the fundamental and third harmonic components for three-phase switching functions are equal to each other. From (11) and (12), the

magnitudes of high frequency components can be given by

$$\sqrt{q_{n,ic}^2 + q_{n,is}^2} = \sum_{j=-\infty}^{\infty} \frac{2}{n\pi} J_{i-3j} \left( \frac{n\pi m_1}{2} \right) J_j \left( \frac{n\pi m_3}{2} \right) \sin \left( \frac{(n+i-2j)\pi}{2} \right), \quad (25)$$

which means that the magnitudes of high frequency components of three-phase switching functions on the same frequency are also equal in the balanced system. Therefore, three-phase switching functions have the same significant harmonic components.

#### IV. SIMULATION RESULTS

In order to examine the proposed inverter MFA model, simulation of the three-phase inverter is discussed in this section. The model is simulated by the ode32tb Simulink solver with a default relative tolerance of  $10^{-3}$  in MATLAB 2013a. The Bessel function of the first kind is implemented using the MATLAB interpreter. The simulation time for each simulation study is 2 s. The run time of the simulation is reported as the mean run time over 100 simulations. The initial values of the state variables in the simulation are equal to the corresponding steady state values.

The structure of the three-phase inverter for the simulation is shown in Fig. 2. The parameters of the three-phase inverter are listed in the Table I. A modulation signal step change is considered. Two configurations of three-phase inverter MFA model are studied. In Configuration 1, the switching functions and state variables of the MFA model are represented using 60-Hz components and 9.88-kHz and 10.12-kHz components that are sidebands to the 10-kHz switching frequency. In Configuration 2, the switching functions and state variables of the MFA model are represented using not only all of components in Configuration 1 but also 19.94-kHz and 20.06-kHz components that are sidebands to double the switching frequency. Two configurations are compared with a detailed model that models every switching action. From (5)–(12), it can be seen that the coefficients of the switching functions for a given harmonic are an infinite sum except for the dc, fundamental, and third harmonic injection components. However, these coefficients are approximated by several terms. In particular, the 9.88-kHz component is approximated by the sum of terms with  $j \in \{-1, 0\}$ . The 10.12-kHz component is approximated by the sum of terms with  $j \in \{0, 1\}$ . The 19.94-kHz and 20.06-kHz components are approximated by the sum of terms with  $j \in \{-1, 0, 1\}$ . Because  $J_{-j}(x) = (-1)^j J_j(x)$ , only four Bessel function evaluations are needed for Configuration 1 of the MFA model and nine Bessel function evaluations are needed for Configuration 2 of the MFA model. The magnitudes of harmonic components of  $a$ -phase switching function given by the approximation and the fast Fourier transform (FFT) are compared in Table II. The sampling frequency of  $a$ -phase switching function for the FFT is 30 MHz. As mentioned in Section III, the magnitudes of harmonic components of three-phase switching functions on same frequency are equal to each

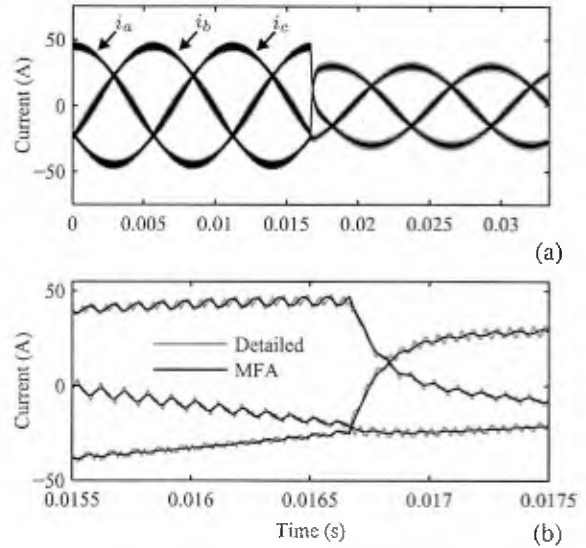


Fig. 4. Configuration 1 three-phase inverter inductor currents

other. So, the magnitudes of harmonic components for  $b$ -phase and  $c$ -phase switching functions given by the approximation and the FFT have the same results. From Table II, it can be seen that the approximations of QFS coefficients have high accuracy.

Three-phase inductor currents during the first two fundamental periods predicted by the detailed model and by Configuration 1 of the MFA model are shown in Fig. 4 (a). Three-phase inductor currents near the step modulation signal change are shown in Fig. 4 (b). From Fig. 4, it can be seen that the inductor currents predicted by Configuration 1 of the MFA model match the inductor currents predicted by the detailed model during both steady-state and transient conditions.

Three-phase inductor currents during the first two fundamental periods predicted by the detailed model and by Configuration 2 of the MFA model are shown in Fig. 5 (a). Three-phase inductor currents near the step modulation signal change are shown in Fig. 5 (b). From Fig. 5, it can be seen that the inductor currents predicted by Configuration 2 of the MFA model also match the inductor currents predicted by the detailed model.

It can be seen that the accuracy of Configuration 2 of the MFA model is increased (with respect to Configuration 1) by including more sideband components. Furthermore, the accuracy of Configuration 1 of the MFA model noticeably suffers after the modulation signal step change (e.g.,  $i_c$  at approximately 17 ms). This decrease in accuracy can be understood from Fig. 1. In Fig. 1, the magnitudes of the 9.88-kHz and 10.12-kHz sideband components are smaller than the magnitudes of the 19.94-kHz and 20.06-kHz sideband components when the magnitude of the fundamental component  $m_1$  is equal to 0.6 (as it is after the step change).

The run times of the detailed model and both configurations

TABLE I  
THREE-PHASE INVERTER SIMULATION PARAMETERS

Input voltage, $V_{dc}$	220 V
Inductance of L filter, $L$	0.276 mH
Load resistance, $R$	2.2 $\Omega$
Switching frequency, $\bar{f}$	10 kHz
Phase angle of switching function, $\bar{\phi}$	0 rad
Modulation signal frequency, $\bar{f}$	60 Hz
Initial modulation signal, $m_a(t)$ (initial)	$0.9 \cos(\bar{\omega}t) - 0.15 \cos(3\bar{\omega}t)$
Final modulation signal, $m_a(t)$ (final)	$0.6 \cos(\bar{\omega}t + \pi/2) - 0.1 \cos(3\bar{\omega}t + 3\pi/2)$
Modulation signal step time	16.7 ms

TABLE II  
MAGNITUDE OF A-PHASE SWITCHING FUNCTION HARMONICS FROM APPROXIMATION AND FAST FOURIER TRANSFORM

Harmonic frequency		9.88 kHz	10.12 kHz	19.94 kHz	20.06 kHz	
Harmonic magnitude	$m_a(t)$ (initial)	FFT	0.0917	0.0917	0.1472	0.1472
		Approximation	0.0917	0.0917	0.1475	0.1475
	$m_a(t)$ (final)	FFT	0.0442	0.0442	0.1953	0.1953
		Approximation	0.0442	0.0442	0.1953	0.1953

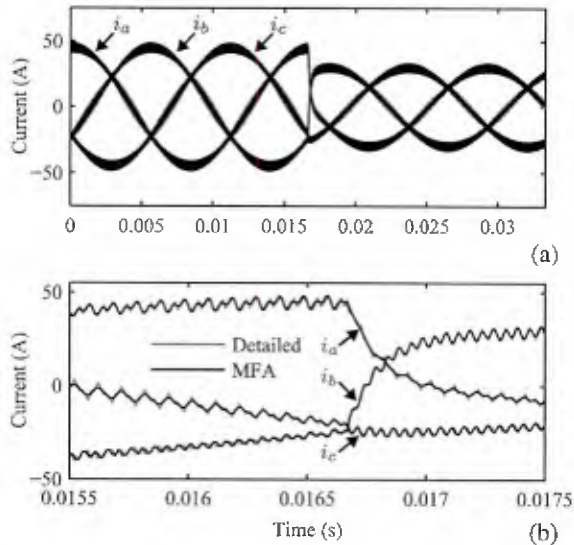


Fig. 5. Configuration 2 three-phase inverter inductor currents

of the MFA model are listed in Table III. It can be seen that the average simulation run time of detailed model is more than 67 times larger than that of Configuration 1 of the MFA model. The average simulation run time of detailed model is more than 35 times larger than that of Configuration 2 of the MFA model. To compare the accuracy of different configurations of the MFA model, the mean deviation between the inductor current of the MFA model and that of the detailed model is defined by

$$\frac{1}{T} \int_0^T \sqrt{(i_{MFA}(t) - i_{detailed}(t))^2}, \quad (26)$$

where  $T$  is the simulation time,  $i_{MFA}$  is the inductor current predicted by the MFA model and  $i_{detailed}$  is the inductor current predicted by the detailed model. The mean deviations

TABLE III  
THREE-PHASE INVERTER SIMULATION RUN TIME

Model	Run time (ms)
Detailed	5162
Configuration 1	76
Configuration 2	140

TABLE IV  
MEAN DEVIATION OF THREE-PHASE INVERTER INDUCTOR CURRENTS

Model	Inductor current mean deviation (A)		
	a phase	b phase	c phase
Configuration 1	1.131	1.131	1.131
Configuration 2	0.482	0.482	0.482

of three-phase inductor currents are listed in Table IV. It can also be seen that the Configuration 2 of the MFA model has better accuracy than Configuration 1 of the MFA model. So, there is a trade-off between the simulation speed and accuracy in the MFA model for three-phase inverters.

## V. CONCLUSION

Achieving the proper balance between accuracy and computational efficiency is necessary in any simulation application. Models based on averaging have been used widely with numerous benefits. MFA techniques have been used to predict both average and switching behavior of converters while retaining the faster simulation speed associated with average-value models. Herein, an MFA model for three-phase PWM inverters with third harmonic injection is proposed. The QFS representation of the switching functions with third harmonic injection are necessary for constructing three-phase inverter MFA model. The QFS representation of the switching functions includes fundamental components, third harmonic components, components corresponding to multiples of the switching frequency and sideband components of multiples of the switching frequency. Due to the third harmonic com-

ponents and components corresponding to multiples of the switching frequency do not exist in the state variables of three-phase inverters, the sideband components of multiples of the switching frequency cause the variations in inductor current ripple magnitude. The accuracy of the MFA model of three-phase inverter can be improved by including more sideband components in average vectors, but the simulation run time will increase. The simulation results show the MFA model have high accuracy and simulation run times that are significantly faster than those associated with detailed models.

#### REFERENCES

- [1] A. Eltamaly, "A modified harmonics reduction technique for a three-phase controlled converter," *IEEE Trans. Ind. Electron.*, vol. 55, no. 3, pp. 1190–1197, Mar. 2008.
- [2] V. Caliskan, G. C. Verghese, and A. Stanković, "Multifrequency averaging of DC/DC converters," *IEEE Trans. Power Electron.*, vol. 14, no. 1, pp. 124–133, Jan. 1999.
- [3] S. Sanders, J. Noworolski, X. Liu, and G. C. Verghese, "Generalized averaging method for power conversion circuits," *IEEE Trans. Power Electron.*, vol. 6, no. 2, pp. 251–259, Apr. 1991.
- [4] J. Mahdavi, A. Ermaadi, M. Bellar, and M. Ehsani, "Analysis of power electronic converters using the generalized state-space averaging approach," *IEEE Trans. Circuits Syst. I*, vol. 44, no. 8, pp. 767–770, Aug. 1997.
- [5] H. Behjati, L. Niu, A. Davoudi, and P. Chapman, "Alternative time-invariant multi-frequency modeling of PWM DC-DC converters," *IEEE Trans. Circuits Syst. I, Reg. Papers*, vol. 60, no. 11, pp. 3069–3079, Nov. 2013.
- [6] D. Holmes and T. Lipo, *Pulse Width Modulation for Power Converters: Principles and Practice*. Piscataway, NJ: Wiley-IEEE Press, 2003.

# Hybrid Position Observer for Brushless DC Motor Drives with Improved Noise Immunity

Xiao Liu, Aaron M. Cramer

Department of Electrical and Computer Engineering

University of Kentucky

Lexington, Kentucky

Email: xiao.liu@uky.edu, aaron.cramer@uky.edu

**Abstract**—A noise immunity improvement for hybrid position observers for brushless dc motor drives is proposed. A finite state machine is used to detect Hall-effect sensor transitions to determine if these transitions are true transitions or the result of momentary glitches. This filter causes a delay in the detection of the Hall-effect sensors that is compensated in the proposed observer. The proposed observer is compared in simulations with the original hybrid position observer under both non-noisy and noisy conditions for both constant and variable speed operation, and it has good performance even under high noise and variable speed conditions.

**Index Terms**—Brushless machines, dc machines, noise, observers

## I. INTRODUCTION

High-performance operation of brushless dc motors with sinusoidal references requires knowledge of the electrical rotor position with relatively high accuracy. Electromagnetic resolvers and optical encoders can provide sufficient position accuracy, but they require larger installation volumes and entail higher costs. Much work has been conducted on sensorless drive techniques (e.g., [1], [2]). Generally, sensorless techniques require detailed motor parameters [1], and the initial rotor position must be estimated for startup [2].

Hall-effect sensors are widely installed in brushless dc motors and provide a reliable and cheap way to obtain the electrical rotor position. Observers have been developed to find the electrical rotor position based on binary Hall-effect sensors [3]–[5]. In [3], a vector-tracking observer with harmonics decoupling is developed, which has good performance in steady state and during transients. However, this method requires a high accuracy estimate of the load torque, is sensitive to the moment of inertia, and needs careful tuning of the observer parameters. In [4], a hybrid observer for high-performance brushless dc motor drives is discussed. Its simple implementation provides a good estimate of the instantaneous rotor position without requiring machine parameter estimates. In [5], a method which is similar to the hybrid observer is proposed: the electrical angle is reset at each Hall-effect sensor transition, and the instantaneous rotor position is estimated by assuming the speed is constant between two Hall-effect sensor transitions.

In [3]–[5], it is assumed that no fault exists in the output of the Hall-effect sensors. However, it is possible that there are some sensor faults in practice. In particular, high-frequency

switching can induce short sensor glitches in brushless dc motor drive systems. Even such short glitches in the output of the Hall-effect sensors can cause large estimation errors, and these errors can persist for a significant interval after the noise is removed. The estimation of the electrical rotor position under sensor faults has been widely studied. In [6], the rotor position can be estimated when there is one or two permanent faults in three Hall-effect sensors. In [7], a periodic timer interrupt function is used to check the output of the Hall-effect sensor to avoid noise between sampling periods. However, a glitch that is longer than one period of the timer or that occurs at the time when the Hall-effect sensor is sampled can still cause errors in the observer.

Herein, a noise immunity improvement for the hybrid position observer is proposed to address experimentally observed Hall-effect sensor noise. A finite state machine is used to detect Hall-effect sensor transitions to determine if these transitions are true transitions or the result of momentary glitches. This filter causes a delay in the detection of the Hall-effect sensors that is compensated in the proposed observer. The proposed observer is compared in simulations with the original hybrid position observer under both non-noisy and noisy conditions for both constant and variable speed operation. The simulation results show that the hybrid observer with noise immunity has good performance even under high noise and variable speed conditions.

The remainder of this paper is organized as follows. A brief review of hybrid observer for brushless dc machines and the proposed noise immunity improvement are described in Section II. In Section III, the proposed noise immunity method is compared with the original hybrid observer. A brief conclusion is given in Section IV.

## II. HYBRID OBSERVER WITH NOISE IMMUNITY

To introduce the noise immunity improvement for the hybrid position observer for brushless dc machines, a brief review of the hybrid observer [4] is described first. An example of the outputs of Hall-effect sensors 1–3 (HS1–3, respectively), the sine of the electrical rotor position  $s$ , and the cosine of the electrical rotor position  $c$  for a three-phase brushless dc machine are shown in Fig. 1. It can be seen that there are six Hall-effect sensor states in one period, and  $s$  and  $c$  have specific values corresponding to each Hall-effect sensor

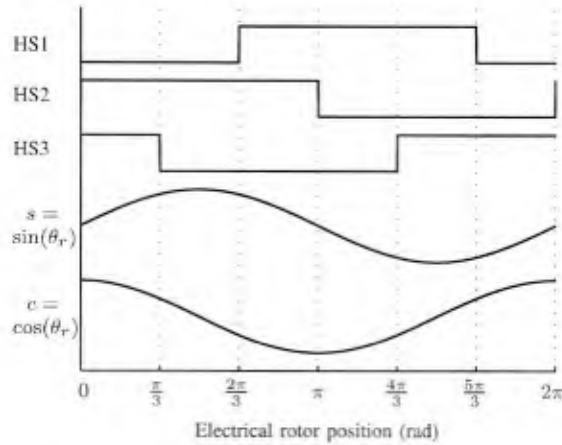


Fig. 1. Relationship among Hall-effect sensor states and sine and cosine of electrical rotor position

transition. As a result, the exact value of the sine and cosine of the electrical rotor position can be determined at the moment of each Hall-effect sensor transition. Between the transitions, the instantaneous sine and cosine of the electrical rotor position can be estimated by

$$\frac{d\hat{c}}{dt} = -\hat{\omega}_r \hat{s} \quad (1)$$

$$\frac{d\hat{s}}{dt} = \hat{\omega}_r \hat{c}, \quad (2)$$

where  $\hat{\omega}_r$  is the estimated electrical rotor speed, and  $\hat{s}$  and  $\hat{c}$  are the estimated sine and cosine of the electrical rotor position, respectively. By assuming the electrical rotor speed is a constant during each Hall-effect sensor state,  $\hat{\omega}_r$  is estimated by

$$\hat{\omega}_r = \frac{\Delta\theta_r}{\Delta t}, \quad (3)$$

where  $\Delta\theta_r$  is the electrical rotor angle difference between the current and previous transitions of the Hall-effect sensors and  $\Delta t$  is the time interval between the current and previous transitions. The values of  $s$  and  $c$  can be bounded in each sensor state to limit the estimation error between transitions, and the boundaries corresponding to each state can be obtained from Fig. 1.

The hybrid observer has been shown to have good performance when no noise exists in the output of the binary Hall-effect sensors. However, once one of the output of Hall-effect sensors has a short glitch, the hybrid observer cannot estimate the rotor position correctly. Without any new glitches, this incorrect estimation takes several Hall-effect sensor transitions to disappear. Such sensor noise has been observed experimentally. In particular, the output of one of the Hall-effect sensors for an 8-hp brushless dc motor is shown in Fig. 2 (a). It can be seen that a glitch occurs at approximately 85 ms, and this glitch is shown in closer proximity to the glitch in Fig. 2 (b). This glitch lasts approximately 40  $\mu$ s and can cause errors in rotor position estimation without an improvement in noise immunity.

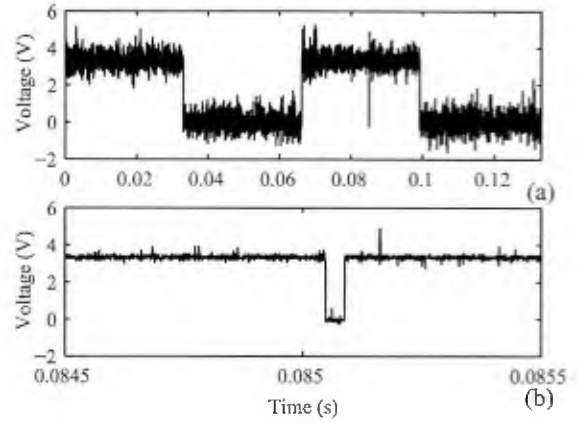


Fig. 2. Experimentally observed Hall-effect sensor noise

Herein, a finite state machine is used to filter noise from a given Hall-effect sensor. The finite state machine maintains a Hall-effect state and a counter. The Hall-effect sensor output is sampled with a sampling time of  $t_{sample}$ . If the output is high, the counter is incremented, and the counter is decremented if the output is low. If the Hall-effect state was previously low and the counter reaches  $N$ , the Hall-effect state transitions to high. Likewise, if the Hall-effect state was previously high and the counter reaches zero, the Hall-effect state transitions to low. The value of  $N$  is given by

$$N = \frac{t_g}{t_{sample}}. \quad (4)$$

In this way, detection of a Hall-effect state transition is delayed (on average by  $t_g$ ), but false transitions are ignored. Such a state machine is implemented for each of the Hall-effect sensors.

The implementation of the state machines will reduce the effects of false Hall-effect sensor transitions, but it will also increase the delay of detecting true transitions. The hybrid position observer can be modified to compensate for this delay. In particular, the values to which the estimates of the sine and cosine of the rotor position should be reset must be adjusted based on the average transition delay  $t_g$ . If  $s^*$  and  $c^*$  represent the values of the sine and cosine at rotor position  $\theta^*$  corresponding to a given Hall-effect sensor transition, the reset values when this transition is detected (i.e.,  $t_g$  later than the actual transition) are calculated as

$$\hat{s} := \sin(\theta^* + \hat{\omega}_r t_g) \approx s^* + c^* \hat{\omega}_r t_g \quad (5)$$

$$\hat{c} := \cos(\theta^* + \hat{\omega}_r t_g) \approx c^* - s^* \hat{\omega}_r t_g, \quad (6)$$

where the first-order approximations are suitable for microcontroller implementation because  $t_g$  is small. The values of  $\hat{s}$  and  $\hat{c}$  at each Hall-effect sensor transition are listed in Table I, where  $x$  denotes the sensor in which a transition occurs.

In a similar way, the boundaries for  $\hat{s}$  and  $\hat{c}$  for each Hall-effect sensor state must be enlarged to account for the delay in detecting the transition to the next state. In particular, the electrical rotor position can be expected to exceed the

TABLE I  
RESET VALUES

Transition	HS1	HS2	HS3	$\hat{s}$	$\hat{c}$
HS1	x	0	1	$-\frac{\sqrt{3}}{2} + \frac{1}{2}\hat{\omega}_r t_g$	$\frac{1}{2} + \frac{\sqrt{3}}{2}\hat{\omega}_r t_g$
HS1	x	1	0	$\frac{\sqrt{3}}{2} - \frac{1}{2}\hat{\omega}_r t_g$	$-\frac{1}{2} - \frac{\sqrt{3}}{2}\hat{\omega}_r t_g$
HS2	0	x	1	$\hat{\omega}_r t_g$	1
HS2	1	x	0	$-\hat{\omega}_r t_g$	-1
HS3	0	1	x	$\frac{\sqrt{3}}{2} + \frac{1}{2}\hat{\omega}_r t_g$	$\frac{1}{2} - \frac{\sqrt{3}}{2}\hat{\omega}_r t_g$
HS3	1	0	x	$-\frac{\sqrt{3}}{2} - \frac{1}{2}\hat{\omega}_r t_g$	$-\frac{1}{2} + \frac{\sqrt{3}}{2}\hat{\omega}_r t_g$

boundary by  $|\hat{\omega}_r|t_g$  before the next transition is detected. This boundary expansion is applied for both counterclockwise and clockwise rotation. The new boundaries for each Hall-effect sensor state can be estimated using a similar first-order approximation to that given in (5) and (6), and these boundaries are listed in Table II, where  $\hat{s}_{max}$  and  $\hat{s}_{min}$  are the maximum and minimum value of estimated sine of electrical rotor position for each Hall-effect sensor state, respectively, and  $\hat{c}_{max}$  and  $\hat{c}_{min}$  are the maximum and minimum value of estimated cosine of electrical rotor position for each Hall-effect sensor state, respectively.

### III. SIMULATION RESULTS

Simulations of the responses of the original hybrid position observer and the proposed hybrid position observer are performed. The electrical rotor position  $\theta_r$  is assumed to be differentiable. The true outputs of HS1–3 are high when  $\cos(\theta_r - \frac{7\pi}{6})$ ,  $\cos(\theta_r - \frac{\pi}{2})$ , and  $\cos(\theta_r - \frac{11\pi}{6})$  are positive, respectively. The sampling time for both observers is 100 kHz, and  $N$  for the proposed observer is 16. The initial value of the state variables  $\hat{s}$ ,  $\hat{c}$  are set to the correct initial values (i.e., those corresponding to the initial rotor position).

Two sets of studies are performed. In the first set, the rotor speed is constant, and the performance of the two observers is compared for both non-noisy and noisy conditions. In the second set, the rotor speed varies, and the performance is again compared for non-noisy and noisy conditions. The noise is modeled by the following process, which is applied independently to each of the three Hall-effect sensors. Glitches arrive according to an exponential distribution with mean time between the conclusion of the previous glitch and the arrival of the following glitch of 3 ms. The duration of each glitch is modeled by a uniform distribution between 0 ms and 0.15 ms. During a glitch, the observed output of the glitched Hall-effect sensor is the logical complement of the true output.

#### A. Steady-state performance

In the first set of studies, the electrical rotor speed is constant at  $120\pi$  rad/s. The observers are simulated for two electrical periods. The results of the non-noisy case are shown in Fig. 3. It can be seen that the sine and cosine estimates of the electrical rotor position from both hybrid observers are essentially identical and essentially identical with the true sine and cosine of the electrical rotor position in this case. The implementation of the proposed method has no detrimental

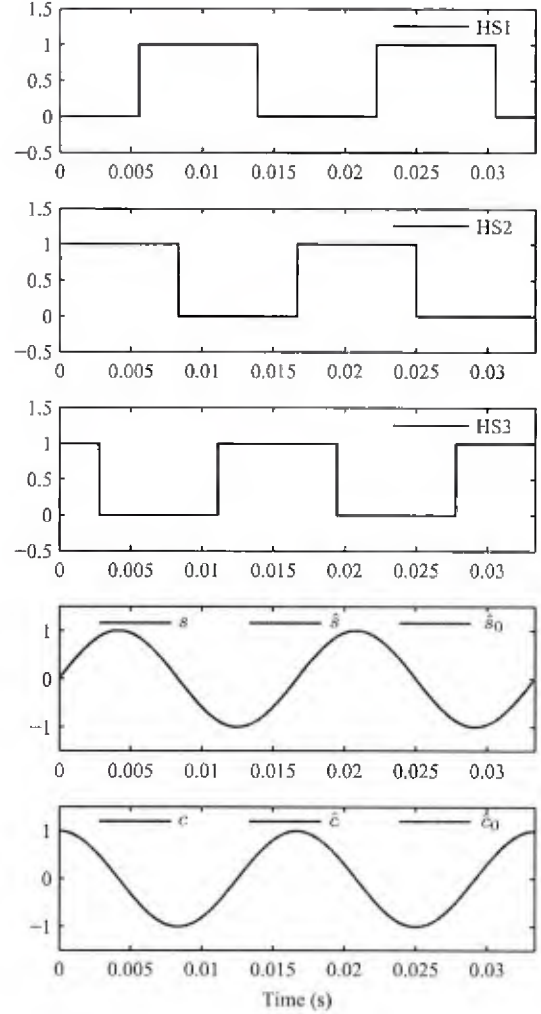


Fig. 3. Simulation results with constant rotor speed and non-noisy conditions. HS1–3 indicate the Hall-effect sensor outputs.  $s$  and  $c$  indicate the true sine and cosine of the electrical rotor position.  $\hat{s}$  and  $\hat{c}$  indicate the estimates of the sine and cosine of the electrical rotor position produced by the proposed observer.  $\hat{s}_0$  and  $\hat{c}_0$  indicate the estimates of the sine and cosine of the electrical rotor position produced by the original observer.

effect on observer performance in this case. In particular, the delay in detecting the Hall-effect sensor transitions does not negatively affect the performance.

The simulation results under noisy conditions are shown in Fig. 4. It can be seen that the original hybrid observer struggles with the noisy conditions throughout the simulation duration, producing estimates that are neither smooth nor correct at many times. It can also be seen that the sine and cosine estimates of the electrical rotor position by the proposed hybrid observer match the true values under these noisy conditions.

#### B. Transient performance

In the second set of studies, the electrical rotor speed is increased linearly from  $40\pi$  rad/s to  $160\pi$  rad/s over the 0.1-s simulation time. The results of the non-noisy case are shown in Fig. 5. It can be seen that the sine and cosine estimates of

TABLE II  
BOUNDARY OF THE HALL-EFFECT SENSOR STATE

State			$\hat{s}_{max}$	$\hat{s}_{min}$	$\hat{c}_{max}$	$\hat{c}_{min}$
HS1	HS2	HS3				
0	1	1	$\frac{\sqrt{3}}{2} + \frac{1}{2} \dot{\omega}_r t_g$	$- \dot{\omega}_r t_g$	1	$\frac{1}{2} - \frac{\sqrt{3}}{2} \dot{\omega}_r t_g$
0	1	0	1	$\frac{\sqrt{3}}{2} - \frac{1}{2} \dot{\omega}_r t_g$	$\frac{1}{2} + \frac{\sqrt{3}}{2} \dot{\omega}_r t_g$	$-\frac{1}{2} - \frac{\sqrt{3}}{2} \dot{\omega}_r t_g$
1	1	0	$\frac{\sqrt{3}}{2} + \frac{1}{2} \dot{\omega}_r t_g$	$- \dot{\omega}_r t_g$	$-\frac{1}{2} + \frac{\sqrt{3}}{2} \dot{\omega}_r t_g$	-1
1	0	0	$ \dot{\omega}_r t_g$	$-\frac{\sqrt{3}}{2} - \frac{1}{2} \dot{\omega}_r t_g$	$-\frac{1}{2} + \frac{\sqrt{3}}{2} \dot{\omega}_r t_g$	-1
1	0	1	$-\frac{\sqrt{3}}{2} + \frac{1}{2} \dot{\omega}_r t_g$	-1	$\frac{1}{2} + \frac{\sqrt{3}}{2} \dot{\omega}_r t_g$	$-\frac{1}{2} - \frac{\sqrt{3}}{2} \dot{\omega}_r t_g$
0	0	1	$ \dot{\omega}_r t_g$	$-\frac{\sqrt{3}}{2} - \frac{1}{2} \dot{\omega}_r t_g$	1	$\frac{1}{2} - \frac{\sqrt{3}}{2} \dot{\omega}_r t_g$

the electrical rotor position from both hybrid observers are essentially identical. It can be seen that small errors exist between the two observers and the true sine and cosine of the electrical rotor position at lower speeds. These errors are unlikely to affect drive performance significantly.

The simulation results under noisy conditions are shown in Fig. 6. The original hybrid observer cannot find the correct electrical rotor position during the transient at many times. The sine and cosine estimates of electrical rotor position estimated by proposed hybrid observer has good performance under these noisy conditions, matching the performance under non-noisy conditions.

#### IV. CONCLUSION

A noise immunity improvement for hybrid position observers for brushless dc motor drives is proposed in this paper. The proposed approach using finite state machines allows short glitches in the output of the Hall-effect sensors to be ignored. This improves noise immunity, but it also delays detection of Hall-effect sensor transitions, which is compensated in the proposed observer. The simulation results show that the proposed method has good performance under high noise conditions during steady-state and transient operation.

#### REFERENCES

- [1] A. Darba, F. De Belie, and J. Melkebeek, "Sensorless commutation and speed control of brushless dc-machine drives based on the back-emf symmetric threshold-tracking," in *IEEE Int. Electric Machines Drives Conf.*, May 2013, pp. 492–497.
- [2] P. Champa, P. Somsiri, P. Wipasuramonton, and P. Nakmahachalasint, "Initial rotor position estimation for sensorless brushless dc drives," *IEEE Trans. Ind. Appl.*, vol. 45, no. 4, pp. 1318–1324, July 2009.
- [3] M. Härke, G. De Donato, F. Capponi, T. Tesch, and R. Lorenz, "Implementation issues and performance evaluation of sinusoidal, surface-mounted pm machine drives with hall-effect position sensors and a vector-tracking observer," *IEEE Trans. Ind. Appl.*, vol. 44, no. 1, pp. 161–173, Jan 2008.
- [4] K. Corzine and S. Sudhoff, "A hybrid observer for high performance brushless dc motor drives," *IEEE Trans. Energy Convers.*, vol. 11, no. 2, pp. 318–323, Jun 1996.
- [5] S. Morimoto, M. Sanada, and Y. Takeda, "Sinusoidal current drive system of permanent magnet synchronous motor with low resolution position sensor," in *IEEE IAS Annu. Meeting*, vol. 1, Oct 1996, pp. 9–14.
- [6] G. Scelba, G. De Donato, G. Scarcella, F. Capponi, and F. Bonaccorso, "Fault-tolerant rotor position and velocity estimation using binary hall-effect sensors for low-cost vector control drives," *IEEE Trans. Ind. Appl.*, vol. 50, no. 5, pp. 3403–3413, Sept 2014.
- [7] Y.-P. Yang and Y.-Y. Ting, "Improved angular displacement estimation based on hall-effect sensors for driving a brushless permanent-magnet motor," *IEEE Trans. Ind. Electron.*, vol. 61, no. 1, pp. 504–511, Jan 2014.

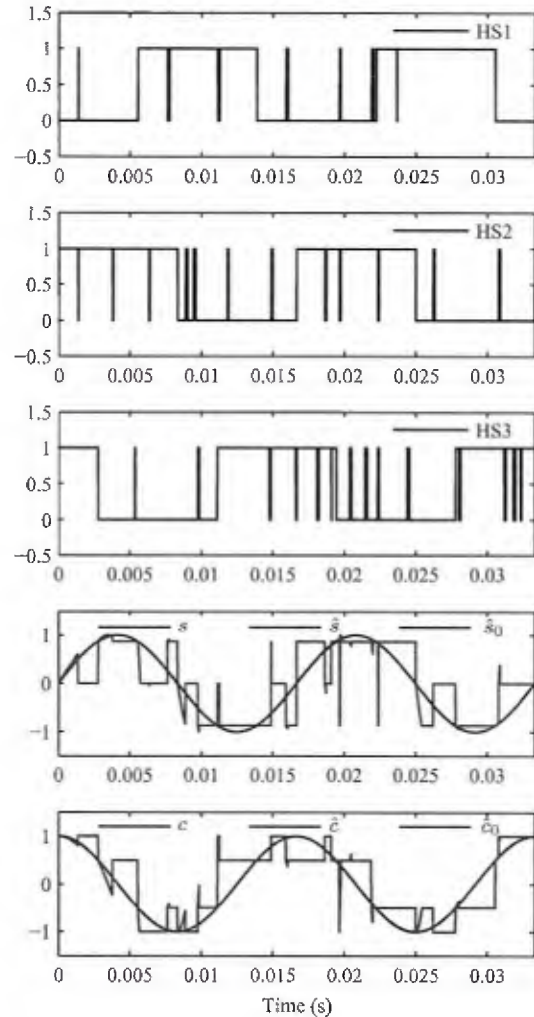


Fig. 4. Simulation results with constant rotor speed and noisy conditions. HS1–3 indicate the Hall-effect sensor outputs.  $s$  and  $c$  indicate the true sine and cosine of the electrical rotor position.  $\hat{s}$  and  $\hat{c}$  indicate the estimates of the sine and cosine of the electrical rotor position produced by the proposed observer.  $\hat{s}_0$  and  $\hat{c}_0$  indicate the estimates of the sine and cosine of the electrical rotor position produced by the original observer.

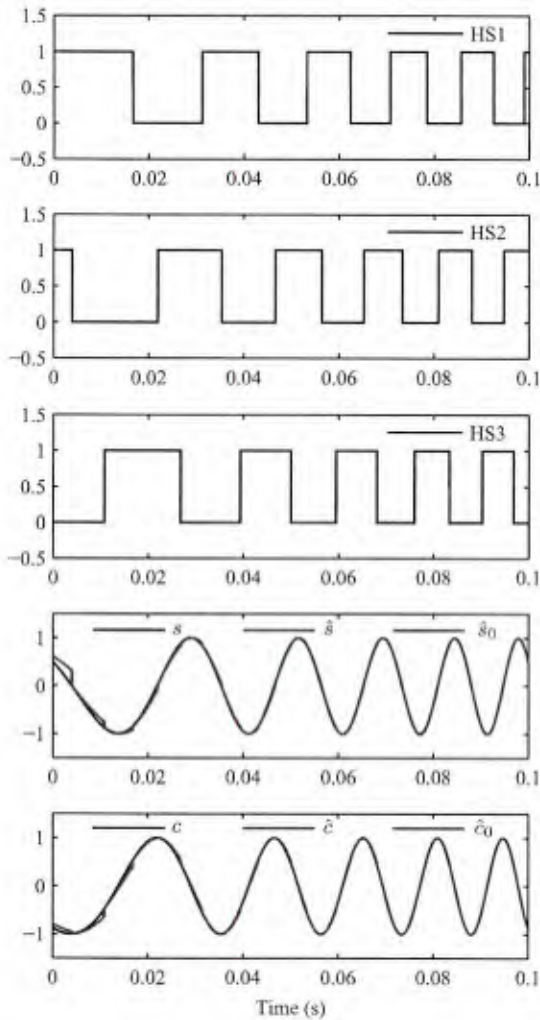


Fig. 5. Simulation results with varying rotor speed and non-noisy conditions. HS1–3 indicate the Hall-effect sensor outputs,  $s$  and  $c$  indicate the true sine and cosine of the electrical rotor position.  $\hat{s}$  and  $\hat{c}$  indicate the estimates of the sine and cosine of the electrical rotor position produced by the proposed observer.  $\hat{s}_0$  and  $\hat{c}_0$  indicate the estimates of the sine and cosine of the electrical rotor position produced by the original observer.

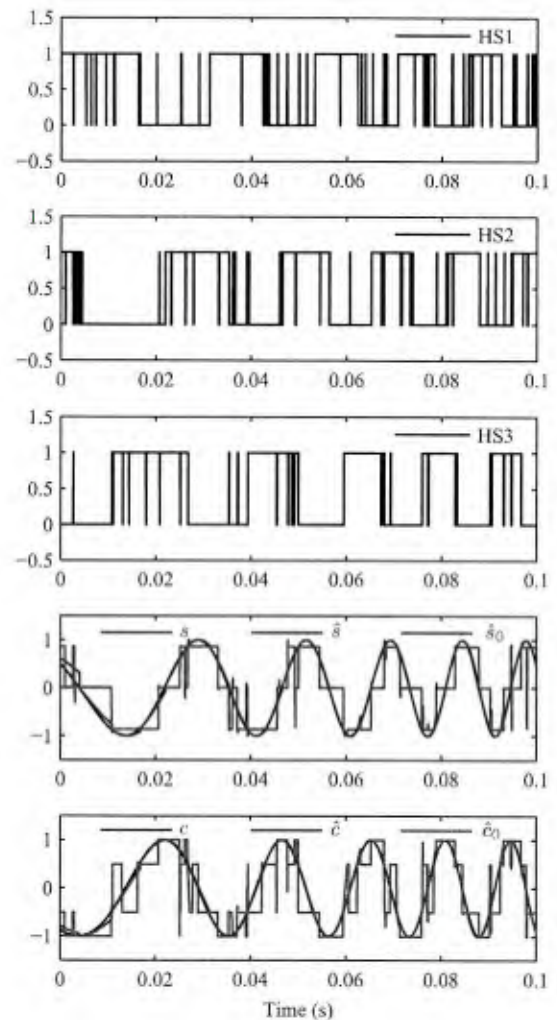


Fig. 6. Simulation results with varying rotor speed and noisy conditions. HS1–3 indicate the Hall-effect sensor outputs,  $s$  and  $c$  indicate the true sine and cosine of the electrical rotor position,  $\hat{s}$  and  $\hat{c}$  indicate the estimates of the sine and cosine of the electrical rotor position produced by the proposed observer.  $\hat{s}_0$  and  $\hat{c}_0$  indicate the estimates of the sine and cosine of the electrical rotor position produced by the original observer.

# Unified Model Formulations for Synchronous Machine Model With Saturation and Arbitrary Rotor Network Representation

YuQi Zhang, *Student Member, IEEE*, and Aaron M. Cramer, *Senior Member, IEEE*

**Abstract**—Numerous models and formulations have been used to study synchronous machines in different applications. Herein, a unified derivation of the various model formulations, which support direct interface to external circuitry in a variety of scenarios, is presented. A synchronous machine model with magnetizing path saturation including cross saturation and an arbitrary rotor network representation is considered. This model has been extensively experimentally validated and includes most existing machine models as special cases. Derivations of the standard voltage-in, current-out formulation as well as formulations in which the stator and/or the field windings are represented in a voltage-behind-reactance form are presented in a unified manner, including the derivation of a field-only voltage-behind-reactance formulation. The formulations are compared in a variety of simulation scenarios to show the relative advantages in terms of time steps, run time, and accuracy. It has been demonstrated that selection of the formulation with the most suitable interface for the simulation scenario has better accuracy, fewer time steps, and less run time.

**Index Terms**—AC machines, electric machines, modeling, simulation.

## I. INTRODUCTION

**A**NALYTICAL modeling of synchronous machines is essential for power systems analysis and studies and other important applications such as the study of dc power systems and rotating rectifiers [1]–[7]. Various models have been proposed from a wide range of perspectives and applications. Specifically, many of these models are derived based on Park's transformation [8]. By transformation to the rotor reference frame, the corresponding equations become time invariant, the state variables become constant in the steady state, and the machine analysis is simplified.

Many improvements to synchronous machine models have been offered. Some models have included alternative rotor networks [9]–[15], e.g., differential leakage inductance to account for unequal coupling of rotor windings with respect to stator windings. Other models have included magnetizing path saturation in the  $d$ -axis [16] or using equivalent isotropic models [17], [18]. The model considered herein, which was proposed

in [19], includes arbitrary linear rotor networks and a general magnetizing path saturation representation that includes cross-saturation. This model has been extensively validated in hardware [19]–[22], and most existing machine models (e.g., the standard  $qd$  model, [15], [16], [23]) are special cases of this model.

While the machine model encompasses the mathematical equations used to represent the machine, the formulation is used herein to indicate the particular arrangement of these equations in order to perform time-domain simulation. A given machine model can have multiple formulations that are each better suited for certain types of simulations. One such case is the consideration of machine-rectifier interactions. For such scenarios, the use of traditional voltage-in, current-out (or signal-flow) formulations results in an interface mismatch between the machine and the rectifier, which is more conducive to a circuit representation. This mismatch can be resolved by inserting fictitious circuit elements (e.g., resistors), but this can lead to inaccuracy and to longer simulation run times [24]. Such situations have been studied using phase-domain (PD) circuit formulations [25]–[30]. In [24], a voltage-behind-reactance (VBR) formulation that achieves direct interfacing between machine models and external networks is derived. This formulation separates the rotor dynamics from the stator circuit representation to achieve better numerical efficiency than PD formulations. In [16], this formulation was extended to models including  $d$ -axis saturation. An interesting recent set of formulations have involved constant-parameter VBR formulations, which can greatly decrease run time [31], [32]. These models inherently require additional model approximations and are beyond the scope of the present work.

Multiple formulations of the model considered herein have been derived [19], [20], [22]. In [20], a voltage-in, current-out ( $qd$ ) formulation is proposed. A stator-only VBR (SVBR) formulation is derived in [19]. A stator and field VBR (SFVBR) formulation was set forth in [22]. Each of these formulations have been successful for certain simulation applications, but these formulations have each entailed complicated derivations with little commonality. Herein, a unified derivation of the model formulations is presented, which avoids the diverse notation, realizations, and transformations found in previous derivations, a field-only VBR (FVBR) formulation that completes the set of formulations for this model is derived, and the relative advantages of each formulation in different simulation applications are demonstrated.

Manuscript received August 27, 2015; revised February 8, 2016; accepted May 30, 2016. Date of publication June 12, 2016; date of current version November 22, 2016. This work was supported by the Office of Naval Research through the United States Naval Academy N00189-14-P-1197 and through the ONR Young Investigator Program N00014-15-1-2475. Paper no. TEC-00617-2015.

The authors are with the University of Kentucky, Lexington, KY 40506 USA (e-mail: yuqi.zhang@uky.edu; aaron.cramer@uky.edu).

Color versions of one or more of the figures in this paper are available online at <http://ieeexplore.ieee.org>.

Digital Object Identifier 10.1109/TEC.2016.2580320

The contributions of this work are: 1) the unified derivation of model formulations for the synchronous machine model, 2) the development of the FVBR formulation, and 3) the demonstration of the relative advantages of the formulations. The remainder of this work is organized as follows. In Section II, the mathematical notation used herein is defined. Section III details the synchronous machine model in sufficient detail to present the model formulations. The model formulations are included in Section IV. Results demonstrating the relative performance of the four synchronous machine formulations are shown and compared in Section V, which is followed by a conclusion in Section VI.

## II. NOTATION

Matrices and vectors are bold faced. Stator phase variables can be represented in vector form as  $\mathbf{f}_{abc s} = [f_{as} \ f_{bs} \ f_{cs}]^T$ . The symbol  $f$  can represent voltage ( $v$ ), current ( $i$ ), or flux linkage ( $\lambda$ ). Such vector quantities can be transformed into the rotor reference frame using

$$\mathbf{f}_{qd0s} = \mathbf{K}_s(\theta_r) \mathbf{f}_{abc s} \quad (1)$$

where the transformation matrix [33] is given by

$$\mathbf{K}_s(\theta_r) = \frac{2}{3} \begin{bmatrix} \cos \theta_r & \cos(\theta_r - \frac{2\pi}{3}) & \cos(\theta_r + \frac{2\pi}{3}) \\ \sin \theta_r & \sin(\theta_r - \frac{2\pi}{3}) & \sin(\theta_r + \frac{2\pi}{3}) \\ \frac{1}{2} & \frac{1}{2} & \frac{1}{2} \end{bmatrix}. \quad (2)$$

The electrical angular position is given by

$$\theta_r = \frac{P}{2} \theta_{rm}, \quad (3)$$

where  $P$  is the number of magnetic poles in the machine and  $\theta_{rm}$  is the mechanical angular position of the machine. Similarly, the electrical angular velocity is given by

$$\omega_r = \frac{P}{2} \omega_{rm}, \quad (4)$$

where  $\omega_{rm}$  is the mechanical angular velocity of the machine. The components of  $\mathbf{f}_{qd0s} = [f_{qs} \ f_{ds} \ f_{0s}]^T$  are the  $q$ - and  $d$ -axis components and the zero-sequence component of the quantity, respectively. When the zero-sequence component is omitted,  $\mathbf{f}_{qds} = [f_{qs} \ f_{ds}]^T$ . The notation  $\mathbf{f}_{dq0s} = [f_{ds} \ -f_{qs} \ 0]^T$  is used for speed voltage terms, and  $\mathbf{f}_{dqs} = [f_{ds} \ -f_{qs}]^T$  when the zero-sequence component is omitted. Throughout, the operator  $p$  denotes differentiation with respect to time.

## III. SYNCHRONOUS MACHINE MODEL

The synchronous machine model that is considered herein is presented in [21] and shown in Fig. 1. It can be seen that the model features arbitrary linear networks to represent the rotor circuits and magnetizing path saturation including cross-saturation. The details of the model that are necessary to derive the relevant formulations are presented below.

The stator voltages are given by

$$\mathbf{v}_{abc s} = r_s \mathbf{i}_{abc s} + p \boldsymbol{\lambda}_{abc s}, \quad (5)$$

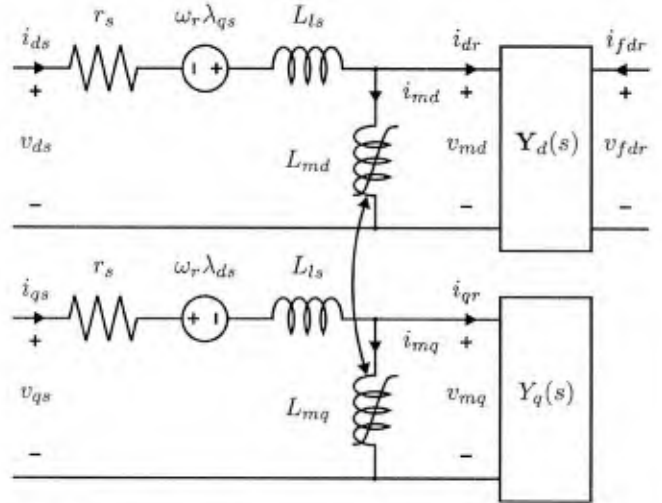


Fig. 1. Synchronous machine model in rotor reference frame.

where  $r_s$  is the stator resistance. Transforming (5) into the rotor reference frame using (1) yields

$$\mathbf{v}_{qd0s} = r_s \mathbf{i}_{qd0s} + \omega_r \boldsymbol{\lambda}_{dq0s} + p \boldsymbol{\lambda}_{qd0s}. \quad (6)$$

The stator  $q$ - and  $d$ -axis flux linkages can be divided into a leakage term and a magnetizing term:

$$\boldsymbol{\lambda}_{qds} = L_{ls} \mathbf{i}_{qds} + \boldsymbol{\lambda}_{mqd}, \quad (7)$$

where  $L_{ls}$  is the stator leakage inductance and  $\boldsymbol{\lambda}_{mqd} = [\lambda_{mq} \ \lambda_{md}]^T$  are the magnetizing flux linkages. By Faraday's law, the magnetizing voltages are equal to the time derivatives of the magnetizing flux linkages:

$$\mathbf{v}_{mqd} = p \boldsymbol{\lambda}_{mqd}. \quad (8)$$

By substitution of (7) into (6), the  $q$ - and  $d$ -axis stator voltages can be expressed as

$$\mathbf{v}_{qds} = r_s \mathbf{i}_{qds} + \omega_r L_{ls} \mathbf{i}_{dq s} + L_{ls} p \mathbf{i}_{qds} + \omega_r \boldsymbol{\lambda}_{mdq} + \mathbf{v}_{mqd}, \quad (9)$$

where  $\boldsymbol{\lambda}_{mdq} = [\lambda_{md} \ -\lambda_{mq}]^T$ . The stator zero-sequence flux linkage can be expressed as

$$\lambda_{0s} = L_{ls} i_{0s}. \quad (10)$$

Substitution of (10) into (6) yields the following expression for the zero sequence stator voltage:

$$v_{0s} = r_s i_{0s} + L_{ls} p i_{0s}. \quad (11)$$

The magnetizing currents are related to the magnetizing flux linkages by

$$i_{mq} = \Gamma_{mq}(\hat{\lambda}_m) \lambda_{mq} \quad (12)$$

$$i_{md} = \Gamma_{md}(\hat{\lambda}_m) \lambda_{md}, \quad (13)$$

where  $\Gamma_{mq}(\cdot)$  and  $\Gamma_{md}(\cdot)$  are inverse inductance functions related to the representation of saturation,

$$\hat{\lambda}_m = \sqrt{\lambda_{md}^2 + \alpha \lambda_{mq}^2}, \quad (14)$$

and  $\alpha$  is a saliency-dependent parameter. The relationship between the time derivatives of the magnetizing currents and of the magnetizing flux linkages is given by

$$p\mathbf{i}_{mqd} = \mathbf{\Gamma}_{mi}(\boldsymbol{\lambda}_{mqd})p\boldsymbol{\lambda}_{mqd} = \mathbf{\Gamma}_{mi}(\boldsymbol{\lambda}_{mqd})\mathbf{v}_{mqd}, \quad (15)$$

where the incremental inverse inductance matrix is given by

$$\mathbf{\Gamma}_{mi}(\boldsymbol{\lambda}_{mqd}) = \begin{bmatrix} \frac{d\Gamma_{mq}(\hat{\lambda}_m)}{d\hat{\lambda}_m} \frac{\alpha\lambda_{mq}^2}{\hat{\lambda}_m} + \Gamma_{mq}(\hat{\lambda}_m), & \frac{d\Gamma_{mq}(\hat{\lambda}_m)}{d\hat{\lambda}_m} \frac{\lambda_{mq}\lambda_{md}}{\hat{\lambda}_m} \\ \frac{d\Gamma_{md}(\hat{\lambda}_m)}{d\hat{\lambda}_m} \frac{\alpha\lambda_{mq}\lambda_{md}}{\hat{\lambda}_m}, & \frac{d\Gamma_{md}(\hat{\lambda}_m)}{d\hat{\lambda}_m} \frac{\lambda_{md}^2}{\hat{\lambda}_m} + \Gamma_{md}(\hat{\lambda}_m) \end{bmatrix}. \quad (16)$$

Because a lossless coupling field is assumed, a functional constraint of  $\Gamma_{md}(\cdot)$  and  $\Gamma_{mq}(\cdot)$  is necessary, which renders the incremental inverse inductance matrix symmetric [20].

The rotor circuit is represented in both the  $q$ - and  $d$ -axes by an arbitrary linear network. In particular, the  $d$ -axis is described by

$$p\mathbf{x}_d = \mathbf{A}_d\mathbf{x}_d + \mathbf{B}_d \begin{bmatrix} v_{md} \\ v_{fdr} \end{bmatrix} \quad (17)$$

$$\begin{bmatrix} i_{dr} \\ i_{fdr} \end{bmatrix} = \mathbf{C}_d\mathbf{x}_d, \quad (18)$$

and the  $q$ -axis is described by

$$p\mathbf{x}_q = \mathbf{A}_q\mathbf{x}_q + \mathbf{b}_q v_{mq} \quad (19)$$

$$i_{qr} = \mathbf{c}_q^T \mathbf{x}_q. \quad (20)$$

The matrices  $\mathbf{A}_d$ ,  $\mathbf{B}_d$ , and  $\mathbf{C}_d$  are a minimal realization of the  $d$ -axis rotor network transfer function, denoted by  $\mathbf{Y}_d(s)$  in Fig. 1, and the components of  $\mathbf{x}_d$  are state variables associated with this realization. Likewise, the matrix  $\mathbf{A}_q$  and the vectors  $\mathbf{b}_q$  and  $\mathbf{c}_q$  are a minimal realization of the  $q$ -axis rotor network transfer function, denoted  $Y_q(s)$ , and the components of  $\mathbf{x}_q$  are its state variables.

It is generally possible by linear transformation to have

$$\mathbf{C}_d = [\mathbf{I}_2 \ \mathbf{0}] \quad (21)$$

$$\mathbf{c}_q^T = [1 \ \mathbf{0}^T]. \quad (22)$$

The construction of such a transformation is given in the appendix. When such a transformation has been applied, it is possible to partition the  $d$ -axis linear system as

$$\begin{bmatrix} pi_{dr} \\ pi_{fdr} \\ p\mathbf{x}_{d3} \end{bmatrix} = \begin{bmatrix} a_{d11} & a_{d12} & \mathbf{a}_{d13}^T \\ a_{d21} & a_{d22} & \mathbf{a}_{d23}^T \\ \mathbf{a}_{d31} & \mathbf{a}_{d32} & \mathbf{A}_{d33} \end{bmatrix} \begin{bmatrix} i_{dr} \\ i_{fdr} \\ \mathbf{x}_{d3} \end{bmatrix} + \begin{bmatrix} b_{d11} & b_{d12} \\ b_{d21} & b_{d22} \\ \mathbf{b}_{d31} & \mathbf{b}_{d32} \end{bmatrix} \begin{bmatrix} v_{md} \\ v_{fdr} \end{bmatrix}. \quad (23)$$

Likewise, the  $q$ -axis system can be partitioned as

$$\begin{bmatrix} pi_{qr} \\ p\mathbf{x}_{q2} \end{bmatrix} = \begin{bmatrix} a_{q11} & \mathbf{a}_{q12}^T \\ \mathbf{a}_{q21} & \mathbf{A}_{q22} \end{bmatrix} \begin{bmatrix} i_{qr} \\ \mathbf{x}_{q2} \end{bmatrix} + \begin{bmatrix} b_{q1} \\ \mathbf{b}_{q2} \end{bmatrix} v_{mq}. \quad (24)$$

By Kirchhoff's current law,

$$\mathbf{i}_{qds} = \mathbf{i}_{mqd} + \mathbf{i}_{qdr}. \quad (25)$$

Using this current relationship, the magnetizing voltages  $\mathbf{v}_{mqd}$  can be eliminated from the equations. Differentiating (25) with respect to time and substituting (15), (23) and (24) yields

$$\begin{aligned} p\mathbf{i}_{qds} &= \left( \mathbf{\Gamma}_{mi}(\boldsymbol{\lambda}_{mqd}) + \begin{bmatrix} b_{q1} & \\ & b_{d11} \end{bmatrix} \right) \mathbf{v}_{mqd} \\ &+ \begin{bmatrix} a_{q11} & \\ & a_{d11} \end{bmatrix} \mathbf{i}_{qdr} + \begin{bmatrix} \mathbf{a}_{q12}^T \mathbf{x}_{q2} \\ \mathbf{a}_{d13}^T \mathbf{x}_{d3} \end{bmatrix} \\ &+ \begin{bmatrix} 0 \\ a_{d12} \end{bmatrix} i_{fdr} + \begin{bmatrix} 0 \\ b_{d12} \end{bmatrix} v_{fdr}. \end{aligned} \quad (26)$$

Substituting (26) into (9) and solving for  $\mathbf{v}_{mqd}$  results in the following:

$$\begin{aligned} \mathbf{v}_{mqd} &= \mathbf{M} \left[ \mathbf{v}_{qds} - r_s \mathbf{i}_{qds} - \omega_r L_{ls} \mathbf{i}_{dq s} - \omega_r \boldsymbol{\lambda}_{mdq} \right. \\ &- L_{ls} \left( \begin{bmatrix} a_{q11} & \\ & a_{d11} \end{bmatrix} \mathbf{i}_{qdr} + \begin{bmatrix} \mathbf{a}_{q12}^T \mathbf{x}_{q2} \\ \mathbf{a}_{d13}^T \mathbf{x}_{d3} \end{bmatrix} \right. \\ &\left. \left. + \begin{bmatrix} 0 \\ a_{d12} \end{bmatrix} i_{fdr} + \begin{bmatrix} 0 \\ b_{d12} \end{bmatrix} v_{fdr} \right) \right], \end{aligned} \quad (27)$$

where

$$\mathbf{M} = \left[ \mathbf{I}_2 + L_{ls} \left( \mathbf{\Gamma}_{mi}(\boldsymbol{\lambda}_{mqd}) + \begin{bmatrix} b_{q1} & \\ & b_{d11} \end{bmatrix} \right) \right]^{-1}. \quad (28)$$

The set of voltage equations can be rearranged into forms suitable for each of the model formulations. In particular, certain voltage equations must be represented in a form suitable for circuit representation for each formulation. For the SVBR formulation, solving (25) for  $\mathbf{i}_{qdr}$ , substituting into (26), solving for  $\mathbf{v}_{mqd}$ , substituting into (9), and combining with (11) yields

$$\begin{aligned} \mathbf{v}_{qd0s} &= r_s \mathbf{i}_{qd0s} + \omega_r L_{ls} \mathbf{i}_{dq0s} + L_{ls} p\mathbf{i}_{qd0s} \\ &+ \hat{\mathbf{R}}_m \mathbf{i}_{qd0s} + \hat{\mathbf{L}}_m p\mathbf{i}_{qd0s} + \mathbf{e}_{qd0s}, \end{aligned} \quad (29)$$

where the definitions of  $\hat{\mathbf{R}}_m$ ,  $\hat{\mathbf{L}}_m$ , and  $\mathbf{e}_{qd0s}$  are given in the appendix. Transforming (29) into phase variables yields

$$\mathbf{v}_{abcs} = \mathbf{R}\mathbf{i}_{abcs} + \mathbf{L}p\mathbf{i}_{abcs} + \mathbf{e}_{abcs}, \quad (30)$$

where the definitions of  $\mathbf{R}$ ,  $\mathbf{L}$ , and  $\mathbf{e}_{abcs}$  are given in the appendix.

For the FVBR formulation, substituting (27) into (23) and solving for  $v_{fdr}$  results in the following:

$$v_{fdr} = R i_{fdr} + L p i_{fdr} + e_{fdr}, \quad (31)$$

where the definitions of  $R$ ,  $L$ , and  $e_{fdr}$  are given in the appendix.

For the SFVBR formulation, substituting (27) into (9) and (23), solving for  $\mathbf{v}_{qds}$  and  $v_{fdr}$ , and combining with (11)

yields:

$$\begin{aligned} \begin{bmatrix} \mathbf{v}_{qd0s} \\ v_{fdr} \end{bmatrix} &= \mathbf{R}'_s \begin{bmatrix} \mathbf{i}_{qd0s} \\ i_{fdr} \end{bmatrix} + \begin{bmatrix} \omega_r L_{ls} \mathbf{i}_{dq0s} \\ 0 \end{bmatrix} \\ &+ \mathbf{L}'_s \begin{bmatrix} p\mathbf{i}_{qd0s} \\ pi_{fdr} \end{bmatrix} + \hat{\mathbf{R}}'_m \begin{bmatrix} \mathbf{i}_{qd0s} \\ i_{fdr} \end{bmatrix} \\ &+ \hat{\mathbf{L}}'_m \begin{bmatrix} p\mathbf{i}_{qd0s} \\ pi_{fdr} \end{bmatrix} + \begin{bmatrix} \mathbf{e}'_{qd0s} \\ e'_{fdr} \end{bmatrix}, \end{aligned} \quad (32)$$

where the definitions of  $\mathbf{R}'_s$ ,  $\mathbf{L}'_s$ ,  $\hat{\mathbf{R}}'_m$ ,  $\hat{\mathbf{L}}'_m$ ,  $\mathbf{e}'_{qd0s}$ , and  $e'_{fdr}$  are given in the appendix. Transforming (32) into phase variables yields

$$\begin{bmatrix} \mathbf{v}_{abcs} \\ v_{fdr} \end{bmatrix} = \mathbf{R}' \begin{bmatrix} \mathbf{i}_{abcs} \\ i_{fdr} \end{bmatrix} + \mathbf{L}' \begin{bmatrix} p\mathbf{i}_{abcs} \\ pi_{fdr} \end{bmatrix} + \begin{bmatrix} \mathbf{e}'_{abcs} \\ e'_{fdr} \end{bmatrix}, \quad (33)$$

where the definitions of  $\mathbf{R}'$ ,  $\mathbf{L}'$ , and  $\mathbf{e}'_{abcs}$  are given in the appendix.

#### IV. MODEL FORMULATIONS

Each of the formulations described below has a similar structure. For each formulation there is a set of state variables, which always includes the magnetizing flux linkages  $\lambda_{mqd}$ . The rotor mechanical speed  $\omega_{rm}$  and (if necessary) the rotor mechanical position  $\theta_{rm}$  are inputs to the model. Each formulation can be thought to operate in a subset of the following six stages. In the first stage, the initial calculations listed below are performed for each of the formulations.

- 1) Calculate  $\omega_r$  from (4) and (if necessary)  $\theta_r$  from (3).
- 2) Calculate  $\hat{\lambda}_m$  from (14) and  $\Gamma_{mq}(\hat{\lambda}_m)$  and  $\Gamma_{md}(\hat{\lambda}_m)$  from their definitions.
- 3) Calculate  $\Gamma_{mi}$  from (16).
- 4) Calculate  $\mathbf{i}_{mqd}$  from (12) and (13).

Depending on the formulation, currents are determined based on the state variables of the model and output to external signal-flow models of connected circuitry in the second stage. In the third stage, the external signal-flow models calculate voltages for such formulations. Depending on the formulation, the parameters of a VBR representation are calculated in the fourth stage. In the fifth stage, the VBR circuit model is combined with circuit models of connected circuitry, and a circuit solver is used to calculate voltages and currents for such formulations. In the final stage, the time derivatives of the state variables are calculated. In this stage, the torque developed by the synchronous machine is calculated by [19]

$$T_e = \frac{3P}{2} (i_{qs} \lambda_{md} - i_{ds} \lambda_{mq}), \quad (34)$$

which is used by the prime mover model to calculate the time derivatives of the mechanical state variables ( $\omega_{rm}$  and (if necessary)  $\theta_{rm}$ ).

##### A. $qd$ Formulation

For a  $qd$  formulation, the state variables of the model are  $\lambda_{mqd}$ ,  $\mathbf{i}_{qdr}$ ,  $i_{fdr}$ ,  $\mathbf{x}_{d3}$ , and  $\mathbf{x}_{q2}$ . If the zero-sequence components are to be represented,  $i_{0s}$  is an additional state variable of

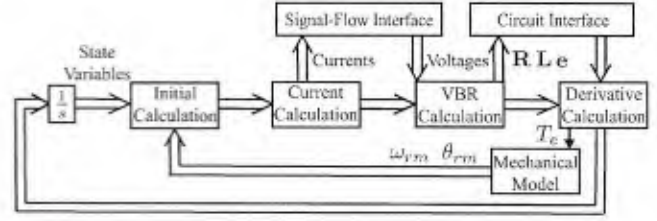


Fig. 2. Summary of model formulations. The integrators associated with the mechanical state variables are represented within the Mechanical Model block.

the model. Such a formulation requires the initial calculation, current calculation, signal-flow interface, and derivative calculation stages shown in Fig. 2. In the current calculation stage, the stator currents  $\mathbf{i}_{qds}$  (or  $\mathbf{i}_{qd0s}$  if the zero-sequence components are to be represented or  $\mathbf{i}_{abcs}$  if phase currents are to be used) and field current  $i_{fdr}$  are determined. The steps required in this stage are listed below.

- 1) Calculate  $\mathbf{i}_{qds}$  from (25). If the zero-sequence components are represented,  $i_{0s}$  is a state variable.
- 2) If necessary, transform  $\mathbf{i}_{qd0s}$  to  $\mathbf{i}_{abcs}$ .
- 3) The field current  $i_{fdr}$  is a state variable.

In the signal-flow interface stage, an external signal-flow model of circuitry connected to the stator and field is used to calculate the stator voltages  $\mathbf{v}_{qds}$  (or  $\mathbf{v}_{qd0s}$  or  $\mathbf{v}_{abcs}$ ) and the field voltage  $v_{fdr}$ .

In the derivative calculation stage, the time derivatives of the state variables are calculated. The steps required in this stage are listed below.

- 1) If necessary, transform  $\mathbf{v}_{abcs}$  to  $\mathbf{v}_{qd0s}$ .
- 2) Calculate  $\mathbf{v}_{mqd}$  from (27).
- 3) Calculate  $p\lambda_{mqd}$  from (8).
- 4) Calculate  $p\mathbf{i}_{qdr}$ ,  $pi_{fdr}$ ,  $p\mathbf{x}_{d3}$ , and  $p\mathbf{x}_{q2}$  from (23) and (24). If the zero-sequence components are represented, calculate  $pi_{0s}$  from (11).

##### B. SVBR Formulation

For an SVBR formulation, the state variables of the model are  $\lambda_{mqd}$ ,  $i_{fdr}$ ,  $\mathbf{x}_{d3}$ , and  $\mathbf{x}_{q2}$ . Such a formulation requires the initial calculation, current calculation, signal-flow interface, VBR calculation, circuit interface, and derivative calculation stages shown in Fig. 2. In the current calculation stage, the field current  $i_{fdr}$  is a state variable.

In the signal-flow interface stage, an external signal-flow model of circuitry connected to the field is used to calculate the field voltage  $v_{fdr}$ .

In the VBR calculation stage, the stator circuit parameters  $\mathbf{R}$ ,  $\mathbf{L}$ , and  $\mathbf{e}_{abcs}$  are calculated from (44)–(46).

In the circuit interface stage, the stator VBR circuit model is combined with circuit models of circuitry connected to the stator, and a circuit solver is used to calculate  $\mathbf{v}_{abcs}$  and  $\mathbf{i}_{abcs}$ .

In the derivative calculation stage, the time derivatives of the state variables are calculated. The steps required in this stage are listed below.

- 1) Transform  $\mathbf{v}_{abcs}$  and  $\mathbf{i}_{abcs}$  to  $\mathbf{v}_{qd0s}$  and  $\mathbf{i}_{qd0s}$ , respectively.
- 2) Calculate  $\mathbf{i}_{qdr}$  from (25).

- 3) Calculate  $\mathbf{v}_{mqd}$  from (27).
- 4) Calculate  $p\lambda_{mqd}$  from (8).
- 5) Calculate  $pi_{fdr}$ ,  $px_{d3}$ , and  $px_{q2}$  from (23) and (24).

### C. FVBR Formulation

For an FVBR formulation, the state variables of the model are  $\lambda_{mqd}$ ,  $i_{qdr}$ ,  $x_{d3}$  and  $x_{q2}$ . If the zero-sequence components are to be represented,  $i_{0s}$  is an additional state variable of the model. Such a formulation requires the initial calculation, current calculation, signal-flow interface, VBR calculation, circuit interface, and derivative calculation stages shown in Fig. 2. In the current calculation stage, the stator currents  $i_{qds}$  (or  $i_{qd0s}$  if the zero-sequence components are to be represented or  $i_{abc}$  if phase currents are to be used) are determined. The steps required in this stage are listed below.

- 1) Calculate  $i_{qds}$  from (25). If the zero-sequence components are represented,  $i_{0s}$  is a state variable.
- 2) If necessary, transform  $i_{qd0s}$  to  $i_{abc}$ .

In the signal-flow interface stage, an external signal-flow model of circuitry connected to the stator is used to calculate the stator voltages  $\mathbf{v}_{qds}$  (or  $\mathbf{v}_{qd0s}$  or  $\mathbf{v}_{abc}$ ). If necessary,  $\mathbf{v}_{abc}$  is transformed to  $\mathbf{v}_{qd0s}$ .

In the VBR calculation stage, the field circuit parameters  $R$ ,  $L$ , and  $e_{fdr}$  are calculated from (61)–(63).

In the circuit interface stage, the field VBR circuit model is combined with a circuit model of circuitry connected to the field, and a circuit solver is used to calculate  $v_{fdr}$  and  $i_{fdr}$ .

In the derivative calculation stage, the time derivatives of the state variables are calculated. The steps required in this stage are listed below.

- 1) Calculate  $\mathbf{v}_{mqd}$  from (27).
- 2) Calculate  $p\lambda_{mqd}$  from (8).
- 3) Calculate  $pi_{qdr}$ ,  $px_{d3}$ , and  $px_{q2}$  from (23) and (24). If the zero-sequence components are represented, calculate  $pi_{0s}$  from (11).

### D. SFVBR Formulation

For an SFVBR formulation, the state variables of the model are  $\lambda_{mqd}$ ,  $x_{d3}$ , and  $x_{q2}$ . Such a formulation requires the initial calculation, the VBR calculation, circuit interface, and derivative calculation stages shown in Fig. 2. In the VBR calculation stage, the circuit parameters  $\mathbf{R}'$ ,  $\mathbf{L}'$ ,  $\mathbf{e}'_{abc}$  and  $e'_{fdr}$  can be calculated from (80)–(82) and (76).

In the circuit interface stage, the circuit parameters are combined with circuit representations of the interconnected equipment. This system is solved using a circuit solver to calculate  $\mathbf{v}_{abc}$ ,  $\mathbf{i}_{abc}$ ,  $v_{fdr}$ , and  $i_{fdr}$ .

The steps required in the derivative calculation stage to calculate the time derivatives of the state variables are below.

- 1) Transform  $\mathbf{v}_{abc}$  and  $\mathbf{i}_{abc}$  to  $\mathbf{v}_{qd0s}$  and  $\mathbf{i}_{qd0s}$ , respectively.
- 2) Calculate  $i_{qdr}$  from (25).
- 3) Calculate  $\mathbf{v}_{mqd}$  from (27).
- 4) Calculate  $p\lambda_{mqd}$  from (8).
- 5) Calculate  $px_{d3}$  and  $px_{q2}$  from (23) and (24).

## V. FORMULATION COMPARISON

In this section, the four model formulations are compared for four distinct cases. The machine model represents the 59-kW, 560-V, four-pole machine characterized in [21], where its parameters may be found. This model of the machine has been extensively validated in hardware in [19], [20], [22]. The simulations are performed using MATLAB R2014a Simulink's ode45 integration algorithm with a maximum time step of 83.3 ms, a relative tolerance of  $10^{-6}$ , and the default absolute tolerance, which is the maximum value that the state variable has assumed over the course of simulation times the relative tolerance [34]. Circuit elements are represented using the Automated State Model Generator, a software package that automatically establishes a state-space model based on the circuit topology [35]. In each case, initial conditions corresponding to steady-state are selected, and each simulation lasts 83.3 ms (5 cycles). The model formulations are all derived from a common set of model equations, but the case studies are selected such that each is most conducive to a particular formulation. For each case, the SFVBR, which makes no model interface approximations, is simulated at a maximum time step of 1  $\mu$ s. For each formulation and each case, the rms errors of the  $i_{as}$  and  $i_{fdr}$  waveforms with respect to the reference waveforms are calculated. These values are normalized by the rms value of the non-average component of the reference waveforms. Also, the run time associated with each formulation and case is recorded by averaging over 20 simulations. The simulations are performed on Intel(R) Core(TM) i7-3770 CPU @3.40 GHz and 8.00 GB RAM.

In Case I, the field winding is excited by a 30-V source, the stator is connected to an infinite 560-V bus, the machine is rotating at 1800 r/min, and the initial rotor angle is  $\pi/8$  rad. The rotor speed increases linearly to 1912.5 r/min over 8.3 ms starting at 20 ms and then decreases linearly back to 1800 r/min at the same rate. This results in the rotor angle increasing to  $3\pi/16$  rad. This case can be studied without introducing any model interface approximations because it is consistent with voltage-in, current-out representations of both the stator and field windings. The time steps, run time, and error results for Case I (and all of the cases) are shown in Table I. It can be seen that each formulation has negligible error in both the stator and field currents because none of the formulations require interface approximations. Because the  $qd$  formulation is simpler and does not involve time-varying circuit elements, it has the fewest time steps and fastest run time. In terms of time steps, there is about a factor of four penalty for simulating in  $abc$  variables on the stator when it is unnecessary (SVBR and SFVBR versus  $qd$  and FVBR). There is relatively little cost to using the circuit model of the field even when it is not required ( $qd$  versus FVBR), which can also be seen in Case II below.

In Case II, the field winding is also excited by a 30-V source, but the stator supplies a rectifier load with  $LC$  filter and constant-current dc load of 48 A shown in Fig. 3. The filter inductance and capacitance are 2.5 mH and 1.4 mF, respectively, and the machine is rotating at 1800 r/min. In such a situation, an

TABLE I  
CASE RESULTS

Case	Formulation	Time steps	Run time (s)	$i_{nserr}$ (%)	$i_{fderr}$ (%)
Case I	$qd$	580	0.30	0.00	0.00
	SVBR	2098	0.54	0.00	0.00
	FVBR	591	0.39	0.00	0.00
	SFVBR	2105	0.66	0.00	0.00
	$qd$	187 388	4.55	1.99	5.37
Case II	SVBR	6613	0.74	0.00	0.00
	FVBR	187 928	6.50	1.99	5.37
	SFVBR	6608	0.95	0.00	0.00
	$qd$	9498	0.56	0.08	0.25
	$qd$ (400 $\Omega$ )	12 943	0.64	0.04	0.12
Case III	SVBR	11 103	1.10	0.08	0.25
	FVBR	6094	0.59	0.00	0.00
	SFVBR	7026	1.08	0.00	0.00
	$qd$	202 545	5.20	2.30	4.16
	SVBR	26 868	1.90	0.03	0.71
Case IV	FVBR	205 599	7.90	2.31	4.71
	SFVBR	10 082	1.35	0.00	0.00

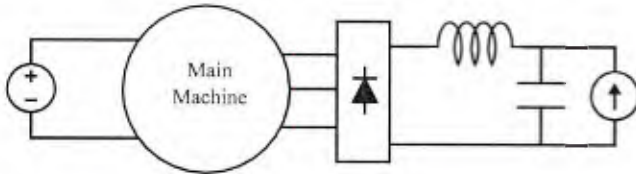


Fig. 3. Case II arrangement.

interface mismatch between stator and rectifier load exists for the  $qd$  and FVBR formulations. This mismatch is resolved by adding 530- $\Omega$  (approximately 100 pu) resistances in parallel with the stator windings. Response to a step increase in field voltage is considered. At  $t = 33.3$  ms, the field voltage is stepped to 45 V. It can be seen in Table I that the SVBR and SFVBR formulations have negligible error because they require no interface approximations. The  $qd$  and FVBR formulations exhibit errors in the stator current due to the interface approximation, but this also results in considerable error in the field current. The reference waveforms and detailed views of the waveforms predicted by each formulation are shown in Fig. 4 and show both these errors and the relatively high number of time steps required by these methods. These methods also require considerably longer run times due to the stiffness introduced by the artificial resistance at the stator. The SVBR formulation had the fastest run time due to lack of artificial stiffness and simplicity relative to the SFVBR formulation. There is about a factor of twenty penalty in number of required time steps for not using the stator circuit interface when required ( $qd$  and FVBR versus SVBR and SFVBR), and this can also be seen in the comparison between the FVBR and SFVBR formulations of Case IV below.

In Case III, the field winding is supplied through a diode rectifier by a 37-V, 120-Hz three-phase source with a series commutating inductance of 2.31 mH and the stator is connected to an infinite 560-V bus shown in Fig. 5. The machine is rotating at 1800 r/min and the rotor angle is  $\pi/8$  rad. In such a situation,

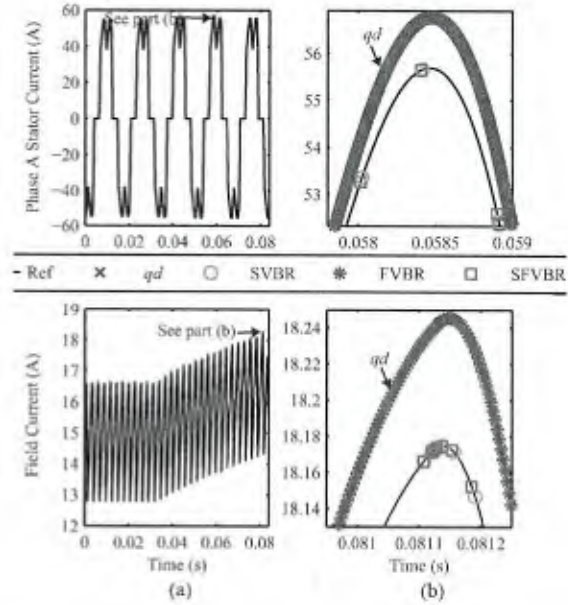


Fig. 4. Case II results.

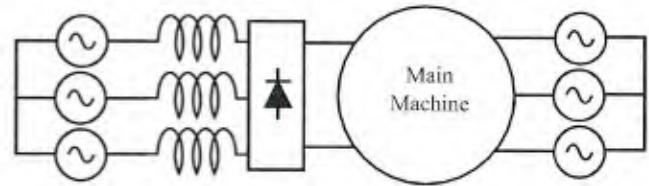


Fig. 5. Case III arrangement.

an interface mismatch between field and rectifier source exists for the  $qd$  and SVBR formulations. This mismatch is resolved by adding a 200- $\Omega$  (approximately 100 times the field resistance) resistance in parallel with the field winding. At  $t = 20$  ms, one of the upper diodes in the rectifier is shorted. The results are shown in Fig. 6. It can be seen in the figure and in Table I that the FVBR and SFVBR formulations have negligible error in both the stator and field currents because neither of the formulations require interface approximations. The  $qd$  and SVBR formulations exhibit errors in the field current due to the interface approximation, but this also results in non-negligible error in the stator current. It is observed that the errors associated with interface mismatches at the field result in relatively smaller errors than interface mismatches at the stator (as in Case II). The run time cost associated with the interface mismatches is also smaller. This is attributed to the relatively slow dynamics associated with the field winding relative to the stator windings. In fact, the  $qd$  formulation has the smallest run time despite the introduction of a large resistance. However, if the artificial resistance is doubled to 400  $\Omega$ , the  $qd$  formulation errors are halved (remaining non-negligible) and the run time exceeds that of the FVBR formulation. The FVBR formulation requires the fewest time steps. There is approximately a factor of two penalty for not using the field circuit representation in this case ( $qd$  and

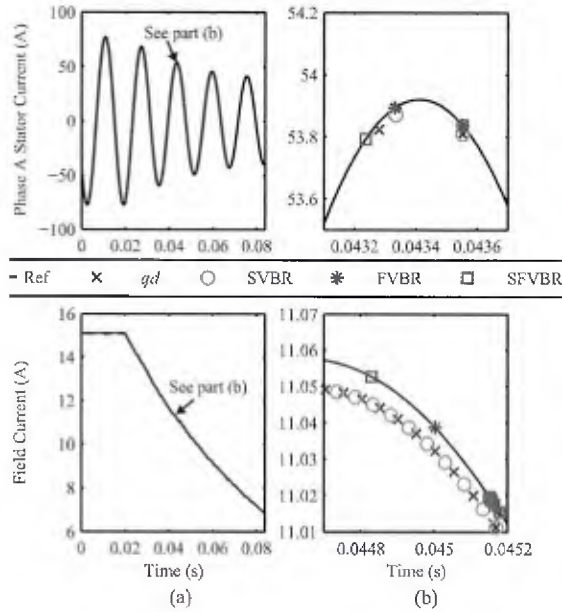


Fig. 6. Case III results.

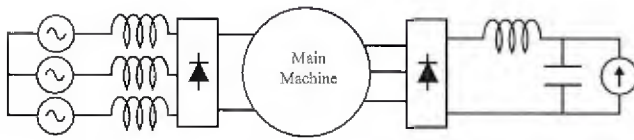


Fig. 7. Case IV arrangement.

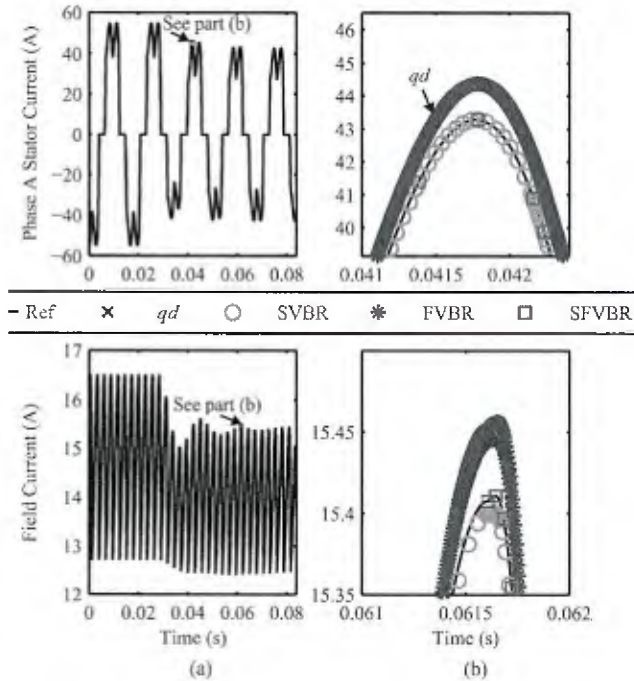


Fig. 8. Case IV results.

SVBR versus FVBR and SFVBR). In this case, the penalty for simulating in *abc* variables on the stator when it is not required (SFVBR versus FVBR) is not as great as in Case I because of the sustained current transient on the stator side.

In Case IV, the field winding is supplied through a diode rectifier as in Case III, and the stator is used to supply a rectifier load as in Case II shown in Fig. 7. The same interface mismatches occur, so the artificial resistances described above are used at the stator for the *qd* and FVBR formulations and at the field for the *qd* and SVBR formulations. At  $t = 28$  ms, the dc load is stepped from 48 A to 36 A. The results are shown in Fig. 8. Only the SFVBR formulation has negligible error in both the stator and field currents. It also has the fewest required time steps and the fastest run time. There is about a factor of twenty penalty for not using the stator circuit interface when required (FVBR versus SFVBR), which corresponds with the results from Case II. It is noted that the SVBR formulation has smaller errors, fewer time steps, and faster run time than the other two formulations, which further indicates that the penalty for inserting artificial resistance at the field is less severe than that for inserting resistance at the stator.

VI. CONCLUSION

The derivation of various formulations of a synchronous machine model that includes arbitrary linear networks to represent rotor circuits and magnetizing path saturation including cross-saturation has been unified. This machine model is significant because it has been extensively experimentally validated and includes most existing machine models as special cases. An FVBR formulation of this model has been derived as well. The benefits in terms of run time and accuracy of each formulation have been examined. In particular, it has been found that the formulation with the most conducive interface for the simulation application produces more accurate results with fewer required time steps and less run time but that having a suitable stator interface is particularly important.

APPENDIX

A. Linear Transformation Matrix

A transformation matrix that achieves the form indicated in (21) and (22) is given by

$$T = [P \ N], \tag{35}$$

where  $P = C^+$  and  $N$  is a matrix formed from columns that span  $\text{null}(C)$ . This transformation is applied such that the linear system in the new coordinates is described using

$$\tilde{A} = T^{-1}AT \tag{36}$$

$$\tilde{B} = T^{-1}A \tag{37}$$

$$\tilde{C} = CT = [I \ 0]. \tag{38}$$

### B. SVBR Formulation Definitions

The matrices and vector in (29) are

$$\hat{\mathbf{R}}_m = \begin{bmatrix} \mathbf{L}_{mi} \begin{bmatrix} a_q & \\ & a_d \end{bmatrix} \\ 0 \end{bmatrix} \quad (39)$$

$$\hat{\mathbf{L}}_m = \begin{bmatrix} \mathbf{L}_{mi} \\ 0 \end{bmatrix} \quad (40)$$

$$\mathbf{e}_{qd0s} = \begin{bmatrix} \mathbf{e}_{qds} \\ 0 \end{bmatrix}, \quad (41)$$

where  $a_q = -a_{q11}$ ,  $a_d = -a_{d11}$ , and

$$\mathbf{L}_{mi} = \left( \mathbf{\Gamma}_{mi}(\lambda_{mqd}) + \begin{bmatrix} b_{q1} & \\ & b_{d11} \end{bmatrix} \right)^{-1} = \begin{bmatrix} L_{mqq} & L_{mqd} \\ L_{mqd} & L_{mdd} \end{bmatrix} \quad (42)$$

$$\begin{aligned} \mathbf{e}_{qds} = \omega_r \lambda_{mdq} + \mathbf{L}_{mi} \left( \begin{bmatrix} a_{q11} & \\ & a_{d11} \end{bmatrix} \mathbf{i}_{mqd} \right. \\ \left. - \begin{bmatrix} \mathbf{a}_{q12}^T \mathbf{x}_{q2} \\ \mathbf{a}_{d13}^T \mathbf{x}_{d3} \end{bmatrix} - \begin{bmatrix} 0 \\ a_{d12} \end{bmatrix} i_{fdr} - \begin{bmatrix} 0 \\ b_{d12} \end{bmatrix} v_{fdr} \right). \end{aligned} \quad (43)$$

The matrices and vector in (30) are

$$\mathbf{R} = r_s \mathbf{I}_3 + \mathbf{R}_m \quad (44)$$

$$\mathbf{L} = L_{ts} \mathbf{I}_3 + \mathbf{L}_m \quad (45)$$

$$\mathbf{e}_{abcs} = \mathbf{K}_s^{-1} \mathbf{e}_{qd0s}, \quad (46)$$

where

$$\begin{aligned} \mathbf{R}_m = R_a \mathbf{M}_1 + (\sqrt{3}/2)(\omega_r L_a - R_d) \mathbf{M}_2 \\ + \begin{bmatrix} R_1(\theta_r) & R_1(\theta_r - \pi/3) & R_1(\theta_r + \pi/3) \\ R_1(\theta_r - \pi/3) & R_1(\theta_r + \pi/3) & R_1(\theta_r) \\ R_1(\theta_r + \pi/3) & R_1(\theta_r) & R_1(\theta_r - \pi/3) \end{bmatrix} \\ + \omega_r \begin{bmatrix} L_2(\theta_r) & L_2(\theta_r - \pi/3) & L_2(\theta_r + \pi/3) \\ L_2(\theta_r - \pi/3) & L_2(\theta_r + \pi/3) & L_2(\theta_r) \\ L_2(\theta_r + \pi/3) & L_2(\theta_r) & L_2(\theta_r - \pi/3) \end{bmatrix} \end{aligned} \quad (47)$$

$$\begin{aligned} \mathbf{L}_m = L_a \mathbf{M}_1 \\ + \begin{bmatrix} L_1(\theta_r) & L_1(\theta_r - \pi/3) & L_1(\theta_r + \pi/3) \\ L_1(\theta_r - \pi/3) & L_1(\theta_r + \pi/3) & L_1(\theta_r) \\ L_1(\theta_r + \pi/3) & L_1(\theta_r) & L_1(\theta_r - \pi/3) \end{bmatrix} \end{aligned} \quad (48)$$

$$L_a = (L_{mqq} + L_{mdd})/3 \quad (49)$$

$$L_b = (L_{mdd} - L_{mqq})/3 \quad (50)$$

$$L_c = 2L_{mqd}/3 \quad (51)$$

$$R_a = (a_q L_{mqq} + a_d L_{mdd})/3 \quad (52)$$

$$R_b = (a_d L_{mdd} - a_q L_{mqq})/3 \quad (53)$$

$$R_c = (a_q + a_d) L_{mqd}/3 \quad (54)$$

$$R_d = (a_d - a_q) L_{mqd}/3 \quad (55)$$

$$L_1(\phi) = -L_b \cos(2\phi) + L_c \sin(2\phi) \quad (56)$$

$$L_2(\phi) = L_1(\phi + \pi/4) \quad (57)$$

$$R_1(\phi) = -R_b \cos(2\phi) + R_c \sin(2\phi) \quad (58)$$

$$\mathbf{M}_1 = \begin{bmatrix} 1 & -1/2 & -1/2 \\ -1/2 & 1 & -1/2 \\ -1/2 & -1/2 & 1 \end{bmatrix} \quad (59)$$

$$\mathbf{M}_2 = \begin{bmatrix} 0 & 1 & -1 \\ -1 & 0 & 1 \\ 1 & -1 & 0 \end{bmatrix}. \quad (60)$$

### C. FVBR Formulation Definitions

The scalars in (31) are

$$R = r_{sfdr} + \sigma a'_f L_{ts} M'_{dd} \quad (61)$$

$$L = L_{sfdr} + \chi \sigma L_{ts} M'_{dd} \quad (62)$$

$$\begin{aligned} \mathbf{e}_{fdr} = \sigma [M'_{qd} \ M'_{dd}] \left[ \mathbf{v}_{qds} - r_s \mathbf{i}_{qds} - \omega_r L_{ts} \mathbf{i}_{dqs} - \omega_r \lambda_{mdq} \right. \\ \left. - L_{ts} \left( \begin{bmatrix} a_{q11} & \\ & a_{d11} \end{bmatrix} \mathbf{i}_{qdr} + \begin{bmatrix} \mathbf{a}_{q12}^T \mathbf{x}_{q2} \\ \mathbf{a}_{d13}^T \mathbf{x}_{d3} \end{bmatrix} \right) \right] \\ - (L_{sfdr} + \chi \sigma L_{ts} M'_{dd})(a_{d21} i_{dr} + \mathbf{a}_{d23}^T \mathbf{x}_{d3}), \end{aligned} \quad (63)$$

where

$$\begin{aligned} \mathbf{M}' = \left[ \mathbf{I}_2 + L_{ts} \left( \mathbf{\Gamma}_{mi}(\lambda_{mqd}) \right. \right. \\ \left. \left. + \begin{bmatrix} b_{q1} & \\ & b_{d11} - \chi \sigma b_{d22} \end{bmatrix} \right) \right]^{-1} = \begin{bmatrix} M'_{qq} & M'_{qd} \\ M'_{qd} & M'_{dd} \end{bmatrix} \end{aligned} \quad (64)$$

$$\chi = -b_{d12}/b_{d22} \quad (65)$$

$$\sigma = -b_{d21}/b_{d22} \quad (66)$$

$$a'_f = -a_{d12} - \chi a_{d22} \quad (67)$$

$$r_{sfdr} = -a_{d22}/b_{d22} \quad (68)$$

$$L_{sfdr} = 1/b_{d22}. \quad (69)$$

#### D. SFVBR Formulation Definitions

The matrices, vector, and scalar in (32) are

$$\mathbf{R}'_s = \begin{bmatrix} r_s \mathbf{I}_3 & \\ & r_{sfdr} \end{bmatrix} \quad (70)$$

$$\mathbf{L}'_s = \begin{bmatrix} L_{ls} \mathbf{I}_3 & \\ & L_{sfdr} \end{bmatrix} \quad (71)$$

$$\hat{\mathbf{R}}'_m = \begin{bmatrix} 0 & 0 & 0 & 0 \\ 0 & 0 & 0 & 0 \\ 0 & 0 & 0 & 0 \\ 0 & r_{mfdr} & 0 & 0 \end{bmatrix} \quad (72)$$

$$+ \begin{bmatrix} -a_q L'_{mqq} & -a_d L'_{mqd} & 0 & -a_f L'_{mqd} \\ -a_q L'_{mqd} & -a_d L'_{mdd} & 0 & -a_f L'_{mdd} \\ 0 & 0 & 0 & 0 \\ \sigma a_q L'_{mqd} & \sigma a_d L'_{mdd} & 0 & \sigma a_f L'_{mdd} \end{bmatrix} \quad (73)$$

$$\hat{\mathbf{L}}'_m = \begin{bmatrix} L'_{mqq} & L'_{mqd} & 0 & -\chi L'_{mqd} \\ L'_{mqd} & L'_{mdd} & 0 & -\chi L'_{mdd} \\ 0 & 0 & 0 & 0 \\ -\sigma L'_{mqd} & -\sigma L'_{mdd} & 0 & \chi \sigma L'_{mdd} \end{bmatrix} \quad (74)$$

$$\mathbf{e}'_{qd0s} = \mathbf{L}'_{mi} \begin{bmatrix} a_{q11} & \\ & a_{d11} \end{bmatrix} \mathbf{i}_{mqd} - \begin{bmatrix} \mathbf{a}_{q12}^T \mathbf{x}_{q2} \\ \mathbf{a}_{d13}^T \mathbf{x}_{d3} \end{bmatrix} \\ - \chi \begin{bmatrix} L'_{mqd} \\ L'_{mdd} \end{bmatrix} (\mathbf{a}_{d23}^T \mathbf{x}_{d3} - a_{d21} i_{md}) + \omega_r \lambda_{mdq} \quad (75)$$

$$\mathbf{e}'_{fdr} = \sigma \begin{bmatrix} L'_{mqd} & L'_{mdd} \end{bmatrix} \left( \begin{bmatrix} a_{q11} & \\ & a_{d11} \end{bmatrix} \mathbf{i}_{mqd} \right. \\ \left. - \begin{bmatrix} \mathbf{a}_{q12}^T \mathbf{x}_{q2} \\ \mathbf{a}_{d13}^T \mathbf{x}_{d3} \end{bmatrix} \right) \\ - (L_{sfdr} + \chi \sigma L'_{mdd}) (\mathbf{a}_{d23}^T \mathbf{x}_{d3} - a_{d21} i_{md}), \quad (76)$$

where

$$\mathbf{L}'_{mi} = \left( \Gamma_{mi}(\lambda_{mqd}) + \begin{bmatrix} b_{q1} & \\ & b_{d11} - b_{d12} b_{d21} / b_{d22} \end{bmatrix} \right)^{-1} \\ = \begin{bmatrix} L'_{mqq} & L'_{mqd} \\ L'_{mqd} & L'_{mdd} \end{bmatrix} \quad (77)$$

$$a'_d = -a_{d11} - \chi a_{d21} \quad (78)$$

$$r_{mfdr} = -a_{d21} / b_{d22}. \quad (79)$$

The matrices and vector in (33) are

$$\mathbf{R}' = \mathbf{R}'_s + \mathbf{R}'_m \quad (80)$$

$$\mathbf{L}' = \mathbf{L}'_s + \mathbf{L}'_m \quad (81)$$

$$\mathbf{e}'_{abcs} = \mathbf{K}_s^{-1} \mathbf{e}'_{qd0s}, \quad (82)$$

where  $\mathbf{R}'_m$  and  $\mathbf{L}'_m$  are defined in (83) and (84), as shown at the bottom of the page

$$L'_a = (L'_{mqq} + L'_{mdd}) / 3 \quad (85)$$

$$L'_b = (L'_{mdd} - L'_{mqq}) / 3 \quad (86)$$

$$L'_c = 2L'_{mqd} / 3 \quad (87)$$

$$R'_a = (a_q L'_{mqq} + a'_d L'_{mdd}) / 3 \quad (88)$$

$$R'_b = (a'_d L'_{mdd} - a_q L'_{mqq}) / 3 \quad (89)$$

$$R'_c = (a_q + a'_d) L'_{mqd} / 3 \quad (90)$$

$$R'_d = (a'_d - a_q) L'_{mqd} / 3 \quad (91)$$

$$L'_1(\phi) = -L'_b \cos(2\phi) + L'_c \sin(2\phi) \quad (92)$$

$$L'_2(\phi) = L'_1(\phi + \pi/4) \quad (93)$$

$$L_x(\phi) = L'_{mqd} \cos(\phi) + L'_{mdd} \sin(\phi) \quad (94)$$

$$L'_3(\phi) = 2\sigma L_x(\phi) / 3 \quad (95)$$

$$L'_4(\phi) = L'_3(\phi + \pi/2) \quad (96)$$

$$\mathbf{R}'_m = \begin{bmatrix} R'_a \mathbf{M}_1 & \\ & \sigma a'_f L'_{mdd} \end{bmatrix} + (\sqrt{3}/2) (\omega_r L'_a - R'_d) \begin{bmatrix} \mathbf{M}_2 & \\ & 0 \end{bmatrix} + \begin{bmatrix} R'_1(\theta_r) & R'_1(\theta_r - \pi/3) & R'_1(\theta_r + \pi/3) & R'_2(\theta_r) \\ R'_1(\theta_r - \pi/3) & R'_1(\theta_r + \pi/3) & R'_1(\theta_r) & R'_2(\theta_r - 2\pi/3) \\ R'_1(\theta_r + \pi/3) & R'_1(\theta_r) & R'_1(\theta_r - \pi/3) & R'_2(\theta_r + 2\pi/3) \\ R'_3(\theta_r) & R'_3(\theta_r - 2\pi/3) & R'_3(\theta_r + 2\pi/3) & 0 \end{bmatrix} \\ + \omega_r \begin{bmatrix} L'_2(\theta_r) & L'_2(\theta_r - \pi/3) & L'_2(\theta_r + \pi/3) & 0 \\ L'_2(\theta_r - \pi/3) & L'_2(\theta_r + \pi/3) & L'_2(\theta_r) & 0 \\ L'_2(\theta_r + \pi/3) & L'_2(\theta_r) & L'_2(\theta_r - \pi/3) & 0 \\ L'_4(\theta_r) & L'_4(\theta_r - 2\pi/3) & L'_4(\theta_r + 2\pi/3) & 0 \end{bmatrix} \quad (83)$$

$$\mathbf{L}'_m = \begin{bmatrix} L'_a \mathbf{M}_1 & \\ & \chi \sigma L'_{mdd} \end{bmatrix} + \begin{bmatrix} L'_1(\theta_r) & L'_1(\theta_r - \pi/3) & L'_1(\theta_r + \pi/3) & L'_5(\theta_r) \\ L'_1(\theta_r - \pi/3) & L'_1(\theta_r + \pi/3) & L'_1(\theta_r) & L'_5(\theta_r - 2\pi/3) \\ L'_1(\theta_r + \pi/3) & L'_1(\theta_r) & L'_1(\theta_r - \pi/3) & L'_5(\theta_r + 2\pi/3) \\ L'_3(\theta_r) & L'_3(\theta_r - 2\pi/3) & L'_3(\theta_r + 2\pi/3) & 0 \end{bmatrix} \quad (84)$$

$$L'_5(\phi) = \chi L_x(\phi) \quad (97)$$

$$R'_1(\phi) = -R'_b \cos(2\phi) + R'_c \sin(2\phi) \quad (98)$$

$$R'_2(\phi) = a'_f L_x(\phi) \quad (99)$$

$$R'_3(\phi) = 2/3(\sigma(a_q L'_{mqd} \cos(\phi) + a'_d L'_{mdd} \sin(\phi)) + r_{mfd} \sin(\phi)). \quad (100)$$

## REFERENCES

- [1] J. G. Kettleborough, I. R. Smith, and B. A. Fanthome, "Simulation of a dedicated aircraft generator supplying a heavy rectified load," *IEE Proc. B, Electr. Power Appl.*, vol. 130, no. 6, pp. 431–435, Nov. 1983.
- [2] T. H. Warner and J. G. Kassakian, "Transient characteristics and modeling of large turboalternator driven rectifier/inverter systems based on field test data," *IEEE Power Eng. Rev.*, vol. PER-5, no. 7, pp. 47–47, Jul. 1985.
- [3] I. Jadrić, D. Borjević, and M. Jadrić, "Modeling and control of a synchronous generator with an active dc load," *IEEE Trans. Power Electron.*, vol. 15, no. 2, pp. 303–311, Mar. 2000.
- [4] J. G. Ciezki and R. W. Ashton, "Selection and stability issues associated with a navy shipboard dc zonal electric distribution system," *IEEE Trans. Power Del.*, vol. 15, no. 2, pp. 665–669, Apr. 2000.
- [5] J. Rivas, D. Perreault, and T. Keim, "Performance improvement of alternators with switched-mode rectifiers," *IEEE Trans. Energy Convers.*, vol. 19, no. 3, pp. 561–568, Sep. 2004.
- [6] S. B. Leeb *et al.*, "How much dc power is necessary?" *Nav. Eng. J.*, vol. 122, no. 2, pp. 79–92, Jun. 2010.
- [7] C. A. Platero, F. Blázquez, P. Frías, and D. Ramírez, "Influence of rotor position in FRA response for detection of insulation failures in salient-pole synchronous machines," *IEEE Trans. Energy Convers.*, vol. 26, no. 2, pp. 671–676, Jun. 2011.
- [8] R. H. Park, "Two-reaction theory of synchronous machines generalized method of analysis-Part I," *Trans. Amer. Inst. Electr. Eng.*, vol. 48, no. 3, pp. 716–727, Jul. 1929.
- [9] I. M. Canay, "Causes of discrepancies on calculation of rotor quantities and exact equivalent diagrams of the synchronous machine," *IEEE Trans. Power App. Syst.*, vol. PAS-88, no. 7, pp. 1114–1120, Jul. 1969.
- [10] R. P. Schulz, W. D. Jones, and D. N. Ewart, "Dynamic models of turbine generators derived from solid rotor equivalent circuits," *IEEE Trans. Power App. Syst.*, vol. PAS-92, no. 3, pp. 926–933, May 1973.
- [11] H. Bissig, K. Reichert, and T. S. Kulig, "Modelling and identification of synchronous machines, a new approach with an extended frequency range," *IEEE Trans. Energy Convers.*, vol. 8, no. 2, pp. 263–271, Jun. 1993.
- [12] I. M. Canay, "Determination of the model parameters of machines from the reactance operators  $x_d(p)$ ,  $x_q(p)$  (evaluation of standstill frequency response test)," *IEEE Trans. Energy Convers.*, vol. 8, no. 2, pp. 272–279, Jun. 1993.
- [13] J. L. Kirtley, "On turbine-generator rotor equivalent circuits," *IEEE Trans. Power Syst.*, vol. 9, no. 1, pp. 262–271, Feb. 1994.
- [14] A. Keyhani and H. Tsai, "Identification of high-order synchronous generator models from SSSR test data," *IEEE Trans. Energy Convers.*, vol. 9, no. 3, pp. 593–603, Sep. 1994.
- [15] *IEEE Guide for Synchronous Generator Modeling Practices and Applications in Power System Stability Analyses*, IEEE Std. pp. 1110–2002, Nov. 2003.
- [16] S. D. Pekarek, E. A. Walters, and B. T. Kuhn, "An efficient and accurate method of representing magnetic saturation in physical-variable models of synchronous machines," *IEEE Trans. Energy Convers.*, vol. 14, no. 1, pp. 72–79, Mar. 1999.
- [17] S.-A. Tahan and I. Kamwa, "A two-factor saturation model for synchronous machines with multiple rotor circuits," *IEEE Trans. Energy Convers.*, vol. 10, no. 4, pp. 609–616, Dec. 1995.
- [18] E. Levi, "Saturation modelling in d-q axis models of salient pole synchronous machines," *IEEE Trans. Energy Convers.*, vol. 14, no. 1, pp. 44–50, Mar. 1999.
- [19] D. C. Aliprantis, O. Wasynczuk, and C. D. Rodríguez Valdez, "A voltage-behind-reactance synchronous machine model with saturation and arbitrary rotor network representation," *IEEE Trans. Energy Convers.*, vol. 23, no. 2, pp. 499–508, Jun. 2008.
- [20] D. C. Aliprantis, S. D. Sudhoff, and B. T. Kuhn, "A synchronous machine model with saturation and arbitrary rotor network representation," *IEEE Trans. Energy Convers.*, vol. 20, no. 3, pp. 584–594, Sep. 2005.
- [21] D. C. Aliprantis, S. D. Sudhoff, and B. T. Kuhn, "Experimental characterization procedure for a synchronous machine model with saturation and arbitrary rotor network representation," *IEEE Trans. Energy Convers.*, vol. 20, no. 3, pp. 595–603, Sep. 2005.
- [22] A. M. Cramer, B. P. Loop, and D. C. Aliprantis, "Synchronous machine model with voltage-behind-reactance formulation of stator and field windings," *IEEE Trans. Energy Convers.*, vol. 27, no. 2, pp. 391–402, Jun. 2012.
- [23] E. Levi and V. A. Levi, "Impact of dynamic cross-saturation on accuracy of saturated synchronous machine models," *IEEE Trans. Energy Convers.*, vol. 15, no. 2, pp. 224–230, Jun. 2000.
- [24] S. D. Pekarek, O. Wasynczuk, and H. J. Hegner, "An efficient and accurate model for the simulation and analysis of synchronous machine/converter systems," *IEEE Trans. Energy Convers.*, vol. 13, no. 1, pp. 42–48, Mar. 1998.
- [25] G. R. Slemon, "An equivalent circuit approach to analysis of synchronous machines with saliency and saturation," *IEEE Trans. Energy Convers.*, vol. 5, no. 3, pp. 538–545, Sep. 1990.
- [26] Y. Xiao, G. R. Slemon, and M. R. Iravani, "Implementation of an equivalent circuit approach to the analysis of synchronous machines," *IEEE Trans. Energy Convers.*, vol. 9, no. 4, pp. 717–723, Dec. 1994.
- [27] X. Cao, A. Kurita, H. Mitsuma, Y. Tada, and H. Okamoto, "Improvements of numerical stability of electromagnetic transient simulation by use of phase-domain synchronous machine models," *Electr. Eng. Jpn.*, vol. 128, no. 3, pp. 53–62, Apr. 1999.
- [28] L. Wang, J. Jatskevich, and S. D. Pekarek, "Modeling of induction machines using a voltage-behind-reactance formulation," *IEEE Trans. Energy Convers.*, vol. 23, no. 2, pp. 382–392, Jun. 2008.
- [29] L. Wang *et al.*, "Methods of interfacing rotating machine models in transient simulation programs," *IEEE Trans. Power Del.*, vol. 25, no. 2, pp. 891–903, Apr. 2010.
- [30] L. Wang and J. Jatskevich, "A phase-domain synchronous machine model with constant equivalent conductance matrix for EMTP-type solution," *IEEE Trans. Energy Convers.*, vol. 28, no. 1, pp. 191–202, Mar. 2013.
- [31] M. Chaparha, L. Wang, J. Jatskevich, H. W. Dommel, and S. D. Pekarek, "Constant-parameter rl-branch equivalent circuit for interfacing ac machine models in state-variable-based simulation packages," *IEEE Trans. Energy Convers.*, vol. 27, no. 3, pp. 634–645, Sep. 2012.
- [32] M. Chaparha, F. Therrien, J. Jatskevich, and H. W. Dommel, "Constant-parameter circuit-based models of synchronous machines," *IEEE Trans. Energy Convers.*, vol. 30, no. 2, pp. 441–452, Jun. 2015.
- [33] P. Krause, O. Wasynczuk, S. Sudhoff, and S. Pekarek, *Analysis of Electric Machinery and Drive Systems*, 3rd ed., Piscataway, NJ, USA: Wiley, 2013.
- [34] *Simulink Users Guide*, MathWorks, Natick, MA, USA.
- [35] *Automated State Model Generator (ASMG) Reference Manual*, P. C. Krause and Associates, Inc., West Lafayette, IN, USA, 2002.



**YuQi Zhang** (S'16) received the B.S. degree in electrical engineering from the Harbin Institute of Technology, Harbin, China, in 2005 and the M.S.E.E. degree from the University of Kentucky, Lexington, KY, USA, in 2014, where she is currently working toward the Ph.D. degree in electrical engineering.

Her research interests include electric machine modeling and simulation, power electronics, and power systems.



**Aaron M. Cramer** (S'02–M'07–SM'13) received the B.S. degree (*summa cum laude*) in electrical engineering from the University of Kentucky, Lexington, KY, USA, in 2003 and the Ph. D. degree from Purdue University, West Lafayette, IN, USA in 2007.

From 2007 to 2010, he was a Senior Engineer with PC Krause and Associates, West Lafayette. He joined the University of Kentucky in 2010 where he is currently an Associate Professor. His research interests include modeling, simulation, and control of power and energy systems.

Dr. Cramer received the ONR Young Investigator Program award in 2015. He serves as an Editor of IEEE TRANSACTIONS ON ENERGY CONVERSION.

# Numerical Average-Value Modeling of Rotating Rectifiers in Brushless Excitation Systems

YuQi Zhang, *Student Member, IEEE*, and Aaron M. Cramer , *Senior Member, IEEE*

**Abstract**—Brushless excitation systems are widely used for synchronous machines. As a critical part of the system, rotating rectifiers have a significant impact on the system behavior. This paper presents a numerical average-value model (AVM) for rotating rectifiers in brushless excitation systems, where the essential numerical functions are extracted from the detailed simulations and vary depending on the loading conditions. Open-circuit voltages of the brushless exciter armature are used to calculate the dynamic impedance that represents the loading condition. The model is validated by comparison with an experimentally validated detailed model of the brushless excitation system in three distinct cases. It has been demonstrated that the proposed AVM can provide accurate simulations in both transient and steady states with fewer time steps and less runtime compared with detailed models of such systems and that the proposed AVM can be combined with AVM models of other rectifiers in the system to reduce the overall computational cost.

**Index Terms**—Brushless machines, converters, generators, simulation.

## I. INTRODUCTION

**B**RUSHLESS excitation systems offer higher reliability and require less maintenance than static excitation systems by eliminating brushes, slip rings, circuit breakers, field breakers, and carbon dust [1]–[3]. These advantages lead to its wide use in large synchronous machines, especially in applications where high reliability is required and maintenance budget is limited [3]–[5]. Rotating rectifiers are commonly employed in brushless excitation systems, where exciter armature windings and rotating rectifiers are all mounted on the same shaft as main machine field windings [4], [6]. Output voltages of exciters are rectified by rotating rectifiers and fed to main machine field circuits. Because brushless exciters are directly related to main machine field voltages and power system dynamic behavior, accurate and computationally efficient modeling of brushless excitation systems with rotating rectifiers is essential for power electronic simulation and power systems analysis. Specific applications in which accurate and efficient modeling are necessary may involve long simulation times, large numbers of components,

and/or repeated simulations with different sets of parameters (e.g., aircraft power systems [7], shipboard power systems [4], [8], and microgrids [9]).

Modeling machine-converter systems has received considerable attention. Although the detailed model of machine-rectifier systems can provide accurate results and design evaluations [10], it is computationally expensive due to repeated switching of the diodes. Average-value models (AVMs) reduce the modeling complexity and enhance the computational efficiency by neglecting or averaging the effects of fast switching with respect to the prototypical switching interval [11], [12]. In early studies, relationships between ac source variables and rectifier dc variables are derived analytically [13]–[15]. However, such characteristics are obtained based on idealized ac systems and the assumption that the commutating reactance is constant. In later work, the AVM for converters connected to synchronous machines is proposed [16]. The commutating reactance is set equal to the  $d$ -axis subtransient reactance of synchronous machines. Because the commutating reactance should also be related to the  $q$ -axis subtransient reactance, the AVM presented in [16] is not accurate. The study in [17] improves the AVM by using a function of both the  $q$ - and  $d$ -axis subtransient reactances and of the converter firing angle as equivalent commutating reactances. In order to accurately predict the output impedance at higher frequencies, dynamic AVMs are developed in [18]. Analytical derivation methods, which are used in [6], [13]–[19], are based upon specific switching patterns and have limited utility outside of these operating modes. Also, many of these methods require implicit solutions to nonlinear equations and numerical integration within each time step, which can increase computational cost.

An alternative method for construction of AVMs of rectifiers has been coined the parametric or numerical approach, wherein numerical solutions are adopted in the earlier model development stage to obtain rectifier AVM parameters from detailed simulations [20]–[24]. In [20], the average behaviors of rectifiers are represented using a set of fixed parameters, which are not able to adaptively evolve according to operating conditions and therefore lead to inaccurate results. An improved AVM with parameters vary dynamically depending on operational conditions is presented in [22]. However, this AVM cannot be directly applied to the rotating rectifier in a brushless excitation system because of some differences between these rectifiers. In particular, the rotating rectifier requires a different reference frame transformation. More importantly, the field winding of the main machine does not resemble an LC filter (e.g., like seen in

Manuscript received January 20, 2017; revised April 26, 2017; accepted May 8, 2017. Date of publication May 22, 2017; date of current version November 22, 2017. This work was supported by the Office of Naval Research (ONR) through the ONR Young Investigator Program N00014-15-1-2475. Paper no. TEC-00051-2017. (Corresponding author: Aaron M. Cramer.)

The authors are with the University of Kentucky, Lexington, KY 40506 USA (e-mail: yuqi.zhang@uky.edu; aaron.cramer@uky.edu).

Color versions of one or more of the figures in this paper are available online at <http://ieeexplore.ieee.org>.

Digital Object Identifier 10.1109/TEC.2017.2706961

[22]); it primarily acts like an RL circuit. This creates a unique interfacing challenge that has not previously been addressed in the literature and is complicated by the saliency of the exciter machine.

Herein, a numerical AVM of the rotating rectifier in a brushless excitation system is proposed. This model averages the periodic switching behavior of the rotating rectifier and integrates these numerical functions with a dynamic model of the exciter machine to allow the nonlinear and dynamic characteristics of the brushless excitation system to be incorporated in simulation models with a traditional voltage-in, current-out formulation of the main machine. This results in accurate and computationally efficient simulations. The proposed model is validated using an experimentally validated machine-exciter system model and the computational efficiency benefits are quantified. It is also shown that the proposed AVM of the brushless excitation system can be combined with a numerical AVM of a stationary rectifier (i.e., [22]) to greatly reduce the computational cost of simulating such a system.

The remainder of this paper is organized as follows. The proposed model is described in Section II. The characterization of the rectifier is described in Section III. The model is validated by comparison with an experimentally validated detailed model of the brushless excitation system in Section IV, which is followed by a conclusion in Section V.

## II. AVERAGE-VALUE MODEL OF THE BRUSHLESS EXCITATION SYSTEM

Numerical average-value modeling has been successfully applied in a variety of cases involving machine-converter interactions. These techniques are adapted to the rotating rectifier in a brushless excitation system below.

### A. Notation

The electrical rotor speed and position of the exciter machine are

$$\omega_r = \frac{P}{2} \omega_{rm} \quad (1)$$

$$\theta_r = \frac{P}{2} \theta_{rm}, \quad (2)$$

respectively, where  $\omega_{rm}$  and  $\theta_{rm}$  are the mechanical rotor speed and position, respectively, and  $P$  is the number of exciter machine poles. The variables associated with the rotor of the exciter machine are denoted  $\mathbf{f}_{abc} = [f_a \ f_b \ f_c]^T$  where  $f$  can be used to indicate voltage ( $v$ ), current ( $i$ ), or flux linkage ( $\lambda$ ). These variables can be transformed into the stationary reference frame by use of the transformation

$$\mathbf{f}_{qd0r} = \mathbf{K}_r \mathbf{f}_{abc}, \quad (3)$$

where

$$\mathbf{K}_r = \frac{2}{3} \begin{bmatrix} \cos \theta_r & \cos(\theta_r + \frac{2\pi}{3}) & \cos(\theta_r - \frac{2\pi}{3}) \\ -\sin \theta_r & -\sin(\theta_r + \frac{2\pi}{3}) & -\sin(\theta_r - \frac{2\pi}{3}) \\ \frac{1}{2} & \frac{1}{2} & \frac{1}{2} \end{bmatrix} \quad (4)$$

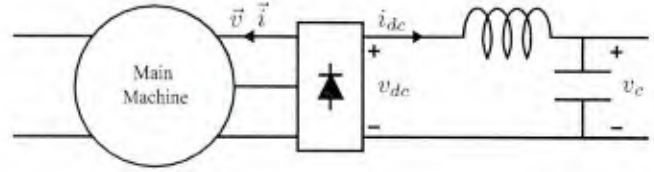


Fig. 1. Stationary rectifier system.

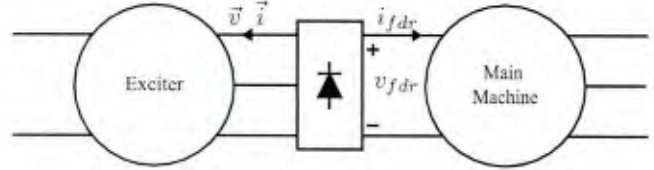


Fig. 2. Rotating rectifier system.

and  $\mathbf{f}_{qd0r} = [f_{qr} \ f_{dr} \ f_{0r}]^T$  are the transformed variables. The zero sequence  $f_{0r}$  is negligible. The transformed variables can also be expressed in space-phaser notation:  $\vec{f} = f_{qr} + j f_{dr}$  for rotating armature variables transformed to the stationary reference frame. Differentiation with respect to time is indicated by the operator  $p$ .

Main machine variables are transformed to the  $qd$  reference frame using Park's transformation.

### B. Rectifier Relationships

The proposed numerical average-value model of the brushless excitation system is based on [22]. In [22], the average behavior of the stationary rectifier depicted in Fig. 1 is represented by the following relationships:

$$\|\vec{v}\| = \alpha_s(z_s) v_{dc} \quad (5)$$

$$i_{dc} = \beta_s(z_s) \|\vec{i}\| \quad (6)$$

$$\angle \vec{v} = \angle \vec{i} + \phi_s(z_s) + \pi, \quad (7)$$

where  $\|\cdot\|$  denotes the 2-norm of a vector,  $\vec{v}$  and  $\vec{i}$  are space phasors associated with the stationary armature variables transformed to the reference frame fixed in the rotor,  $\alpha_s(\cdot)$ ,  $\beta_s(\cdot)$ , and  $\phi_s(\cdot)$  are algebraic functions of the loading condition, the phase offset of  $\pi$  accounts for the fact that the current space phasor  $\vec{i}$  is into the machine and thus out of the rectifier, and  $z_s$  is a "conveniently defined" dynamic impedance that represents the loading condition and is defined as

$$z_s = \frac{v_c}{\|\vec{i}\|}. \quad (8)$$

Similar relationships are utilized for the rotating rectifier in the brushless excitation system shown in Fig. 2, but these relationships are modified to account for the differences between the stationary and rotating rectifiers. The rotating rectifier is on the rotor and requires a different reference frame transformation, i.e., (3). Additionally, the field winding of the main machine does not resemble the LC filter studied in [22]. In particular, the average behavior of the rectifier is represented by the following

relationships:

$$v_{fd_r} = \alpha(z) \|\vec{v}\| \quad (9)$$

$$\|\vec{i}\| = \beta(z) i_{fd_r} \quad (10)$$

$$\angle \vec{v} = \angle \vec{i} + \phi(z) + \pi, \quad (11)$$

where  $z$  is a dynamic impedance that represents the loading condition. The dynamic impedance considered in [22] was selected because it is readily available in simulation as the capacitor voltage of the LC filter is a state variable. The field winding of the main machine does not exhibit such a voltage. Therefore, an alternative dynamic impedance is employed:

$$z = \frac{\|\mathbf{e}_{qdr}\|}{i_{fd_r}}, \quad (12)$$

where  $\mathbf{e}_{qdr}$  are the open-circuit voltages of the brushless exciter armature as described below.

### C. Brushless Exciter Model

The brushless exciter machine can be described in the rotor reference frame as

$$v_{qr} = r_r i_{qr} - \omega_r \lambda_{dr} + p \lambda_{qr} \quad (13)$$

$$v_{dr} = r_r i_{dr} + \omega_r \lambda_{qr} + p \lambda_{dr} \quad (14)$$

$$v'_{fds} = r'_{fds} i'_{fds} + p \lambda'_{fds}, \quad (15)$$

where

$$\lambda_{qr} = L_{lr} i_{qr} + L_{mq} i_{qr} \quad (16)$$

$$\lambda_{dr} = L_{lr} i_{dr} + L_{md} (i_{dr} + i'_{fds}) + \lambda_{md0} \quad (17)$$

$$\lambda'_{fds} = L'_{ifds} i'_{fds} + L_{md} (i_{dr} + i'_{fds}) + \lambda_{md0}, \quad (18)$$

the primed variables represent field variables referred to the rotor,  $r_r$  and  $r'_{fds}$  are the rotor and (referred) field resistances,  $L_{lr}$  and  $L'_{ifds}$  are the rotor and (referred) field leakage inductance,  $L_{mq}$  and  $L_{md}$  are the  $q$ - and  $d$ -axis magnetizing inductances, and  $\lambda_{md0}$  is an affine term added to the  $d$ -axis magnetizing flux to represent the effects of magnetic hysteresis.

The brushless exciter machine model can be expressed in the stationary reference frame as

$$v_{qr} = r_r i_{qr} - \omega_r L_d i_{dr} + L_q p i_{qr} + e_{qr} \quad (19)$$

$$v_{dr} = r_r i_{dr} + \omega_r L_q i_{qr} + L_d'' p i_{dr} + e_{dr}, \quad (20)$$

where

$$L_q = L_{lr} + L_{mq} \quad (21)$$

$$L_d = L_{lr} + L_{md} \quad (22)$$

$$L_d'' = L_{lr} + \frac{L'_{ifds} L_{md}}{L'_{ifds} + L_{md}} \quad (23)$$

$$e_{qr} = -\omega_r (L_{md} i'_{fds} + \lambda_{md0}) \quad (24)$$

$$e_{dr} = \frac{L_{md}}{L'_{ifds} + L_{md}} (v'_{fds} - r'_{fds} i'_{fds}). \quad (25)$$

It can be seen that  $\mathbf{e}_{qdr} = [e_{qr} \ e_{dr}]^T$  are the open-circuit voltages of the brushless exciter armature. Furthermore, substituting (17) into (14), (18) into (15), and solving for the time derivative of the field current results in the following:

$$p i'_{fds} = \frac{L_d (v'_{fds} - r'_{fds} i'_{fds}) - L_{md} (v_{dr} - r_r i_{dr} - \omega_r L_q i_{qr})}{L_d L'_{ifds} - L_{md}^2}. \quad (26)$$

### D. Differentiator Approximation

Both the armature windings of the exciter machine and the field winding of the main machine are most easily represented using voltage-in, current-out formulations, which corresponds to the case of the stationary rectifier where the main machine and the LC filter are most conveniently represented using voltage-in, current-out formulations. It is noted in [22] that this formulation is problematic because of the representation given in (5)–(7). In [22], this issue is resolved by using a current-in, voltage-out formulation of the LC filter. In doing this, the inductor in the LC filter acts as a differentiator and has an improper transfer function; this differentiator is replaced with a low-frequency approximation with a proper transfer function. Herein, an alternative approach is pursued that is consistent with the fact that the open-circuit voltages calculated in (24) and (25) are used to calculate the dynamic impedance  $z$  in (12).

In the proposed approach, the armature windings of the exciter machine are represented using a current-in, voltage-out formulation. It can be seen from (19) and (20) that such an approach also entails differentiators. Using a similar approach to that used in [22], a low-frequency approximation with proper transfer function is proposed. In particular,

$$p \mathbf{x} = \mathbf{A} \mathbf{x} + \mathbf{B} \begin{bmatrix} i_{qr} \\ i_{dr} \end{bmatrix} \quad (27)$$

$$\begin{bmatrix} p i_{qr} \\ p i_{dr} \end{bmatrix} \approx \mathbf{C} \mathbf{x} + \mathbf{D} \begin{bmatrix} i_{qr} \\ i_{dr} \end{bmatrix}, \quad (28)$$

where  $\mathbf{A}$ ,  $\mathbf{B}$ ,  $\mathbf{C}$ , and  $\mathbf{D}$  are  $2 \times 2$  matrices associated with the realization of the approximation and  $\mathbf{x}$  is a vector of two state variables associated with the realization. It is convenient to express the rows of  $\mathbf{C}$  and the elements of  $\mathbf{D}$  as

$$\mathbf{C} = \begin{bmatrix} \mathbf{c}_1^T \\ \mathbf{c}_2^T \end{bmatrix} \quad (29)$$

$$\mathbf{D} = \begin{bmatrix} d_{11} & d_{12} \\ d_{21} & d_{22} \end{bmatrix}. \quad (30)$$

This realization is an appropriate low-frequency approximation of the differentiators in (19) and (20) if

$$\lim_{s \rightarrow 0} \frac{\mathbf{C}(s\mathbf{I} - \mathbf{A})^{-1} \mathbf{B} + \mathbf{D}}{s} = \mathbf{I}, \quad (31)$$

where  $\mathbf{I}$  is the  $2 \times 2$  identity matrix.

It is shown below that specifying a certain structure for  $\mathbf{D}$  can facilitate the model integration. For a given  $\mathbf{D}$ , the condition in

(31) is satisfied if the remaining matrices are expressed as

$$\mathbf{A} = -\mathbf{A} \quad (32)$$

$$\mathbf{B} = \mathbf{V}^{-1} \quad (33)$$

$$\mathbf{C} = -\mathbf{V}\mathbf{A}^2, \quad (34)$$

where  $\mathbf{D} = \mathbf{V}\mathbf{A}\mathbf{V}^{-1}$  and  $\mathbf{A}$  is a diagonal matrix. The eigenvalues of  $\mathbf{A}$ , i.e., the negatives of the eigenvalues of  $\mathbf{D}$ , are associated with the bandwidth of the differentiator approximation and should be situated sufficiently far into the left half plane.

### E. Model Integration

By substitution of (28) into (19) and (20), the rotor voltages can be approximated as

$$\begin{aligned} v_{qr} &\approx r_r i_{qr} - \omega_r L_d i_{dr} + e_{qr} + L_q \mathbf{c}_1^T \mathbf{x} \\ &\quad + L_q d_{11} i_{qr} + L_q d_{12} i_{dr} \\ &= r_r i_{qr} - \omega_r L_d i_{dr} + u_q \\ &\quad + L_q d_{11} i_{qr} + L_q d_{12} i_{dr} \end{aligned} \quad (35)$$

$$\begin{aligned} v_{dr} &\approx r_r i_{dr} + \omega_r L_q i_{qr} + e_{dr} + L_d'' \mathbf{c}_2^T \mathbf{x} \\ &\quad + L_d'' d_{21} i_{qr} + L_d'' d_{22} i_{dr} \\ &= r_r i_{dr} + \omega_r L_q i_{qr} + u_d \\ &\quad + L_d'' d_{21} i_{qr} + L_d'' d_{22} i_{dr}, \end{aligned} \quad (36)$$

where

$$u_q = e_{qr} + L_q \mathbf{c}_1^T \mathbf{x} \quad (37)$$

$$u_d = e_{dr} + L_d'' \mathbf{c}_2^T \mathbf{x}. \quad (38)$$

It can be seen that (35) and (36) transform into

$$v_{qr} \approx R i_{qr} - X i_{dr} + u_q \quad (39)$$

$$v_{dr} \approx R i_{dr} + X i_{qr} + u_d \quad (40)$$

if the following conditions hold:

$$R = r_r + L_q d_{11} = r_r + L_d'' d_{22} \quad (41)$$

$$X = \omega_r L_d - L_q d_{12} = \omega_r L_q + L_d'' d_{21} \quad (42)$$

for some constants  $R$  and  $X$ . Furthermore, if approximately constant speed is assumed, i.e.,  $\omega_r \approx \omega_r^*$ , where  $\omega_r^*$  is the nominal speed, then

$$X \approx X^* = \omega_r^* L_d - L_q d_{12} = \omega_r^* L_q + L_d'' d_{21} \quad (43)$$

and is approximately constant. These conditions can be made to hold by choice of  $\mathbf{D}$ . For example,  $\mathbf{D}$  can be defined as

$$\mathbf{D} = \begin{bmatrix} \frac{R-r_r}{L_q} & \frac{\omega_r^* L_d - X^*}{L_q} \\ \frac{X^* - \omega_r^* L_q}{L_d''} & \frac{R-r_r}{L_d''} \end{bmatrix}. \quad (44)$$

By choice of a sufficiently large  $R$  the eigenvalues of  $\mathbf{D}$  can be placed sufficiently far into the right half plane. It is noted that  $\mathbf{D}$  is selected based on a constant speed assumption and that variation from the nominal speed will introduce error in the exciter representation.

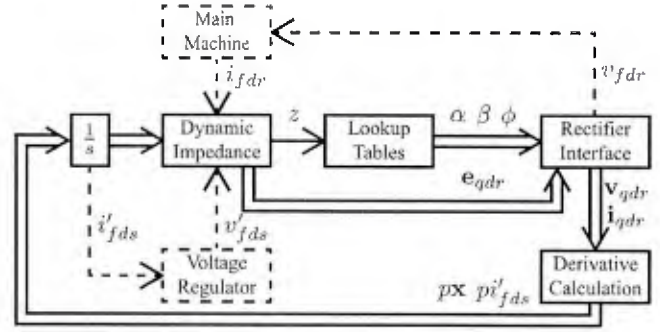


Fig. 3. Summary of model formulation (dashed lines represent external interfaces to/from the proposed model).

With such a suitable differentiator approximation, the voltage equations can be expressed in space-phasor form as

$$\vec{v} \approx Z \vec{i} + \vec{u}, \quad (45)$$

where  $Z = R + jX$  and  $\vec{u} = u_q + ju_d$ . In this form, the model can be integrated. The magnitude of the exciter machine currents can be found from (10). The voltage equation (45) can be combined with (11) and expressed as

$$\|\vec{v}\| e^{j(\angle \vec{i} + \phi(z))} \approx -Z \|\vec{i}\| e^{j\angle \vec{i}} - \vec{u}. \quad (46)$$

This relationship can be used to calculate

$$\|\vec{v}\| \approx \sqrt{\|\vec{u}\|^2 - \text{Im}^2[Z \|\vec{i}\| e^{-j\phi(z)}] - \text{Re}[Z \|\vec{i}\| e^{-j\phi(z)}]} \quad (47)$$

$$\angle \vec{i} \approx \angle \frac{-\vec{u}}{\|\vec{v}\| e^{j\phi(z)} + Z \|\vec{i}\|}. \quad (48)$$

Finally, (9) can be used to determine the main machine field voltage.

### F. Model Summary

The proposed model is depicted graphically in Fig. 3 and summarized in the steps below.

- 1) The main machine field current  $i_{fdr}$  is calculated by the model of the main machine.
- 2) The exciter field current  $i'_{fds}$  is a state variable and used in the voltage regulator model.
- 3) The exciter machine field voltage  $v'_{fds}$  is calculated by the model of the voltage regulator.
- 4) The open-circuit voltages of the exciter machine  $e_{qdr}$  are calculated using (24) and (25)
- 5) The dynamic impedance  $z$  is calculated using (12).
- 6) The magnitude of the exciter machine currents  $\|\vec{i}\|$  is calculated using (10).
- 7) The magnitude of the exciter machine voltages  $\|\vec{v}\|$  and the angle of the exciter machine currents  $\angle \vec{i}$  are calculated using (47) and (48), respectively.
- 8) The main machine field voltage  $v_{fdr}$  is calculated using (9) and used in the model of the main machine.
- 9) The derivatives of the state variables associated with the differentiator approximation  $px$  are calculated using (27).

- 10) The time derivative of the exciter field current  $pi_{fds}'$  is calculated using (26).

### III. RECTIFIER CHARACTERIZATION

In order to use the proposed model, the numerical functions  $\alpha(\cdot)$ ,  $\beta(\cdot)$ , and  $\phi(\cdot)$  must be extracted from the detailed simulations. The extraction of such functions has been discussed in [23]. In particular, it is found that because the functions describe algebraic relationships that are assumed to hold continuously, these functions can be extracted from transient simulations rather than requiring numerous steady-state simulations. This is important in the case of the rotating rectifier in a brushless excitation system because the steady-state dynamic impedance  $z$  varies over a very narrow range. Transient simulations are necessary to characterize the performance of the rectifier over a wide loading range.

The system considered herein is shown in Fig. 2. The main machine is a four-pole, 59 kVA, 560 V synchronous generator with the model and parameters presented in [25] and [26]. This machine model has been extensively validated against experimental measurements [25], [27], [28]. For detailed simulation, it is modeled using the field-only voltage-behind-reactance (FVBR) formulation [29]. The exciter machine formulation, an armature-only voltage-behind-reactance (AVBR) formulation, and its parameters are given in the appendix [27]. The detailed simulations is performed using MATLAB R2016a Simulink's ode23tb integration algorithm with a maximum time step of  $10.85 \mu\text{s}$  and default values for the relative and absolute tolerances. Circuit elements are represented using the Automated State Model Generator, a software package that automatically establishes a state-space model based on the circuit topology and switch states [30].

For the characterization of the rectifier, the main machine is loaded with a balanced three-phase resistive load that draws rated power at rated voltage. Initial conditions are set corresponding to a zero-flux state. The shaft is rotated at a constant  $2\pi 30 \text{ rad/s}$  (1800 RPM), and the frequency of the switching ripple in the rotor quantities is 720 Hz. The field voltage of the exciter is ramped from  $-0.8 \text{ V}$  (corresponding to zero flux linkage) to  $8 \text{ V}$  in 3.33 s (200 cycles) and then ramped back down to  $-0.8 \text{ V}$  in the following 3.33 s (200 cycles). Averaging the waveforms from the detailed simulation over 60-Hz windows every  $1/720 \text{ s}$  yields the values shown in Fig. 4. The least-squares spline approximation SPAP2 algorithm is used to select support points, and it can be seen in Fig. 4 that these data are well represented using cubic splines with relatively few support points, which are given in Table I. Furthermore, both the  $\alpha(\cdot)$  and  $\phi(\cdot)$  functions have discontinuities occurring at approximately  $2.97 \Omega$ . For values of dynamic impedance smaller than this, the values of both  $\alpha(\cdot)$  and  $\phi(\cdot)$  are zero.

### IV. MODEL VALIDATION

In this section, the brushless excitation system AVM is validated with the detailed model in three distinct cases. All simulations are performed using MATLAB R2016a Simulink's ode23tb integration algorithm with the automatic maximum time step, a relative tolerance of  $10^{-6}$ , and the default absolute

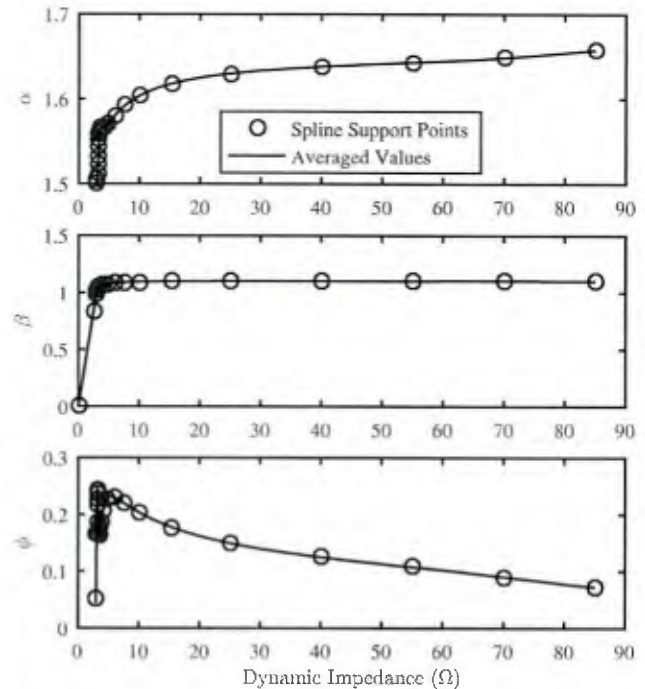


Fig. 4. Functions  $\alpha(\cdot)$ ,  $\beta(\cdot)$ , and  $\phi(\cdot)$ .

TABLE I  
SUPPORT POINTS FOR FUNCTIONS  $\alpha(\cdot)$ ,  $\beta(\cdot)$ , AND  $\phi(\cdot)$

$z$	$\alpha(\cdot)$	$\beta(\cdot)$	$\phi(\cdot)$
0.000	—	0.000	—
2.529	—	0.842	—
2.976	1.500	0.990	0.051
3.059	1.505	1.016	0.167
3.141	1.512	1.035	0.228
3.223	1.524	1.047	0.246
3.269	1.534	1.051	0.237
3.299	1.543	1.053	0.216
3.334	1.553	1.053	0.187
3.378	1.559	1.054	0.171
3.454	1.562	1.055	0.163
3.594	1.565	1.058	0.167
3.738	1.565	1.060	0.176
3.864	1.565	1.063	0.187
4.122	1.566	1.068	0.206
4.829	1.570	1.077	0.228
5.973	1.580	1.085	0.230
7.707	1.592	1.091	0.220
10.034	1.604	1.094	0.205
15.480	1.618	1.098	0.178
25.106	1.630	1.100	0.150
40.098	1.638	1.102	0.125
55.089	1.643	1.103	0.108
70.080	1.649	1.103	0.091
85.072	1.658	1.102	0.073

tolerance. Circuit elements are represented using the Automated State Model Generator [30]. In order to place the eigenvalues of  $D$  sufficiently far into the right half plane,  $R$  and  $X^*$  are selected to be  $r_r + \sqrt{L_q L_d''} \times 10^5 \text{ rad/s}$  and  $\omega_r^* \sqrt{L_q L_d}$ , respectively. In each case, initial conditions corresponding to steady state are selected, and each simulation lasts 0.5 s (30 cycles). Also, the run time associated with each model and case is recorded

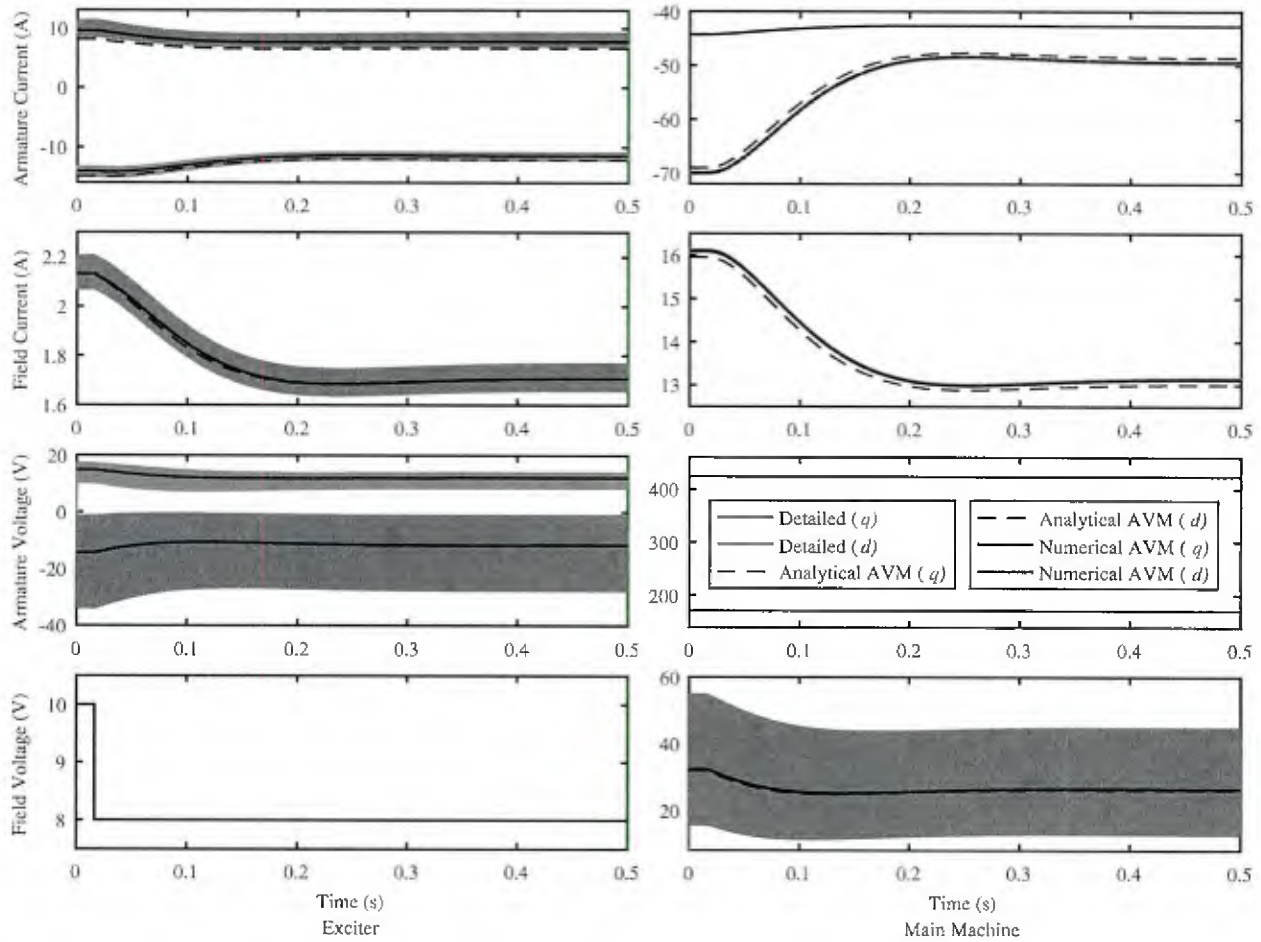


Fig. 5. Case I (excitation voltage step change) results.

by averaging over 20 simulations. The simulations are performed on an Intel Core i7-3770 CPU running at 3.40 GHz with 8.00 GB of RAM. For comparison, the analytical AVM presented in [6] is also simulated in these cases.

In Case I, the main machine field winding is supplied through a rotating rectifier, which is connected to an exciter with 10-V field voltage. The stator is connected to an infinite 560-V bus. The machine is rotating constantly at  $2\pi 30$  rad/s, and the initial rotor angle is  $22^\circ$ . Under this condition, the generator is supplying 46 kW at a power factor of 0.8 lagging. At  $t = 1/60$  s, the field voltage of the exciter is stepped down to 8 V, resulting in the power factor increasing to 0.9 lagging and the reactive power delivered being decreased by 38%. For the detailed simulation, the FVBR formulation of the main machine is used with the detailed representation of the rotating rectifier and the AVBR formulation of the exciter machine. For the analytical AVM simulation, the  $qd$  formulation of the main machine is used with an analytical AVM of the brushless excitation system with a reduced-order exciter machine representation [6]. For the numerical AVM simulation, the  $qd$  formulation of the main machine is used with the AVM of the brushless excitation system. The time steps and run time for all of the cases are given in Table II. The armature and field currents and voltages of both the exciter and main machine are shown in Fig. 5. It can be seen in

 TABLE II  
 MODEL COMPUTATIONAL EFFICIENCY

Case	Simulation	Time steps	Run time (s)
Case I	Detailed	160179	4.05
	Analytical AVM	1626	4.21
	Numerical AVM	1664	0.24
Case II	Detailed	149575	3.90
	Analytical AVM	12043	26.89
	Numerical AVM	4129	0.26
Case III	Detailed	186778	8.41
	Analytical AVM	143918	323.82
Numerical	Stationary AVM	201952	5.98
	Rotating AVM	180903	6.73
	Full AVM	4347	0.39

the figure that the proposed numerical AVM faithfully represents the low-frequency behavior of the main machine and brushless excitation system. The waveforms predicted by the numerical AVM lie within the switching envelope of the waveforms predicted by the detailed model. The deviations of the analytical AVM from the detailed model and numerical AVM are fairly small and largely due to assumptions made in the derivation of the analytical model. Furthermore, it can be seen in Table II, the number of time steps required by the numerical AVM is

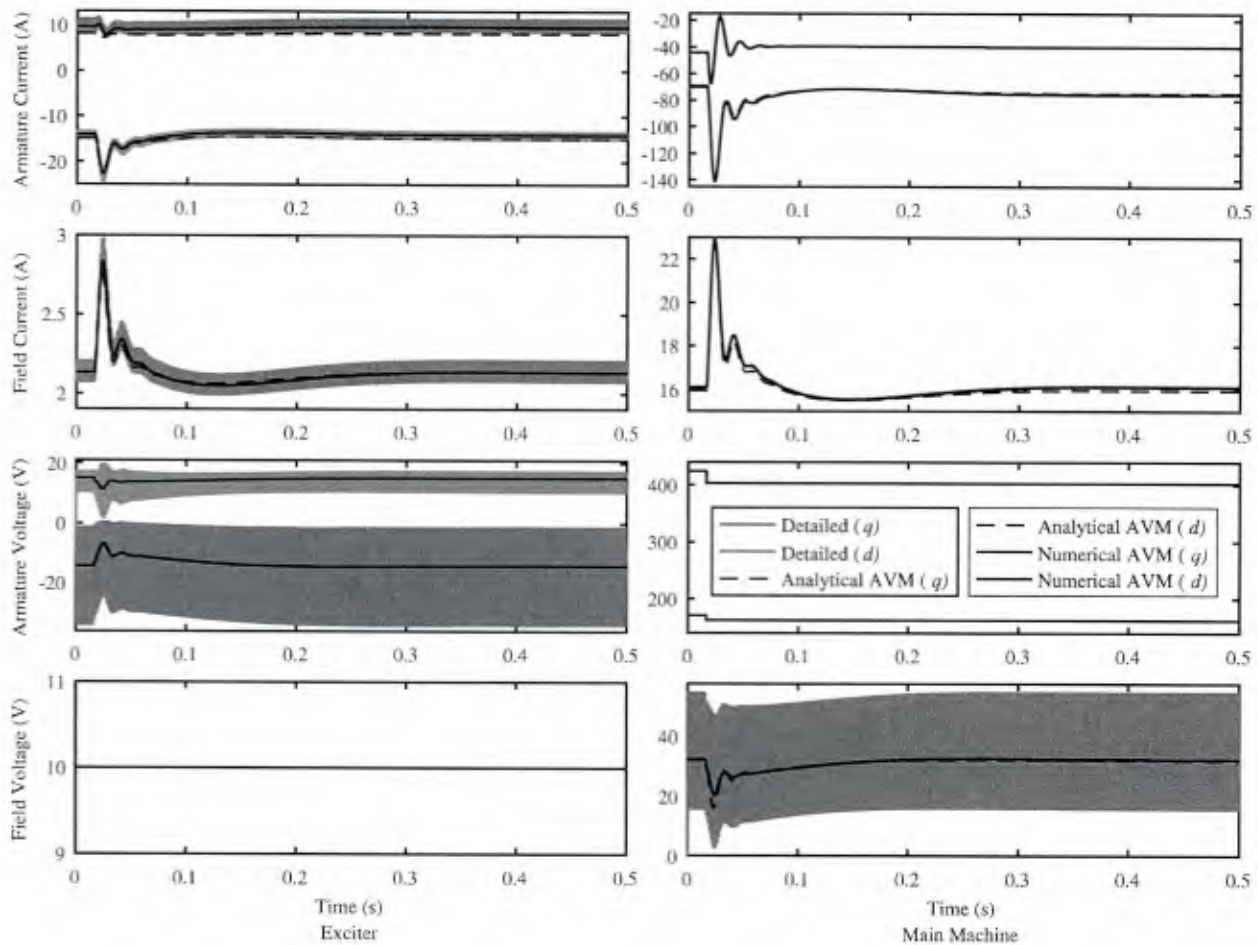


Fig. 6. Case II (terminal voltage step change) results.

slightly greater than that required for the analytical AVM, but the run time is reduced by a factor of 15. Both the numbers of time steps and the run time required by the simulation algorithm are drastically reduced compared with the detailed model; the number of time steps is reduced by a factor of 96, and the run time is reduced by a factor of 17.

In Case II, the main machine field winding is supplied through a rotating rectifier, and the stator is connected to an infinite 560-V bus and starts from the same conditions as in Case I. At  $t = 1/60$  s, a voltage sag occurs, and the magnitude of the output voltage drops to 95% of the initial value. The same machine formulations and rectifier representations used in Case I are used for the detailed and AVM simulations. The waveforms predicted by the AVM model and the detailed model are compared in Fig. 6. As with Case I, the AVM model waveforms are situated within the switching envelope of the detailed model waveforms, and the AVM model is capable of representing the low-frequency behavior of the system. The analytical AVM demonstrates similarly small deviations from the detailed model and numerical AVM. In Table II, it can be seen that similarly drastic reductions in computational cost are obtained. The number of time steps is reduced by a factor of 36, and the run time is reduced by a factor of 15. When compared with the analytical AVM, the number

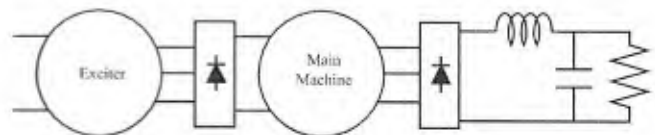


Fig. 7. Case III circuit.

of time steps is reduced by a factor of 3, and the run time is reduced by a factor of 104.

In Case III, the main machine field winding is supplied through a rotating rectifier, which is connected to an exciter with 7.27-V field voltage. The stator is used to supply a rectifier load with  $LC$  filter and resistive load of  $11.1 \Omega$  shown in Fig. 7. The filter inductance and capacitance are 2.5 mH and 1.4 mF, respectively, and the machine is rotating at  $2\pi 30$  rad/s. At  $t = 1/60$  s, the resistive load is stepped from  $11.1 \Omega$  to  $34.4 \Omega$ . This case corresponds to the experimental results used to validate the machine model in [26]. For the detailed simulation, the detailed representation of the stationary rectifier load, the SFVBR formulation of the main machine, the detailed representation of the rotating rectifier, and the AVBR formulation of the exciter machine are used. As this case includes two

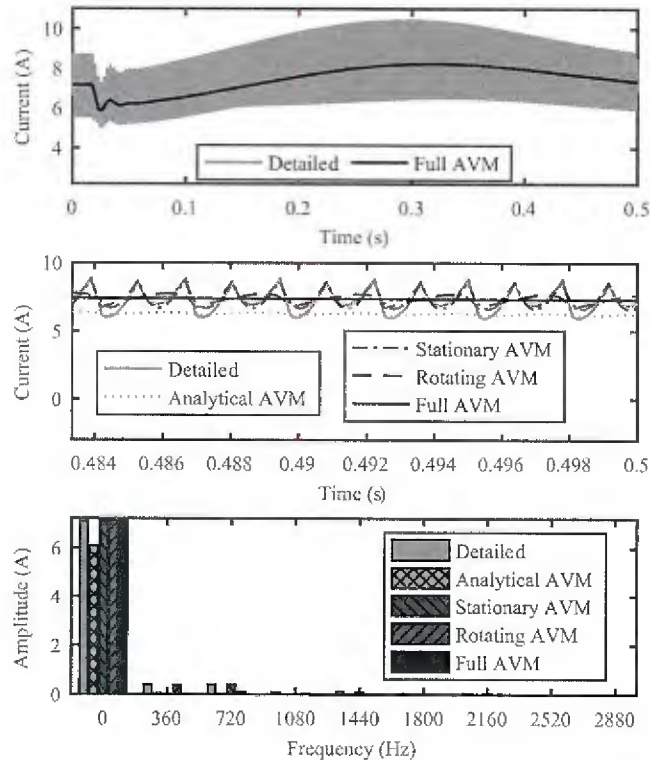


Fig. 8. Case III (rectifier load step change) results (exciter armature  $q$ -axis current during transient and steady-state conditions and FFT results). The stationary, rotating, and full AVM each represent numerical AVMs.

rectifiers, it is possible to perform averaging with either or both of these rectifiers. For the stationary AVM simulation, the numerical AVM of the stationary rectifier load, the FVBR formulation of the main machine, the detailed representation of the rotating rectifier, and the AVBR formulation of the exciter machine are used. The numerical AVM of the stationary rectifier load is implemented as described in [22] and parameterized using the SVBR formulation of the main machine excited with constant dc voltage and loaded with a varying resistive load as described in [23]. For the rotating AVM simulation, the detailed representation of the stationary rectifier load, the SVBR formulation of the main machine, and the numerical AVM of the brushless excitation system are used. For the full AVM simulation, the numerical AVM of the stationary rectifier load, the  $qd$  formulation of the main machine, and the numerical AVM of the brushless excitation system are used. For the analytical AVM simulation, the detailed representation of the stationary rectifier load, the SVBR formulation of the main machine, and an analytical AVM of the brushless excitation system with a reduced-order exciter machine representation are used; this corresponds most closely to the rotating AVM simulation. Because of the complexity of the waveforms in this case, the  $q$ -axis armature current of the exciter is examined more carefully in Fig. 8. In this case, the two rectifiers produce harmonics at two different specific frequencies because of the difference in the number of poles in the main and exciter machines. The rotating rectifier produces harmonics at 720 Hz and multiples thereof, and the stationary rectifier produces harmonics at 360 Hz and

multiples thereof, which includes smaller components at multiples of 720 Hz. Each AVM averages out the harmonics that correspond to the rectifier in question. The partial AVMs, models that only represent one of the rectifiers with an AVM, retain the harmonics associated with the other rectifier. The results of the detailed model and full AVM are shown in the top plot, and it can be seen that the full AVM is capable of representing the low-frequency behavior of the system. In the middle plot, the steady-state behavior of the four models is shown. It can be seen that the full AVM waveform is dc, that the stationary AVM waveform appears periodic with a frequency of 720 Hz, and that the rotating AVM appears periodic with a frequency of 360 Hz. The detailed model waveform clearly contains components at each of these frequencies. This corresponds to the interpretation that the stationary AVM removes the 360-Hz components associated with the stationary rectifier while retaining the 720-Hz components associated with the rotating rectifier and that the rotating AVM does the opposite. A fast Fourier transform (FFT) of these waveforms confirms this interpretation as can be seen in the bottom plot of Fig. 8. The full AVM only retains the dc component, and the partial AVMs retain the harmonics associated with the rectifier that is not averaged by the AVM. It can be seen that both of the partial AVMs have much less improvement in computational cost. The number of time steps for the detailed model, and the rotating AVM only reduces this number by 3%. The run times of the stationary and rotating AVMs are only reduced by 29% and 20%, respectively. However, the full AVM results in a factor of 43 decrease in time steps and a factor of 22 decrease in run time. The computational cost benefits of the AVM are only realized fully when all of the rectifiers in the system are represented by an AVM. Because of the high computational cost of each time step in the analytical AVM, the use of a partial analytical AVM is very costly in such a scenario.

## V. CONCLUSION

A numerical AVM for rotating rectifiers in brushless excitation systems is developed, wherein open-circuit voltages of the brushless exciter armature are used to calculate the dynamic impedance that represents the loading condition. This model averages the periodic switching behavior of the rotating rectifier. Numerical functions describing relationships between averaged dc variables and exciter ac variables in rotating rectifiers are extracted from detailed simulations and vary depending on the loading conditions. The proposed AVM model is validated with the detailed model and compared with an analytical AVM model. It is shown to accurately represent the low-frequency behavior of the system and to have high computational efficiency.

## APPENDIX

### Exciter Machine AVBR Formulation and Parameters

The exciter machine AVBR formulation described below is used to perform detailed simulations. The parameters of the machine are found in Table III. The voltage equation is

$$\mathbf{v}_{abc} = \mathbf{R}\mathbf{i}_{abc} + \mathbf{L}\mathbf{p}\mathbf{i}_{abc} + \mathbf{e}_{abc}. \quad (49)$$

TABLE III  
BRUSHLESS EXCITER PARAMETERS

$P$	8	$N_r/N_{fds}$	0.07
$r_r$	0.121 $\Omega$	$L_{lr}$	0.49 mH
$r_{fds}$	4.69 $\Omega$	$L'_{fds}$	0.117 mH
$L_{mq}$	1.82 mH	$L_{md}$	3.49 mH
$\lambda_{md0}$	5.69 mVs		

The resistance matrix is

$$\mathbf{R} = r_r \mathbf{I}_3 + p \mathbf{L}_r - \frac{2 \mathbf{L}'_{rfd s} p \mathbf{L}'_{rfd s} \mathbf{T}'_r}{3 L'_{fds}}, \quad (50)$$

where

$$\mathbf{L}_r = \begin{bmatrix} L_{lr} + L_A & -\frac{1}{2} L_A & -\frac{1}{2} L_A \\ -\frac{1}{2} L_A & L_{lr} + L_A & -\frac{1}{2} L_A \\ -\frac{1}{2} L_A & -\frac{1}{2} L_A & L_{lr} + L_A \end{bmatrix} - L_B \begin{bmatrix} \cos(2\theta_r) & \cos(2(\theta_r + \frac{\pi}{3})) \\ \cos(2(\theta_r + \frac{\pi}{3})) & \cos(2(\theta_r + \frac{2\pi}{3})) \\ \cos(2(\theta_r - \frac{\pi}{3})) & \cos(2(\theta_r - \pi)) \\ \cos(2(\theta_r - \frac{\pi}{3})) & \cos(2(\theta_r - \frac{2\pi}{3})) \\ \cos(2(\theta_r - \pi)) & \cos(2(\theta_r - \frac{2\pi}{3})) \end{bmatrix} \quad (51)$$

$$\mathbf{L}'_{rfd s} = -L_{md} \begin{bmatrix} \sin \theta_r \\ \sin(\theta_r + \frac{2\pi}{3}) \\ \sin(\theta_r - \frac{2\pi}{3}) \end{bmatrix} \quad (52)$$

$$L'_{fds} = L'_{i'fds} + L_{md} \quad (53)$$

$$L_A = \frac{L_{md} + L_{mq}}{3} \quad (54)$$

$$L_B = \frac{L_{md} - L_{mq}}{3} \quad (55)$$

The inductance matrix is

$$\mathbf{L} = \mathbf{L}_r - \frac{2 \mathbf{L}'_{rfd s} \mathbf{L}'_{rfd s} \mathbf{T}'_r}{3 L'_{fds}}, \quad (56)$$

The voltage vector is

$$\mathbf{e}_{aber} = -\omega_r \lambda_{md0} \begin{bmatrix} \cos \theta_r \\ \cos(\theta_r + \frac{2\pi}{3}) \\ \cos(\theta_r - \frac{2\pi}{3}) \end{bmatrix} + \frac{\mathbf{L}'_{rfd s}}{L'_{fds}} \mathbf{v}'_{fds} + (p \mathbf{L}'_{rfd s} - \frac{\mathbf{L}'_{rfd s} r'_{fds}}{L'_{fds}}) \mathbf{i}'_{fds}. \quad (57)$$

## REFERENCES

- [1] R. W. Ferguson, R. Herbst, and R. W. Miller, "Analytical studies of the brushless excitation system," *Trans. Amer. Inst. Elect. Eng. III, Power App. Syst.*, vol. 78, no. 4, pp. 1815–1821, Dec. 1959.
- [2] E. C. Whitney, D. B. Hoover, and P. O. Bobo, "An electric utility brushless excitation system," *Trans. Amer. Inst. Elect. Eng. III, Power App. Syst.*, vol. 78, no. 4, pp. 1821–1824, Dec. 1959.
- [3] S. Feng, X. Jianbo, W. Guoping, and X. Yong-hong, "Study of brushless excitation system parameters estimation based on improved genetic algorithm," in *Proc. 3rd Int. Conf. Electric Utility Deregulation Restructuring Power Technol.*, Apr. 2008, pp. 915–919.
- [4] V. Ruuskanen, M. Niemela, I. Pyrhonen, S. Kanerva, and J. Kaukonen, "Modelling the brushless excitation system for a synchronous machine," *IET Electr. Power Appl.*, vol. 3, no. 3, pp. 231–239, May 2009.
- [5] A. Griffo, R. Wrobel, P. H. Mellor, and J. M. Yon, "Design and characterization of a three-phase brushless exciter for aircraft starter/generator," *IEEE Trans. Ind. Appl.*, vol. 49, no. 5, pp. 2106–2115, Sep. 2013.
- [6] D. C. Aliprantis, S. D. Sudhoff, and B. T. Kuhn, "A brushless exciter model incorporating multiple rectifier modes and Preisach's hysteresis theory," *IEEE Trans. Energy Convers.*, vol. 21, no. 1, pp. 136–147, Mar. 2006.
- [7] T. L. Skvarenina, S. Pekarek, O. Wasynczuk, P. C. Krause, R. J. Thibodeaux, and J. Weimer, "Simulation of a more-electric aircraft power system using an automated state model approach," in *Proc. 31st Intersoc. Energy Convers. Eng. Conf.*, Aug. 1996, vol. 1, pp. 133–136.
- [8] A. M. Cramer, X. Liu, Y. Zhang, J. D. Stevens, and E. L. Zivi, "Early-stage shipboard power system simulation of operational vignettes for dependability assessment," in *Proc. IEEE Electr. Ship Technol. Symp.*, Jun. 2015, pp. 382–387.
- [9] D. Montenegro, G. A. Ramos, and S. Bacha, "A-diakoptics for the multicore sequential-time simulation of microgrids within large distribution systems," *IEEE Trans. Smart Grid*, vol. 8, no. 3, pp. 1211–1219, May 2017.
- [10] T. Zouaghi and M. Poloujadoff, "Modeling of polyphase brushless exciter behavior for failing diode operation," *IEEE Trans. Energy Convers.*, vol. 13, no. 3, pp. 214–220, Sep. 1998.
- [11] S. Chiniforoosh *et al.*, "Definitions and applications of dynamic average models for analysis of power systems," *IEEE Trans. Power Del.*, vol. 25, no. 4, pp. 2655–2669, Oct. 2010.
- [12] S. Chiniforoosh, H. Atighechi, and J. Jatskevich, "A generalized methodology for dynamic average modeling of high-pulse-count rectifiers in transient simulation programs," *IEEE Trans. Energy Convers.*, vol. 31, no. 1, pp. 228–239, Mar. 2016.
- [13] H. A. Petrosian and P. C. Krause, "A direct-and quadrature-axis representation of a parallel ac and dc power system," *IEEE Trans. Power App. Syst.*, vol. PAS-85, no. 3, pp. 210–225, Mar. 1966.
- [14] P. C. Krause and T. A. Lipo, "Analysis and simplified representations of a rectifier-inverter induction motor drive," *IEEE Trans. Power App. Syst.*, vol. PAS-88, no. 5, pp. 588–596, May 1969.
- [15] E. Kimbark, *Direct Current Transmission*. New York, NY, USA: Wiley-Interscience, 1971.
- [16] T. H. Warner and J. G. Kassakian, "Transient characteristics and modeling of large turboalternator driven rectifier/inverter systems based on field test data," *IEEE Power Eng. Rev.*, vol. PER-5, no. 7, pp. 47–47, Jul. 1985.
- [17] S. D. Sudhoff and O. Wasynczuk, "Analysis and average-value modeling of line-commutated converter-synchronous machine systems," *IEEE Trans. Energy Convers.*, vol. 8, no. 1, pp. 92–99, Mar. 1993.
- [18] S. D. Sudhoff, K. A. Corzine, H. J. Hegner, and D. E. Delisle, "Transient and dynamic average-value modeling of synchronous machine fed load-commutated converters," *IEEE Trans. Energy Convers.*, vol. 11, no. 3, pp. 508–514, Sep. 1996.
- [19] M. Shahnazari and A. Vahedi, "Improved dynamic average modelling of brushless excitation system in all rectification modes," *IET Electr. Power Appl.*, vol. 4, no. 8, pp. 657–669, Sep. 2010.
- [20] I. Jadric, D. Borojevic, and M. Jadric, "Modeling and control of a synchronous generator with an active dc load," *IEEE Trans. Energy Convers.*, vol. 15, no. 2, pp. 303–311, Mar. 2000.
- [21] J. Jatskevich and T. Aboul-Seoud, "Impedance characterization of a six-phase synchronous generator-rectifier system using average-value model," in *Proc. Can. Conf. Electr. Comput. Eng.*, vol. 4, May 2004, pp. 2231–2234.
- [22] J. Jatskevich, S. D. Pekarek, and A. Davoudi, "Parametric average-value model of synchronous machine-rectifier systems," *IEEE Trans. Energy Convers.*, vol. 21, no. 1, pp. 9–18, Mar. 2006.
- [23] J. Jatskevich, S. D. Pekarek, and A. Davoudi, "Fast procedure for constructing an accurate dynamic average-value model of synchronous machine-rectifier systems," *IEEE Trans. Energy Convers.*, vol. 21, no. 2, pp. 435–441, Jun. 2006.

- [24] J. Jatskevich and S. D. Pekarek, "Numerical validation of parametric average-value modeling of synchronous machine-rectifier systems for variable frequency operation," *IEEE Trans. Energy Convers.*, vol. 23, no. 1, pp. 342–344, Mar. 2008.
- [25] D. C. Aliprantis, S. D. Sudhoff, and B. T. Kuhn, "A synchronous machine model with saturation and arbitrary rotor network representation," *IEEE Trans. Energy Convers.*, vol. 20, no. 3, pp. 584–594, Sep. 2005.
- [26] D. C. Aliprantis, S. D. Sudhoff, and B. T. Kuhn, "Experimental characterization procedure for a synchronous machine model with saturation and arbitrary rotor network representation," *IEEE Trans. Energy Convers.*, vol. 20, no. 3, pp. 595–603, Sep. 2005.
- [27] A. M. Cramer, B. P. Loop, and D. C. Aliprantis, "Synchronous machine model with voltage-behind-reactance formulation of stator and field windings," *IEEE Trans. Energy Convers.*, vol. 27, no. 2, pp. 391–402, Jun. 2012.
- [28] D. C. Aliprantis, O. Wasynczuk, and C. D. Rodríguez Valdez, "A voltage-behind-reactance synchronous machine model with saturation and arbitrary rotor network representation," *IEEE Trans. Energy Convers.*, vol. 23, no. 2, pp. 499–508, Jun. 2008.
- [29] Y. Zhang and A. M. Cramer, "Unified model formulations for synchronous machine model with saturation and arbitrary rotor network representation," *IEEE Trans. Energy Convers.*, vol. 31, no. 4, pp. 1356–1365, Dec. 2016.
- [30] *Automated State Model Generator (ASMG) Reference Manual*, P. C. Krause and Associates, Inc., West Lafayette, IN, USA, 2002.



**YuQi Zhang** (S'16) received the B.S. degree in electrical engineering from Harbin Institute of Technology, Harbin, China, in 2005, and the M.S.E.E. degree from the University of Kentucky, Lexington, KY, USA, in 2014, where she is currently working toward the Ph.D. degree in electrical engineering.

Her research interests include electric machine modeling and simulation, power electronics, and power systems.



**Aaron M. Cramer** (S'02–M'07–SM'13) received the B.S. degree (*summa cum laude*) in electrical engineering from the University of Kentucky, Lexington, KY, USA, in 2003, and the Ph.D. degree from Purdue University, West Lafayette, IN, USA, in 2007.

From 2007 to 2010, he was a Senior Engineer with P C Krause and Associates, West Lafayette. In 2010, he joined the University of Kentucky, where he is currently an Associate Professor. His research interests include modeling, simulation, and control of power and energy systems.

Dr. Cramer received the ONR Young Investigator Program Award in 2015. He serves as an Editor of the IEEE TRANSACTIONS ON ENERGY CONVERSION.

# Formulation of Rectifier Numerical Average-Value Model for Direct Interface with Inductive Circuitry

YuQi Zhang, *Member, IEEE*, and Aaron M. Cramer, *Senior Member, IEEE*

**Abstract**—The computational cost for the simulation of detailed models of machine-rectifier systems is expensive because of repetitive diodes switching. Average-value models (AVMs) of machine-rectifier systems have been developed that can alleviate the computational burden by neglecting the details of the switching of each individual diode while retaining the average characteristics. This paper proposes an alternative formulation of numerical AVMs of machine-rectifier systems, which makes direct use of the natural dynamic impedance of the rectifier without introducing low-frequency approximations or algebraic loops. By using this formulation, direct interface of the AVM is achieved with inductive circuitry on both the ac and dc sides allowing traditional voltage-in, current-out formulations of the circuitry on these sides to be used with the proposed formulation directly. This numerical AVM formulation is validated against an experimentally validated detailed model and compared with previous AVM formulations. It is demonstrated that the proposed AVM formulation accurately predicts the system's low-frequency behavior during both steady and transient states, including in cases where previous AVM formulations cannot predict accurate results. Both run times and numbers of time steps needed by the proposed AVM formulation are comparable to those of existing AVM formulations and significantly decreased compared with the detailed model.

**Index Terms**—ac machines, generators, converters, simulation.

## I. INTRODUCTION

Machine-rectifier systems are generally utilized in the electrical subsystems of electric vehicles, including ships, aircraft, and automobiles, and for the brushless excitation of large synchronous machines. Modeling and simulation of machine-rectifier systems have great significance in the design and analysis of such applications because they can predict the dynamic behavior of each component and the overall system prior to the actual realization in hardware. Accurate and efficient modeling of machine-rectifier systems is particularly beneficial in applications with long run times, iterative simulations with diverse sets of parameters, and/or a high component count, such as microgrids [1], shipboard power systems [2], [3], and aircraft power systems [4].

Different approaches have been proposed to simulate and model machine-rectifier systems. The traditional detailed model of such systems has the ability to predict results accurately and offer design evaluations [5] and can be easily developed utilizing different simulation software packages [6].

Manuscript received January 19, 2018; revised May 1, 2018; accepted September 19, 2018. This work was supported by the Office of Naval Research (ONR) through the ONR Young Investigator Program N00014-15-1-2475.

Y. Q. Zhang and A. M. Cramer are with the University of Kentucky, Lexington, KY 40506 USA (e-mail: yuqi.zhang@uky.edu, aaron.cramer@uky.edu).

However, it requires long simulation times due to repetitive switching of the diodes. To reduce the computational cost, average-value models (AVMs) have been developed by neglecting the details of each individual switching [7], [8]. Construction methods for AVMs of rectifiers can be generally classified into two categories, i.e., analytical derivation [9]–[16] and parametric or numerical approaches [17]–[22]. In analytical derivation methods, analytical relationships between variables on the ac and dc sides are derived. In early studies, such relationships are derived based on strong assumptions (e.g., idealized ac system, constant commutating reactance) [9]–[11]. In [12], the  $d$ -axis subtransient reactance is used to represent the ac-side commutating reactance, which neglects the effect of the  $q$ -axis subtransient reactance. In [13], the commutating reactance is determined by a function of the converter firing angle and of both the  $q$ - and  $d$ -axis subtransient reactances. Subsequently, dynamic AVMs are developed to accurately predict frequency-domain impedance characteristic [14]. Analytical derivation methods are based upon specific operating mode and require significant work to solve nonlinear equations and/or numerical integration, which may significantly reduce the computational efficiency.

As an alternative to analytical derivations, the parametric or numerical approach simplifies the development of AVMs. In parametric or numerical approaches, rectifier AVM parameters are obtained from detailed simulations at an earlier model development stage using numerical solutions [17]–[21]. The study in [17] uses a set of fixed parameters to model the averaged rectifier behavior. In [19], the AVM is improved by using dynamic parameters which vary depending on operational conditions. The approach in [19] (and subsequently [20], [21]) introduces a low-frequency approximation of the inductor in the dc filter. It was found in [22] that this approximation was not useful for rotating rectifiers in brushless excitation systems because the field winding being fed by the rectifier did not have similar dynamics to the LC dc filters considered in [19] and subsequent work. Therefore, in [22], a low-frequency approximation was introduced to the ac side for such systems. The difference between these two approaches is not really about stationary versus rotating but about feeding an LC circuit with load versus a field winding that resembles an RL circuit. The parametric or numerical approach has been extended in numerous ways (e.g., ac harmonics and frequency dependency for thyristor-controlled rectifiers are considered in [23]). The fundamental approach is the same, based on numerical averaging of the results of detailed simulations in order to establish a numerical representation of the relationship between the ac and dc variables. However, previous approaches for numeri-

cal AVMs introduce low-frequency approximations to avoid improper transfer functions on either the ac or dc side of the rectifier. These approximations can create inaccuracy in highly dynamic situations and can also complicate the interfacing of traditional models of equipment on either the ac or dc side of the rectifier.

Herein, a numerical AVM formulation is proposed that provides a means of directly coupling the AVM with inductive circuitry (e.g., machine on the ac side and dc filter on the dc side). While the proposed formulation uses a model with similar mathematical relationships to existing AVM formulations, it makes direct use of the natural dynamic impedance of the rectifier without the introduction of low-frequency approximations on either the ac or the dc side of the rectifier, a source of significant inaccuracy that is demonstrated in the paper. By using this formulation, direct interface of the AVM that is demonstrated herein is achieved with inductive circuitry on both the ac and dc sides allowing traditional voltage-in, current-out formulations of the circuitry on these sides to be used with the proposed formulation directly. In the proposed alternative formulation, it is not necessary to introduce low-frequency approximations or to invert the voltage-current interfaces on either the ac or dc side for interfacing with an LC circuit with load or a field winding that resembles an RL circuit. Therefore, the proposed formulation is equally valid for the stationary rectifier applications considered in [19]–[21] and for the rotating rectifier application considered in [22]. Direct interfacing with inductive branches on the ac and dc sides of the rectifier is achieved without introducing low-frequency approximations or algebraic loops. The proposed model is validated against an experimentally validated detailed model and compared with previous AVM formulations in six cases. The results show that the low-frequency behavior of the system is accurately represented (even in cases in which previous AVM formulations fail to accurately represent this behavior) and that the high computational efficiency associated with existing AVMs is retained. Because the proposed AVM can be directly interfaced with simulation models with traditional voltage-in, current-out formulations of the ac and dc equipment, it can be readily used with existing models of such equipment in commercial simulation toolboxes.

The organization of this paper is as below. Section II describes the proposed model, while Section III explains the rectifier characterization procedure. The model validation and comparison are presented in Section IV, and Section V concludes the paper.

## II. AVERAGE-VALUE MODEL OF MACHINE-RECTIFIER SYSTEMS

An alternative approach for applying parametric or numerical AVMs is presented below that reformulates the relationships between variables on the ac and dc side of the rectifier to avoid introducing low-frequency approximations, inverting the voltage-current interfaces on either the ac or dc side, or creating algebraic loops. The notation used herein is summarized in the appendix.

### A. Rectifier relationships

The method presented for modeling the relationships in the rectifier shown in Fig. 1 are based on [19] and [22]. In [19], the relationships that represent the average behavior of the stationary rectifier are:

$$||\vec{v}|| = \alpha_s(z_s)v_{dc} \quad (1)$$

$$i_{dc} = \beta_s(z_s)||\vec{i}|| \quad (2)$$

$$\angle \vec{v} = \angle \vec{i} + \phi_s(z_s) + \pi, \quad (3)$$

where  $\vec{v}$  and  $\vec{i}$  are the stationary armature variables on the ac side transformed to the rotating reference frame in space phasor form,  $\alpha_s(\cdot)$ ,  $\beta_s(\cdot)$ , and  $\phi_s(\cdot)$  are the essential numerical functions,  $\pi$  is the phase offset since the current  $\vec{i}$  is out of the rectifier, and  $z_s$  is a “conveniently defined” dynamic impedance, which is defined in [19] as

$$z_s = \frac{v_C}{||\vec{i}||}, \quad (4)$$

where  $v_C$  is the capacitor voltage of the LC filter. In [19], the dynamic impedance  $z_s$  was selected because  $v_C$  is a state variable and  $z_s$  is readily available in simulation.

For rotating rectifiers in brushless excitation systems, similar relationships to (1)–(3) are used in [22]. Because the main machine field winding is different from the LC filter and does not have a capacitor voltage, an alternative dynamic impedance is used:

$$z_r = \frac{||e_{qdr}||}{i_{fdr}}, \quad (5)$$

where  $e_{qdr}$  is the brushless exciter armature open-circuit voltages and  $i_{fdr}$  is the current into the main machine field winding.

The natural formulations of both the machine on the ac side and the inductor on the dc side in both cases would be a voltage-in, current-out formulation in which the rectifier model would input the ac and dc currents and calculate the ac and dc voltages. Such models involve proper state models, but they are not directly consistent with the relationships (1)–(3). To address the inconsistency, low-frequency approximations are introduced in both [19] and [22] to transform either the dc or ac model to a current-in, voltage-out formulation. It is argued, for example in [24], that such approximations do not significantly effect the behavior of the model.

The proposed reformulation of numerical AVMs for machine-rectifier systems uses similar relationships for the ac and dc voltages and currents. These relationships are modified in order to model rectifiers without using the low-pass filter [19], [20] and the differentiator approximation [22]. The relationships represent the average behavior of the rectifier shown in Fig. 1 are:

$$||\vec{v}|| = \alpha(z)v_{dc} \quad (6)$$

$$i_{dc} = \beta(z)||\vec{i}|| \quad (7)$$

$$\angle \vec{v} = \angle \vec{i} + \phi(z) + \pi. \quad (8)$$

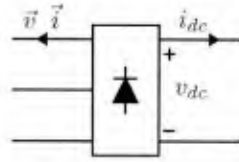


Fig. 1. Rectifier.

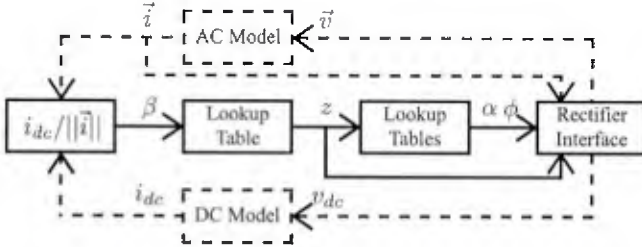


Fig. 2. Summary of model formulation (dashed lines represent external interfaces from/to the proposed model).

Instead of a “conveniently defined” dynamic impedance set some distance from the rectifier in [19], [20], [22], a natural dynamic impedance is employed:

$$z = \frac{v_{dc}}{\|i\|}, \quad (9)$$

where  $v_{dc}$  is the terminal voltage of the rectifier. The proposed numerical AVM of machine-rectifier systems includes both stationary rectifiers and rotating rectifiers in the brushless excitation systems.

### B. Model summary

The proposed AVM formulation is graphically described in Fig. 2 and summarized in the steps below.

- 1) The input current of the rectifier  $\|i\|$  is calculated by the ac model. For the stationary rectifier, the ac model is the main machine armature. For the rotating rectifier, the ac model is the exciter armature.
- 2) The rectifier dc current  $i_{dc}$  is calculated by the dc model. For the stationary rectifier,  $i_{dc}$  is the filter current. For the rotating rectifier,  $i_{dc}$  is the main machine field current.
- 3) The numerical function  $\beta(\cdot)$  is calculated using (7).
- 4) The dynamic impedance  $z$  is obtained by inverting the numerical function  $\beta(\cdot)$ .
- 5) The numerical functions  $\alpha(\cdot)$  and  $\phi(\cdot)$  are obtained through lookup tables.
- 6) The magnitude  $\|\vec{v}\|$  and angle  $\angle \vec{v}$  of the ac voltage are calculated using (6) and (8), respectively, and the ac voltage  $\vec{v}$  is used in the ac model.
- 7) The rectifier dc voltage  $v_{dc}$  is calculated using (9) and used in the dc model.

### III. RECTIFIER CHARACTERIZATION

The essential numerical functions  $\alpha(\cdot)$ ,  $\beta(\cdot)$ , and  $\phi(\cdot)$  are able to be extracted from the detailed simulations numerically, which has been discussed in [20]. Based on the assumption

that algebraic relationships formulated by those functions are continuous, the rectifier characterization over a wide loading range can be done by transient simulations instead of repeated steady-state simulations. For both characterizations of stationary and rotating rectifiers, the ode23tb integration algorithm in MATLAB R2016a Simulink is used in the detailed simulations. The maximum time step is set to be 0.1  $\mu$ s. The values of relative and absolute tolerances are set to their default values. Automated State Model Generator (ASM), which can automatically establish state-space models based upon topological states of the circuits, is used to represent circuit elements [25].

A four-pole synchronous generator rated for 59 kVA, 560 V at 1800 r/min is considered here as the main machine. Its model and parameters are adopted from studies in [26] and [27], and these models have been validated with multiple experimental measurements [26], [28], [29]. For the stationary rectifier characterization, the stator-only voltage-behind-reactance (SVBR) formulation [30] is used to model the main machine. The main machine is connected to a rectifier, which supplies a resistive load through an LC filter with a 2.5-mH inductance and a 1.4-mF capacitance. The resistive load exponentially increases from 0.01  $\Omega$  to 100  $\Omega$  in 1 s. The main machine field winding is connected to a 30-V voltage source. Initial conditions corresponding to a zero-flux state are selected. The resultant waveforms exhibit switching ripple at 360 Hz. The waveforms are averaged over 60-Hz windows every 1/360 s, and the values are plotted in Fig. 3.

For the rotating rectifier characterization, the field-only voltage-behind-reactance (FVBR) formulation [30] is used to model the main machine. A balanced three-phase resistive load is connected to the main machine and draws rated power at rated voltage. The armature-only voltage-behind-reactance (AVBR) formulation of the exciter machine and its parameters are provided in [30]. Initial conditions corresponding to a zero-flux state are selected. The initial value of the exciter field voltage is  $-0.8$  V. In the first 3.33 s, the exciter field voltage linearly increases to 8 V and then linearly decreases to the initial value in the next 3.33 s. The resultant waveforms exhibit switching ripple at 720 Hz. The waveforms are averaged over 60-Hz windows every 1/720 s, and the values are plotted in Fig. 4.

Relatively few support points are selected using the least-squares spline approximation SPAP2 algorithm, and cubic splines can accurately represent these data as shown in Fig. 3 and Fig. 4. The support points are provided in Tables II in the appendix.

### IV. MODEL VALIDATION

The proposed AVM formulation of machine-rectifier systems is validated against the detailed model and compared with previous AVM formulations in this section. The ode23tb integration algorithm is adopted with the default absolute tolerance and the automatic maximum time step in MATLAB R2016a Simulink. The relative tolerance is set to be  $10^{-6}$ . ASM is used to represent circuit elements. Each simulation starts at steady state and lasts 1 s (60 cycles). The run time is

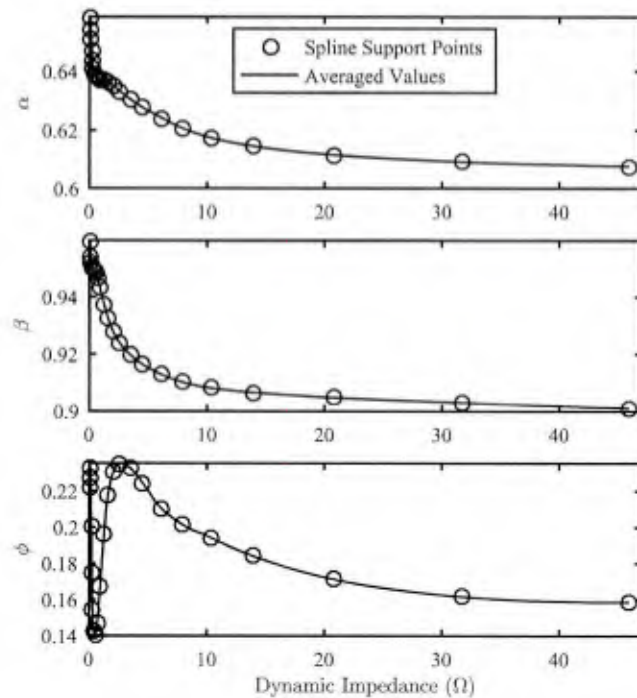


Fig. 3. Stationary functions  $\alpha(\cdot)$ ,  $\beta(\cdot)$ , and  $\phi(\cdot)$ .

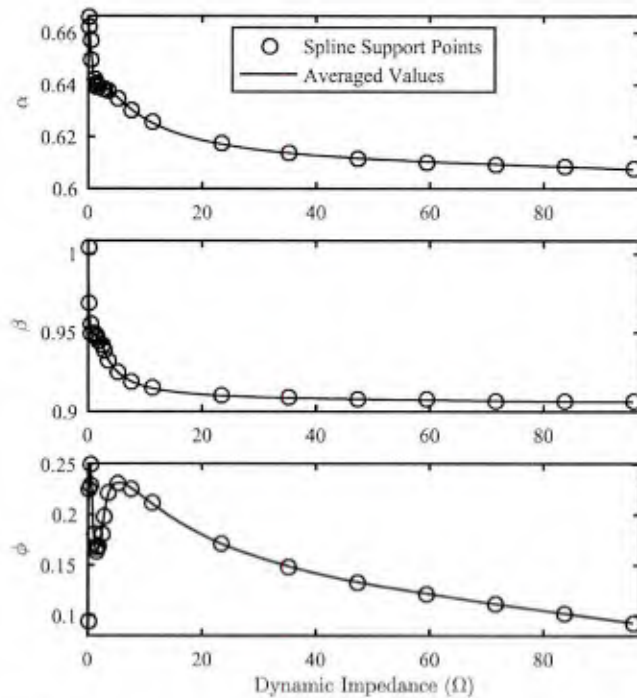


Fig. 4. Rotating functions  $\alpha(\cdot)$ ,  $\beta(\cdot)$ , and  $\phi(\cdot)$ .

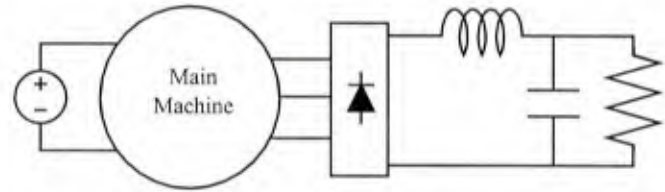


Fig. 5. Case I and Case II arrangement.

averaged over 20 simulations for each model and case. A Dell Optiplex 7010 computer with an Intel Core i7-3770 3.40 GHz processor and 8.00 GB of RAM is used to perform all the simulations.

#### A. Main machine and stationary rectifier load

In Case I, the main machine field winding is connected to a 25-V voltage source as shown in Fig. 5. The stator is connected to a rectifier which feeds a  $12\ \Omega$  resistive load via the LC filter. At  $t = 1/60$  s, the excitation voltage is stepped up to 150% of the initial value. The SVBR formulation of the main machine and the detailed representation of the rectifier load are used in the detailed simulation. The  $qd$  formulation of the main machine and the previous AVM formulation of the stationary rectifier are adopted with a current-in, voltage-out formulation of the LC filter in the previous AVM simulation. The inductor in the LC filter operates as a differentiator with an improper transfer function. This improper transfer function is represented with a low-frequency approximation, and the time constant associated with the approximation is set to be  $10\ \mu\text{s}$  [19]. The  $qd$  formulation of the main machine and the proposed AVM formulation of the rectifier are used in the proposed AVM simulation. In all cases, the time steps and the run times are listed in Table I. Fig. 6 shows the armature voltages and currents and the field current of the main machine. The main machine's low-frequency behavior is accurately represented by both the previous and proposed AVMs in this case. Both sets of waveforms predicted by the AVMs are essentially identical and follow the tendency of detailed model waveforms. Furthermore, it can be seen in Table I, both the run time and the number of time steps required by the proposed AVM are comparable with those required for the previous AVM. The run time are reduced by 97%, and the number of time steps is reduced by 99% compared with the detailed model.

The same excitation of the main machine, rectifier load and initial conditions used in Case I are used in Case II as shown in Fig. 5. At  $t = 1/60$  s, a bolted fault across the capacitor occurs at the dc side. For Case II, the same machine formulations and rectifier representations as in Case I are used in the detailed simulation and AVM simulations. Fig. 7 shows the comparisons of the waveforms obtained from the proposed AVM, the previous AVM, and the detailed model. One can find that resultant waveforms from the proposed AVM follow the overall tendency of the waveforms obtained from the detailed model. It can be concluded that the proposed AVM is capable of representing the system's low-frequency responses. In contrast, it can be observed that the previous

TABLE I  
MODEL COMPUTATIONAL EFFICIENCY

Case	Simulation	Time steps	Run time (s)
Case I	Detailed	337978	7.62
	Previous AVM	3959	0.23
	Proposed AVM	3999	0.23
Case II	Detailed	67182	1.70
	Previous AVM	6661	0.26
	Proposed AVM	5258	0.25
Case III	Detailed	293059	7.36
	Previous AVM	3805	0.26
	Proposed AVM	4108	0.24
Case IV	Detailed	244518	5.82
	Previous AVM	6141	0.28
	Proposed AVM	7361	0.25
Case V	Detailed	372815	16.40
	Previous AVM	2710	0.26
	Proposed AVM	2548	0.24
Case VI	Detailed	246953	10.59
	Previous AVM	8947	0.35
	Proposed AVM	8716	0.32

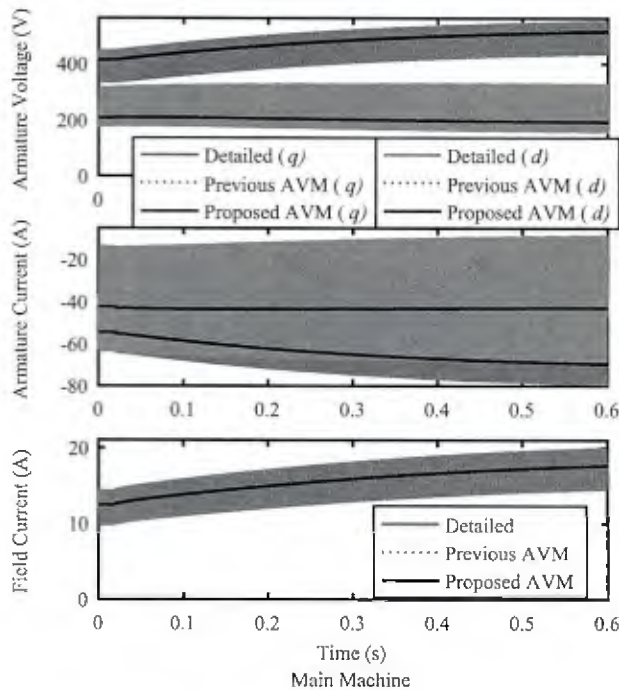


Fig. 6. Case I (excitation voltage step change) results.

AVM exhibits significant deviations from the behavior predicted by the detailed model during the transition. The cause of these deviations is the use of different dynamic impedances and the introduction of low-frequency approximations in the previous AVM. As can be seen in Table I, the computational cost, i.e., the run time and the number of time steps, of the proposed AVM is slightly less than that of the previous AVM. The run time and the number of time steps are reduced by 85% and 92% compared with the detailed model, respectively. The computational cost of the detailed model in Case II is lower than in Case I because the dc fault causes the rectifier diodes to stop switching on and off.

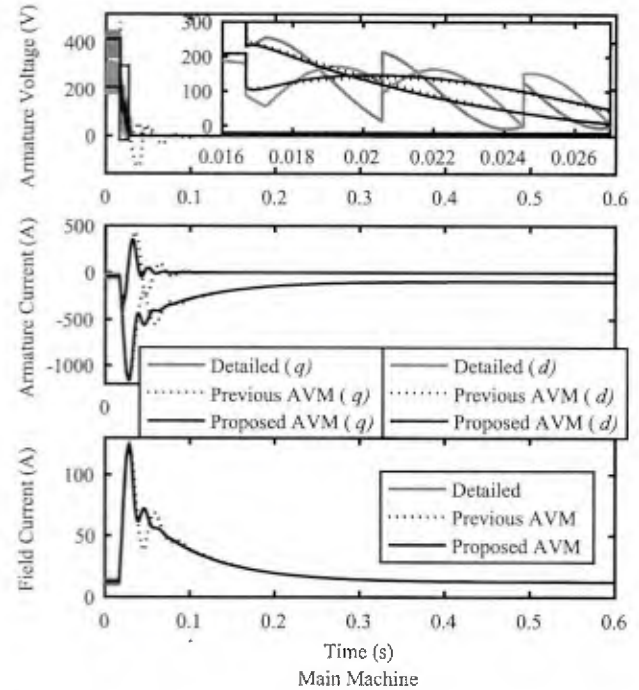


Fig. 7. Case II (dc fault) results.

### B. Exciter, rotating rectifier, main machine, and infinite bus

In Case III, the field winding of the main machine is connected to a rotating rectifier, which is fed by an exciter with 7.5-V field voltage as shown in Fig. 8. The stator is used to supply power to an infinite 560-V bus. The rotor angle of the machine is  $\pi/8$  rad. At  $t = 1/60$  s, the rotor speed linearly increases from 1800 r/min to 1912.5 r/min over  $1/120$  s and then linearly decreases back to the original value over  $1/120$  s. As a consequence, the rotor angle increases to  $3\pi/16$  rad. The FVBR formulation of the main machine, the armature-only voltage-behind-reactance (AVBR) formulation of the brushless exciter machine presented in [30] and the detailed representation of the rotating rectifier are used in the detailed simulation. The  $qd$  formulation of the main machine, the previous AVM formulation of the exciter machine and rotating rectifier presented in [22] are used in the previous AVM simulation. The exciter machine is represented using a low-frequency approximation described in [22] with poles located at  $-1.4 \times 10^5$  rad/s and  $-0.7 \times 10^5$  rad/s. The  $qd$  formulation of the main machine, the  $qd$  formulation of the exciter and the proposed AVM formulation of the rectifier are used in the proposed AVM simulation. Fig. 9 shows the armature currents and the field voltage and current of the main machine. The waveforms are predicted accurately by the proposed AVM even when the rotor speed changes significantly. In contrast, there are significant deviations exhibited in the previous AVM waveforms from the detailed model waveforms and the proposed AVM waveforms during the transient state in this case. Comparing the computational cost with the previous AVM shown in Table I, though the number of time steps is slightly greater, the run time is slightly smaller. The run time

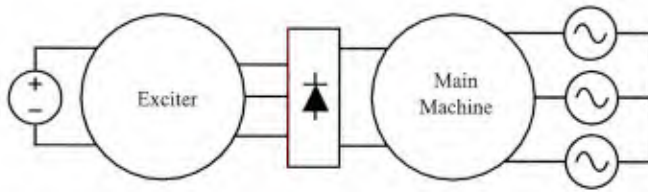


Fig. 8. Case III and Case IV arrangement.

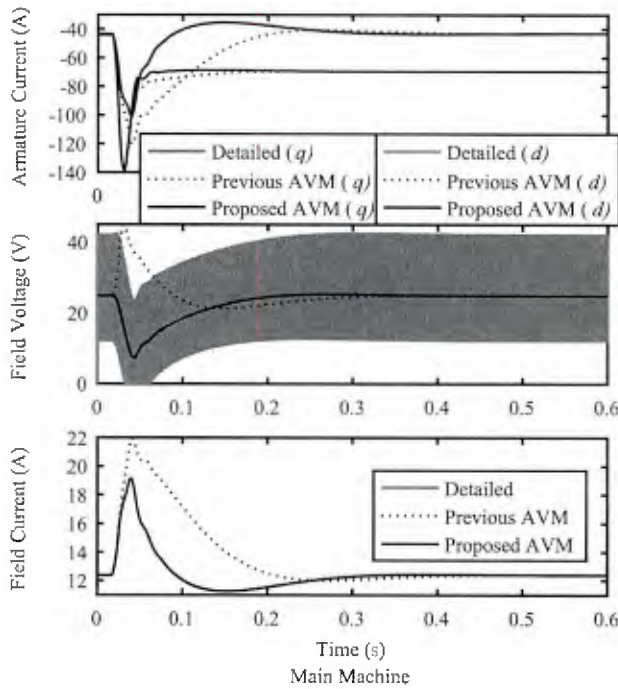


Fig. 9. Case III (rotor angle change) results.

and the number of time steps are reduced by 97% and 99% compared with the detailed model, respectively.

The same arrangement of the exciter, rotating rectifier, main machine, infinite 560-V bus and initial conditions used in Case III are used in Case IV as shown in Fig. 8. At  $t = 1/60$  s, a three-phase bolted fault occurs at the ac side, i.e., the armature voltages of the main machine are stepped down to 0 V. Case IV uses the same rectifier representations and machine formulations for the detailed and AVM simulations as Case III. Fig. 10 shows the armature voltages and currents and the field current of the exciter machine. It shows that the waveforms obtained from the proposed AVM follow the waveforms obtained from the detailed model very well, but the previous AVM cannot capture the rapid decline of the voltages or the low-frequency oscillations observed in the currents. From Table I, it can be seen that the proposed AVM again has comparable number of time steps and run time compared with the previous AVM. The run time is reduced by 96%, and the number of time steps is reduced by 97% compared with the detailed model.

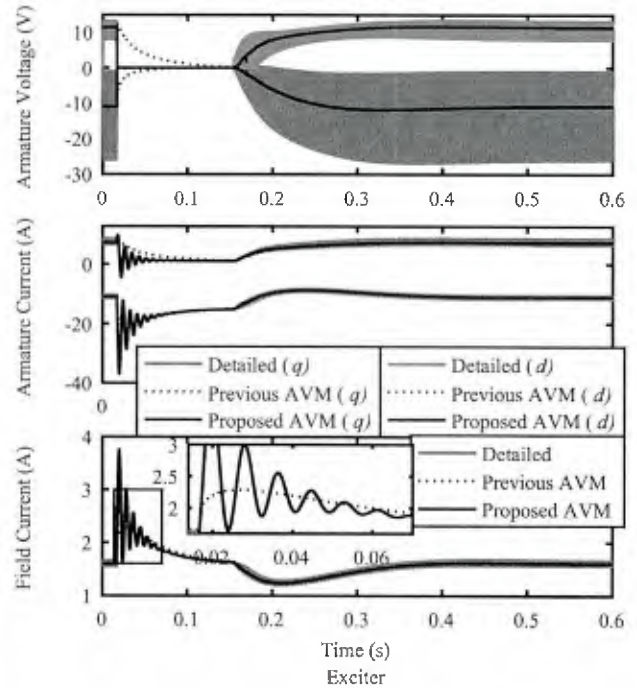


Fig. 10. Case IV (ac fault) results.

### C. Exciter, rotating Rectifier, main machine, and stationary rectifier load

In Case V, the field winding of the main machine is connected to a rotating rectifier, which is fed by an exciter with 7.5-V field voltage shown in Fig. 11. The stator is connected to a rectifier which feeds a  $12 \Omega$  resistive load via an  $LC$  filter. At  $t = 1/60$  s, the excitation voltage of the exciter drops to 6 V. The SFVBR formulation of the main machine, the detailed representation of the rectifier load, the AVBR formulation of the brushless exciter machine, and the detailed representation of the rotating rectifier are used in the detailed simulation. The  $qd$  formulation of the main machine, the previous AVM formulation of the stationary rectifier presented in [19], and the previous AVM formulation of the exciter machine and rotating rectifier presented in [30] are used in the previous AVM simulation. The  $qd$  formulations of the main and exciter machines, the proposed AVM formulations of the stationary and rotating rectifiers are used in the proposed AVM simulation. The armature voltages and currents and the field current of the exciter machine are plotted in Fig. 12. As with Case I, the figure shows that the waveforms obtained from the proposed AVM are identical to the waveforms obtained from the previous AVM and faithfully follow the trace predicted by the detailed model. The proposed AVM performs similarly to the previous AVM and significantly improves the computational efficiency with respect to the detailed model as shown in Table I. Both the run time and the number of time steps required by the proposed AVM are reduced by 99% compared with the detailed model.

The same arrangement of the exciter, rotating rectifier, main machine, stationary rectifier load and initial conditions used

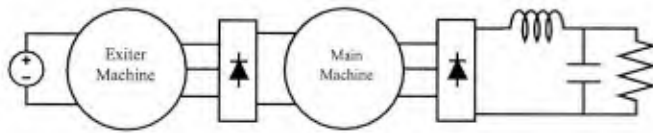


Fig. 11. Case V and Case VI arrangement.

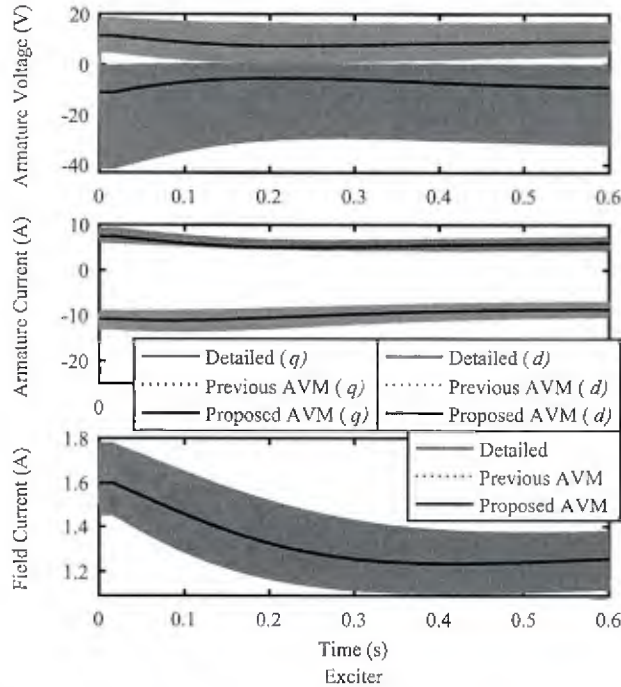


Fig. 12. Case V (excitation voltage step change) results.

in Case V are used in Case VI as shown in Fig. 11. At  $t = 1/60$  s, a bolted fault across the capacitor occurs at the dc side. Case VI uses the same machine formulations and rectifier representations as in Case V in the detailed and AVM simulations. Fig. 13 shows the field voltage and the output voltage and current of the main machine. It is shown that the waveforms obtained from the proposed AVM follow the waveforms obtained from the detailed model very well. It is also shown in Fig. 13 that the previous AVM had significant discrepancies on the dc side of the stationary rectifier. The waveforms shown in Fig. 7 for Case II are not shown for this case, but the previous AVM also demonstrated the same discrepancies in this case. As with the other cases, it can be seen in Table I that the proposed AVM has a comparable computational cost with the previous AVM and that its computational costs are much smaller than those associated with the detailed model. The run time and the number of time steps are reduced by 97% and 96% compared with the detailed model, respectively.

## V. CONCLUSION

An alternative formulation of numerical AVMs of machine-rectifier systems is proposed, which can directly interface with branches on the ac and dc sides of the rectifier without introducing low-frequency approximations or algebraic

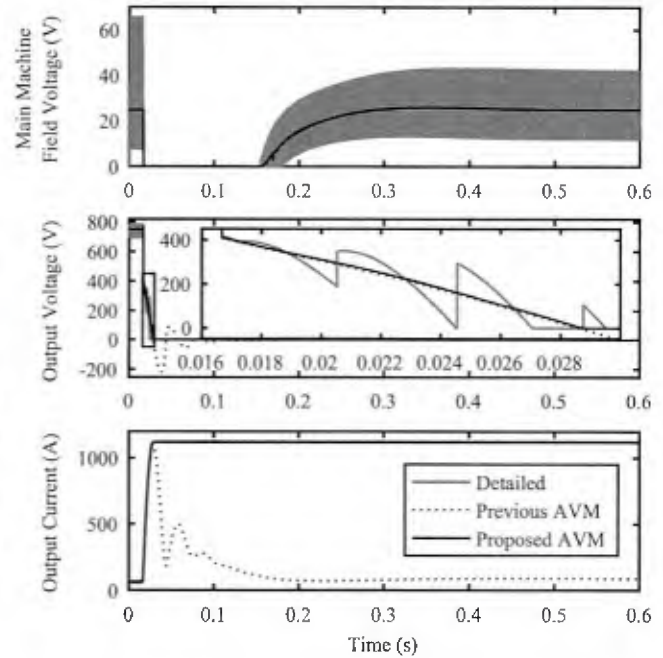


Fig. 13. Case VI (dc fault) results.

loops. The key numerical functions are similar to those used in previous AVM formulations and are extracted from detailed simulations over varying loading conditions. The natural dynamic impedance of the rectifier, calculated using the terminal quantities of the rectifier, is directly used without introducing low-frequency approximations or algebraic loops. The proposed AVM formulation, which encompasses both stationary rectifiers and rotating rectifiers in brushless excitation systems, does not require inversion of voltage-current interfaces on either the ac or dc side and can be directly interfaced with simulation models with traditional voltage-in, current-out formulations of the ac and dc equipment. This AVM formulation is validated against the detailed model and compared with previous AVM formulations in six distinct cases. The proposed AVM formulation is shown to be accurate in providing simulations during both steady and transient states, including in cases where previous AVM formulations do not accurately predict the waveforms, while retaining the computational cost advantages of existing AVM formulations over detailed models.

## APPENDIX

### A. Notation

Matrices and vectors are bold faced. The electrical angular speed and position of the machine are

$$\omega_r = \frac{P}{2}\omega_{rm} \quad (10)$$

$$\theta_r = \frac{P}{2}\theta_{rm}, \quad (11)$$

respectively, where  $\omega_{rm}$  and  $\theta_{rm}$  are the mechanical angular velocity and position of the machine, respectively, and  $P$  is the

number of magnetic poles in the machine. The armature variables associated with a machine with a stationary armature can be expressed in vector form as  $\mathbf{f}_{abc s} = [f_{as} \ f_{bs} \ f_{cs}]^T$ , where  $f$  may represent voltage ( $v$ ), current ( $i$ ), or flux linkage ( $\lambda$ ). Such stationary armature variables are able to be transformed into the rotor reference frame [31] using

$$\mathbf{f}_{qd0s} = \mathbf{K}_s \mathbf{f}_{abc s}, \quad (12)$$

where

$$\mathbf{K}_s = \frac{2}{3} \begin{bmatrix} \cos \theta_r & \cos(\theta_r - \frac{2\pi}{3}) & \cos(\theta_r + \frac{2\pi}{3}) \\ \sin \theta_r & \sin(\theta_r - \frac{2\pi}{3}) & \sin(\theta_r + \frac{2\pi}{3}) \\ \frac{1}{2} & \frac{1}{2} & \frac{1}{2} \end{bmatrix} \quad (13)$$

and  $\mathbf{f}_{qd0s} = [f_{qs} \ f_{ds} \ f_{0s}]^T$  represents the  $q$ - and  $d$ -axis, and the zero-sequence components of the quantity. For systems considered herein, the zero-sequence component will be zero and can be ignored. Stationary variables transformed to the rotating reference frame are also able to be represented in space-phaser notation:  $\vec{f}_{qds} = f_{qs} - j f_{ds}$ .

The armature variables associated with a machine with a rotating armature are denoted  $\mathbf{f}_{abc r} = [f_{ar} \ f_{br} \ f_{cr}]^T$ . Such rotating armature variables are able to be transformed into the stationary reference frame using

$$\mathbf{f}_{qd0r} = \mathbf{K}_r \mathbf{f}_{abc r}, \quad (14)$$

where

$$\mathbf{K}_r = \frac{2}{3} \begin{bmatrix} \cos \theta_r & \cos(\theta_r + \frac{2\pi}{3}) & \cos(\theta_r - \frac{2\pi}{3}) \\ -\sin \theta_r & -\sin(\theta_r + \frac{2\pi}{3}) & -\sin(\theta_r - \frac{2\pi}{3}) \\ \frac{1}{2} & \frac{1}{2} & \frac{1}{2} \end{bmatrix} \quad (15)$$

and  $\mathbf{f}_{qd0r} = [f_{qr} \ f_{dr} \ f_{0r}]^T$  represent the transformed variables. For systems considered herein, the zero-sequence component will be zero and can be ignored. Rotating armature variables transformed to the stationary reference frame are also able to be represented in space-phaser notation:  $\vec{f}_{qdr} = f_{qr} + j f_{dr}$ .

The operator  $p$  indicates the differentiation with respect to time, and  $\|\cdot\|$  denotes the magnitude of a complex number or the 2-norm of a vector.

### B. Support Points for Stationary and Rotating Rectifiers Functions

The support points for stationary and rotating rectifiers functions  $\alpha(\cdot)$ ,  $\beta(\cdot)$ , and  $\phi(\cdot)$  are found in Table II.

### REFERENCES

- [1] D. Montenegro, G. A. Ramos, and S. Bacha, "A-diakoptics for the multicore sequential-time simulation of microgrids within large distribution systems," *IEEE Trans. Smart Grid*, vol. 8, no. 3, pp. 1211–1219, May 2017.
- [2] V. Ruuskanen, M. Niemela, J. Pyrhonen, S. Kanerva, and J. Kaukonen, "Modelling the brushless excitation system for a synchronous machine," *IET Electric Power Applications*, vol. 3, no. 3, pp. 231–239, May 2009.
- [3] A. M. Cramer, X. Liu, Y. Zhang, J. D. Stevens, and E. L. Zivi, "Early-stage shipboard power system simulation of operational vignettes for dependability assessment," in *2015 IEEE Electric Ship Technologies Symposium (ESTS)*, Jun. 2015, pp. 382–387.
- [4] T. L. Skvarenina, S. Pekarek, O. Wasynczuk, P. C. Krause, R. J. Thibodeaux, and J. Weimer, "Simulation of a more-electric aircraft power system using an automated state model approach," in *IECEC 96. Proceedings of the 31st Intersociety Energy Conversion Engineering Conference*, vol. 1, Aug. 1996, pp. 133–136 vol.1.

TABLE II  
SUPPORT POINTS FOR FUNCTIONS

Stationary Rectifier				Rotating Rectifier			
$z$ ( $\Omega$ )	$\alpha$	$\beta$	$\phi$	$z$ ( $\Omega$ )	$\alpha$	$\beta$	$\phi$
0.075	0.658	0.960	0.228	0.000	0.666	1.003	0.094
0.115	0.654	0.954	0.233	0.163	0.662	0.969	0.224
0.149	0.651	0.952	0.222	0.352	0.657	0.956	0.251
0.189	0.647	0.951	0.201	0.653	0.650	0.950	0.229
0.241	0.644	0.950	0.175	1.032	0.643	0.949	0.181
0.309	0.641	0.950	0.154	1.360	0.640	0.948	0.167
0.396	0.639	0.949	0.143	1.477	0.640	0.947	0.164
0.507	0.638	0.949	0.140	1.542	0.640	0.947	0.164
0.675	0.638	0.947	0.147	1.625	0.639	0.947	0.164
0.922	0.637	0.943	0.168	1.951	0.639	0.945	0.169
1.233	0.637	0.938	0.196	2.368	0.639	0.942	0.180
1.579	0.636	0.933	0.218	2.795	0.639	0.939	0.198
2.012	0.635	0.928	0.230	3.603	0.638	0.932	0.221
2.597	0.633	0.924	0.235	5.232	0.635	0.925	0.231
3.433	0.631	0.920	0.233	7.684	0.630	0.919	0.225
4.564	0.628	0.916	0.224	11.172	0.625	0.915	0.211
6.116	0.624	0.913	0.211	23.252	0.617	0.910	0.172
7.962	0.621	0.910	0.202	35.332	0.614	0.909	0.149
10.413	0.617	0.908	0.194	47.411	0.612	0.908	0.133
13.990	0.615	0.907	0.184	59.491	0.610	0.907	0.122
20.801	0.612	0.905	0.171	71.571	0.609	0.907	0.112
31.760	0.609	0.903	0.162	83.651	0.609	0.906	0.102
45.949	0.608	0.901	0.159	95.731	0.608	0.906	0.093

- [5] T. Zouaghi and M. Poloujadoff, "Modeling of polyphase brushless exciter behavior for failing diode operation," *IEEE Trans. Energy Convers.*, vol. 13, no. 3, pp. 214–220, Sep. 1998.
- [6] H. Atighechi, S. Chiniforoosh, K. Tabarraee, and J. Jatskevich, "Average-value modeling of synchronous-machine-fed thyristor-controlled-rectifier systems," *IEEE Transactions on Energy Conversion*, vol. 30, no. 2, pp. 487–497, Jun. 2015.
- [7] S. Chiniforoosh, J. Jatskevich, A. Yazdani, V. Sood, V. Dinavahi, J. A. Martinez, and A. Ramirez, "Definitions and applications of dynamic average models for analysis of power systems," *IEEE Trans. Power Del.*, vol. 25, no. 4, pp. 2655–2669, Oct. 2010.
- [8] S. Chiniforoosh, H. Atighechi, and J. Jatskevich, "A generalized methodology for dynamic average modeling of high-pulse-count rectifiers in transient simulation programs," *IEEE Trans. Energy Convers.*, vol. 31, no. 1, pp. 228–239, Mar. 2016.
- [9] H. A. Petroson and P. C. Krause, "A direct-and quadrature-axis representation of a parallel ac and dc power system," *IEEE Trans. Power App. Syst.*, vol. PAS-85, no. 3, pp. 210–225, Mar. 1966.
- [10] P. C. Krause and T. A. Lipo, "Analysis and simplified representations of a rectifier-inverter induction motor drive," *IEEE Trans. Power App. Syst.*, vol. PAS-88, no. 5, pp. 588–596, May 1969.
- [11] E. Kimbark, *Direct current transmission*. Wiley-Interscience, 1971.
- [12] T. H. Warner and J. G. Kassakian, "Transient characteristics and modeling of large turboalternator driven rectifier/inverter systems based on field test data," *IEEE Power Engineering Review*, vol. PER-5, no. 7, pp. 47–47, Jul. 1985.
- [13] S. D. Sudhoff and O. Wasynczuk, "Analysis and average-value modeling of line-commutated converter-synchronous machine systems," *IEEE Trans. Energy Convers.*, vol. 8, no. 1, pp. 92–99, Mar. 1993.
- [14] S. D. Sudhoff, K. A. Corzine, H. J. Hegner, and D. E. Delisle, "Transient and dynamic average-value modeling of synchronous machine fed load-commutated converters," *IEEE Trans. Energy Convers.*, vol. 11, no. 3, pp. 508–514, Sep. 1996.
- [15] D. C. Aliprantis, S. D. Sudhoff, and B. T. Kuhn, "A brushless exciter model incorporating multiple rectifier modes and Preisach's hysteresis theory," *IEEE Trans. Energy Convers.*, vol. 21, no. 1, pp. 136–147, Mar. 2006.
- [16] M. Shahnazari and A. Vahedi, "Improved dynamic average modelling of brushless excitation system in all rectification modes," *IET Electric Power Applications*, vol. 4, no. 8, pp. 657–669, Sep. 2010.
- [17] I. Jadric, D. Borojevic, and M. Jadric, "Modeling and control of a synchronous generator with an active dc load," *IEEE Trans. Energy Convers.*, vol. 15, no. 2, pp. 303–311, Mar. 2000.
- [18] J. Jatskevich and T. Aboul-Seoud, "Impedance characterization of a six-phase synchronous generator-rectifier system using average-value

model," in *Canadian Conference on Electrical and Computer Engineering*, vol. 4, May 2004, pp. 2231–2234 Vol.4.

[19] J. Jatskevich, S. D. Pekarek, and A. Davoudi, "Parametric average-value model of synchronous machine-rectifier systems," *IEEE Trans. Energy Convers.*, vol. 21, no. 1, pp. 9–18, Mar. 2006.

[20] —, "Fast procedure for constructing an accurate dynamic average-value model of synchronous machine-rectifier systems," *IEEE Trans. Energy Convers.*, vol. 21, no. 2, pp. 435–441, Jun. 2006.

[21] J. Jatskevich and S. D. Pekarek, "Numerical validation of parametric average-value modeling of synchronous machine-rectifier systems for variable frequency operation," *IEEE Trans. Energy Convers.*, vol. 23, no. 1, pp. 342–344, Mar. 2008.

[22] Y. Zhang and A. M. Cramer, "Numerical average-value modeling of rotating rectifiers in brushless excitation systems," *IEEE Transactions on Energy Conversion*, vol. PP, no. 99, pp. 1–1, 2017.

[23] S. Ebrahimi, N. Amiri, H. Atighechi, Y. Huang, L. Wang, and J. Jatskevich, "Generalized parametric average-value model of line-commutated rectifiers considering ac harmonics with variable frequency operation," *IEEE Transactions on Energy Conversion*, vol. PP, no. 99, pp. 1–1, 2017.

[24] F. Therrien, M. Chapariha, and J. Jatskevich, "Pole selection procedure for explicit constant-parameter synchronous machine models," *IEEE Transactions on Energy Conversion*, vol. 29, no. 3, pp. 790–792, Sep. 2014.

[25] *Automated State Model Generator (ASMG) Reference Manual*, P. C. Krause and Associates, Inc., West Lafayette, IN, 2002.

[26] D. C. Aliprantis, S. D. Sudhoff, and B. T. Kuhn, "A synchronous machine model with saturation and arbitrary rotor network representation," *IEEE Trans. Energy Convers.*, vol. 20, no. 3, pp. 584–594, Sep. 2005.

[27] —, "Experimental characterization procedure for a synchronous machine model with saturation and arbitrary rotor network representation," *IEEE Trans. Energy Convers.*, vol. 20, no. 3, pp. 595–603, Sep. 2005.

[28] A. M. Cramer, B. P. Loop, and D. C. Aliprantis, "Synchronous machine model with voltage-behind-reactance formulation of stator and field windings," *IEEE Trans. Energy Convers.*, vol. 27, no. 2, pp. 391–402, Jun. 2012.

[29] D. C. Aliprantis, O. Wasynczuk, and C. D. Rodríguez Valdez, "A voltage-behind-reactance synchronous machine model with saturation and arbitrary rotor network representation," *IEEE Trans. Energy Convers.*, vol. 23, no. 2, pp. 499–508, Jun. 2008.

[30] Y. Zhang and A. M. Cramer, "Unified model formulations for syn-

chronous machine model with saturation and arbitrary rotor network representation," *IEEE Trans. Energy Convers.*, vol. 31, no. 4, pp. 1356–1365, Dec. 2016.

[31] P. Krause, O. Wasynczuk, S. Sudhoff, and S. Pekarek, *Analysis of Electric Machinery and Drive Systems*, 3rd ed. Piscataway, NJ: Wiley-IEEE Press, 2013.



**YuQi Zhang** (S'16) received the B.S. degree in electrical engineering from Harbin Institute of Technology, Harbin, China, in 2005, the M.S.E.E. and Ph.D. degrees from University of Kentucky, Lexington, KY, in 2014 and 2018, respectively.

Her research interests include electric machine modeling and simulation, power electronics, and power systems.



**Aaron M. Cramer** (S'02–M'07–SM'13) received the B.S. degree (summa cum laude) in electrical engineering from the University of Kentucky, Lexington, KY, USA, in 2003 and the Ph.D. degree from Purdue University, West Lafayette, IN, USA in 2007.

From 2007 to 2010, he was a Senior Engineer with PC Krause and Associates, West Lafayette. He joined the University of Kentucky in 2010 where he is currently an Associate Professor. His research interests include modeling, simulation, and control

of power and energy systems.

Dr. Cramer was a recipient of the ONR Young Investigator Program award in 2015. He serves as an Editor of IEEE TRANSACTIONS ON ENERGY CONVERSION.

---

## Genetic algorithm with integrated computing budget allocation for stochastic problems

---

Mengmei Liu and Aaron M. Cramer\*

Department of Electrical and Computer Engineering,  
University of Kentucky,  
Lexington, KY 40506, USA  
Email: mengmei.liu@uky.edu  
Email: aaron.cramer@uky.edu  
\*Corresponding author

**Abstract:** Stochastic problems are of great interest in many applications, and genetic algorithms (GAs) have been widely used to solve these kinds of problems. Normally, a large number of samples are needed to evaluate the stochastic function such that the sample mean closely approximates the actual mean in order to rank and select accurately in the GA; however, this method is computationally expensive. Some researchers have integrated different computing budget allocation schemes into the evaluation procedure of the GA to reduce the total computing cost. Herein, a GA is proposed in which computing budget allocation techniques are integrated directly into the selection operator rather than being used during fitness evaluation. This allows fitness evaluations to be allocated towards specific individuals for whom the algorithm requires more information, and this selection-integrated method is shown to be more accurate for the same computing budget than the existing evaluation-integrated methods on several test problems. Different computing budget allocation methods are studied on both traditional test functions and benchmark functions from a recent conference competition, and it is shown that the existing evaluation-integrated algorithm may require up to 225% of the samples required by the proposed selection-integrated GA to achieve results with the same accuracy.

**Keywords:** genetic algorithms; optimisation methods; statistical distributions; stochastic problems.

**Reference** to this paper should be made as follows: Liu, M. and Cramer, A.M. (2016) 'Genetic algorithm with integrated computing budget allocation for stochastic problems', *Int. J. Metaheuristics*, Vol. 5, No. 2, pp.115–135.

**Biographical notes:** Mengmei Liu received her BS in Electrical Engineering from Wuhan University of Technology, Wuhan, China, in 2010, and MS from University of Kentucky, Lexington, in 2013. She is currently a PhD candidate in Electrical Engineering in University of Kentucky. Her current research interests include optimisation methods and power electronics.

Aaron M. Cramer received his BS (summa cum laude) in Electrical Engineering from the University of Kentucky, Lexington, in 2003 and the PhD from Purdue University, West Lafayette, IN, in 2007. From 2007 to 2010, he was a Senior Engineer with PC Krause and Associates, West Lafayette. He is currently an Assistant Professor with the University of Kentucky. His research interests include modelling, simulation, analysis, and optimisation of electric machines, power electronics, power systems, and control systems.

## 1 Introduction

Stochastic problems are widely encountered in almost every field of science and engineering. Many realistic industrial problems are subject to randomness or to uncertainties that can be modelled stochastically, e.g., problems include stochastic scheduling (Jensen, 2003; Wang, Zhang, and Zheng, 2005), computation of optimal power flow and optimisation of an operating point with constraints (Xu et al, 2012), stochastic network partitioning and clustering (Stan et al, 2014; Buadhachain and Provan, 2015), stochastic vehicle routing problem (Mendoza, Rousseau, and Villegas, 2015), and design of power system stabilisers (Dill and e Silva, 2013). A common feature of these example problems is the relatively high computational expense of performing the required simulations. The straightforward approach of collecting a large number of samples can be computationally very expensive. Improvements to this approach can be made by use of efficient sampling in the search algorithm for these types of problems, potentially improving both the runtime and the accuracy of the search algorithm.

Meta-heuristic methods, such as genetic algorithms (GAs), particle swarm optimisation, simulated annealing and ant colony optimisation, have been widely used to solve optimisation problems (Nesmachnow, 2014; Blum and Roli, 2003), and they have been particularly successful when the derivative of the objective function is unknown or does not exist. However, when randomness is introduced into these problems, appropriate methods for addressing it are necessary. Some methods seek a robust solution, which is insensitive to small variations (Tsutsui and Ghosh, 1997), such as analog circuits designed to be robust against certain faults (Liu and He, 2013). Variations of the heuristic algorithms have been proposed to find solutions to stochastic problems. Such variations include specifying the probability of constraint satisfaction as part of the fitness function of a GA (Chan and Sudhoff, 2010), introducing a probability vector in the extension of each colony for ant colony optimisation (Ho et al, 2014), integrating statistical sequential selection into simulated annealing (Branke, Meisel, and Schmidt, 2008), incorporating equal re-sampling methods into particle swarm optimisation (Rada-Vilela, Johnston, and Zhang, 2014), integrating mathematical approximations of a solution's reliability into evolutionary algorithms and investigating the situation case by case (Deb et al, 2009), employing the concept of global and local optimisation and improving the efficiency of globally robust search by dividing the search space into regions (Tu and Lu, 2004), and by constructing local approximate models of the fitness function (Paenke, Branke, and Jin, 2016). These approaches have primarily focused on the quality of the solutions, with only secondary concern for computational efficiency.

Applying ordinal optimisation techniques, which seek to allocate adequate numbers of samples to promising individuals and reduce unnecessary sampling of noncritical individuals, is a promising approach to improve efficiency while maintaining accuracy at locating the solution to stochastic problems (Liu et al, 2013; Liu, Fernández, and Gielen, 2011). In this direction, the optimal computing budget allocation (OCBA) methods, which are sequential ranking and allocation procedures developed from ordinal optimisation (Chen, Lin, Yücesan, and Chick, 2000), have been developed. OCBA methods and other methods for computing budget allocation (CBA) are used to allocate the samples that are performed on a set of individuals in order to reveal the relative merit of the

individuals. Combining CBA methods into heuristic search algorithms, such as GAs, is a good way of improving the sampling efficiency in robust optimisation methods. A technique for integrating statistical ranking into evolutionary algorithms is presented in (Schmidt, Branke, and Chick, 2006). The OCBA method is proposed to guide the allocation of sampling budget and identification of good particles in particle swarm optimisation (Pan, Wang, and Liu, 2006), and it is further developed and investigated with various distributions in (Rada-Vilela, Zhang, and Johnston, 2013). The previous usage of CBA methods with evolutionary algorithms has focused on the integration of the CBA methods into the evaluation and ranking process (Lee et al, 2008; Schmidt, Branke, and Chick, 2006; Horng and Lin, 2013). In (Xiao and Lee, 2014), the OCBA rule for selecting the best  $m$  individuals out of a set of  $k$  is integrated with GA evaluation to improve the search efficiency. A GA involving CBA methods in this way is called an evaluation-integrated GA (EIGA).

The contribution of this work is to propose a selection-integrated GA (SIGA) in which CBA techniques are integrated directly into the GA selection operator rather than being used during fitness evaluation. This allows fitness evaluations to be allocated towards specific individuals for whom the GA requires more information. Several stochastic test problems are considered under different noise levels, including problems based on benchmark functions from a recent conference competition, and the performance of the EIGA and the SIGA with different CBA methods is compared. Statistical significance tests are performed on those problems to verify the accuracy of the proposed algorithm. It is shown that the SIGA is capable of achieving more accurate results for the same computational budget or results with the same accuracy for a considerably decreased computing budget.

The remainder of this paper is organised as follows. First, descriptions of the problem and different CBA methods are given. Then, the existing EIGA and proposed SIGA approaches for integrating CBA methods into GAs are described. Next, test functions, including various noise levels, are presented, and experimental results and analysis are given.

## 2 Stochastic problems and computing budget allocation methods

The stochastic problems and the CBA methods considered herein are described below.

### 2.1 Stochastic problem statement

The stochastic problems considered herein have the following form (Ermoliev, 1998):

$$\min_X J(X) = E[L(X, \xi)], \quad (1)$$

where  $X$  is the (possibly multi-dimensional) decision variable,  $L(\cdot, \cdot)$  is the sample performance and can only be calculated through simulation,  $\xi$  is a random variable representing the noise integrated within the function, and  $J(\cdot)$  represents the expected performance. For the test problems considered herein, the randomness is modelled as additive noise with a Gaussian distribution, but it can be represented in other ways as well.

It is also assumed that such a problem is unconstrained in the sense that any constraint that bind the solution is appropriately penalised in  $L(\cdot, \cdot)$ .

For a deterministic problem  $J(X) = L(X)$ , GAs are widely applied to find the optimal solution  $X^* = \arg \min_X L(X)$ . For a stochastic problem, the fitness function  $J(X)$  can only be estimated by calculating the mean of a limited number of random samples. For individual  $i$ , the mean performance measure can be estimated as:

$$J(X_i) \approx \bar{L}_i = \frac{1}{n_i} \sum_{j=1}^{n_i} L(X_i, \xi_{ij}), \quad (2)$$

where  $n_i$  represents the number of samples and  $\xi_{ij}$  represents the noise of the  $j$ th sample for individual  $i$ . The variance  $\sigma_i^2$  for individual  $i$  is unknown and can be approximated by the sample variance  $s_i^2$ ; the sample mean for individual  $i$  is denoted as  $\bar{L}_i$ ; the optimum individual given previous samples is denoted as  $b$ , which has the smallest sample mean, i.e.,  $\bar{L}_b \leq \bar{L}_i, \forall i$ .

Due to the law of large numbers, increasing  $n_i$  will result in  $\bar{L}_i$  being a better estimate of the actual mean  $J(X_i)$ . However, evaluating more samples requires more computational time. GAs, depending on the fitness scaling and selection methods used, often require an understanding of the relative fitness of smaller sets of individuals rather than a precise understanding of the absolute fitness of each individual. The goal of the proposed SIGA is to provide this information to the GA. If two individuals have sufficiently different sample means or small sample variances such that one individual is very likely better than the other, then there is no need to evaluate more samples of these individuals.

## 2.2 Computing budget allocation methods

Various CBA methods exist in the literature, and the CBA methods applied in this study are discussed in this subsection. For each of these methods, it is assumed that  $N$  samples are being allocated among  $k$  individuals.

### 2.2.1 Equal allocation method

The simplest allocation technique to conduct sampling is the equal allocation (EQU) technique, and it often serves as a benchmark for comparison (Chen, 2010). The available computing budget is equally distributed to all individuals being compared:

$$\tilde{n}_i = \frac{N}{k}, \quad (3)$$

where  $\tilde{n}_i$  is the number of additional samples to be allocated to individual  $i$ .

### 2.2.2 Optimal computing budget allocation methods

Optimal computing budget allocation methods are based on asymptotic arguments that show that allocating samples in a certain manner will result in the highest probability of correct selection. The two OCBA methods used herein, described in (Chen et al, 2008), are based on different assumptions and are treated separately. In both OCBA methods, a number of initial samples  $n_i$  have been performed for each individual, and information

about the sample mean  $\bar{L}_i$  and variance  $\sigma_i^2$  of each individual is used to perform allocation. The available  $N$  samples are allocated to individuals based on assumptions about distribution and asymptotic behaviour in order to maximise the probability of correctly selecting the best individual (OCBA) or selecting the best  $m$  individual subset (OCBAM). In this study,  $m = 1$ , and the OCBAM represents an alternative OCBA method of correctly selecting the best individual.

For the OCBA method, the best individual is identified:

$$b = \arg \min_i \bar{L}_i, \quad (4)$$

and this individual is used to calculate a distance

$$\delta_{b,i} = \bar{L}_i - \bar{L}_b. \quad (5)$$

This distance and the sample variance are used to establish the ratio of samples allocated to different individuals:

$$\frac{\tilde{n}_i}{\tilde{n}_j} = \left( \frac{\sigma_i / \delta_{b,i}}{\sigma_j / \delta_{b,j}} \right)^2, \quad i \neq b, j \neq b \quad (6)$$

The number of samples allocated to the best individual is given by

$$\tilde{n}_b = \sigma_b \sqrt{\sum_{i=1, i \neq b}^k \frac{\tilde{n}_i^2}{\sigma_i^2}}, \quad (7)$$

and the total number of allocated samples must be  $N$ .

For the OCBAM method, the individuals are sorted such that  $i$  is the rank of the individual (i.e., the first individual is the best individual). A boundary between the best  $m$  individual subset and the remainder of the set is established as:

$$c = \frac{\hat{\sigma}_{m+1} \bar{L}_m + \hat{\sigma}_m \bar{L}_{m+1}}{\hat{\sigma}_m + \hat{\sigma}_{m+1}}, \quad (8)$$

where  $\hat{\sigma}_i = \sigma_i / \sqrt{\tilde{n}_i}$ . This boundary is used to calculate a distance

$$\delta_i = \bar{L}_i - c. \quad (9)$$

This distance and the sample variance are used to establish the ratio of samples allocated to different individuals:

$$\frac{\tilde{n}_i}{\tilde{n}_j} = \left( \frac{\sigma_i / \delta_i}{\sigma_j / \delta_j} \right)^2, \quad (10)$$

and the total number of allocated samples must be  $N$ .

2.2.3 Proportional to variance method

Like the OCBA methods, the proportional to variance (PTV) method uses information about the initial  $n_i$  samples of each individual (i.e., the variance  $\sigma_i^2$ ) to perform allocation. The PTV method allocates budget in proportion to the variances due to the fact that a smaller calculated sample variance usually implies more certainty (Fu, Chen, and Shi, 2008). The allocation is given by

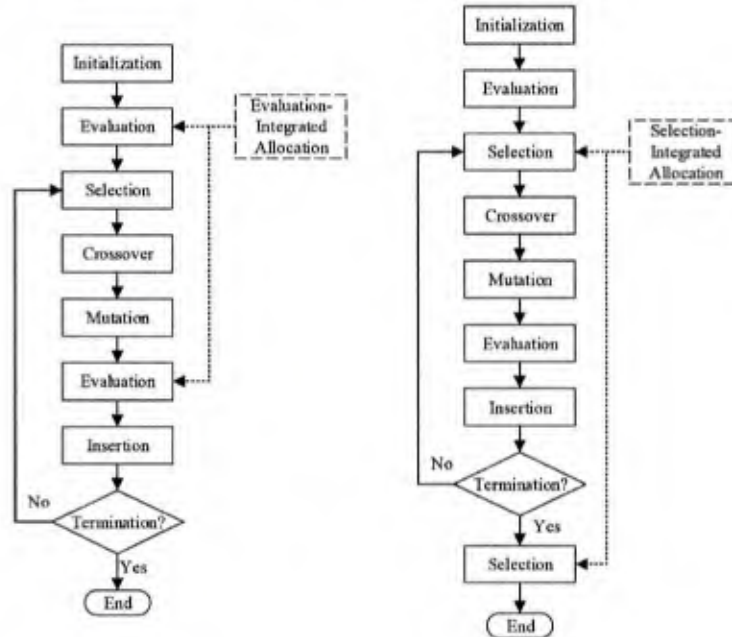
$$\frac{\tilde{n}_i}{\tilde{n}_j} = \frac{\sigma_i^2}{\sigma_j^2}, \tag{11}$$

and the total number of allocated samples must be  $N$ .

3 Computing budget allocation method integrated GAs

Herein, two fundamental GAs for solving optimisation of stochastic problems are considered. The first algorithm is the EIGA and is the traditional approach for integrating CBA schemes with GAs. The second algorithm is the SIGA and is proposed herein as an alternative method for solving stochastic problems. Figure 1 gives the flow chart of the integrated GAs for either option. From Figure 1, the EIGA integrates the CBA procedure into the evaluation process. The SIGA integrates the CBA procedure after the evaluation process, at the point in which order information is required by the GA. Therefore, it includes an additional application of the CBA method after termination in order to determine the final solution.

Figure 1 Flow chart of the integrated genetic algorithms (left figure for evaluation-integrated genetic algorithm; right figure for selection-integrated genetic algorithm)



Pseudocode for the two algorithms is listed in Algorithm 1, and steps specific for each algorithm are marked in italics. The integrated GAs have the following steps:

---

**Algorithm 1** Integrated genetic algorithms
 

---

```

1: Initialise population of individuals with random values in search space
2: Evaluate each individual in initial population with number of initial samples
3: if EIGA then
4:   Apply CBA to allocate additional samples for each individual in initial population
5: end if
6: while Maximum generation not reached do
7:   if SIGA then
8:     for Each tournament do
9:       Apply CBA to allocate additional samples for each individual in tournament
10:    end for
11:  end if
12:  for Each tournament do
13:    Select best individual from tournament into mating pool
14:  end for
15:  Perform crossover for each pair of individuals in mating pool
16:  Perform mutation on each individual in mating pool
17:  Evaluate each individual in mating pool with number of initial samples
18:  if EIGA then
19:    Apply CBA to allocate additional samples for each individual in mating pool
20:  end if
21:  Insert mating pool into population
22: end while
23: if SIGA then
24:   Apply CBA to allocate additional samples for each individual in final population
25: end if

```

---

Step 1: The population of  $n_{ind}$  individuals is uniformly randomly initialised in the search domain.

Step 2: Each individual is initially sampled  $n_0$  times, and the sample mean and variance of each individual are calculated. In the EIGA, the CBA method uses the sample means and variances to allocate  $n_1 n_{ind}$  additional samples across the population.

Step 3: Tournament selection is used. The tournament size is  $n_{tour}$  with one individual selected from each tournament, and  $n_{pool}$  tournaments are used to form the mating pool. For the EIGA, the selection is performed using the previously updated sample means. For the SIGA,  $n_1$  additional samples are allocated to each tournament by the CBA method, and the tournament winner is decided after these samples are performed. The tournaments are processed sequentially such that samples allocated to an individual in one tournament are considered if the individual participates in subsequent tournaments.

Step 4: Individuals in the mating pool are arranged in pairs, and crossover is performed on each pair. The simulated binary crossover (SBX) method (Deb and Agrawal, 1994; Deb et al, 2002) is used with crossover constant  $\eta$ .

Step 5: Polynomial mutation for real-valued GAs (Deb and Deb, 2014) is performed on each individual in the mating pool with probability  $p_m$ .

Step 6: Each individual in the mating pool is initially sampled  $n_0$  times, and the sample mean and variance of each individual are calculated. In the EIGA, the CBA method uses the sample means and variances to allocate  $n_1 n_{pool}$  additional samples across the mating pool.

Step 7: The new  $n_{pool}$  individuals randomly replace  $n_{pool}$  individuals in the population. Elitism is not used as the fitness evaluation is uncertain due to the noise.

Step 8: The algorithm terminates after  $n_{gen}$  generation. After the SIGA completes its final generation, the CBA method is used to allocate  $n_1 n_{ind}$  samples across the final population in order to identify the best individual.

The total samples required by each method is equal to  $n(n_{ind} + n_{gen} n_{pool})$ , where  $n = n_0 + n_1$  is the total number of samples to be performed per individual per generation.

The primary focus of this work is to compare EIGA with SIGA. The particular genetic operators employed by these algorithms or their parameters are considered to be secondary to the manner in which CBA is performed. The parameters for the GAs are given in Table 1. While the parameters can certainly affect the performance of the GA, the selection of these parameters is not the focus of this work. Therefore, the parameters are selected manually in order to achieve acceptable performance on the deterministic versions of the test functions described below and used for both the EIGA and the SIGA. It should also be noted that elitism is not used by any of the algorithms. While elitism has been shown near universally to improve the performance of GAs, the stochastic problems pose particular difficulties for the use of elitism. In particular, knowledge of whether an individual is elite is based on an imperfect sample mean. Elitism combined with a particularly unlucky sample can derail the algorithm.

**Table 1** Parameters of genetic algorithms

Parameter	Parameter	Value
$n_{gen}$	Number of generations	300
$n_{ind}$	Number of individuals	100
$n_{pool}$	Number of individuals in mating pool	60
$n_{tour}$	Tournament size	4
$\eta$	Crossover constant	2
$p_c$	Crossover probability	100%
$p_m$	Mutation probability	0.05
$n_0$	Initial samples per individual	50
$n_1$	Allocated samples per individual	200

#### 4 Results and analysis

This section presents several stochastic test problems, describes experimental results, and compares the EIGA and SIGA as well as the CBA methods.

#### 4.1 Test functions

Several deterministic test functions with known global minima are selected. Zero-mean Gaussian noise is added to each deterministic test function in order to form a stochastic test function with known global expected minima:

$$L(X, \xi) = f(X) + \xi \quad (12)$$

$$\xi = \mathcal{N}(0, D^2) \quad (13)$$

where  $D$  is a parameter establishing the noise level associated with the problem. The global expected minimiser of the stochastic problem is equal to the global minimiser of the deterministic problem:

$$X^* = \arg \min_X E[L(X, \xi)] = \arg \min_X f(X), \quad (14)$$

and the global expected minimum is equal to the global minimum of the deterministic problem:

$$E[L(X^*, \xi)] = f(X^*). \quad (15)$$

In order to evaluate the quality of a solution  $X$  proposed by one of the optimisation methods, its error with respect to the global minimum is computed:

$$\Delta = f(X) - f(X^*), \quad (16)$$

which is possible for the test functions because the global minimum is known.

The algorithms are tested on four traditional test functions and three functions based on benchmark functions from a recent conference competition. The plate-shaped Matyas function has one global optimum and no local optima. The valley-shaped Rosenbrock function is one of the most popular optimisation test problems. Its global optima is situated inside a parabolic valley that makes convergence difficult. The two higher dimensional test functions are the bowl-shaped Sphere function and the plate-shaped Zakharov function. The traditional test functions are listed in Table 2. Three test functions from the 2014 IEEE Congress on Evolutionary Computation competition are used (Liang, Qu, and Suganthan, 2014). The three functions used are the Griewank, HappyCat and HGBat functions, and these functions are shifted and rotated. The dimensions used for these functions are  $d = 10$  for the Griewank function and  $d = 30$  for the both the HappyCat and HGBat functions. The search domain for these functions is  $[-100, 100]^d$ . It is noted that these problems are intended to be representative of modern benchmark functions but that not all functions that are appropriate benchmark functions for deterministic optimisation are suitable stochastic problems.

#### 4.2 Choice of noise level

In order to determine suitable noise levels for each of the test functions, a traditional GA with the same genetic operators and parameters is applied to the deterministic test functions. The traditional GA is a special case of both the EIGA and the SIGA when  $n_0 = 1$  and  $n_1 = 0$ . This GA was applied 1600 times for each allocation method with each problem and noise level, and the mean error and the standard deviation (STD) of the error for each case (when  $D = 0$ ) are given in Table 3.

**Table 2** Traditional test functions

<i>Function</i>	<i>d</i>	<i>Definition</i>	<i>Global minimum</i>	<i>Search domain</i>
Matyas	2	$f(X) = 0.26(x_1^2 + x_2^2) - 0.48x_1x_2$	$f(0, 0) = 0$	$x_i \in [-10, 10]$
Rosenbrock	2	$f(X) = (1 - x_1)^2 + 100(x_2 - x_1^2)^2$	$f(1, 1) = 0$	$x_i \in [-2.048, 2.048]$
Sphere	8	$f(X) = \sum_{i=1}^d x_i^2$	$f(0, \dots, 0) = 0$	$x_i \in [-5, 5]$
Zakharov	5	$f(X) = \sum_{i=1}^d x_i^2 + \left(\sum_{i=1}^d 0.5ix_i\right)^2 + \left(\sum_{i=1}^d 0.5ix_i\right)^4$	$f(0, \dots, 0) = 0$	$x_i \in [-5, 5]$

**Table 3** Mean and standard deviation (STD) of error under different noise levels

<i>Function</i>	<i>D</i>	<i>Mean</i>	<i>STD</i>
Matyas	0	$4.59 \times 10^{-5}$	$1.12 \times 10^{-4}$
	0.01	$1.74 \times 10^{-4}$	$3.04 \times 10^{-4}$
	0.05	$4.89 \times 10^{-4}$	$7.01 \times 10^{-4}$
	0.1	$7.64 \times 10^{-4}$	$1.02 \times 10^{-3}$
Rosenbrock	0	$1.41 \times 10^{-2}$	$2.78 \times 10^{-2}$
	1	$3.89 \times 10^{-2}$	$5.27 \times 10^{-2}$
	5	$7.46 \times 10^{-2}$	$8.83 \times 10^{-2}$
	10	$1.10 \times 10^{-1}$	$1.17 \times 10^{-1}$
Sphere	0	$4.38 \times 10^{-3}$	$4.08 \times 10^{-3}$
	0.1	$7.86 \times 10^{-3}$	$5.27 \times 10^{-3}$
	0.5	$1.69 \times 10^{-2}$	$9.99 \times 10^{-3}$
	2	$3.68 \times 10^{-2}$	$1.98 \times 10^{-2}$
Zakharov	0	$5.17 \times 10^{-3}$	$5.95 \times 10^{-3}$
	0.1	$8.73 \times 10^{-3}$	$7.35 \times 10^{-3}$
	1	$2.54 \times 10^{-2}$	$2.07 \times 10^{-2}$
	2	$3.82 \times 10^{-2}$	$2.93 \times 10^{-2}$
Griewank	0	1.13	$2.82 \times 10^{-1}$
	50	2.14	$5.55 \times 10^{-1}$
	250	5.18	2.16
	500	8.90	4.23
HappyCat	0	$5.09 \times 10^{-1}$	$1.27 \times 10^{-1}$
	10	1.57	$7.82 \times 10^{-1}$
	50	4.55	$7.54 \times 10^{-1}$
	100	5.99	1.03
HGBat	0	1.08	1.85
	10	2.14	2.81
	50	7.46	4.78
	100	$1.27 \times 10^1$	5.24

The choice of noise level  $D$  is related to the performance of the traditional GA on the deterministic test problems. Using the EIGA with EQU (EQUE) as a benchmark, the noise levels were selected so that the mean errors of the EQUE when executed 1600 times were within the range of 1–20 times the mean error of the traditional GA on the deterministic test problems. Three different noise levels in the range were compared to measure the performance of the GAs under relatively small, moderate, and large noise conditions. The performance of the benchmark EQUE under these noise levels is also shown in Table 3.

### 4.3 Comparison of different strategies

Experiments were performed to compare the EIGA and SIGA with different CBA methods under the various noise levels identified in Table 3. The EIGA and SIGA with different CBA schemes are denoted as EQUE, EQUUS, OCBAE, OCBAS, OCBAME, OCBAMS, PTVE, PTVS, with the last letter ‘E’ or ‘S’ denoting the EIGA or SIGA, respectively. Detailed nomenclature can be seen in Table 4. Each algorithm was applied to each problem with each noise level using each CBA method 1600 times. Table 5 shows the mean error for each method. The best algorithm for each problem and noise level is indicated with boldfaced text. An example visualisation of the table data is shown in Figure 2.

**Table 4** Detailed nomenclature of EIGA and SIGA with different CBA schemes

<i>Name</i>	<i>Method</i>	<i>Name</i>	<i>Method</i>
EQUE	EIGA with EQU	EQUUS	SIGA with EQU
OCBAE	EIGA with OCBA	OCBAS	SIGA with OCBA
OCBAME	EIGA with OCBAM	OCBAMS	SIGA with OCBAM
PTVE	EIGA with PTV	PTVS	SIGA with PTV

#### 4.3.1 Comparison of EIGA and SIGA

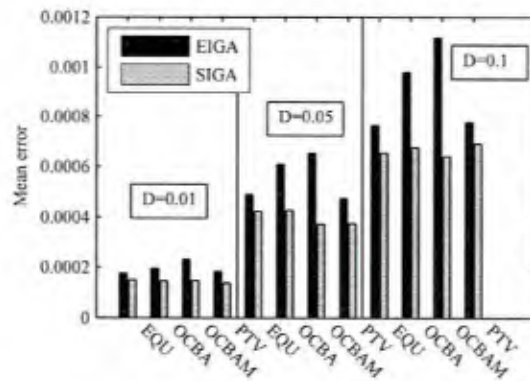
By examining Table 5 vertically, it can be seen that the SIGA with a given CBA method generally outperforms the EIGA with the same CBA method. The errors are assumed to follow a Rayleigh distribution, so an F-test can be used to determine the statistical significance of the results (Siddiqui, 1964). The null hypothesis is that the mean error of the SIGA for a given CBA method is less than or equal to the mean error of the EIGA for the same CBA method. A significance level of  $\alpha = 5\%$  is used to determine whether this hypothesis can be rejected. The results of these statistical tests are shown in Table 6. Due to the large number of samples (1600), many of the calculated p-values are smaller than the machine epsilon, and these are denoted in the table as ‘ $< \epsilon$ ’. Statistically significant results are indicated with boldfaced text. It can be seen that in most cases, the SIGA has statistically significantly less error than the EIGA for a given CBA method. The SIGA only has a larger sample mean error than the EIGA in two cases out of 84 scenarios: the Rosenbrock function with  $D = 1$  and PTV and the Griewank function with  $D = 500$  and PTV, and not statistically significantly so in either case. In general, it can be concluded that by integrating the CBA method into the selection process of the SIGA, the search algorithm allocates samples as needed in order to make the comparisons between individuals that are

**Table 5** Comparison of mean error for test functions (bold-face text indicates the best algorithm for each problem and noise level)

Function	Method	Mean	Method	Mean	Method	Mean	Method	Mean
Matyas $D = 0.01$	EQUE	$1.74 \times 10^{-4}$	OCBAE	$1.95 \times 10^{-4}$	OCBAME	$2.30 \times 10^{-4}$	PTVE	$1.83 \times 10^{-4}$
	EQUUS	$1.50 \times 10^{-4}$	OCBAS	$1.46 \times 10^{-4}$	OCBAMS	$1.47 \times 10^{-4}$	<b>PTVS</b>	<b><math>1.37 \times 10^{-4}</math></b>
Matyas $D = 0.05$	EQUE	$4.89 \times 10^{-4}$	OCBAE	$6.09 \times 10^{-4}$	OCBAME	$6.54 \times 10^{-4}$	PTVE	$4.75 \times 10^{-4}$
	EQUUS	$4.22 \times 10^{-4}$	OCBAS	$4.26 \times 10^{-4}$	<b>OCBAMS</b>	<b><math>3.72 \times 10^{-4}</math></b>	PTVS	$3.73 \times 10^{-4}$
Matyas $D = 0.1$	EQUE	$7.64 \times 10^{-4}$	OCBAE	$9.81 \times 10^{-4}$	OCBAME	$1.12 \times 10^{-3}$	PTVE	$7.77 \times 10^{-4}$
	EQUUS	$6.55 \times 10^{-4}$	OCBAS	$6.76 \times 10^{-4}$	<b>OCBAMS</b>	<b><math>6.41 \times 10^{-4}</math></b>	PTVS	$6.90 \times 10^{-4}$
Rosenbrock $D = 1$	EQUE	$3.89 \times 10^{-2}$	OCBAE	$3.92 \times 10^{-2}$	OCBAME	$4.07 \times 10^{-2}$	PTVE	$3.56 \times 10^{-2}$
	EQUUS	$3.72 \times 10^{-2}$	OCBAS	$3.73 \times 10^{-2}$	<b>OCBAMS</b>	<b><math>3.52 \times 10^{-2}</math></b>	PTVS	$3.68 \times 10^{-2}$
Rosenbrock $D = 5$	EQUE	$7.46 \times 10^{-2}$	OCBAE	$8.06 \times 10^{-2}$	OCBAME	$8.90 \times 10^{-2}$	PTVE	$7.28 \times 10^{-2}$
	EQUUS	$7.45 \times 10^{-2}$	OCBAS	$7.71 \times 10^{-2}$	OCBAMS	$7.20 \times 10^{-2}$	<b>PTVS</b>	<b><math>7.11 \times 10^{-2}</math></b>
Rosenbrock $D = 10$	EQUE	$1.10 \times 10^{-1}$	OCBAE	$1.15 \times 10^{-1}$	OCBAME	$1.32 \times 10^{-1}$	PTVE	$1.07 \times 10^{-1}$
	EQUUS	$1.07 \times 10^{-1}$	OCBAS	$1.09 \times 10^{-1}$	OCBAMS	$1.06 \times 10^{-1}$	<b>PTVS</b>	<b><math>1.00 \times 10^{-1}</math></b>
Sphere $D = 0.1$	EQUE	$7.86 \times 10^{-3}$	OCBAE	$8.70 \times 10^{-3}$	OCBAME	$9.70 \times 10^{-3}$	PTVE	$7.98 \times 10^{-3}$
	EQUUS	$7.09 \times 10^{-3}$	OCBAS	$7.22 \times 10^{-3}$	<b>OCBAMS</b>	<b><math>6.99 \times 10^{-3}</math></b>	PTVS	$7.05 \times 10^{-3}$
Sphere $D = 0.5$	EQUE	$1.69 \times 10^{-2}$	OCBAE	$1.89 \times 10^{-2}$	OCBAME	$2.16 \times 10^{-2}$	PTVE	$1.71 \times 10^{-2}$
	EQUUS	<b><math>1.37 \times 10^{-2}</math></b>	OCBAS	$1.51 \times 10^{-2}$	OCBAMS	$1.38 \times 10^{-2}$	PTVS	$1.37 \times 10^{-2}$
Sphere $D = 2$	EQUE	$3.68 \times 10^{-2}$	OCBAE	$4.48 \times 10^{-2}$	OCBAME	$5.29 \times 10^{-2}$	PTVE	$3.76 \times 10^{-2}$
	EQUUS	<b><math>3.18 \times 10^{-2}</math></b>	OCBAS	$3.65 \times 10^{-2}$	OCBAMS	$3.28 \times 10^{-2}$	PTVS	$3.24 \times 10^{-2}$
Zakharov $D = 0.1$	EQUE	$8.73 \times 10^{-3}$	OCBAE	$9.41 \times 10^{-3}$	OCBAME	$1.02 \times 10^{-2}$	PTVE	$9.01 \times 10^{-3}$
	EQUUS	$7.79 \times 10^{-3}$	OCBAS	$7.97 \times 10^{-3}$	<b>OCBAMS</b>	<b><math>7.77 \times 10^{-3}</math></b>	PTVS	$7.90 \times 10^{-3}$
Zakharov $D = 1$	EQUE	$2.54 \times 10^{-2}$	OCBAE	$3.06 \times 10^{-2}$	OCBAME	$3.38 \times 10^{-2}$	PTVE	$2.61 \times 10^{-2}$
	EQUUS	<b><math>2.12 \times 10^{-2}</math></b>	OCBAS	$2.29 \times 10^{-2}$	OCBAMS	$2.23 \times 10^{-2}$	PTVS	$2.16 \times 10^{-2}$
Zakharov $D = 2$	EQUE	$3.82 \times 10^{-2}$	OCBAE	$4.83 \times 10^{-2}$	OCBAME	$5.56 \times 10^{-2}$	PTVE	$3.92 \times 10^{-2}$
	EQUUS	$3.45 \times 10^{-2}$	OCBAS	$3.58 \times 10^{-2}$	OCBAMS	$3.48 \times 10^{-2}$	<b>PTVS</b>	<b><math>3.41 \times 10^{-2}</math></b>
Griewank $D = 50$	EQUE	2.14	OCBAE	2.42	OCBAME	2.64	PTVE	2.16
	EQUUS	2.02	OCBAS	2.12	OCBAMS	2.04	<b>PTVS</b>	<b>2.02</b>
Griewank $D = 250$	EQUE	5.18	OCBAE	6.67	OCBAME	7.79	PTVE	5.32
	EQUUS	5.12	OCBAS	5.56	OCBAMS	5.27	<b>PTVS</b>	<b>5.10</b>
Griewank $D = 500$	EQUE	8.90	OCBAE	$1.20 \times 10^1$	OCBAME	$1.39 \times 10^1$	PTVE	8.97
	EQUUS	<b>8.76</b>	OCBAS	$1.02 \times 10^1$	OCBAMS	9.51	PTVS	9.09
HappyCat $D = 10$	EQUE	1.57	OCBAE	2.10	OCBAME	2.47	PTVE	1.59
	EQUUS	<b>1.40</b>	OCBAS	1.63	OCBAMS	1.48	PTVS	1.43

**Table 5** Comparison of mean error for test functions (bold-face text indicates the best algorithm for each problem and noise level) (Continued)

Function	Method	Mean	Method	Mean	Method	Mean	Method	Mean
HappyCat $D = 50$	EQUE	4.55	OCBAE	5.16	OCBAME	5.60	PTVE	4.59
	EQUS	4.44	OCBAS	4.66	OCBAMS	4.43	<b>PTVS</b>	<b>4.40</b>
HappyCat $D = 100$	EQUE	5.99	OCBAE	6.87	OCBAME	7.34	PTVE	6.07
	EQUS	5.93	OCBAS	6.20	OCBAMS	5.94	<b>PTVS</b>	<b>5.92</b>
HGBat $D = 10$	EQUE	2.14	OCBAE	2.51	OCBAME	2.84	PTVE	2.27
	<b>EQUS</b>	<b>1.99</b>	OCBAS	2.24	OCBAMS	2.16	PTVS	2.13
HGBat $D = 50$	EQUE	7.46	OCBAE	9.32	OCBAME	$1.08 \times 10^1$	PTVE	7.74
	EQUS	6.92	OCBAS	7.24	OCBAMS	6.84	<b>PTVS</b>	<b>6.73</b>
HGBat $D = 100$	EQUE	$1.27 \times 10^1$	OCBAE	$1.58 \times 10^1$	OCBAME	$1.76 \times 10^1$	PTVE	$1.30 \times 10^1$
	EQUS	$1.16 \times 10^1$	OCBAS	$1.24 \times 10^1$	<b>OCBAMS</b>	<b><math>1.15 \times 10^1</math></b>	PTVS	$1.18 \times 10^1$

**Figure 2** Comparison of mean error for Matyas function

required by the algorithm. The relatively small size of each tournament with respect to the size of the mating pool may also improve the accuracy of the sampling.

#### 4.3.2 Comparison of computing budget allocation methods

By examining Table 5 horizontally, comparisons among the CBA methods can be made. For EIGA, the EQU and PTV methods generally have the smallest error. There are large differences in the error when applying these methods compared to the application of the OCBA methods. For the SIGA, there are relatively small differences in the error regardless of the CBA method used. The OCBAM method generally outperformed the OCBA method when used in the SIGA. However, the EQU and PTV methods also resulted in similar errors. Among the 21 different cases in this study, there are nine times the

PTVS gave the best results and six times each that the EQU and OCBAMS gave the best results.

**Table 6** P-value of comparison between SIGA over EIGA for each CBA method ( $< \epsilon$  indicates p-value less than machine epsilon, bold-face text indicates statistical significance with significance level  $\alpha = 0.05$ )

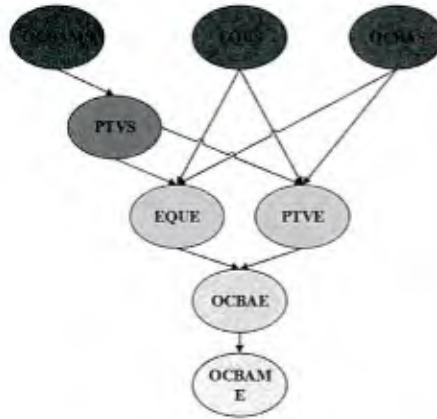
<i>Function</i>	<i>D</i>	<i>EQU</i>	<i>OCBA</i>	<i>OCBAM</i>	<i>PTV</i>
Matyas	0.01	<b><math>1.29 \times 10^{-5}</math></b>	$< \epsilon$	$< \epsilon$	<b><math>1.11 \times 10^{-16}</math></b>
	0.05	<b><math>1.56 \times 10^{-5}</math></b>	$< \epsilon$	$< \epsilon$	<b><math>6.46 \times 10^{-12}</math></b>
	0.1	<b><math>6.42 \times 10^{-6}</math></b>	$< \epsilon$	$< \epsilon$	<b><math>3.94 \times 10^{-4}</math></b>
Rosenbrock	1	$1.07 \times 10^{-1}$	$8.04 \times 10^{-2}$	<b><math>2.49 \times 10^{-5}</math></b>	$8.24 \times 10^{-1}$
	5	$4.88 \times 10^{-1}$	$1.06 \times 10^{-1}$	<b><math>1.22 \times 10^{-9}</math></b>	$2.50 \times 10^{-1}$
	10	$2.88 \times 10^{-1}$	$5.93 \times 10^{-2}$	<b><math>3.72 \times 10^{-10}</math></b>	<b><math>2.36 \times 10^{-2}</math></b>
Sphere	0.1	<b><math>1.85 \times 10^{-3}</math></b>	<b><math>6.59 \times 10^{-8}</math></b>	$< \epsilon$	<b><math>2.60 \times 10^{-4}</math></b>
	0.5	<b><math>1.18 \times 10^{-9}</math></b>	<b><math>1.52 \times 10^{-10}</math></b>	$< \epsilon$	<b><math>9.30 \times 10^{-11}</math></b>
	2	<b><math>1.71 \times 10^{-5}</math></b>	<b><math>2.94 \times 10^{-9}</math></b>	$< \epsilon$	<b><math>1.26 \times 10^{-5}</math></b>
Zakharov	0.1	<b><math>6.21 \times 10^{-4}</math></b>	<b><math>1.31 \times 10^{-6}</math></b>	<b><math>1.15 \times 10^{-14}</math></b>	<b><math>9.97 \times 10^{-5}</math></b>
	1	<b><math>1.98 \times 10^{-7}</math></b>	<b><math>1.1 \times 10^{-16}</math></b>	$< \epsilon$	<b><math>6.28 \times 10^{-8}</math></b>
	2	<b><math>1.72 \times 10^{-3}</math></b>	$< \epsilon$	$< \epsilon$	<b><math>4.55 \times 10^{-5}</math></b>
Griewank	50	$5.95 \times 10^{-2}$	<b><math>9.34 \times 10^{-5}</math></b>	<b><math>9.79 \times 10^{-14}</math></b>	<b><math>3.60 \times 10^{-2}</math></b>
	250	$3.62 \times 10^{-1}$	<b><math>1.42 \times 10^{-7}</math></b>	$< \epsilon$	$1.12 \times 10^{-1}$
	500	$3.28 \times 10^{-1}$	<b><math>1.04 \times 10^{-6}</math></b>	$< \epsilon$	<b><math>3.77 \times 10^{-1}</math></b>
HappyCat	10	<b><math>5.00 \times 10^{-4}</math></b>	<b><math>2.97 \times 10^{-13}</math></b>	$< \epsilon$	<b><math>1.68 \times 10^{-3}</math></b>
	50	$2.46 \times 10^{-1}$	<b><math>1.80 \times 10^{-3}</math></b>	<b><math>1.77 \times 10^{-11}</math></b>	$1.17 \times 10^{-1}$
	100	$3.78 \times 10^{-1}$	<b><math>1.83 \times 10^{-3}</math></b>	<b><math>1.17 \times 10^{-9}</math></b>	$2.42 \times 10^{-1}$
HGBat	10	<b><math>2.33 \times 10^{-2}</math></b>	<b><math>6.21 \times 10^{-4}</math></b>	<b><math>9.10 \times 10^{-15}</math></b>	<b><math>3.38 \times 10^{-2}</math></b>
	50	<b><math>1.79 \times 10^{-2}</math></b>	<b><math>5.32 \times 10^{-13}</math></b>	$< \epsilon$	<b><math>3.78 \times 10^{-5}</math></b>
	100	<b><math>7.22 \times 10^{-3}</math></b>	<b><math>9.34 \times 10^{-12}</math></b>	$< \epsilon$	<b><math>4.08 \times 10^{-3}</math></b>

In order to make these comparisons more formally, post hoc pairwise F-tests are applied to the data for the eight methods using the Matyas function with  $D = 0.01$ . The post hoc pairwise F-tests give the p-value of statistical comparison tests, comparing each method with each of the methods that performed worse than it. These tests provide insight into the statistical significance of the ranking of the methods for this problem. A significance level of  $\alpha = 5\%$  is used, and the p-values associated with these tests are shown in Table 7. Several of the calculated p-values are smaller than the machine epsilon, and these are denoted in the table as ' $< \epsilon$ '. Statistically significant results are indicated in boldfaced text. These pairwise statistical comparisons induce a partial ordering of the GAs for this problem. This ordering is illustrated in Figure 3. For this problem, it can be seen that OCBAME is statistically dominated by the other methods and that OCBAMS, EQU, and OCBAS are not statistically dominated by any other method. It can also be seen that each of the SIGA methods dominates each of the EIGA methods for this problem.

**Table 7** P-values of post hoc pairwise comparison of all GA methods for Matyas function with  $D = 0.01$  ( $< \epsilon$  indicates p-value less than machine epsilon, bold-face text indicates statistical significance with significance level  $\alpha = 0.05$ )

Method	OCBAMS	EQUS	OCBAS	PTVS	EQUE	PTVE	OCBAE
EQUS	$2.75 \times 10^{-1}$						
OCBAS	$6.66 \times 10^{-2}$	$1.83 \times 10^{-1}$					
PTVS	$1.82 \times 10^{-2}$	$6.77 \times 10^{-2}$	$2.78 \times 10^{-1}$				
EQUE	$3.52 \times 10^{-7}$	<b><math>6.42 \times 10^{-6}</math></b>	<b><math>2.69 \times 10^{-4}</math></b>	$2.05 \times 10^{-3}$			
PTVE	$2.58 \times 10^{-8}$	<b><math>6.23 \times 10^{-7}</math></b>	<b><math>3.97 \times 10^{-5}</math></b>	$3.94 \times 10^{-4}$	$3.13 \times 10^{-1}$		
OCBAE	$< \epsilon$	$< \epsilon$	$< \epsilon$	$< \epsilon$	<b><math>8.65 \times 10^{-13}</math></b>	$2.51 \times 10^{-11}$	
OCBAME	$< \epsilon$	$< \epsilon$	$< \epsilon$	$< \epsilon$	$< \epsilon$	$< \epsilon$	$1.11 \times 10^{-4}$

**Figure 3** Partial ordering of all GA methods for Matyas function with  $D = 0.01$  based on post hoc pairwise comparison with significance level  $\alpha = 0.05$  (see online version for colours)



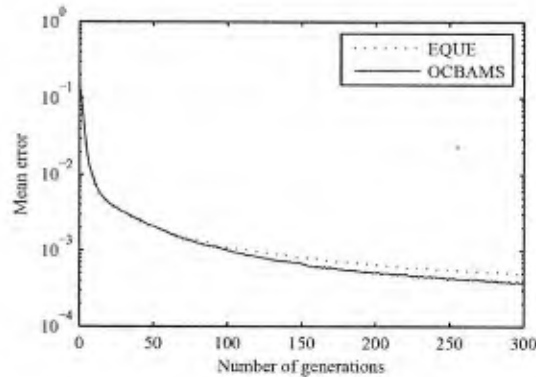
The dominance of SIGA methods over the EIGA methods is significant and easy to understand as the SIGA methods allocate samples as needed by the selection procedure and improves the quality of the GA. The difference between different allocation methods is more problem oriented and difficult to understand. The OCBA and OCBAM methods, which may be the best static allocation methods to identify the best individuals from a set, are not necessarily the best methods to identify the ordering of a set. The sampling with the OCBA and OCBAM methods is mostly allocated to the individuals that are currently the best ones or close to the best ones, focusing a large number of samples on those individuals and neglecting to sample other inferior individuals. When integrating with the EIGA, these two methods may greatly over sample very few individuals and under-sample other individuals that might have the potential to exhibit better means when more samples are allocated. Thus, integrating OCBA or OCBAM methods with the EIGA can lead to worse solutions than the EQU or PTV methods with EIGA. However, the adverse impact on over-sample current good individuals can be greatly reduced when integrating with SIGA, since the tournament has a small size and the goal is to identify the best individual, the sampling allocation calculated by OCBA and OCBAM methods is more evenly and reasonably distributed than when integrating with EIGA or the other allocation methods, and the statistical results are greatly improved. Also, the reason that the OCBAM exhibits better solutions than OCBA may be caused by the fact that the OCBAM uses a distance measure that involves both information from the good individuals and the inferior individuals.

#### 4.3.3 Comparison of convergence

To visualise the effect that integrating the CBA methods into either the evaluation or the selection step of the GA has on the convergence of the algorithm, the OCBAMS and the EQU method are considered for the Matyas function with  $D = 0.05$ . These methods are generally the best SIGA and EIGA methods, respectively, performing the best for the greatest number of problems and noise levels. The errors of the best individual at each generation averaged over the 1600 trials are plotted in Figure 4. It can be seen that the errors associated with both algorithms initially decline at approximately the same rate. However,

as the solutions approach the optimal solution, the OCBAMS method is better able to allocate the samples that it performs. This results in faster and continued progress during the later phase of the algorithm, resulting in a better solution. Alternatively, the OCBAMS method can reach a solution of the same quality as the EQU method in approximately 200 generations compared with the 300 generations when using the same numbers of individuals and samples per individual per generation.

**Figure 4** Example convergence of EQU and OCBAMS (Matyas function,  $D = 0.05$ ) (see online version for colours)



#### 4.3.4 Comparison of sampling efficiency

To understand the improvement of sampling efficiency due to the use of the SIGA, the EQU methods are selected as the baseline for the comparison since the improvement of other SIGA over EIGA are more significant than the EQU methods. The results of the EQU for each problem and noise level are compared with the EQU method with improved sampling. The number of allocated samples per individual  $n_1$  for the EQU method is increased in steps of 100 from 250 to 550, and the EQU method was executed 1600 times in order to determine the mean error. A second-order polynomial fit between the total number of samples per individual per generation  $n$  and the error of the EQU method is established for each problem and noise level. This linear relationship is used to determine the equivalent number of samples per individual per generation required to obtain the same error with the EQU method that was obtained with the EQU method using 250 samples per individual per generation. An example of this process is shown in Figure 5. For each noise level ( $D \in \{0.01, 0.05, 0.1\}$ ), the mean errors are plotted in the figure, and a linear relationship is extracted. Bars indicating the mean error obtained using the EQU method with 250 samples and the equivalent number of samples as the EQU method with same mean error are shown. The calculated equivalent samples and the relative cost of obtaining the same error are shown in Table 8. It can be seen that the relative costs average approximately 143% with a maximal value of 225%. Generally, the relative cost of high noise levels is smaller than that of low noise levels. In such problems, the noise present in samples can dominate the differences in the expected fitness of individuals, requiring large number of samples for each individual. While there is still improvement with using the SIGA in these cases, this improvement can be made more dramatic with a higher

computing budget. Also, it can be seen in Table 5 that the SIGA results in a more dramatic improvement relative to the EIGA when other CBA methods are used.

**Figure 5** Equivalent numbers of samples per individual per generation for EQU method to match the mean error of EQU method with 250 samples per individual per generation for Matyas function (all three noise levels included) (circles denote the mean error by EQU method with corresponding number of samples per individual per generation, the lines indicate the second-order polynomial relationship between number of samples per individual per generation and mean error, the bars indicate number of samples per individual per generation required by EQU method to match mean error of EQU method) (see online version for colours)

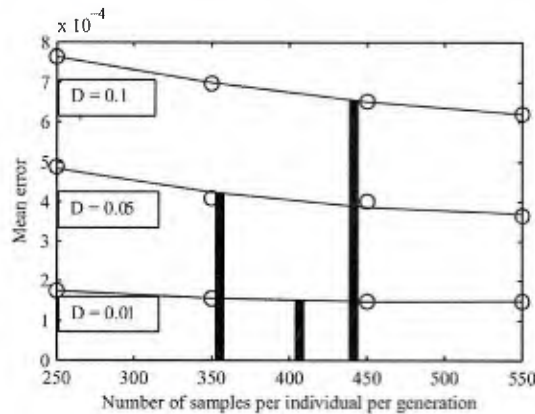


**Table 8** Equivalent numbers of samples per individual per generation and relative costs of EQU versus EQU to match EQU mean error with 250 samples per individual per generation

Function	D	Equivalent Samples	Relative Cost
Matyas	0.01	407	163%
	0.05	355	142%
	0.1	441	176%
Rosenbrock	1	289	116%
	5	251	100%
	10	262	105%
Sphere	0.1	441	176%
	0.5	562	225%
	2	410	164%
Zakharov	0.1	511	204%
	1	468	187%
	2	356	142%

**Table 8** Equivalent numbers of samples per individual per generation and relative costs of EQU versus EQUUS to match EQUUS mean error with 250 samples per individual per generation (Continued)

<i>Function</i>	<i>D</i>	<i>Equivalent Samples</i>	<i>Relative Cost</i>
Griewank	50	343	137%
	250	260	104%
	500	263	105%
HappyCat	10	314	126%
	50	285	114%
	100	266	106%
HGBat	10	396	158%
	50	295	118%
	100	323	129%

## 5 Conclusion

An SIGA is proposed in which CBA methods are integrated into the selection process of the GA. This algorithm is compared with the EIGA, the common existing approach of integrating CBA methods within the evaluation and ranking process of the GA. These algorithms are compared on several stochastic test problems with various levels of noise. It should be noted that only test functions with additive Gaussian noise are considered herein. This limitation is consistent with the traditional application of CBA methods (Lee et al, 2010). However, future research may include the consideration of more general forms of stochastic problems. In particular, practical problems (e.g., design of shipboard power systems subject to hostile disruptions (Cramer, Sudhoff, and Zivi, 2011), a future application area) may have different forms. Furthermore, neither the existing EIGA nor the proposed SIGA can be directly applied to multi-objective stochastic problems, and the future extension to such problems would be of clear value.

In this study, it is found that the SIGA generally outperforms the EIGA in terms of mean error for a given CBA method. This is attributed to the manner in which the SIGA allocates fitness evaluations towards specific individuals for whom the GA requires more information. It is also found that EIGA generally performs best with the EQU method of CBA. The performance of the SIGA is found to be less sensitive to choice of CBA method. Finally, it is found that the SIGA can find solutions with comparable mean error to solutions found with EIGA when using the EQU method while requiring significantly fewer samples for the test problems. The average relative cost of the EQU methods is 143% of that of the EQUUS method and can be as high as 225%, but these costs vary with test function, noise level, and choice of CBA method.

**References**

- Blum C. and Roli, A. (2003) 'Metaheuristics in combinatorial optimization: overview and conceptual comparison', *ACM Computing Surveys (CSUR)*, Vol. 35, No. 3, pp.268–308.
- Branke, J., Meisel, S. and Schmidt, C. (2008) 'Simulated annealing in the presence of noise', *Journal of Heuristics*, Vol. 14, No. 6, pp.627–654.
- Buadhachain, S. and Provan, G. (2015) 'An efficient decentralized clustering algorithm for aggregation of noisy multi-mean data', *Journal of Heuristics*, Vol. 21, No. 2, pp.301–328.
- Chan, R.R. and Sudhoff, S.D. (2010) 'An evolutionary computing approach to robust design in the presence of uncertainties', *IEEE Transactions on Evolutionary Computation*, Vol. 14, No. 6, pp.900–912.
- Chen, Ch. (2010) 'Stochastic simulation optimization: an optimal computing budget allocation', World Scientific, Singapore.
- Chen, C.H., He, D., Fu, M. and Lee, L.H. (2008) 'Efficient simulation budget allocation for selecting an optimal subset', *INFORMS Journal on Computing*, Vol. 20, No. 4, pp.579–595.
- Chen, C.H., Lin, J., Yücesan, E. and Chick, S.E. (2000) 'Simulation budget allocation for further enhancing the efficiency of ordinal optimization', *Discrete Event Dynamic Systems*, Vol. 10, No. 3, pp.251–270.
- Cramer, A.M., Sudhoff, S.D., Zivi, E.L. (2011) 'Metric optimization-based design of systems subject to hostile disruptions', *IEEE Transactions on Systems, Man and Cybernetics, Part A: Systems and Humans*, Vol. 41, No. 5, pp.989–1000.
- Deb, K. and Agrawal, R.B. (1994) 'Simulated binary crossover for continuous search space', *Complex Systems*, Vol. 9, pp.1–34.
- Deb, K. and Deb, D. (2014) 'Analysing mutation schemes for real-parameter genetic algorithms', *International Journal of Artificial Intelligence and Soft Computing*, Vol. 4, No. 1, pp.1–28.
- Deb, K., Gupta, S., Daum, D., Branke, J., Mall, A.K. and Padmanabhan, D. (2009) 'Reliability-based optimization using evolutionary algorithms', *IEEE Transactions on Evolutionary Computation*, Vol. 13, No. 5, pp.1054–1074.
- Deb, K., Pratap, A., Agarwal, S. and Meyerivan, T. (2002) 'A fast and elitist multiobjective genetic algorithm: NSGA-II', *IEEE Transactions on Evolutionary Computation*, Vol. 6, No. 2, pp.182–197.
- Dill, G.K. and e Silva, A.S. (2013) 'Robust design of power system controllers based on optimization of pseudospectral functions', *IEEE Transactions on Power Systems*, Vol. 28, No. 2, pp.1756–1765.
- Ernoliev, Y. (1988) *Numerical Techniques for Stochastic Optimization*, Springer-Verlag, New York, NY.
- Fu, M.C., Chen, C.H. and Shi, L. (2008) 'Some topics for simulation optimization', *Proceedings of the 40th Conference on Winter Simulation*, pp.27–38, Amsterdam, The Netherlands.
- Ho, S.L., Yang, S., Bai, Y. and Huang, J. (2014) 'A robust metaheuristic combining clonal colony optimization and population-based incremental learning methods', *IEEE Transactions on Magnetics*, Vol. 50, No. 2, pp.677–680.
- Hornig, S.C. and Lin, S.Y. (2013) 'Auctionary algorithm assisted by surrogate model in the framework of ordinal optimization and optimal computing budget allocation', *Information Sciences*, Vol. 233, pp.214–229.
- Jensen, M.T. (2003) 'Generating robust and flexible job shop schedules using genetic algorithms', *IEEE Transactions on Evolutionary Computation*, Vol. 7, No. 3, pp.275–288.
- Lee, L.H., Chen, C., Chew, E.P., Li, J., Pujowidianto, N.A. and Zhang, S. (2010) 'A review of optimal computing budget allocation algorithms for simulation optimization problem', *International Journal of Operations Research*, Vol. 7, No. 2, pp.19–31.

- Lee, L.H., Chew, E.P., Teng, S. and Chen, Y. (2008) 'Multi-objective simulation-based evolutionary algorithm for an aircraft spare parts allocation problem', *European Journal of Operational Research*, Vol. 189, No. 2, pp.476–491.
- Liang, J., Qu, B. and Suganthan, P. (2014) 'Problem definitions and evaluation criteria for the CEC 2014 special session and competition on single objective real-parameter numerical optimization', Computational Intelligence Laboratory and Nanyang Technological University, China and Singapore, Tech. Rep. 201311.
- Liu, B., Fernández, F.V. and Gielen, G.G. (2011) 'Efficient and accurate statistical analog yield optimization and variation-aware circuit sizing based on computational intelligence techniques', *IEEE Transactions on Computer-Aided Design of Integrated Circuits and Systems*, Vol. 30, No. 6, pp.793–805.
- Liu, B., Zhang, Q., Fernández, F.V., Gielen, G.G. (2013) 'An efficient evolutionary algorithm for chance-constrained bi-objective stochastic optimization', *IEEE Transactions on Evolutionary Computation*, Vol. 17, No. 6, pp.786–796.
- Liu, M. and He, J. (2013) 'An evolutionary negative-correlation framework for robust analog-circuit design under uncertain faults', *IEEE Transactions on Evolutionary Computation*, Vol. 17, No. 5, pp.640–665.
- Mendoza, J., Rousscau, L.M. and Villegas, J. (2015) 'A hybrid metaheuristic for the vehicle routing problem with stochastic demand and duration constraints', *Journal of Heuristics*, online, Vol. 1572–9397, pp.1–28.
- Nesmachnow, S. (2014) 'An overview of metaheuristics: accurate and efficient methods for optimisation', *International Journal of Metaheuristics*, Vol. 3, No. 4, pp.320–347.
- Paenke, I., Branke, J. and Jin, Y. (2006) 'Efficient search for robust solutions by means of evolutionary algorithms and fitness approximation', *IEEE Transactions on Evolutionary Computation*, Vol. 10, No. 4, pp.405–420.
- Pan, H., Wang, L. and Liu, B. (2006) 'Particle swarm optimization for function optimization in noisy environment', *Applied Mathematics and Computation*, Vol. 181, No. 2, pp.908–919.
- Rada-Vilela, J., Johnston, M. and Zhang, M. (2014) 'Population statistics for particle swarm optimization: resampling methods in noisy optimization problems', *Swarm and Evolutionary Computation*, Vol. 17, pp.37–59.
- Rada-Vilela, J., Zhang, M. and Johnston, M. (2013) 'Optimal computing budget allocation in particle swarm optimization', *Proceedings of the 15th Annual Conference on Genetic and Evolutionary Computation*, pp.81–88, Miami, FL.
- Schmidt, C., Branke, J. and Chick, S.E. (2006) 'Integrating techniques from statistical ranking into evolutionary algorithms', *Applications of Evolutionary Computing*, Vol. 3907, pp.752–763.
- Siddiqui, M. (1964) 'Statistical inference for rayleigh distributions', *Journal of Research of the National Bureau of Standards*, Vol. Sec D 68, pp.1005–1010.
- Stan, O., Sirdey, R., Carlier, J. and Nace, D. (2014) 'The robust binomial approach to chance-constrained optimization problems with application to stochastic partitioning of large process networks', *Journal of Heuristics*, Vol. 20, No. 3, pp.261–290.
- Tsutsui, S. and Ghosh, A. (1997) 'Genetic algorithms with a robust solution searching scheme', *IEEE Transactions on Evolutionary Computation*, Vol. 1, No. 3, pp.201–208.
- Tu, Z. and Lu, Y. (2004) 'A robust stochastic genetic algorithm (stGA) for global numerical optimization', *IEEE Transactions on Evolutionary Computation*, Vol. 8, No. 5, pp.456–470.
- Wang, L., Zhang, L. and Zheng, D.Z. (2005) 'Genetic ordinal optimisation for stochastic flow shop scheduling', *The International Journal of Advanced Manufacturing Technology*, Vol. 27, Nos. 1–2, pp.166–173.
- Xiao, H. and Lee, L.H. (2014) 'Simulation optimization using genetic algorithms with optimal computing budget allocation', *Simulation*, Vol. 90, No. 10, pp.1146–1157.
- Xu, Y., Dong, Z.Y., Meng, K., Zhao, J.H. and Wong, K.P. (2012) 'A hybrid method for transient stability-constrained optimal power flow computation', *IEEE Transactions on Power Systems*, Vol. 27, No. 4, pp.1769–1777.

# Computing Budget Allocation in Multi-Objective Evolutionary Algorithms for Stochastic Problems

Mengmei Liu<sup>\*,\*</sup>, Aaron M. Cramer<sup>a</sup>

<sup>a</sup>*Department of Electrical and Computer Engineering, University of Kentucky, Lexington, KY USA*

---

## Abstract

Multi-objective stochastic problems are important problems in practice and are often solved through multi-objective evolutionary algorithms. Researchers have developed different noise handling techniques to improve the efficiency and accuracy of such algorithms, primarily by integrating these methods into the evaluation or environmental selection steps of the algorithms. In this work, a combination of studies that compare integration of different computing budget allocation methods into either the evaluation or the environmental selection steps are conducted. These comparisons are performed on stochastic problems derived from benchmark multi-objective optimization problems and consider varying levels of noise. The algorithms are compared in terms of both proximity to and coverage of the true Pareto-optimal front and sufficient studies are performed to allow statistically significant conclusions to be drawn. It is shown that integrating computing budget allocation methods into the environmental selection step is better than integration within the evaluation step.

## Keywords:

Computational complexity, evolutionary computation, Gaussian noise, genetic algorithms, Pareto analysis

---

## 1. Introduction

Real-world optimization problems are often multi-objective and stochastic problems [1, 2]. Multi-objective evolutionary algorithms (MOEAs) are widely applied to solve those problems [3]. MOEAs combine operators such as mating selection [4], which selects child genes, crossover, and mutation to construct new generations of individuals. Among MOEAs, popular elitist approaches archive non-dominated solutions from the previous generation and combine them with non-dominated solutions from the current generation to produce the subsequent generation, a process which is referred to as environmental selection [4].

Researchers have developed different noise handling techniques to solve stochastic problems, aiming to improve the accuracy and efficiency of the algorithms. For example, a probabilistic method to improve sampling using loopy belief propagation for probabilistic model building genetic programming is described in [5]. Population statistics based re-sampling technique is introduced in [6] with the particle swarm optimization al-

gorithm to solve stochastic optimization problems. For the elitist MOEAs, because of the stochastic nature of the objective functions, MOEAs must perform repeated computationally expensive samples in order to assess the fitness of each individual. The noise handling techniques seek to obtain more accurate results with fewer total evaluations. For example, the optimal computing budget allocation (OCBA) method proposed in [7] is integrated into the evaluation procedure to reduce the computing cost in [8]. In [9], fitness inheritance from parent genes is proposed to reduce the computational intensity required for evaluation. A probabilistic method based on statistical analysis of dominance is used to estimate Pareto-optimal front in [10]. In [11], confidence-based dynamic re-sampling is proposed to improve the confidence of Pareto ranking. A reliability-based optimization method which utilizes mathematical approximations of a solution's reliability to integrate into evolutionary algorithms is described in [12]. Optimal design considering the worst-case scenario for safety can be approached by applying anti-optimization factors into stochastic optimization problems [13]. A noise-aware dominance operator is integrated into the mating selection in [14]. However, due to the nature of the elitist

---

\*Corresponding author. mengmei.liu@uky.edu, +1 (859) 257-9113, 453 F. Paul Anderson Tower, Lexington, KY 40506 USA

MOEAs, environmental selection plays a more critical role than mating selection because it controls the evolving set of non-dominated solutions [15].

Herein, a fundamental question regarding the application of computing budget allocation (CBA) methods to MOEAs is considered. The CBA methods refer to methods of allocating a fixed number of total samples to a pool of individuals in the solution set of a stochastic problem. The effect of integrating CBA methods in either the evaluation or environmental selection on the accuracy of the MOEA is examined. In previous work with re-sampling applied as a noise handling technique, it is proposed either in evaluation [8] or in environmental selection [11]. However, there is no clear comparison between these two techniques; the comparisons focused only on whether the proposals improved the results or not. There exists no comprehensive study that examines, for a fixed total computing budget, where the re-sampling procedure should be integrated to best improve the algorithms. A previous work in [16] proposed integration of CBA techniques into selection procedure instead of evaluation procedure of genetic algorithm for single-objective stochastic problems and showed that the selection integration method greatly improved the accuracy of the algorithm. Inspired by this work, a combination of studies that compare the alternative approaches to integrating CBA methods into genetic algorithms (GA), namely evaluation-integrated GA (EIGA) and selection-integrated GA (SIGA), are described. It is shown that the SIGA outperforms the EIGA statistically for the reason that the SIGA allocates fitness evaluations toward specific individuals when the algorithm needs more information for evolving. Various CBA techniques are compared, including the most basic equal allocation (EQU) method [17], OCBA method [7, 18], and the proportional-to-variance (PTV) method [19]. These algorithms and CBA techniques are applied to stochastic multi-objective problems constructed from benchmark multi-objective optimization problems [20, 21, 22]. Numerical experiments are performed, and statistical testing is used to validate the significance of the comparisons. The results suggest two significant findings: 1) applying SIGA other than EIGA, the generational distance (GD) metrics had improved for at least one decimal level to up to two decimal levels with statistical significance for all the test cases, which implies that the SIGA method produces more accurate front when solving multi-objective stochastic problems; 2) even though OCBA method is a better allocation method for correct selection from a static pool [7], it performs worse than the EQU and PTV allocation methods when integrated into an elitist MOEA where the

pool changes dynamically from generation to generation.

The remainder of this paper is organized as follows. First, descriptions of the considered stochastic multi-objective problems and different CBA methods are given in Section 2. In Section 3, the structure of the EIGA and SIGA approaches for integrating CBA methods into GAs are described. Test functions, performance metrics, and experimental results are presented in Section 4. Conclusion for this study is in Section 5.

## 2. Multi-Objective Stochastic Problems and Computing Budget Allocation Methods

The multi-objective stochastic problems and the CBA methods considered herein are described below.

### 2.1. Stochastic problem statement

The multi-objective stochastic problems considered herein can be defined as

$$\min_X J_1(X), J_2(X), \dots, J_H(X), \quad (1)$$

where  $X$  is the (possibly multi-dimensional) decision variable,  $J_1, J_2, \dots$ , and  $J_H$  are the  $H$  objectives to be minimized,  $J_l(X) = E[L_l(X, \xi)]$ ,  $l \in \{1, 2, \dots, H\}$ ,  $L_l(\cdot, \cdot)$  is the sample performance of  $l$ th objective, and  $\xi$  is a random variable describing the problem noise. For the test problems considered herein, Noise can be introduced in variable values or environment levels and can follow different kinds of distributions. The stochastic nature of problems varies from case to case, depending on application details and difficult to generalize. For the problems considered herein, the noise for each objective is modeled with additive independent and identical Gaussian distributions, with the noise sampled at each function evaluation. It is also assumed that such a problem is unconstrained in the sense that any constraints that bind the solution are appropriately penalized in  $L(\cdot, \cdot)$ .

For a deterministic multi-objective problem where  $J_l(X) = L_l(X)$ , the Pareto optimal front [23] is the complete set of non-dominated solutions. A solution for the multi-objective problem is defined as a non-dominated solution if it is not dominated by any other solutions. A solution  $a$  dominates solution  $b$  if  $J_l(a) \leq J_l(b) \forall l \in \{1, 2, \dots, H\}$  and  $\exists l \in \{1, 2, \dots, H\}$  such that  $J_l(a) < J_l(b)$ . For the non-dominated solutions, each objective is minimized to the extent that it is not possible to further minimize one objective without making one or more other objectives bigger (worse).

For a stochastic multi-objective problem, the fitness function of each objective can only be estimated by a limited number of random samples. Mean value from the random samples is used to evaluate the fitness in this study. For a certain number of realistic problems, it is assumed that the evaluation of the samples takes far more computation time and effort than the algorithm itself. It is desired to be able to allocate the samples, or the total computing budget, appropriately to obtain the best approximation of the fitness function when evaluates, thus to obtain the best approximation of the Pareto optimal front when the search terminates. The quality of a Pareto optimal front approximation is measured by both its proximity to the true front and the degree to which it covers the true front.

## 2.2. Computing budget allocation methods

The CBA methods determine, given a total number of samples, how samples should be allocated to each individual in the solution set. The motivation of applying CBA methods to a stochastic problem is to improve the accuracy of solving a stochastic problem and avoid wasting samples on unwanted individuals. Various CBA methods have been studied, and the three such CBA methods applied in this study are discussed below. For each of these methods, it is assumed that  $N$  samples are being allocated among  $k$  individuals.

### 2.2.1. Equal allocation method

The simplest allocation technique to conduct sampling is the EQU technique, and it often serves as a benchmark for comparison [24]. The available computing budget is equally distributed to all individuals:

$$\bar{n}_i = \frac{N}{k}, \quad (2)$$

where  $\bar{n}_i$  is the number of additional samples to be allocated to individual  $i$ .

### 2.2.2. Optimal computing budget allocation method

The OCBA method [7] for multi-objective optimization is based on maximizing the asymptotic probability that the selected subset is the non-dominated set. One such implementation is described below.

For a set of unique individuals  $S$ ,  $S_P$  is defined as the non-dominated set, and  $S_D$  is defined as the dominated set. In deterministic problems,  $S_P$  and  $S_D$  can be determined by non-dominated sorting [25]. The OCBA allocation rule aims to maximize the probability of correctly selecting the Pareto optimal set in stochastic problems.

For an individual  $i$ , which has previously been sampled,  $\bar{L}_{il}$  is the sample mean, and  $\sigma_{il}^2$  denotes the sample

variance corresponding to the  $l$ th objective. For two individuals,  $i$  and  $j$ , the difference of sample means for objective  $l$  is expressed as

$$\delta_{ijl} = \bar{L}_{jl} - \bar{L}_{il}. \quad (3)$$

The individual that dominates  $i$  with the highest probability is approximated as

$$j_i \approx \arg \max_{j \in S, j \neq i} \prod_{l=1}^H P(L_{jl} \leq L_{il}) \approx \arg \min_{j \in S, j \neq i} \frac{\delta_{ijl_j} \left| \delta_{ijl_j} \right|}{\sigma_{il_j}^2 + \sigma_{jl_j}^2}, \quad (4)$$

where  $l_j$  denotes the objective for which  $j$  is better than  $i$  with the lowest probability and can be calculated as

$$l_j \equiv \arg \min_{l \in \{1, \dots, H\}} P(L_{jl} \leq L_{il}) \approx \arg \max_{l \in \{1, \dots, H\}} \frac{\delta_{ijl} \left| \delta_{ijl} \right|}{\sigma_{il}^2 + \sigma_{jl}^2}. \quad (5)$$

The set of individuals  $S$  is partitioned into subsets  $S_A$  or  $S_B$  based on the following equation:

$$S_A = \left\{ h \mid h \in S, \frac{\delta_{jh}^2}{\sigma_{hh}^2 + \sigma_{jh}^2} \leq \min_{i \in \Theta_h} \frac{\delta_{ih}^2}{\sigma_{ih}^2 + \sigma_{jh}^2} \right\} \quad (6)$$

$$S_B = S \setminus S_A, \quad (7)$$

where

$$\Theta_h = \{i \mid i \in S, j_i = h\}. \quad (8)$$

The samples are allocated to each individual based on its membership in  $S_A$  or  $S_B$ . In particular, for  $h, m \in S_A$ ,

$$\frac{\bar{n}_h}{\bar{n}_m} = \left( \frac{\sigma_{hh}^2 / \delta_{hh}^2}{\sigma_{mm}^2 / \delta_{mm}^2} \right)^2. \quad (9)$$

For  $d \in S_B$ ,

$$\bar{n}_d^2 = \sum_{h \in \Theta_d^*} \frac{\sigma_{dh}^2}{\sigma_{hh}^2} \bar{n}_h^2, \quad (10)$$

where

$$\Theta_d^* = \{h \mid h \in S_A, j_h = d\}. \quad (11)$$

### 2.2.3. Proportional-to-variance method

The PTV method utilizes the variance information from the existing samples [26]. This method allocates computing budget proportional to the summation of the variance over all the objectives:

$$\frac{\bar{n}_i}{\bar{n}_j} = \frac{\sum_{l=1}^H \sigma_{il}^2}{\sum_{l=1}^H \sigma_{jl}^2}. \quad (12)$$

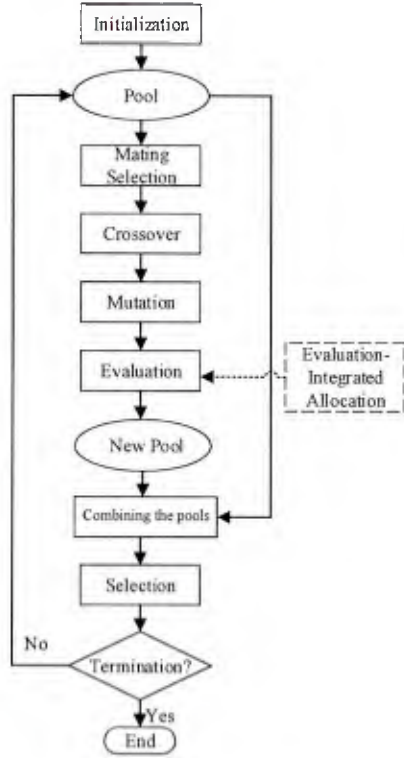


Figure 1: Flow chart of EIGA

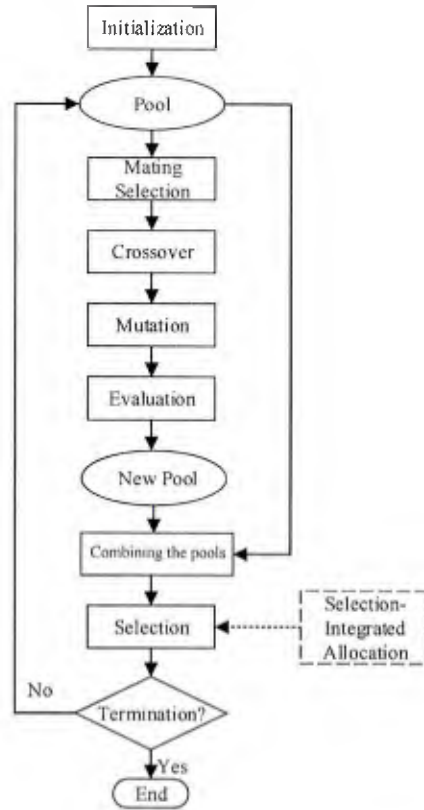


Figure 2: Flow chart of SIGA

### 3. Computing Budget Allocation Method Integrated Genetic Algorithms

NSGA-II is a widely used elitist MOEA for solving multi-objective optimization problems [25]. Herein, the CBA techniques described above are embedded in the framework of NSGA-II. Two methods of integrating CBA techniques into NSGA-II are considered. One is to integrate the allocation procedure into the evaluation step, and a GA using this approach is referred to as an EIGA [8]. The second is to integrate the allocation in the combining and environmental selection procedure, which is to allocate the budget across the merged pool, and a GA using this approach is referred to as a SIGA. The flow charts of the integrated GA for either option are shown in Figure 1 and Figure 2.

Pseudocode for the two algorithms is listed in Algorithm 1 and Algorithm 2, and steps specific for each algorithm are marked in italics. The integrated GAs have the following steps:

Step 1: The population of  $n_{ind}$  individuals is uniformly randomly initialized in the search domain and

is initially sampled  $n_0$  times. An initial non-dominated sort is applied across the population [25]. The rank number and crowding distance [25] are assigned to each individual by the calculation of non-dominated sort in the fitness domain.

Step 2: Tournament selection is performed: for a total of  $n_{ind}$  randomly generated tournaments, each tournament contains two randomly selected individuals. Among each tournament, the individual with the smaller front number is selected. If the front numbers are equal, the individual with a larger crowding distance index is selected.

Step 3: Simulated binary crossover [27] and simulated binary mutation [25] are performed to generate the new pool of size  $n_{ind}$ .

Step 4: Each individual in the new pool is evaluated with  $n_0$  number of samples. In the EIGA, the CBA method is used to allocate a total of  $n_1 n_{ind}$  additional samples across the new pool.

Step 5: Combine the new pool and the old pool to

---

**Algorithm 1** EIGA

---

- 1: Initialize population of individuals with random values in search space and evaluate the initial population with a number of initial samples; assign rank and crowding distance to each individual through non-dominated sort.
  - 2: **while** Maximum generation not reached **do**
  - 3:   Perform mating selection, selecting the individual out of each tournament with minimum rank and maximum crowding distance
  - 4:   Perform crossover for each pair of individuals in the mating pool
  - 5:   Perform mutation on each individual in the mating pool with selected mutation rate
  - 6:   Evaluate each individual in the mating pool with a number of initial samples
  - 7:   **if** EIGA **then**
  - 8:     *Apply CBA to allocate additional samples for each individual in the mating pool*
  - 9:   **end if**
  - 10:   Combine the new pool of size  $n_{ind}$  with the old pool of size  $n_{ind}$ , and generate a temporary pool of  $2n_{ind}$
  - 11:   Perform non-dominated sort on the temporary pool, and select  $n_{ind}$  individuals to form the pool for the next generation based on rank and crowding distance
  - 12: **end while**
- 

form a temporary pool of size  $2n_{ind}$ . In the SIGA, the CBA method is used to allocate  $n_1 n_{ind}$  samples to the temporary pool.

Step 6: Non-dominated sorting is applied across the temporary pool to update the front index and crowding distance. The next generation pool is subsequently filled with  $n_{ind}$  individuals with minimum rank and maximum crowding distance.

Step 7: The algorithm terminates after  $n_{gen}$  generations. Otherwise, the algorithm continues at Step 2. The same number of total samples per generation are used in both EIGA and SIGA. The total number of samples allocated per algorithm is  $(n_0 + n_1)n_{ind}n_{gen} + n_0 n_{ind}$ .

The primary focus of this work is to compare EIGA with SIGA. NSGA-II is used as a representative multi-objective optimization framework, and the parameters for the GAs are given in Table 1. The parameters of the GAs are selected manually to achieve acceptable performance on the deterministic versions of the test functions included in this study. And they are used for both EIGA and SIGA. Different sets of parameters can certainly affect the performance of the GAs, but since they are used

---

**Algorithm 2** SIGA

---

- 1: Initialize population of individuals with random values in search space and evaluate the initial population with a number of initial samples; assign rank and crowding distance to each individual through non-dominated sort.
  - 2: **while** Maximum generation not reached **do**
  - 3:   Perform mating selection, selecting the individual out of each tournament with minimum rank and maximum crowding distance
  - 4:   Perform crossover for each pair of individuals in the mating pool
  - 5:   Perform mutation on each individual in the mating pool with selected mutation rate
  - 6:   Evaluate each individual in the mating pool with a number of initial samples
  - 7:   Combine the new pool of size  $n_{ind}$  with the old pool of size  $n_{ind}$ , and generate a temporary pool of  $2n_{ind}$
  - 8:   **if** SIGA **then**
  - 9:     *Apply CBA to allocate additional samples for each individual in the temporary pool*
  - 10:   **end if**
  - 11:   Perform non-dominated sort on the temporary pool, and select  $n_{ind}$  individuals to form the pool for the next generation based on rank and crowding distance
  - 12: **end while**
- 

Table 1: Parameters of Genetic Algorithms

Parameter	Parameter	Value
$n_{gen}$	Number of generations	500
$n_{ind}$	Number of individuals in pool	100
$n_{tour}$	Tournament size	2
$\eta$	Crossover constant	2
$p_m$	Mutation probability	0.05
$n_0$	Initial samples per individual	50
$n_1$	Allocated samples per individual	200

as a baseline, the selection of these parameters is not the focus of this work. The sampling allocation procedure is performed sequentially in 10 steps. Assuming the total computing budget is  $N$ , then in each step,  $N/10$  samples are allocated, and sample means and variances are calculated for use in the next allocation step.

## 4. Results and Analysis

This section presents stochastic test problems and performance metrics, describes experimental results and compares the EIGA and SIGA as well as the CBA methods.

### 4.1. Test functions

Several multi-objective test problems are selected for constructing the stochastic problems. More specifically, ZDT1 ZDT2, ZDT3, and UF2 [20, 28] are selected for examples of 2D test problems, DTLZ2 and DTLZ5 [21, 22] are selected for testing 3D cases. A typical setting of 30 variables in the ZDT and UF test sets and 12 variables in the DTLZ test sets is followed. These problems are well-known test problems with known Pareto optimal sets. Independent zero-mean Gaussian noise is added to each objective of the deterministic test function:

$$L_i(X, \xi_i) = f_i(X) + \xi_i \quad (13)$$

$$\xi_i = \mathcal{N}(0, \sigma_i^2) \quad (14)$$

where  $\sigma_i^2$  is the parameter establishing the noise level associated with the problem. In this study, values of  $\sigma_i$  of 1%, 10% and 20% of the maximum of each objective in the true Pareto-optimal set are used [29], indicating low, medium, and high noise levels, respectively. A letter ‘L’, ‘M’, or ‘H’ is appended to the names of the test problems to specify the specific stochastic test functions, e.g. ‘ZDT1L’ specifies the test function of ZDT1 with the low noise level.

### 4.2. Performance metrics

There are many different kinds of metrics measuring the performance of multi-objective optimization algorithms, such as generational distance (GD) [30], maximum spread [31], hypervolume ratio [32], and inverse generational distance (IGD) [33], and each metric may have different versions. Despite the diversity of metrics, they often measure two properties of the evolved front: how close is the evolved front to the true front and how well does the evolved front cover the true front. These two properties can be assessed with the GD and the IGD. The GD is calculated by averaging Euclidean distances from the evolved front to the true front and is the one of the widely used metric for convergence testing in multi-objective problems. The GD gives a good indication of the error between evolved front and the true front. The IGD is calculated by averaging the Euclidean distance from each true front sample to the

evolved front and in this way, it conveys the measurement of both convergence and diversity. 1000 evenly distributed individuals on the true front are used to approximate the true front in the calculations. The GD is calculated as

$$GD = \sqrt{\frac{1}{n_{EPF}} \sum_{i=1}^{n_{EPF}} d_i^2}, \quad (15)$$

where  $n_{EPF}$  is the number of individuals in the evolved front, and  $d_i$  is the Euclidean distance of the individual  $i$  to the true front in the objective space, which is calculated by the distance of individual  $i$  to the closest individuals in the true front. The IGD is calculated as

$$IGD = \sqrt{\frac{1}{n_{TPF}} \sum_{i=1}^{n_{TPF}} \bar{d}_i^2}, \quad (16)$$

where  $n_{TPF}$  is the number of individuals in the true front, and  $\bar{d}_i$  is the Euclidean distance of the individual  $i$  in the true front to the closest individual in the evolved front in the objective space. The GD and IGD metrics are two different metrics for the measurement of performance for multi-objective optimization, and they are intended to quantify the two properties of the evolved front. In both cases, lower values indicate better results, i.e., the evolved front is closer to the true front and well spread over the true front.

### 4.3. Comparison of different strategies

Experiments were performed to compare the EIGA and SIGA with different CBA methods under the various noise levels. The EIGA and SIGA with different CBA schemes are denoted as EQU, EQU, OCB, OCB, PTVE and PTVS with the last letter ‘E’ or ‘S’ denoting the EIGA or SIGA, respectively. Each algorithm was applied to each problem with each noise level using each CBA method 1200 times. Table 2 shows the mean GD and IGD for each method. The lowest value of GD and IGD for each problem and noise level is indicated with boldfaced text. Graphical examples of ZDT1 and DTLZ2 are shown in Figs. 3–4.

#### 4.3.1. Comparison of EIGA and SIGA

By examining Table 2 vertically, it can be seen that the SIGA with a given CBA method generally outperforms the EIGA with the same CBA method. The distances are assumed to follow a Rayleigh distribution, so an F-test can be used to determine the statistical significance of the results [34]. The null hypothesis is that the mean distance of the SIGA for a given CBA method

Table 2: Comparison of mean error for test functions (bold-face text indicates the best algorithm for each problem and noise level)

Function	Method	GD	IGD	Method	GD	IGD	Method	GD	IGD
ZDT1L	EQUE	9.76E-02	7.22E-03	OCBAE	1.05E-01	7.79E-03	PTVE	9.87E-02	<b>7.05E-03</b>
	EQUS	4.83E-03	7.08E-03	OCBAS	6.00E-03	7.29E-03	PTVS	<b>4.80E-03</b>	7.09E-03
ZDT1M	EQUE	1.16E-01	1.90E-02	OCBAE	1.18E-01	3.25E-02	PTVE	1.23E-01	1.47E-02
	EQUS	<b>7.85E-03</b>	<b>1.11E-02</b>	OCBAS	1.07E-02	1.38E-02	PTVS	7.91E-03	<b>1.11E-02</b>
ZDT1H	EQUE	1.37E-01	3.52E-02	OCBAE	1.52E-01	5.51E-02	PTVE	1.63E-01	2.68E-02
	EQUS	<b>1.19E-02</b>	<b>1.71E-02</b>	OCBAS	1.59E-02	2.12E-02	PTVS	<b>1.19E-02</b>	1.73E-02
ZDT2L	EQUE	1.45E-01	9.82E-03	OCBAE	1.55E-01	9.39E-03	PTVE	1.47E-01	9.94E-03
	EQUS	<b>3.79E-03</b>	<b>7.15E-03</b>	OCBAS	5.17E-03	7.24E-03	PTVS	3.82E-03	<b>7.15E-03</b>
ZDT2M	EQUE	1.54E-01	2.60E-02	OCBAE	1.49E-01	4.97E-02	PTVE	1.68E-01	2.19E-02
	EQUS	<b>7.89E-03</b>	<b>1.49E-02</b>	OCBAS	1.14E-02	1.79E-02	PTVS	8.00E-03	<b>1.49E-02</b>
ZDT2H	EQUE	1.63E-01	5.48E-02	OCBAE	1.97E-01	9.77E-02	PTVE	1.99E-01	3.82E-02
	EQUS	<b>1.15E-02</b>	<b>2.36E-02</b>	OCBAS	1.66E-02	3.23E-02	PTVS	1.20E-02	2.47E-02
ZDT3L	EQUE	9.71E-02	8.62E-03	OCBAE	1.09E-01	1.00E-02	PTVE	2.63E-01	1.45E-02
	EQUS	<b>4.50E-03</b>	<b>7.92E-03</b>	OBAS	5.71E-03	8.37E-03	PTVS	4.78E-03	8.05E-03
ZDT3M	EQUE	1.15E-01	5.27E-02	OCBAE	1.57E-01	4.75E-02	PTVE	2.68E-01	5.82E-02
	EQUS	<b>9.75E-03</b>	<b>1.43E-02</b>	OCBAS	1.31E-02	2.08E-02	PTVS	1.26E-02	2.71E-02
ZDT3H	EQUE	1.50E-01	6.41E-02	OCBAE	2.18E-01	9.48E-02	PTVE	3.13E-01	7.49E-02
	EQUS	1.52E-02	3.75E-02	OCBAS	2.29E-02	4.71E-02	PTVS	<b>1.46E-02</b>	<b>3.74E-02</b>
UF2L	EQUE	9.05E-02	5.32E-02	OCBAE	8.25E-02	5.50E-02	PTVE	9.08E-02	5.35E-02
	EQUS	<b>5.64E-02</b>	<b>5.25E-02</b>	OBAS	5.73E-02	5.45E-02	PTVS	5.68E-02	<b>5.25E-02</b>
UF2M	EQUE	7.56E-02	6.86E-02	OCBAE	8.11E-02	7.02E-02	PTVE	7.40E-02	6.44E-02
	EQUS	4.27E-02	<b>6.43E-02</b>	OCBAS	4.26E-02	6.88E-02	PTVS	<b>4.23E-02</b>	<b>6.43E-02</b>
UF2H	EQUE	8.58E-02	8.29E-02	OCBAE	1.12E-01	1.03E-01	PTVE	9.12E-02	7.73E-02
	EQUS	4.85E-02	7.89E-02	OCBAS	4.31E-02	7.92E-02	PTVS	<b>4.25E-02</b>	<b>7.67E-02</b>
DTLZ2L	EQUE	3.73E-01	1.15E-01	OCBAE	6.66E-01	1.44E-01	PTVE	3.70E-01	1.14E-01
	EQUS	5.66E-02	9.15E-02	OCBAS	1.75E-01	1.03E-01	PTVS	<b>5.63E-02</b>	<b>9.13E-02</b>
DTLZ2M	EQUE	3.74E-01	1.21E-01	OCBAE	6.82E-01	1.57E-01	PTVE	3.77E-01	1.21E-01
	EQUS	5.33E-02	<b>9.37E-02</b>	OCBAS	1.87E-01	1.10E-01	PTVS	<b>5.18E-02</b>	9.38E-02
DTLZ2H	EQUE	3.82E-01	1.24E-01	OCBAE	7.03E-01	1.67E-01	PTVE	3.82E-01	1.23E-01
	EQUS	<b>4.59E-02</b>	<b>9.41E-02</b>	OCBAS	2.00E-01	1.14E-01	PTVS	4.66E-02	9.45E-02
DTLZ6L	EQUE	1.77E+00	1.18E-02	OCBAE	3.10E+00	2.60E-02	PTVE	1.76E+00	1.16E-02
	EQUS	<b>1.01E-01</b>	<b>8.23E-03</b>	OCBAS	4.78E-01	1.03E-02	PTVS	1.02E-01	8.26E-03
DTLZ6M	EQUE	2.06E+00	1.63E-02	OCBAE	4.18E+00	1.33E-01	PTVE	2.03E+00	<b>1.58E-02</b>
	EQUS	1.00E-01	1.70E-02	OCBAS	5.30E-01	1.92E-02	PTVS	<b>8.99E-02</b>	1.72E-02
DTLZ6H	EQUE	2.19E+00	2.60E-02	OCBAE	4.49E+00	2.88E-01	PTVE	2.15E+00	<b>2.13E-02</b>
	EQUS	<b>7.50E-02</b>	2.64E-02	OCBAS	5.77E-01	2.91E-02	PTVS	7.96E-02	2.66E-02

is greater than or equal to the mean distance of the EIGA for the same CBA method. A significance level of  $\alpha = 5\%$  is used to determine whether this hypothesis can be rejected. The results of these statistical tests are shown in Table 3. Due to a large number of samples (1200), many of the calculated p-values are smaller than the machine epsilon, and these are denoted in the table as ' $< \epsilon$ '. Statistically, significant results are indicated with boldfaced text. It can be seen that with the few ex-

ceptions in the IGD, the SIGA statistically significantly outperforms the EIGA for a given CBA method. For the GD metrics, the SIGA was significantly better than the EIGA in each case considered.

A close examine on the differences from Table 2 shows that while the IGD metrics are statistically improved or maintained at the same decimal level with the very few exceptions, the GD metrics are improved at least one decimal level and up to two decimal lev-

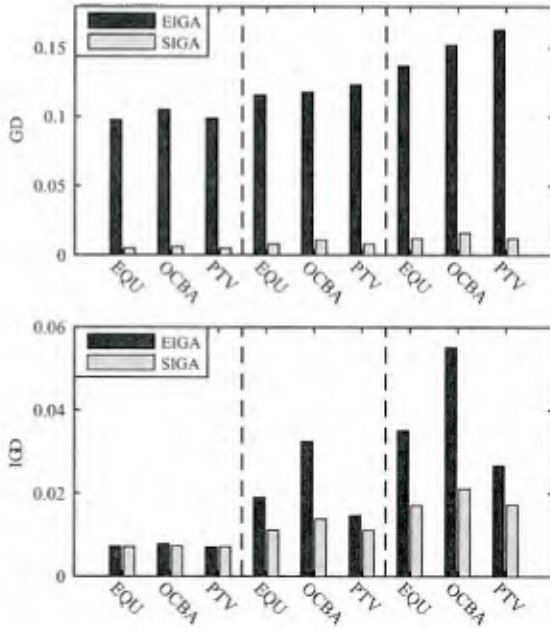


Figure 3: Comparison of generational distance (GD) and inverse generational distance (IGD) for ZDT1 function (the cases are divided by dashed lines from left to right corresponding to low, medium, and high noise levels)

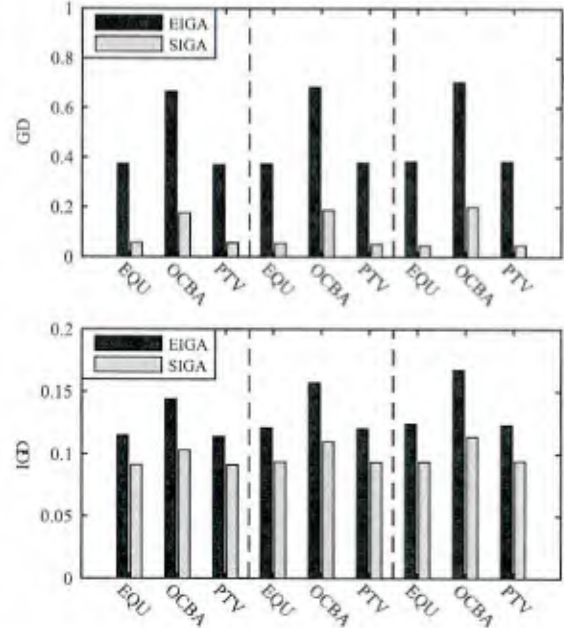


Figure 4: Comparison of generational distance (GD) and inverse generational distance (IGD) for DTLZ2 function (the cases are divided by dashed lines from left to right corresponding to low, medium, and high noise levels)

els. This suggests that while the generated fronts from SIGA and EIGA may well cover the true Optimal front in spectrum of front range, the front from SIGA should reside much closer to the true front than EIGA, which means the SIGA produces more accurate results when solving the multi-objective stochastic problems.

Generally, it can be concluded that the SIGA outperforms the EIGA statistically. The underlying reason is that by applying SIGA, the search algorithm allocates samples as needed in order to make the comparisons between individuals that are required by the algorithm and more accurately select the correct individuals into the next generation.

#### 4.3.2. Comparison of computing budget allocation methods

The comparisons among different CBA methods can be made by examining Table 2 horizontally. The smallest GD and IGD among each case are boldfaced. It is shown that EQU and PTV allocation methods give similar results, and they are consistently better than the OCBA method. This may be due to the dynamic nature of GAs. It has been shown that the OCBA method works well in static selection problems [24], but the

OCBA rule may not allocate samples as well as the population evolves.

From the previous discussion, the differences between SIGA and EIGA are dramatic and mostly statistically significant when using the same allocation method. However, for the same integration method, the differences between different allocation methods are less dramatic and may not be statistically significant, especially in the IGD metrics. An example analysis is performed on ZDT1L. A post hoc pairwise F-test is applied to the data for the six methods, and a significance level of  $\alpha = 5\%$  is used. The p-values associated with these tests are shown in Tables 4 and 5 for the GD and IGD, respectively. Several of the calculated p-values are smaller than the machine epsilon, and these are denoted in the table as ' $< \epsilon$ '. Statistically, significant results are indicated in boldfaced text. These pairwise statistical comparisons induce a partial ordering of the GAs for this problem. In this specific example, the differences between the methods for the GD metrics are mostly statistically significant, but for IGD metrics the differences are largely not significant. The cases of ZDT1L, UF2, DTLZ6M and DTLZ6H are the cases that the IGD metrics are very close to each other. In the other problems,

Table 3: P-Value of Comparison between SIGA and EIGA for each CBA Method ( $< \epsilon$  indicates p-value less than machine epsilon, boldfaced text indicates statistical significance with significance level  $\alpha = 0.05$ )

Function	EQU		OCBA		PTV	
	GD	IGD	GD	IGD	GD	IGD
ZDT1L	$< \epsilon$	3.16E-01	$< \epsilon$	5.21E-02	$< \epsilon$	5.55E-01
ZDT1M	$< \epsilon$	$< \epsilon$	$< \epsilon$	$< \epsilon$	$< \epsilon$	<b>3.24E-12</b>
ZDT1H	$< \epsilon$	$< \epsilon$	$< \epsilon$	$< \epsilon$	$< \epsilon$	$< \epsilon$
ZDT2L	$< \epsilon$	<b>4.44E-15</b>	$< \epsilon$	<b>1.01E-10</b>	$< \epsilon$	<b>4.44E-16</b>
ZDT2M	$< \epsilon$	$< \epsilon$	$< \epsilon$	$< \epsilon$	$< \epsilon$	$< \epsilon$
ZDT2H	$< \epsilon$	$< \epsilon$	$< \epsilon$	$< \epsilon$	$< \epsilon$	$< \epsilon$
ZDT3L	$< \epsilon$	<b>1.90E-02</b>	$< \epsilon$	<b>6.65E-06</b>	$< \epsilon$	$< \epsilon$
ZDT3M	$< \epsilon$	$< \epsilon$	$< \epsilon$	$< \epsilon$	$< \epsilon$	$< \epsilon$
ZDT3H	$< \epsilon$	$< \epsilon$	$< \epsilon$	$< \epsilon$	$< \epsilon$	$< \epsilon$
UF2L	$< \epsilon$	3.80E-01	$< \epsilon$	4.06E-01	$< \epsilon$	3.15E-01
UF2M	$< \epsilon$	5.60E-02	$< \epsilon$	3.10E-01	$< \epsilon$	4.76E-01
UF2H	$< \epsilon$	1.14E-01	$< \epsilon$	<b>9.50E-11</b>	$< \epsilon$	4.20E-01
DTLZ2L	$< \epsilon$	<b>1.12E-08</b>	$< \epsilon$	<b>1.11E-16</b>	$< \epsilon$	<b>2.77E-08</b>
DTLZ2M	$< \epsilon$	<b>2.00E-10</b>	$< \epsilon$	$< \epsilon$	$< \epsilon$	<b>2.36E-10</b>
DTLZ2H	$< \epsilon$	<b>7.53E-12</b>	$< \epsilon$	$< \epsilon$	$< \epsilon$	<b>5.72E-11</b>
DTLZ6L	$< \epsilon$	$< \epsilon$	$< \epsilon$	$< \epsilon$	$< \epsilon$	$< \epsilon$
DTLZ6M	$< \epsilon$	8.48E-01	$< \epsilon$	$< \epsilon$	$< \epsilon$	9.81E-01
DTLZ6H	$< \epsilon$	6.46E-01	$< \epsilon$	$< \epsilon$	$< \epsilon$	1.00E+00

the differences are much larger.

The differences between different computing budget allocation methods for the same integration method may also rely on the properties of the specific function. Although these differences are less dramatic, the EQU and PTV allocation methods are more favorable than the OCBA method when integrated into NSGA-II.

#### 4.3.3. Comparison of convergence

To visualize the effect of EIGA comparing SIGA on the convergence of the algorithm, an example comparison of the EQU and EQU methods is made on the ZDT1H test case. The GD and IGD metrics are calculated on one reproduction run and are plotted in Figure 5-Figure 6. It is shown that for the GD metric, the EQU method converges much faster than the EQU method and the final result is also significantly better. The convergence of IGD metric for EQU and EQU methods are very close, however, a zoomed in plot of the final result still shows that the EQU method is slightly better than the EQU method.

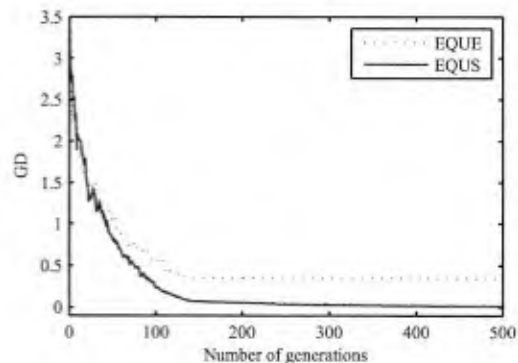


Figure 5: Convergence of GD for the comparison of EQU and EQU on ZDT1H (one experimental run)

## 5. Conclusion

Several noise handling techniques for multi-objective stochastic problems are studied. Various re-sampling

Table 4: P-Values of Post Hoc Pairwise Comparison of Generalized Distance for all Methods on ZDT1L ( $< \epsilon$  indicates p-value less than machine epsilon, boldfaced text indicates statistical significance with significance level  $\alpha = 0.05$ )

Method	PTVS	EQU	OCBAS	EQUE	PTVE
EQU	4.39E-01				
OCBAS	<b>2.39E-08</b>	<b>5.56E-08</b>			
EQUE	$< \epsilon$	$< \epsilon$	$< \epsilon$		
PTVE	$< \epsilon$	$< \epsilon$	$< \epsilon$	3.92E-01	
OCBAE	$< \epsilon$	$< \epsilon$	$< \epsilon$	<b>3.67E-02</b>	6.48E-02

Table 5: P-Values of Post Hoc Pairwise Comparison of Inverse Generalized Distance for all Methods on ZDT1L ( $< \epsilon$  indicates p-value less than machine epsilon, boldfaced text indicates statistical significance with significance level  $\alpha = 0.05$ )

Method	PTVE	EQU	PTVS	EQUE	OCBAS
EQU	4.59E-01				
PTVS	4.45E-01	4.86E-01			
EQUE	2.80E-01	3.16E-01	3.28E-01		
OCBAS	2.06E-01	2.37E-01	2.48E-01	4.07E-01	
OCBAE	<b>7.26E-03</b>	<b>9.64E-03</b>	<b>1.06E-02</b>	<b>3.14E-02</b>	5.21E-02

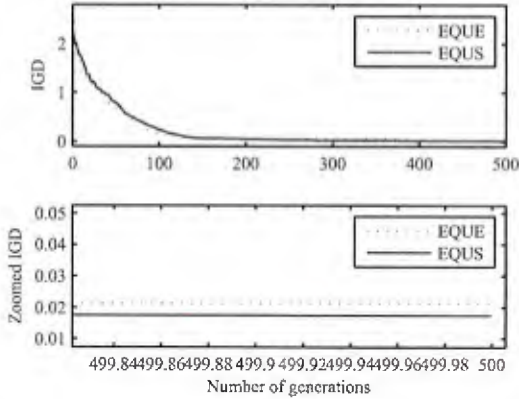


Figure 6: Convergence of IGD for the comparison of EQUE and EQU on ZDT1L (one experimental run)

techniques for allocating a given computing budget in either the environmental selection step or the evaluation process within an NSGA-II implementation are compared. These algorithms are compared on both 2D and 3D stochastic test problems with various levels of noise. It is found that the SIGA generally outperforms the EIGA in terms of both GD and IGD metrics. This is attributed to the manner in which the SIGA allocates fitness evaluations towards specific individuals for whom

the GA requires more information when evolving the Pareto front. The idea of allocating samples for a search and optimization algorithm to where the algorithm requires other than where the evaluation occurs was originated from [16] and can be extended to other optimization algorithms. Among the CBA methods, even though the OCBA method has been found to be a better method of allocating samples to maximize the probability of correctly selecting the best individual from a static pool [7], it is found to perform less favorably than the EQU and PTV methods when integrated into an elitist MOEA.

The comparison is done in the framework of NSGA-II. There are other more powerful and recently invented MOEAs, such as the MOEA/D in [35], and the SPEA2 in [4]. The MOEA/D decomposes optimization problems into subproblems and optimizes them simultaneously to improve performance over traditional MOEA. The SPEA2 is a refined version of SPEA in terms of fitness assignment, density estimation and archive truncation in the search process. And similar integration for noise handling can also be applied to those algorithms. These are good topics for future work.

This work can be applied to solve practical multi-objective stochastic problems. Future study in the areas of optimization of photovoltaic inverters subject to solar irradiance variation [36] and the design of shipboard power systems subject to hostile disruptions [37, 38]

will be performed to evaluate the relative merits of the CBA integration approaches on more practical optimization problems.

## 6. References

- [1] D. P. Heyman, M. J. Sobel, *Stochastic Models in Operations Research: Stochastic Optimization*, Courier Corporation, 2003.
- [2] C. Kahraman, *Fuzzy multi-criteria decision making: theory and applications with recent developments*, Springer Science & Business Media, 2008.
- [3] C. C. Coello, G. B. Lamont, D. A. Van Veldhuizen, *Evolutionary algorithms for solving multi-objective problems*, Springer Science & Business Media, 2007.
- [4] E. Zitzler, M. Laumanns, L. Thiele, *Spea2: Improving the strength pareto evolutionary algorithm*.
- [5] H. Sato, Y. Hasegawa, D. Bollegaia, H. Iba, *Improved sampling using loopy belief propagation for probabilistic model building genetic programming*, *Swarm and Evol. Comput.* 23 (2015) 1–10.
- [6] J. Rada-Vilela, M. Johnston, M. Zhang, *Population statistics for particle swarm optimization: Resampling methods in noisy optimization problems*, *Swarm and Evol. Comput.* 17 (2014) 37–59.
- [7] L. H. Lee, E. P. Chew, S. Teng, D. Goldsman, *Optimal computing budget allocation for multi-objective simulation models*, in: *Proc. 2004 Winter on Simulation Conf.*, Vol. 1, 2004, p. 594.
- [8] L. H. Lee, E. P. Chew, S. Teng, Y. Chen, *Multi-objective simulation-based evolutionary algorithm for an aircraft spare parts allocation problem*, *Eur. J. Oper. Res.* 189 (2) (2008) 476–491.
- [9] L. T. Bui, H. A. Abbass, D. Essam, *Fitness inheritance for noisy evolutionary multi-objective optimization*, in: *Proc. 7th Annu. Conf. Genetic and Evol. Comput.*, 2005, pp. 779–785.
- [10] H. Eskandari, C. D. Geiger, R. Bird, *Handling uncertainty in evolutionary multiobjective optimization: Spga*, in: *IEEE Congr. Evol. Comput.*, 2007, pp. 4130–4137.
- [11] A. Syberfeldt, A. Ng, R. I. John, P. Moore, *Evolutionary optimisation of noisy multi-objective problems using confidence-based dynamic resampling*, *Eur. J. Oper. Res.* 204 (3) (2010) 533–544.
- [12] K. Deb, S. Gupta, D. Daum, J. Branke, A. K. Mall, D. Padmanabhan, *Reliability-based optimization using evolutionary algorithms*, *IEEE Transactions on Evolutionary Computation* 13 (5) (2009) 1054–1074.
- [13] I. Elishakoff, M. Ohsaki, *Optimization and anti-optimization of structures under uncertainty*, World Scientific, 2010.
- [14] P. Boonma, J. Suzuki, *A confidence-based dominance operator in evolutionary algorithms for noisy multiobjective optimization problems*, in: *21st Int. Conf. Tools with Artificial Intell.*, 2009, pp. 387–394.
- [15] E. Zitzler, M. Laumanns, S. Bleuler, *A tutorial on evolutionary multiobjective optimization*, in: *Metaheuristics for multiobjective optimisation*, 2004, pp. 3–37.
- [16] M. Liu, A. M. Cramer, *Genetic algorithm with integrated computing budget allocation for stochastic problems*, *International Journal of Metaheuristics* 5 (2) (2016) 115–135.
- [17] D. He, L. H. Lee, C.-H. Chen, M. C. Fu, S. Wasserkrug, *Simulation optimization using the cross-entropy method with optimal computing budget allocation*, *ACM Trans. Modeling and Computer Simulation (TOMACS)* 20 (1) (2010) 4.
- [18] E. J. Chen, L. H. Lee, *A multi-objective selection procedure of determining a pareto set*, *Computers and Operations Research* 36 (6) (2009) 1872–1879.
- [19] Q.-S. Jia, *Efficient computing budget allocation for simulation-based policy improvement*, *IEEE Trans. Automation Science and Engineering* 9 (2) (2012) 342–352.
- [20] E. Zitzler, K. Deb, L. Thiele, *Comparison of multiobjective evolutionary algorithms: Empirical results*, *Evol. Comput.* 8 (2) (2000) 173–195.
- [21] K. Deb, L. Thiele, M. Laumanns, E. Zitzler, *Scalable Test Problems for Evolutionary Multiobjective Optimization*, Springer London, 2005, pp. 105–145.
- [22] K. Deb, L. Thiele, M. Laumanns, E. Zitzler, *Scalable multi-objective optimization test problems*, in: *Proc. Congr. Evol. Comput. (CEC-2002)*, 2002, pp. 825–830.
- [23] T. Goel, R. Vaidyanathan, R. T. Haftka, W. Shyy, N. V. Queipo, K. Tucker, *Response surface approximation of pareto optimal front in multi-objective optimization*, *Comput. Methods Appl. M.* 196 (4) (2007) 879–893.
- [24] C.-h. Chen, *Stochastic simulation optimization: an optimal computing budget allocation*, World Scientific, Singapore, 2010.
- [25] K. Deb, A. Pratap, S. Agarwal, T. Meyarivan, *A fast and elitist multiobjective genetic algorithm: Nsga-II*, *IEEE Tran. Evol. Comput.* 6 (2) (2002) 182–197.
- [26] C.-H. Chen, D. He, M. Fu, L. H. Lee, *Efficient selection of an optimal subset for optimization under uncertainty*, in: *Proc. 2007 INFORMS Simulation Society Research Workshop*, Vol. 28, 2007, pp. 1–297.
- [27] K. Deb, R. B. Agrawal, *Simulated binary crossover for continuous search space*, *Compl. Syst.* 9 (1994) 1–34.
- [28] Q. Zhang, A. Zhou, S. Zhao, P. N. Suganthan, W. Liu, S. Tiwari, *Multiobjective optimization test instances for the cec 2009 special session and competition*, University of Essex, Colchester, UK and Nanyang technological University, Singapore, special session on performance assessment of multi-objective optimization algorithms, technical report 264.
- [29] L. T. Bui, D. Essam, H. A. Abbass, D. Green, *Performance analysis of evolutionary multi-objective optimization methods in noisy environments*, in: *Proc. 8th Asia Pacific Symp. Intell. and Evol. Syst.*, 2004, pp. 29–39.
- [30] C. K. Goh, K. C. Tan, *An investigation on noisy environments in evolutionary multiobjective optimization*, *IEEE Tran. Evol. Comput.* 11 (3) (2007) 354–381.
- [31] T. Okabe, Y. Jin, B. Sendhoff, *A critical survey of performance indices for multi-objective optimisation*, in: *2003 Congr. Evol. Comput.*, Vol. 2, 2003, pp. 878–885.
- [32] X. Li, J. Branke, M. Kirley, *On performance metrics and particle swarm methods for dynamic multiobjective optimization problems*, in: *2007 Congr. Evol. Comput.*, 2007, pp. 576–583.
- [33] G. G. Yen, Z. He, *Performance metric ensemble for multiobjective evolutionary algorithms*, *IEEE Tran. Evol. Comput.* 18 (1) (2014) 131–144.
- [34] M. Siddiqui, *Statistical inference for rayleigh distributions*, *J. Res. NBS D Rad. Sci.* 68 (1964) 1005–1010.
- [35] Q. Zhang, H. Li, *Moea/d: A multiobjective evolutionary algorithm based on decomposition*, *IEEE Transactions on evolutionary computation* 11 (6) (2007) 712–731.
- [36] M. Fortunato, A. Giustiniani, G. Petrone, G. Spagnuolo, M. Vitelli, *Maximum power point tracking in a one-cycle-controlled single-stage photovoltaic inverter*, *IEEE Trans. Ind. Electron.* 55 (7) (2008) 2684–2693.
- [37] A. M. Cramer, S. D. Sudhoff, E. L. Zivi, *Performance metrics for electric warship integrated engineering plant battle damage response*, *IEEE Trans. Aero. Elec. Sys.* 47 (1) (2011) 634–646.
- [38] A. M. Cramer, S. D. Sudhoff, E. L. Zivi, *Metric optimization-based design of systems subject to hostile disruptions*, *IEEE Trans. Syst., Man, Cybern. A* 41 (5) (2011) 989–1000.